



Duncan, Anna (2019) *A search for top-antitop quark resonances with the ATLAS detector at the LHC*. PhD thesis.

<https://theses.gla.ac.uk/73014/>

Copyright and moral rights for this work are retained by the author

A copy can be downloaded for personal non-commercial research or study, without prior permission or charge

This work cannot be reproduced or quoted extensively from without first obtaining permission in writing from the author

The content must not be changed in any way or sold commercially in any format or medium without the formal permission of the author

When referring to this work, full bibliographic details including the author, title, awarding institution and date of the thesis must be given

Enlighten: Theses

<https://theses.gla.ac.uk/>
research-enlighten@glasgow.ac.uk



Ph. D. Thesis

A search for top-antitop quark resonances with
the ATLAS detector at the LHC

Anna Duncan

Submitted in fulfilment of the requirements for the
degree of Doctor of Philosophy

School of Physics and Astronomy
College of Science and Engineering
University of Glasgow

September 2018

Abstract

Various extensions to the Standard Model postulate the existence of heavy particles that decay to a top-antitop quark pair. If one of these particles exists with a mass of a few TeV then it may be produced during proton-proton collisions at the Large Hadron Collider (LHC). The analysis presented in this thesis searches 36 fb^{-1} of $\sqrt{s} = 13 \text{ TeV}$ proton-proton collision data collected by the ATLAS detector for evidence of a top-antitop quark resonance, and sets upper limits on the production cross section of new heavy particles in a set of benchmark models. The observed top-antitop quark invariant mass spectrum agrees well with the spectrum expected under the Standard Model and no evidence of a top-antitop quark resonance is found. A 1% width Z' boson in a topcolour-assisted technicolour model is observed to be excluded at masses below 3.0 TeV, a 30% (15%) width Kaluza-Klein gluon in a Randall-Sundrum model is observed to be excluded at masses below 3.7 TeV (3.8 TeV), and a 3-6% width Kaluza-Klein graviton in a Randall-Sundrum model is observed to be excluded in the mass interval $0.45 < m_{G_{KK}} < 0.65 \text{ TeV}$. Some techniques developed to improve the sensitivity of the analysis are described: a new method of electron-in-jet overlap removal and a reconstruction of semi-boosted and very boosted top-antitop quark decay topologies. A study evaluating the prospects of this search at the High Luminosity LHC is also presented. It estimates that a search of 3000 fb^{-1} of proton-proton collision data collected using an upgraded ATLAS detector will be able to exclude a Z' boson at masses below 4 TeV.

Contents

Abstract	i
Acknowledgements	xxii
Declaration	xxiii
1 Introduction	1
2 Theoretical Background	3
2.1 Quantum Field Theory Framework	3
2.2 The Standard Model	4
2.2.1 Field and Particle Content	5
2.2.2 Electroweak Theory and the Higgs Mechanism	6
2.2.3 Quantum Chromodynamics	10
2.2.4 Standard Model $t\bar{t}$ production	11
2.2.5 $t\bar{t}$ cross-section measurements	12
2.3 Beyond the Standard Model	12
2.4 Theory and the LHC	14
2.4.1 Proton-proton Collisions	14
2.4.2 Monte Carlo Event generation	15
2.4.3 Detector Simulation	17
3 The LHC and the ATLAS Experiment	18
3.1 Introduction	18
3.2 LHC	19
3.2.1 The Collider	19
3.2.2 The Collisions	20
3.3 ATLAS Detector	22
3.3.1 Introduction	22
3.3.2 Notes on the Coordinate System	24

3.3.3	Inner Detector	25
3.3.4	Calorimeters	27
3.3.5	Muon Spectrometer (MS)	31
3.3.6	Trigger System	33
4	Physics Objects	35
4.1	Tracks and Vertices	36
4.2	Electrons	38
4.2.1	Trigger	38
4.2.2	Reconstruction	38
4.2.3	Identification	39
4.2.4	Energy scale and resolution	42
4.3	Muons	42
4.3.1	Reconstruction	42
4.3.2	Identification	43
4.3.3	Efficiency Measurements	43
4.3.4	Momentum scale and resolution	44
4.4	Jets	44
4.4.1	Jet formation	44
4.4.2	Jet reconstruction: the anti- k_t algorithm	46
4.4.3	Types of Jet	47
4.4.4	Jet calibration	49
4.5	b -tagging	52
4.5.1	Impact-parameter based algorithms	53
4.5.2	Secondary Vertex Finding Algorithm	53
4.5.3	Decay Chain Multi-Vertex Algorithm	53
4.5.4	Multivariate Algorithm	54
4.6	Top Tagging	55
4.7	Missing Transverse Energy	55
4.8	Lepton Isolation	56
4.9	Overlap Removal	56
5	Statistical Methods	58
5.1	The Role of Statistics in Searches for New Physics	58
5.2	Quantifying the agreement between data and prediction	59
5.2.1	Trials Factor	61
5.3	Parameter Estimation in New Physics Searches	62
5.3.1	Confidence Intervals	62

5.3.2	Log-likelihood Ratio	63
5.3.3	Limit Setting with CL_s	64
5.3.4	Incorporating systematic uncertainties	66
6	A Search for $t\bar{t}$ resonances	68
6.1	Introduction	68
6.2	Object Definitions	70
6.2.1	Leptons	71
6.2.2	Jets and Missing Transverse Energy	71
6.2.3	Trimming parameters for large-R jets	72
6.2.4	Overlap Removal	72
6.3	Signal, Backgrounds and Data	74
6.3.1	Signal	74
6.3.2	Standard Model Backgrounds	75
6.3.3	Data	76
6.4	Data driven backgrounds	76
6.4.1	Multijets normalisation and kinematic distributions	76
6.4.2	W + jets normalisation and flavour components	77
6.5	Event Selection	79
6.5.1	Preselection	79
6.5.2	Boosted Selection	80
6.5.3	Resolved Selection	81
6.5.4	b -tag Categories	81
6.6	Event Reconstruction	82
6.6.1	Leptonically decaying W boson	82
6.6.2	Boosted Channel	83
6.6.3	Resolved Channel	83
6.7	Corrections applied to simulated events	84
6.8	Systematic Uncertainties	84
6.8.1	Luminosity and pile-up	85
6.8.2	Leptons	85
6.8.3	Jets	86
6.8.4	$t\bar{t}$ cross-section	86
6.8.5	Single top	86
6.8.6	W+jets	86
6.8.7	Multijets	87
6.9	Results	87

6.9.1	Compatibility of data with expectation	87
6.9.2	Limit Setting	95
7	Improving the sensitivity of the $t\bar{t}$ resonances search	100
7.1	Introduction	100
7.2	Electron in Jet Overlap Removal	100
7.2.1	Modified Overlap Removal Procedure: Electron-in-jet Subtraction . .	101
7.2.2	Determining the p_T cut with $Z \rightarrow ee$ events.	102
7.2.3	Impact on Signal Acceptance	103
7.2.4	Jet Performance	105
7.2.5	Electron Performance	106
7.2.6	Scale factor for electrons near jets	107
7.2.7	Impact on Sensitivity of the Search	114
7.3	Other Decay Topologies	115
7.3.1	Motivation	115
7.3.2	Very boosted events	119
7.3.3	Semi-boosted events	142
7.4	Summary	158
8	Prospects of a $t\bar{t}$ Resonances Search at the High Luminosity LHC	160
8.1	HL-LHC and the Phase-II Upgrade	160
8.2	$t\bar{t}$ Resonances Prospects Study	161
8.3	Signal and Background Samples	162
8.4	Detector Effects and Object Definitions	163
8.5	Event Selection	165
8.5.1	Boosted Channel	165
8.5.2	Resolved Channel	166
8.6	Event Reconstruction	166
8.7	Statistical Analysis and Results	167
9	Beam-Induced Background in the SCT	171
9.1	Introduction	171
9.2	Analysis with timing information	173
9.2.1	Characteristics of Beam-induced Background Events (Run 276689) .	173
9.3	Analysis Without Timing Information	184
9.3.1	Comparing 2015 and 2016	184
9.3.2	Pressure Bump Runs	185
9.3.3	BCM Trigger	191

9.4	Summary	197
9.4.1	Analysis with timing information	197
9.4.2	Analysis without timing information	198
9.4.3	Pressure Bump Runs	198
10	Summary	199

List of Tables

2.1	The fermions and their quantum numbers.	5
2.2	The bosons and their quantum numbers	6
6.1	The systematic uncertainties on the background yields resulting from each source that are the most significant in terms of percentage uncertainty. The sources of smaller uncertainties are left out.	85
6.2	Data and background yields in the boosted electron, boosted muon, resolved electron and resolved muons channel, and the systematic uncertainty on the background, after the background-only fit.	96
7.1	Values of Gaussian mean + 2σ from the Δp_T plots in Figure 1.2. These values - “cuts 1” - are used to indicate what p_T cut should be applied to the subtracted jet in the new overlap removal procedure. A default cut > 25 GeV is applied to all jets, including subtracted jets. A higher p_T cut is applied to the subtracted jet if the p_T of the original jet is sufficiently high.	103
7.2	Final p_T cuts (“cuts 3”) applied to subtracted jets to decide whether they will be removed from the event.	104
8.1	Systematic uncertainties on the signal and background yield in each channel.	167
8.2	Signal cutflows for 3000 fb^{-1} in the electron channel.	169
8.3	Signal cutflows for 3000 fb^{-1} in the muon channel.	169
8.4	Background cutflows for 3000 fb^{-1} in the electron channel.	169
8.5	Background cutflows for 3000 fb^{-1} in the muon channel.	169
9.1	Fraction of events selected as BIB in run 283270 (2015) and 300279 (2016). . .	185
9.2	Information about the pressure bumps in run 298771. The average bunch intensity was 0.99×10^{11} protons in beam 1 and 0.98×10^{11} protons in beam 2.	189
9.3	Fraction of events in run 298771 selected as BIB.	191
9.4	Information about the pressure bumps in run 301918. The average bunch intensity was 1.02×10^{11} protons in beam 1 and 1.07×10^{11} in beam 2.	192

9.5	Fraction of events in run 301918 selected as BIB.	192
9.6	Fraction of events passing the BCM trigger selected as BIB	197
9.7	Fraction of run 298771 events passing the BCM trigger selected as BIB. . . .	197
9.8	Fraction of run 301918 events passing the BCM trigger selected as BIB. . . .	197
9.9	Approximate average BIB occupancy contribution for each pair of end-cap disks.	198

List of Figures

2.1	Shape of the scalar field potential $V(\phi)$ with minima around the circle $\phi_3^2 + \phi_4^2 = \frac{-\mu^2}{\lambda}$ [14].	9
2.2	Feynman diagrams for the main $t\bar{t}$ production processes at the LHC [16]. . .	11
2.3	Possible $t\bar{t}$ decay modes after $t \rightarrow Wb$ [18].	12
2.4	A summary, taken from [21], of the latest $t\bar{t}$ production cross-section measurements made by ATLAS and CMS at $\sqrt{s} = 13$ TeV, with their uncertainties, compared to the Standard Model prediction calculated at NNLO and its theoretical uncertainty.	13
2.5	A diagram from [26] representing the simulation of a proton-proton collision. The incoming partons are shown in blue, with the location of the hard scatter marked by the red circle. The parton shower initiated by the hard scatter is shown in red; as the energy decreases, hadrons (in green) form. The underlying event is shown in purple and also results in outgoing hadrons.	16
3.1	A schematic of the LHC accelerator complex taken from [31].	21
3.2	A plot taken from [33] showing the luminosity contribution and mean number of interactions per crossing of LHC runs in 2015 and 2016. The average in-time pile-up $\langle\mu\rangle$ (i.e. the delivered luminosity weighted average mean number of interactions per crossing) over each year, and over both years combined, are labelled.	22
3.3	A schematic of the ATLAS detector taken from [34], showing the location of the subdetectors and the magnet systems.	24
3.4	A digram from [34] showing the layout of the ATLAS inner detector barrel sections and the radius of each layer from the centre. Closest to the beam is the insertable b-layer (IBL) followed by the rest of the pixel detector layers, the semiconductor tracker (SCT) and the transition radiation tracker (TRT).	26
3.5	A digagram from [35] showing the layout of the ATLAS calorimeter system.	28
3.6	A figure from [36] showing the accordion geometry of the absorber and active layers in calorimeter cells.	30

3.7	A diagram from [37] showing a tile calorimeter module. The tile calorimeter comprises 64 of these modules, segmented in ϕ and arranged in three longitudinal layers. The source tubes allow movable radioactive ^{137}Cs sources to pass through the calorimeter: the γ rays emitted by the sources have a well known energy, allowing the response of the scintillator tiles to be calibrated.	32
3.8	A diagram from [42] showing the layout of the subsystems inside the muon spectrometer.	34
4.1	Plots from reference [47] that show the fraction of electrons reconstructed from (a) simulated $Z \rightarrow ee$ events and (b) simulated dijet events that were identified as electrons by the loose, medium and tight identification algorithms. (a) shows the identification efficiencies with respect to reconstructed electrons, and (b) shows the misidentification rates with respect to reconstructed electrons. (In (b) the identification efficiency in the y axis refers to the probability to falsely identify a jet as an electron.)	40
4.2	A plot from [40] showing the efficiency of selecting muons from $Z \rightarrow \mu\mu$ events and $J/\psi \rightarrow \mu\mu$ events using the medium identification criteria in data and simulation.	44
4.3	A diagram from [52] showing the stages of jet formation from the hard-scatter to energy deposits in the calorimeters.	46
4.4	A plot from [53] showing the shapes of jets clustered using the anti- k_T algorithm with $R=1.0$. The shapes are regular and centred around the largest energy deposit. The red jet is an example of the anti- k_T algorithm applied to case 1 - a single hard constituent, isolated from other constituents by $> 2R$, surrounded by soft constituents - which results in a regular cone shape of radius ΔR around the original hard constituent. The blue jet is an example of case 2 - two hard constituents i and j with $\Delta_{ij} < R$, surrounded by soft constituents - which results in a slightly more irregularly shaped jet centred around the two hard constituents. The green and purple jets are an example of the algorithm applied to case 3 - two hard constituents i and j separated by $R < \Delta_{ij} < 2R$ - which results in two jets, the one centred on the hardest constituent having the most regular shape as the surrounding soft constituents are added to that jet first, and the one centred on the second hardest constituent having a more irregular shape as it loses some nearby constituents to the harder jet.	48
4.5	A schematic from [56] showing the series of calibrations applied to EM scale jets.	51

4.6	A plot from [60] showing the output of the MV2c10 BDT for b -jets, c -jets and light jets in simulated $t\bar{t}$ events.	54
5.1	Events were generated randomly according to the PDFs in equations 5.3 and 5.4, where H_0 had 1000 expected background events and H_1 had 1000 expected background events plus 100 expected signal events. The left hand side plot shows the distribution of the number of observed events in a bin, n_{obs} , under H_0 and H_1 . The right hand side plot shows the distribution of a test statistic t calculated from the number of observed events. The test statistic used here is the log likelihood ratio, defined in equation 5.17. The test statistic distribution is shifted to the left for H_1 , so the critical region is defined beginning in the left tail of the H_0 distribution and extends out to negative infinity.	60
5.2	CL_{s+b} and CL_s plotted against signal strength for positive (a) and negative (b) signal strengths, where the background only and signal plus background models are represented by equations 5.3 and 5.4 respectively. When the signal strength is large, it is clearer whether the data is more compatible with signal or background. CL_{s+b} and CL_s converge. When the signal strength is small, data that is very incompatible with the signal will also be incompatible with the background. In this case it is harder to exclude μ using CL_s	65
6.1	Semileptonic $t\bar{t}$ decay.	69
6.2	$t\bar{t}$ decay channel ratios.	69
6.3	Depiction of the change in hadronic top decay topology as the top p_T increases.	70
6.4	Mean and standard deviation (in GeV) of Gaussians fitted to the peaks of mass distributions of top-tagged large-R jets in Z' signal samples, for a range of combinations of the large-R jet trimming parameters f_{cut} (or f in the plots) and R_{sub} (or R in the plots).	73
6.5	The large-R jet mass distribution after trimming with parameters $f_{\text{cut}} = 0.05$ and $R_{\text{sub}} = 0.3$ was applied to top-tagged large-R jets in $Z' = 5$ TeV events: the large tails on the distribution should be taken into account when tuning the parameters.	74
6.6	Transverse momentum of the lepton. Data and simulation agree within the uncertainties. There is a small deficit of data events observed in the boosted channels and a small excess observed in the resolved channels, which may be explained by event generators predicting more $t\bar{t}$ events with high top quark p_T than are observed in data.	88

6.7	Missing transverse energy. There is a small deficit of data events observed in the boosted channels and a small excess observed in the resolved channels, which may be explained by event generators predicting more $t\bar{t}$ events with high top quark p_T than are observed in data.	89
6.8	Transverse momentum of the top-tagged large-R jet. There are fewer data events compared to simulated events and this disagreement increases with increasing large-R jet p_T . This is a feature observed in different event generators [84].	90
6.9	Mass of the leptonic top. There is a small deficit of data events observed in the boosted channels and a small excess observed in the resolved channels, which may be explained by event generators predicting more $t\bar{t}$ events with high top quark p_T than are observed in data.	91
6.10	Mass of the hadronic top. There is a small deficit of data events observed in the boosted channels and a small excess observed in the resolved channels, which may be explained by event generators predicting more $t\bar{t}$ events with high top quark p_T than are observed in data.	92
6.11	Invariant mass of the $t\bar{t}$ system in the boosted channel. There tends to be a small deficit of data events in each boosted channel, which may be explained by event generators predicting more $t\bar{t}$ events with high top quark p_T than are observed in data.	93
6.12	Invariant mass of the $t\bar{t}$ system in the resolved channel. There tends to be a small deficit of data events in each resolved channel, which may be explained by event generators predicting more $t\bar{t}$ events with high top quark p_T than are observed in data.	94
6.13	Observed and expected 95% CL limits on the cross-section \times branching ratio of the Z' boson for each signal mass point. The theoretical cross-sections are given to show the Z' masses that can be excluded: a 1% width Z' boson can be excluded for masses less than 3.0 TeV (2.6 TeV expected).	97
6.14	Observed and expected 95% CL limits on the cross-section \times branching ratio of the 15% width (left) and 30% width (right) Kaluza-Klein gluon for each signal mass point. The theoretical cross-sections are given to show the g_{KK} masses that can be excluded: a 15% width Kaluza-Klein gluon is excluded for masses less than 3.7 TeV (3.2 TeV expected) and a 30% width Kaluza-Klein gluon is excluded for masses less than 3.8 TeV (3.5 TeV expected).	98

6.15	Observed and expected 95% CL limits on the cross-section \times branching ratio of the Kaluza-Klein graviton for each signal mass point. The theoretical cross-sections are given to show the G_{KK} masses that can be excluded: a 3 – 6% width Kaluza-Klein graviton is excluded in the mass interval $0.45 < m_{G_{KK}} < 0.65$ TeV, as expected.	99
7.1	$\Delta R(\text{truth electron, truth } b\text{-jet})$ plotted against top quark p_T for simulated $t\bar{t}$ events and a 3 TeV Z' sample.	101
7.2	$\Delta p_T(\text{electron, jet})$ distributions (normalised to 1), where $\Delta R(\text{electron, jet}) < 0.4$, in simulated $Z \rightarrow ee$ events. The plots are separated by jet p_T range: 30-50 GeV, 50-100 GeV, 100-400 GeV, 400-800 GeV, > 800 GeV. It is assumed that the electron-jet pairs plotted here are reconstructions from the same (electron) energy cluster.	103
7.3	Event selection cutflows in the boosted electron, boosted muon, resolved electron and resolved muon channels, for each overlap removal method, with simulated SM $t\bar{t}$ events.	105
7.4	Event selection cutflows in the boosted electron, boosted muon, resolved electron and resolved muon channels, for each overlap removal method, with simulated Z' at 2 TeV events.	106
7.5	New/old signal acceptance ratio (equation 7.1) plotted against truth $m_{t\bar{t}}$ in each channel, shown for SM $t\bar{t}$ and two Z' samples.	107
7.6	Jet p_T resolutions plotted for subtracted jets, the same jets with no electron subtracted, and jets not involved in overlap removal.	108
7.7	Electron p_T resolution for electrons with $\Delta R(\text{electron, nearest jet}) \in (0.2, 0.4)$ and for electrons with $\Delta R(\text{electron, nearest jet}) > 0.4$	109
7.8	Electron identification efficiency in data for (a) egamma reference, (b) probes > 0.4 from jets and (c) probes < 0.4 from jets.	113
7.9	Electron identification efficiency in simulation for (a) egamma reference, (b) probes > 0.4 from jets and (c) probes < 0.4 from jets.	114
7.10	Data efficiency/ simulation efficiency for (a) egamma reference, (b) probes > 0.4 from jets and (c) probes < 0.4 from jets.	115
7.11	The efficiency of probes > 0.4 from jets ((a), (b)) and probes < 0.4 from jets ((c), (d)) plotted against probe p_T in two example η bins.	116
7.12	Expected 95% CL upper limits set on a Z' boson using standard overlap removal (black dashed line) and the subtraction method (red dashed line), shown for the boosted electron channel only on the left had side and all channels on the right hand side.	117

7.13	$t\bar{t}$ event selection efficiency for the boosted electron channel, resolved electron channel, and events that pass neither channel but do pass an electron channel preselection. The selection efficiency is shown in bins of truth $m_{t\bar{t}}$ after final state radiation (FSR).	118
7.14	$t\bar{t}$ event selection efficiency for the boosted muon channel, resolved muon channel, and events that pass neither channel but do pass a muon channel preselection. The selection efficiency is shown in bins of truth $m_{t\bar{t}}$ after final state radiation (FSR).	119
7.15	“Very boosted” scenario (right): the W_{had} decay and the b_{had} decay are detected inside two separate small-R jets. The small-R jet containing the W boson decay is expected to have mass > 60 GeV.	120
7.16	“Semi-boosted” scenario (middle): The W_{had} decay is detected inside one large-R jet, and the b_{had} decay is detected inside a nearby small-R hjet.	120
7.17	Truth $m_{t\bar{t}}$ distribution (after final state radiation) in the boosted electron, resolved electron and very boosted electron channel for SM $t\bar{t}$ and Z' samples. The proportion of very boosted events increases with Z' mass.	121
7.18	Truth $m_{t\bar{t}}$ distribution (after final state radiation) in the boosted muon, resolved muon and very boosted muon channel for SM $t\bar{t}$ and Z' samples. The proportion of very boosted events increases with Z' mass.	122
7.19	Truth $m_{t\bar{t}}$ distribution (after final state radiation) for boosted electron events, and boosted electron events that also meet the very boosted criteria (a small-R jet with mass > 60 GeV). The majority of boosted events from the $m_{Z'} = 2$ TeV and $m_{Z'} = 3$ TeV sample are also very boosted.	123
7.20	Truth $m_{t\bar{t}}$ distribution (after final state radiation) for boosted muon events, and boosted muon events that also meet the very boosted criteria (a small-R jet with mass > 60 GeV). The majority of boosted events from the $m_{Z'} = 2$ TeV and $m_{Z'} = 3$ TeV sample are also very boosted.	124

- 7.21 These plots show the masses of objects assumed to be part of the hadronic top quark decay: the high mass small-R jet (j_{hm}) and the large-R jet. These objects may be used alone or combined with another object in order to reconstruct t_{had} . The masses of these objects are considered in different scenarios to help understand which combination of objects should be used to reconstruct t_{had} . For example, if the j_{hm} (or the large-R jet) mass distribution peaked around m_{top} when there was no other nearby small-R jet to add to it, and peaked around m_W when there was, this would indicate how to reconstruct t_{had} in each scenario. For $t\bar{t}$ and $Z' = 1, 2, 3$ TeV events, these plots show the masses of j_{hm} and the closest large-R jet (if there is one within $\Delta R < 0.8$) in very boosted events in the case where there exists another small-R jet within $\Delta R < 2.0$ of j_{hm} (in black and blue respectively) and in the case where there is not (in pink and green respectively) (electron channel). 126
- 7.22 These plots show the masses of objects assumed to be part of the hadronic top quark decay: the high mass small-R jet (j_{hm}) and the large-R jet. These objects may be used alone or combined with another object in order to reconstruct t_{had} . The masses of these objects are considered in different scenarios to help understand which combination of objects should be used to reconstruct t_{had} . For example, if the j_{hm} (or the large-R jet) mass distribution peaked around m_{top} when there was no other nearby small-R jet to add to it, and peaked around m_W when there was, this would indicate how to reconstruct t_{had} in each scenario. For $t\bar{t}$ and $Z' = 1, 2, 3$ TeV events, these plots show the masses of j_{hm} and the closest large-R jet (if there is one within $\Delta R < 0.8$) in very boosted events in the case where there exists another small-R jet within $\Delta R < 2.0$ of j_{hm} (in black and blue respectively) and in the case where there is not (in pink and green respectively) (muon channel). 128
- 7.23 Mass distributions of j_{hm} , j_{hm} plus nearby small-R jet and large-R jet (electron channel). There is a peak in the mass distribution of the $j_{hm} +$ other small-R jet system around m_{top} as well as a long high mass tail indicating that the small-R jet need not always be added, and sometimes j_{hm} or the large-R jet should be used to reconstruct t_{had} instead. 129
- 7.24 Mass distributions of j_{hm} , j_{hm} plus nearby small-R jet and large-R jet (muon channel). There is a peak in the mass distribution of the $j_{hm} +$ other small-R jet system around m_{top} as well as a long high mass tail indicating that the small-R jet need not always be added, and sometimes j_{hm} or the large-R jet should be used to reconstruct t_{had} instead. 130
- 7.25 Mass distributions of the reconstructed t_{had} in the very boosted electron channel. 131

7.26	Mass distributions of the reconstructed t_{had} in the very boosted muon channel.	132
7.27	These plots explore the topology of very boosted events selected from a Z' at 2 TeV sample. They show the ΔR separation between j_{hm} and the truth-level quantities: the b quark decaying from t_{had} (b_h) and the two quarks decaying from W_{had} ($W_{1,h}$ and $W_{2,h}$). The top left hand side plot shows that many very boosted events do have the whole W_{had} decay inside j_{hm} . The top right and bottom left plots show that there are also events where the b_{had} decay and at least part of the W_{had} decay fall inside j_{hm} . The bottom right plot shows $\Delta R(W_{1,h}, W_{2,h})$ for events where $\Delta R(j_{\text{hm}}, b_h) < 0.4$, suggesting that sometimes j_{hm} contains the entire top quark decay.	133
7.28	t_{had} mass resolution for reconstruction methods (a) j_{hm} , (b) j_{hm} +small-R jet, and (c) large-R jet, and the final hybrid reconstruction method (electron channel).	134
7.29	t_{had} mass resolution for reconstruction methods (a) j_{hm} , (b) j_{hm} +small-R jet, and (c) large-R jet, and the final hybrid reconstruction method (muon channel).	135
7.30	t_{had} p_T resolution for reconstruction methods (a) j_{hm} , (b) j_{hm} +small-R jet, and (c) large-R jet, and the final hybrid reconstruction method (electron channel).	136
7.31	t_{had} p_T resolution for reconstruction methods (a) j_{hm} , (b) j_{hm} +small-R jet, and (c) large-R jet, and the final hybrid reconstruction method (muon channel).	137
7.32	$m_{t\bar{t}}$ resolution in the very boosted electron, boosted electron and resolved electron channels.	138
7.33	$m_{t\bar{t}}$ resolution in the very boosted muon, boosted muon and resolved muon channels.	139
7.34	$m_{t\bar{t}}$ resolution in the boosted electron channel for boosted events that also meet the very boosted criteria, using the standard boosted $m_{t\bar{t}}$ reconstruction method and the reconstruction method used in the very boosted channel.	140
7.35	$m_{t\bar{t}}$ resolution in the boosted muon channel for boosted events that also meet the very boosted criteria, using the standard boosted $m_{t\bar{t}}$ reconstruction method and the reconstruction method used in the very boosted channel.	141
7.36	Event selection efficiency of the very boosted electron, boosted electron and resolved electron channels.	142
7.37	Event selection efficiency of the very boosted electron, boosted electron and resolved muon channels.	143
7.38	Signal sensitivity (signal/background and signal/ $\sqrt{\text{background}}$) in the electron channels.	144
7.39	Signal sensitivity (signal/background and signal/ $\sqrt{\text{background}}$) in the muon channels.	145

7.40	Comparing electron channel signal sensitivity (signal/background and signal/ $\sqrt{\text{background}}$) with (3 channels) and without (2 channels) including the very boosted channel.	146
7.41	Comparing muon channel signal sensitivity (signal/background and signal/ $\sqrt{\text{background}}$) with (3 channels) and without (2 channels) including the very boosted channel.	147
7.42	Large-R jet mass plotted against τ_{32} (defined in section 4.6) in the boosted and in events that pass the semi-boosted preselection.	148
7.43	Reconstructing t_{had} in the semi-boosted electron channel and semi-boosted muon channel, for SM $t\bar{t}$ events, and for 1 TeV Z' events.	149
7.44	t_{had} mass resolution in the semi-boosted electron channel and semi-boosted muon channel, for SM $t\bar{t}$ events, and for 1 TeV Z' events.	150
7.45	$t_{\text{had}} p_T$ resolution in the semi-boosted electron channel and semi-boosted muon channel, for SM $t\bar{t}$ events, and for 1 TeV Z' events.	151
7.46	$m_{t\bar{t}}$ resolution in the semi-boosted channels (electron and muon) for SM $t\bar{t}$ events and 1 TeV Z' events.	152
7.47	Truth $m_{t\bar{t}}$ distribution in the semi-boosted channels (electron and muon) for SM $t\bar{t}$ events and 1 TeV Z' events.	153
7.48	Event selection efficiency in the boosted, semi-boosted and resolved channels for SM $t\bar{t}$ events and 1 TeV Z' events. The selection efficiency is shown in bins of truth $m_{t\bar{t}}$ after final state radiation (FSR).	154
7.49	Signal sensitivity (signal/background and signal/ $\sqrt{\text{background}}$) in the electron channels.	155
7.50	Signal sensitivity (signal/background and signal/ $\sqrt{\text{background}}$) in the muon channels.	156
7.51	Comparing electron channel signal sensitivity (signal/background and signal/ $\sqrt{\text{background}}$) with (3 channels) and without (2 channels) including the semi-boosted channel.	157
7.52	Comparing muon channel signal sensitivity (signal/background and signal/ $\sqrt{\text{background}}$) with (3 channels) and without (2 channels) including the semi-boosted channel.	158
8.1	Timeline of the LHC program [89]. The HL-LHC machinery and phase-II detector upgrades will be installed during long shutdown 3, prior to run 4. During run 4, the total integrated luminosity delivered by the LHC will be increased from 300 fb^{-1} to 3000 fb^{-1}	161
8.2	Ratios of parton luminosities in LHC collisions [90]. A $\sqrt{s} = 14 \text{ TeV}$ collision energy increases the luminosities by a factor of 10 compared to $\sqrt{s} = 7 \text{ TeV}$ for parton-parton centre of mass energies greater than 1.1 TeV.	162

- 8.3 The reconstructed mass spectrum of $t\bar{t}$ pairs selected from signal and background events in the resolved electron channel (top left), resolved muon channel (top right), boosted electron channel (bottom left) and boosted muon channel (bottom right), using simulated $\sqrt{s} = 14$ TeV p - p collisions with an integrated luminosity of 3000 fb^{-1} . The background normalisations are obtained from the theoretical cross-sections. The cross-sections of the signal samples, Z' (2 TeV) and Z' (3 TeV), are multiplied by 50 for visibility and shown on the boosted channel plots. These signals are not visible in the resolved channel, so a Z' (1 TeV) sample is shown on the resolved channel plots with its cross-section multiplied by 50. 168
- 8.4 The expected upper limits set on the cross-section \times branching ratio of the Topcolour Z' boson for masses 1-7 TeV, with (a) 300 fb^{-1} and (b) 3000 fb^{-1} of simulated $\sqrt{s} = 14$ TeV p - p collisions. The theoretical signal cross-section intersects with the 300 fb^{-1} limits line at $\simeq 3$ TeV and with the 3000 fb^{-1} line at $\simeq 4$ TeV. We can expect to exclude this resonance for $m_{Z'} < 3$ TeV after run 3 and $m_{Z'} < 4$ TeV after HL-LHC. 170
- 9.1 A figure from [97] showing a beam halo event in 3D. 172
- 9.2 A diagram of the inner detector showing the SCT end-cap disks and their distances from IP1, taken from reference [99]. 174
- 9.3 Distribution of the time bin pattern of hits in disks 7 and 8 of the SCT end-caps, during unpaired, isolated bunches. During beam 1 unpaired isolated bunches (a), there are fewer hits in the outer disks of end-cap A than end-cap C, and about 50% of end-cap A hits count as early hits, whereas the end-cap C hits are mostly in-time. The result is symmetrical for beam 2 (b). 175

- 9.4 The z -asymmetry distribution of (a) events during unpaired isolated bunches containing no primary vertices, (b) events during unpaired, isolated bunches containing a primary vertex, (c) events during non- unpaired, isolated bunches containing no primary vertices, (d) events during non- unpaired isolated bunches containing a primary vertex. Beam-induced background activity during unpaired, isolated bunches causes the high z -asymmetry of events in (a) and (b). In noise-only events (c), the distribution of hits should be random. The z -asymmetry distribution is approximately uniform, with statistical fluctuations. The peaks at $|z_{\text{asym}}| = 1$ in (a), (b) and (c) are a result of events where there are only hits in the outer disks of one end-cap. The peak at 0 is a result of events where there are no or an equal number of hits in the outer end-cap disks. Collision events (d) have a low z -asymmetry, centred on 0; asymmetric BIB effects are negligible compared to the symmetric collision hits. 176
- 9.5 The distribution of early hit multiplicity (a), (b), in the outer end-caps, and the distribution of in-time hit multiplicity (c), (d), (e), (f) in the outer end-caps in events during unpaired, isolated bunches. (a) and (b) show that the EC1 early hit multiplicity distribution has a peak at $N_{\text{early hits}} < 25$. This peak is due to events containing little or no BIB activity. The large tail of events with high early hit multiplicity is due to BIB events. The EC2 early hit multiplicity also has a peak at $N_{\text{early hits}} < 25$. This peak is larger than the peak for EC1, since both BIB and noise-only events have low early hit multiplicity in EC2. The EC2 in-time distribution peaks at low multiplicity, the contribution of noise-only events, and has a large tail, due to BIB. The EC1 in-time distribution also peaks at low multiplicity, due to noise-only events, with a smaller tail, a result of EC1 in-time hits during BIB events. Subfigures (e) and (f), zoomed-in versions of (c) and (d), show the in-time hit distributions at low in-time hit multiplicities; it can be seen that the EC1 and EC2 in-time distributions are similar in shape, but the effect is amplified for EC2 hits. The EC1 in-time hits tail extends to ~ 500 hits, the EC1 early hits tail extends to ~ 600 hits, and the EC2 in-time hits tail extends to ~ 4000 hits. 178

- 9.6 The early and in-time hit multiplicity distributions in each pair of end-cap disks are shown for events selected as BIB, and events not selected as BIB. This illustrates the relationship between the distance of the end-cap from IP1 and the average occupancy contribution from BIB. The distributions (b), (f), (j), (n), show that the EC2 early hit multiplicity distributions are very similar for selected and non-selected events, as these hits are from noise only. The distributions (a), (e), (i), (m), show that the average EC1 early hit multiplicity in selected events increases with the z distance of the disk from IP1. (c), (g), (k), (o), show that the average in-time EC1 hits is significantly greater in selected BIB events than noise events. This is expected for disks closer to IP1, as many BIB hits will arrive at the disk in-time with expected collision hits. The EC2 in-time distribution tail extends out to ~ 3000 hits for the inner disks, and decreases with distance from IP1, extending to ~ 600 hits for the outer disks, indicating that BIB hits still cause in-time EC1 hits in the outer disks. (d), (h), (l) and (p) show that the largest occupancy difference between selected BIB and noise events is the average EC2 in-time hit multiplicity, and this difference is present in all disks. 182
- 9.7 In-time outer end-cap hits plotted against early outer end-cap hits for all ((a), (d)), selected ((b), (e)), and non-selected ((f), (g)) unpaired, isolated beam 2 events. In-time outer EC1 hit multiplicity is proportional to early outer EC1 hit multiplicity in selected BIB events. The EC2 hits in selected BIB events are mainly in-time. 183
- 9.8 The average in-time EC1 hit multiplicity per UIBE (a), selected UIBE (b) and non-selected UIBE (c). The high in-time EC1 occupancy in BIB events appear to be uniformly distributed in lumi block and bcid. 184
- 9.9 EC1 and EC2 hit multiplicity distributions for events during unpaired, isolated bunches. The EC2 distribution has a peak at low multiplicity due to noise-only events, and a tail out to high multiplicity due to events with BIB activity. The EC1 distribution also has a peak at low multiplicity, and a smaller tail due to excess early and in-time EC1 hits in BIB events. 186
- 9.10 The z -asymmetry distributions for events during unpaired, isolated bunches, comprised of high z -asymmetry BIB events, and noise events with uniform z -asymmetry. The average BIB event z -asymmetry for beam 1 (2) has changed $+z \rightarrow -z$ ($-z \rightarrow +z$) because all hits, instead of early hits, are now used. . . 187

9.11	EC1 and EC2 hit multiplicity distributions for beam 1 and beam 2 UIBE in the 2015 and 2016 runs. Selected events have on average a larger EC1 and EC2 hit multiplicity than non-selected events. The greatest difference between noise and BIB events is the average EC2 hit multiplicity.	189
9.12	EC1 and EC2 hit multiplicity distributions for UIBE during lumi blocks corresponding to the 150 m, 58 m and 19 m pressure bumps, and during lumi blocks where there was no increase in pressure. The high multiplicity tails on the pressure bump distributions indicate that there are more high occupancy BIB events during pressure bumps.	191
9.13	z -asymmetry distributions for UIBE during the 150 m pressure bump, and with normal pressure. A larger fraction of high z -asymmetry events can be seen in the pressure bump plots.	192
9.14	Global phi distributions of end-cap hits for UIBE during the 150 m, 19 m and 58 m pressure bumps, and no pressure bump. A phi asymmetry can be seen in the EC2 hit distribution for events during the pressure bump.	193
9.15	End-cap hit multiplicity distributions for selected and non-selected BIB events during each pressure bump and no pressure bump.	196

Acknowledgements

First I'd like to thank my supervisor Craig Buttar for advising me on each of the projects I worked on throughout my research, for many helpful discussions and for reading my thesis. I'd also like to thank Danilo Ferreira de Lima and Saverio D'Auria for all their help in the $t\bar{t}$ resonances and non-collision background analyses, and for always answering my many questions. I am grateful to the rest of the $t\bar{t}$ resonances analysis team, and to everyone in the University of Glasgow's particle physics group. Finally, I want to thank the STFC for funding this research.

Declaration

The research presented in this thesis is the result of a collaborative effort and is built on past work of experimentalists and theorists within and outside the ATLAS collaboration. In particular, chapters 2-4 provide context for the analyses presented in later chapters and use results and plots from many different sources. I was part of the analysis team that carried out the $t\bar{t}$ resonances search in chapter 6 on behalf of the ATLAS collaboration, which has been published in [1]. I performed optimisation studies for the large-R jet trimming described in section 6.2, and studies on signal and background fitting functions for use in an unbinned version of the limit setting, which are not shown here. I carried out the electron-in-jet overlap removal studies in section 6.10 and developed the semi-boosted and very boosted channels described in section 6.11. The $t\bar{t}$ resonances HL-LHC prospects study in chapter 7, which has been made public in [2], and the beam-induced background study in chapter 8, which is documented here [3], were both performed by me.

Chapter 1

Introduction

The top quark, discovered at the Tevatron in 1995, is the heaviest known elementary particle. Its properties make it uniquely useful for studying Standard Model physics. It has a lifetime of approximately 0.5×10^{-24} s and at 173 GeV [4] is massive enough to decay to an on-shell W boson and a b quark - its preferred same-generation weak decay mode - meaning that the $t \rightarrow Wb$ decay has a branching ratio close to 100%. The top quark is the only quark to decay through the weak interaction before it has a chance to undergo hadronisation. It couples strongly to the Higgs boson, and the measurement of this coupling is an important part of characterising the Higgs.

Since its discovery, properties of the top quark, including its mass and the top-antitop quark ($t\bar{t}$) production cross-section, have been measured at the Tevatron and the Large Hadron Collider (LHC) with increasing precision. The top quark is also the focus of several searches for new physics. In particular, it would couple strongly to new heavy particles predicted to exist by theories of physics beyond the Standard Model. Evidence of such a particle would be a $t\bar{t}$ resonance - a local excess or deficit in the invariant mass spectrum of $t\bar{t}$ pairs produced in proton-proton collisions compared to Standard Model expectation - around the mass of the new particle.

In this thesis, a search for a $t\bar{t}$ resonance using $t\bar{t}$ pairs produced in $\sqrt{s} = 13$ TeV LHC proton-proton collisions with a total integrated luminosity of 36.1 fb^{-1} is presented. The invariant mass spectrum of the $t\bar{t}$ pairs is reconstructed using data collected by the ATLAS detector. The expected $t\bar{t}$ invariant mass spectrum is built from collisions simulated assuming the Standard Model is true. The results of the search are expressed as 95% CL upper limits on the cross-sections of new particles in a set of benchmark models: a narrow width Z' boson in a topcolour-assisted technicolour model [5], a Kaluza-Klein excitation of the gluon in a Randall-Sundrum (RS) model [6], and a Bulk RS graviton in an RS model [7].

Previous searches performed using data collected by ATLAS and CMS at $\sqrt{s} = 7$ TeV and 8 TeV placed constraints on the existence of these particles. A search of 20.3 fb^{-1} of $\sqrt{s} = 8$

TeV collision data collected by the ATLAS detector, using $t\bar{t}$ events in the semileptonic decay mode, excluded a 1.2% (3%) width Z' boson at masses below 1.8 TeV (2.3 TeV), and a 15.3% width Kaluza-Klein gluon at masses below 2.2 TeV [8]. A search of 19.6 fb^{-1} of $\sqrt{s} = 8$ TeV collision data collected by the CMS detector, which combined the three $t\bar{t}$ decay modes, excluded a 1.2% width Z' boson at masses below 2.4 TeV and a 15-20% width Kaluza-Klein gluon at masses below 2.8 TeV [9]. More recently, a search performed on 2.6 fb^{-1} of $\sqrt{s} = 13$ TeV collision data collected by the CMS detector, which combined the semileptonic and all-hadronic decay channels, excluded a 1% width Z' boson at masses below 2.5 TeV and a 17% width Kaluza Klein gluon at masses below 3.3 TeV [10].

Chapter 2 gives a brief summary of the Standard Model - the theoretical context in which we currently understand the top quark and $t\bar{t}$ production - and introduces some theories of physics beyond the standard model that predict $t\bar{t}$ resonances. Chapter 3 describes the LHC and the ATLAS experiment and Chapter 4 describes the physics objects that are created from ATLAS data in order to reconstruct $t\bar{t}$ events. Chapter 5 introduces the statistical methods used to compare the Standard Model $t\bar{t}$ mass spectrum to the data $t\bar{t}$ mass spectrum and subsequently set limits on the cross-sections of new particles. The $t\bar{t}$ resonances search is presented in Chapter 6. Chapter 7 is an account of a study carried out on the prospects of a $t\bar{t}$ search at the High-Luminosity LHC with the upgraded ATLAS detector. Chapter 8 contains a study on beam-induced background in ATLAS' Semiconductor Tracker. Finally, chapter 9 summarises the results of the $t\bar{t}$ resonances search and the outlook for future searches.

Chapter 2

Theoretical Background

The analysis presented in this thesis is one of many attempts to improve our understanding of the universe by exploring the boundaries of the best model of fundamental physics to date: the Standard Model of Particle Physics. An in depth description of this theory can be found in reference [11] The Standard Model describes a wide range of observed phenomena in terms of three fundamental interactions between particles: strong, weak and electromagnetic. Its predictions have been repeatedly confirmed in experiments of increasing precision, but it does not provide a complete description of nature. The most notable omission in the Standard Model is gravity. This omission is only acceptable because gravity has a negligible effect in particle interactions at presently accessible energies. Unfortunately, gravitational effects are not expected to become important until energies $\mathcal{O}(10^{16})$ TeV [12] (known as the Planck scale), and producing interactions at this energy is outside the scope of currently conceivable technology. Additionally, the Standard Model does not contain a candidate for dark matter or a source of matter-antimatter asymmetry. There are also aesthetical issues; odd features of the Standard Model that seem to warrant further explanation, pointing to underlying causes originating in a deeper theory. These include the little hierarchy problem, which states that the Higgs boson has an unnaturally small mass [13]. Assuming that the Standard Model holds up to the Planck scale, the Higgs boson's observed mass can only be explained with a suspicious amount of fine tuning. The hierarchy problem offers an incentive to search for new physics at the TeV scale which could restore naturalness to the Standard Model. This chapter will describe our current theoretical understanding of fundamental physics and top quark production.

2.1 Quantum Field Theory Framework

In a quantum field theory, it is fields, not particles, that are taken to be fundamental entities. Fields have a value at every spacetime point, $\phi_a(x^\mu)$, which can be scalar, spinor, or

higher rank tensor. Different types of fields give rise to different types of particles¹ upon quantisation. A field's dynamics are encoded in a Lagrangian: $L(t) = \int d^3x \mathcal{L}(\phi_a, \partial_\mu \phi_a)$; the Euler-Lagrange equations [11] specify the field's path through spacetime. Symmetries - transformations of the fields that leave the theory invariant - play a central role in quantum field theories. They are connected to conserved quantities and the dynamics of the theory. Noether's theorem [11] states that every continuous symmetry of the Lagrangian has an associated conservation law. Infinitesimal spacetime translations, rotations and Lorentz boosts physically change the field by an infinitesimal amount without affecting the Euler-Lagrange equations, and are associated with the conservation of energy-momentum, angular momentum, and the centre of mass' velocity respectively. Theories can also exhibit gauge symmetry; invariance under a gauge transformation. Gauge transformations are transformations of the field that are not physical but reflect a choice in the mathematical description of the field that can be used to write the same Lagrangian. For example, a field theory that is invariant under $\phi(x) \rightarrow \phi'(x) = \phi(x)e^{i\theta}$ is said to be symmetric under the U(1) gauge group [11]. Gauge transformations of a field can be global - the same transformation applied at every spacetime point, or local - spacetime dependent $\phi(x) \rightarrow \phi'(x) = e^{i\theta(x)}\phi(x)$. Invariance under global gauge transformations is associated with the conservation of internal quantities such as electric charge. The requirement of symmetry under local gauge transformations can be used to generate interactions in the Standard Model [11].

2.2 The Standard Model

The Standard Model is a quantum field theory whose Lagrangian is invariant under local $SU(3)_C \times SU(2)_L \times U(1)_Y$ gauge transformations of the fields [11]. It is also invariant under Poincare group transformations². A set of fields exists in the Standard Model whose particles are spin- $\frac{1}{2}$ particles, or *fermions*. They are called *matter fields*. Requiring symmetry of the matter field Lagrangians, $\mathcal{L}_{Matter,free}$, under $SU(2)_L \times U(1)_Y$ transformations gives rise to weak and electromagnetic interactions, while invariance under $SU(3)_C$ transformations gives rise to the strong interaction. This happens because the symmetry is achieved by introducing *gauge fields*, and modifying $\mathcal{L}_{Matter,free} \rightarrow \mathcal{L}_{Matter,int}$, where $\mathcal{L}_{Matter,int}$ contains interaction terms between matter fields mediated by gauge fields. The gauge fields are associated with spin-1 particles, or *bosons*. They are the photons, vector bosons and gluons that mediate the three fundamental interactions between particles. The gauge fields have their own Lagrangian, \mathcal{L}_{Gauge} . Finally, a scalar field, called the *Higgs field*, whose spin-0 particle is the Higgs boson,

¹The quantisation of scalar, spinor and vector fields gives rise to spin-0, spin- $\frac{1}{2}$ and spin-1 particles respectively.

²Poincare group transformations represent Lorentz boosts, translations and rotations.

	Generation			Quantum Numbers				
	1	2	3	I	I_3	Y	Q	C
Quarks	u_L	c_L	t_L	1/2	1/2	1/3	2/3	(r,g,b)
	d_L	s_L	b_L	1/2	-1/2	1/3	-1/3	(r,g,b)
	u_R	c_R	t_R	0	0	4/3	2/3	(r,g,b)
	d_R	s_R	b_R	0	0	-2/3	-1/3	(r,g,b)
Leptons	$\nu_{e,L}$	$\nu_{\mu,L}$	$\nu_{\tau,L}$	1/2	1/2	-1	0	none
	e_L	μ_L	τ_L	1/2	-1/2	-1	-1	none
	e_R	μ_R	τ_R	0	0	-2	-1	none

Table 2.1: The fermions and their quantum numbers.

is introduced to explain the breaking of the $SU(2)_L \times U(1)_Y$ symmetry that leads the vector bosons to acquire mass. The Higgs field has a Lagrangian, \mathcal{L}_{Higgs} , and interactions with matter fields determined by \mathcal{L}_{Yukawa} . The following sections will describe the field content of the Standard Model and how their dynamics combine in the Standard Model Lagrangian:

$$\mathcal{L}_{SM} = \mathcal{L}_{Matter,int} + \mathcal{L}_{Gauge} + \mathcal{L}_{Yukawa} + \mathcal{L}_{Higgs} \quad (2.1)$$

2.2.1 Field and Particle Content

Particles are distinguished by the following quantum numbers: colour charge C , weak isospin I , weak hypercharge Y and electric charge Q , and by mass. The fermions are divided into quarks and leptons based on whether they have colour charge. Quarks and leptons are both divided into flavour types based on I_3 (the 3rd component of I) and electric charge Q . This splits the quarks and the leptons in two i.e. there are two flavour types of quarks³ and two flavour types of leptons. However, a mass hierarchy is also observed. There are three copies of each flavour type; particles with exactly the same quantum numbers but different mass. These copies are known as generations (the first generation being the lightest) and lead to six flavours of quarks and six flavours of leptons. Finally, since only left-handed particles possess weak isospin, it is convenient to further divide the quark and lepton flavours based on left and right handedness⁴. The fermions and their quantum properties are summarised in Table 2.1.

The subscripts in the Standard Model symmetry group $SU(3)_C \times SU(2)_L \times U(1)_Y$ indicate which configurations of the matter fields undergo the gauge transformation, and by extension which particles experience the resulting interaction. $SU(2)_L \times U(1)_Y$ transformations act on left-handed weak isospin doublets - pairs of fermion fields with identical Y and I and different

³The flavour types of quarks are called up-type and down-type

⁴Right handed neutrinos are not included in the Standard Model because none have been found in nature. The left-handed neutrinos are assumed to be massless in the Standard Model although observed neutrino oscillations imply that they have a non-zero mass

Interaction	Boson	Spin	I	I_3	Y	Q	C
electromagnetic	γ	1	0	0	0	0	none
weak	W^\pm	1	± 1	± 1	0	± 1	none
	Z	1	0	0	0	0	none
strong	g	1	0	0	0	0	$c\bar{c}'$ (c=r,g,b)
none	Higgs, h	0	$-\frac{1}{2}$	$-\frac{1}{2}$	1	0	none

Table 2.2: The bosons and their quantum numbers

I_3 ($\pm\frac{1}{2}$) - and right-handed singlets. The left-handed doublet fields and right-handed singlet fields are denoted ψ_L and ψ_R respectively and comprise:

$$\begin{array}{cccccc}
 \begin{pmatrix} u \\ d \end{pmatrix}_L & \begin{pmatrix} c \\ s \end{pmatrix}_L & \begin{pmatrix} t \\ b \end{pmatrix}_L & \begin{pmatrix} \nu_e \\ e \end{pmatrix}_L & \begin{pmatrix} \nu_\mu \\ \mu \end{pmatrix}_L & \begin{pmatrix} \nu_\tau \\ \tau \end{pmatrix}_L \\
 u_R & c_R & t_R & e_R & \mu_R & \tau_R \\
 d_R & s_R & b_R & & &
 \end{array}$$

$SU(3)_C$ acts on colour triplets of quarks and colour singlets of leptons.

The gauge fields arising from the $U(1)_Y$ and $SU(2)_L$ symmetries, $B_\mu(x)$ and W_μ^a ($a = 1, 2, 3$), have $Y = 1$ and $I = 1$ respectively. Due to the spontaneous breaking of the $SU(2)_L \times U(1)_Y$ symmetry, described in the next section, the physical gauge fields are linear combinations of $B_\mu(x)$ and W_μ^a . The physical spin-1 bosons are the photon γ , and the W^\pm and Z vector bosons, and they possess electric charge $Q = I_3 + Y/2$. The fields associated with $SU(3)_C$ symmetry carry two colour charges; their particles are called gluons. The last field is a scalar field called the Higgs field, which is responsible for the $SU(2)_L \times U(1)_Y$ symmetry breaking. Its particle is a spin-0 Higgs boson. The boson content of the Standard Model is summarised in Table 2.2.

For each particle in the Standard Model there is a corresponding *anti-particle* with the same mass and opposite quantum numbers. These particles are collectively known as *antimatter*. A particle may or may not be its own anti-particle, depending on its quantum numbers.

2.2.2 Electroweak Theory and the Higgs Mechanism

Quantum electrodynamics (QED) is the prototype gauge invariant field theory. Consider the Dirac Lagrangian, which describes free fields associated with spin- $\frac{1}{2}$ charged particles:

$$\mathcal{L}_{\text{Dirac}} = \bar{\psi}(i\gamma^\mu\partial_\mu - m)\psi \quad (2.2)$$

Imposing the condition of invariance under local U(1) gauge transformations, $\psi \rightarrow \psi' = e^{-i\theta(x)}\psi$ and $\bar{\psi} \rightarrow \bar{\psi}' = e^{-i\theta(x)}\bar{\psi}$, necessitates the introduction of a covariant derivative

$$D_\mu\psi = (\partial_\mu + ieA_\mu)\psi \quad (2.3)$$

to replace ∂_μ in the Dirac Lagrangian, which recovers invariance provided the gauge field A_μ transforms as

$$A_\mu(x) \rightarrow A'_\mu(x) + \frac{1}{e}\partial_\mu\theta(x) \quad (2.4)$$

A_μ is interpreted as the electromagnetic field (equation 2.4 is the transformation of the vector potential that leaves Maxwell's equations invariant). By adding the electromagnetic field Lagrangian to the modified $\mathcal{L}_{\text{Dirac}}$, the full U(1) invariant QED Lagrangian is written:

$$\mathcal{L}_{QED} = \bar{\psi}i\gamma^\mu(\partial_\mu + ieA_\mu)\psi - m\bar{\psi}\psi - \frac{1}{4}F_{\mu\nu}F^{\mu\nu} \quad (2.5)$$

where $F_{\mu\nu} = \partial_\mu A_\nu - \partial_\nu A_\mu$ is the electromagnetic field strength tensor.

The same principle is applied to generate the remaining fundamental interactions. A symmetry of the matter field Lagrangian is postulated and a covariant derivative is invoked to achieve this symmetry. This generates gauge fields and interaction terms. The number of gauge fields is the number of unique generators of the symmetry group. In general, a symmetry group with a generators T_a has a associated fields, V_μ^a , that appear in the covariant derivative, $D_\mu = \partial_\mu + igT_a V_\mu^a$, and have field strength $F_{\mu\nu}^a = \partial_\mu V_\nu^a - \partial_\nu V_\mu^a + g\epsilon^{abc}V_\mu^b V_\nu^c$. g is the coupling constant of the interaction.

The Lagrangian for free matter fields, written in terms of spinors ⁵, ψ , is:

$$\mathcal{L} = i\bar{\psi}\gamma^\mu\partial_\mu\psi \quad (2.6)$$

Together, transformations of the left and right handed fields, ψ_L and ψ_R , under $SU(2)_L$:

$$\psi_L \rightarrow e^{i\alpha(x)\cdot T}\psi_L \quad (2.7)$$

$$\psi_R \rightarrow \psi_R \quad (2.8)$$

and $U(1)_Y$:

$$\psi_L \rightarrow e^{i\beta(x)Y(\psi_L)}\psi_L \quad (2.9)$$

$$\psi_R \rightarrow e^{i\beta(x)Y(\psi_R)}\psi_R \quad (2.10)$$

⁵Two-component Weyl spinors that transform under $SU(2)_L \times U(1)_Y$. Fermion fields are naturally written as Weyl spinors in electroweak theory as it is a chiral theory; this is not necessary for developing the QED Lagrangian in equation 2.5.

are denoted as transformations under $SU(2)_L \times U(1)_Y$, where $\mathbf{T} = (T^1, T^2, T^3)$ are the generators of $SU(2)_L$, $\mathbf{Y}(\psi)$ is the weak hypercharge of the field ψ , and $\alpha(x)$ and $\beta(x)$ are arbitrary three-component and one-component functions of spacetime respectively. Requiring local invariance of the free matter field Lagrangian under $SU(2)_L \times U(1)_Y$ yields the covariant derivative:

$$D_\mu \psi = (\partial_\mu - ig_1 W_\mu^a T^a - ig_2 Y(\psi) B_\mu) \psi \quad (2.11)$$

with gauge fields $W_\mu^a = (W_\mu^1, W_\mu^2, W_\mu^3)$ and B_μ . Including all left-handed and right-handed fermion fields and kinetic gauge field terms, the electroweak Lagrangian is:

$$\mathcal{L}_{EW} = \sum_{\psi_L} i \bar{\psi}_{Lj} \gamma^\mu D_\mu \psi_L^j + \sum_{\psi_R} i \bar{\psi}_{Rj} \gamma^\mu D_\mu \psi_R^j - \frac{1}{4} W^{a\mu\nu} W_{\mu\nu}^a - \frac{1}{4} B^{\mu\nu} B_{\mu\nu} \quad (2.12)$$

where

$$W_{\mu\nu}^a = \partial_\mu W_\nu^a - \partial_\nu W_\mu^a + g\epsilon^{abc} W_\mu^b W_\nu^c \quad (2.13)$$

$$B_{\mu\nu} = \partial_\mu B_\nu - \partial_\nu B_\mu \quad (2.14)$$

The mass eigenstates of the electroweak field - the physical bosons - are related to the gauge fields by:

$$W_\mu^\pm = \frac{1}{\sqrt{2}} (W_\mu^1 \mp iW_\mu^2) \quad (2.15)$$

$$A_\mu = B_\mu \cos \theta_W + W_\mu^3 \sin \theta_W \quad (2.16)$$

$$Z_\mu = -B_\mu \sin \theta_W + W_\mu^3 \cos \theta_W \quad (2.17)$$

where θ_W is the weak mixing angle.

\mathcal{L}_{EW} has no mass terms for the gauge fields, but empirically three of the spin-1 boson (W^\pm and Z) are massive. Adding mass terms for these fields, as well as for the fermion fields, destroys the gauge invariance. The mechanism that breaks the electroweak symmetry, allowing the vector bosons to acquire mass, is the Higgs mechanism. A doublet of charged and neutral complex scalar fields is introduced:

$$\phi = \begin{pmatrix} \phi^+ \\ \phi^- \end{pmatrix} = \frac{1}{\sqrt{2}} \begin{pmatrix} \phi_1 + i\phi_2 \\ \phi_3 + i\phi_4 \end{pmatrix} \quad (2.18)$$

with Lagrangian

$$\mathcal{L}_{Higgs} = D_\mu \phi D^\mu \phi - V(\phi) \quad (2.19)$$

$$V(\phi) = \mu^2 \phi^\dagger \phi + \lambda (\phi^\dagger \phi)^2. \quad (2.20)$$

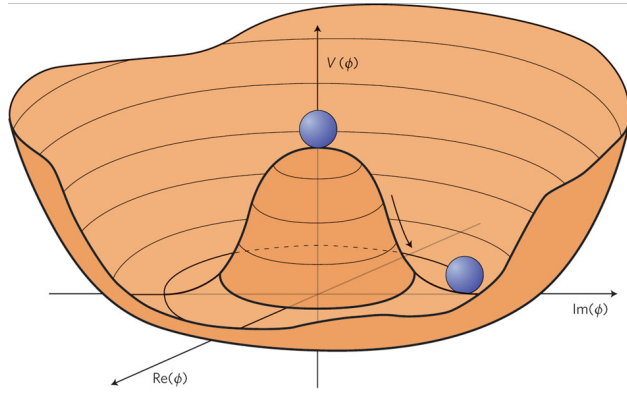


Figure 2.1: Shape of the scalar field potential $V(\phi)$ with minima around the circle $\phi_3^2 + \phi_4^2 = \frac{-\mu^2}{\lambda}$ [14].

which has a kinetic, mass and self-interaction term. If $\mu^2 < 0$ and $\lambda^2 > 0$, then $V(\phi)$ has a shape shown in Figure 2.1 and is at a minimum when $\phi^\dagger \phi = -\frac{\mu^2}{2\lambda}$. There is a continuum of configurations of ϕ that minimise $V(\phi)$, lying on a circle of radius $v = \sqrt{\frac{-\mu^2}{\lambda}}$. By setting $\phi_1 = \phi_2 = \phi_3 = 0$ and letting ϕ_4 have the non-zero vacuum expectation value v , ϕ can be written as:

$$\langle 0|\phi|0\rangle = \frac{1}{\sqrt{2}} \begin{pmatrix} 0 \\ v \end{pmatrix} \quad (2.21)$$

and expanded around its minimum:

$$\phi(x) = \frac{1}{\sqrt{2}} \begin{pmatrix} 0 \\ v + h(x) \end{pmatrix}. \quad (2.22)$$

Writing out the Higgs Lagrangian for ϕ using the electroweak covariant derivative in equation 2.11 gives

$$\frac{1}{2}(\partial_\mu h)^2 + \frac{g_2^2}{8}(v+h)^2 W_\mu^+ W^{\mu-} + \frac{1}{8}(v+h)^2(g_1^2 + g_2^2)Z_\mu Z^\mu - \frac{\mu^2}{2}(v+h)^2 - \frac{\lambda}{4}(v+h)^4. \quad (2.23)$$

Interaction with ϕ_3 , the Higgs field, has generated mass terms for three of the four electroweak gauge bosons:

$$m_{W^\pm} = \frac{g_2 v}{2} \quad m_Z = \frac{1}{2}v\sqrt{g_1^2 + g_2^2} \quad m_\gamma = 0 \quad (2.24)$$

The four degrees of freedom introduced with the complex scalar field doublet are manifest in the masses of the W^\pm and Z bosons, which gain three polarisation degrees of freedom, and one massive Higgs boson with $m_H = \sqrt{2\mu^2}$. The Higgs field also interacts with the matter fields, generating mass terms for each fermion. Higgs-fermion interactions are called Yukawa

couplings and make up the section of the Standard Model described by \mathcal{L}_{Yukawa} .

2.2.3 Quantum Chromodynamics

$SU(3)_C$ transformations are written:

$$\psi \rightarrow e^{i\kappa(x)\cdot\mathbf{t}}\psi \quad (2.25)$$

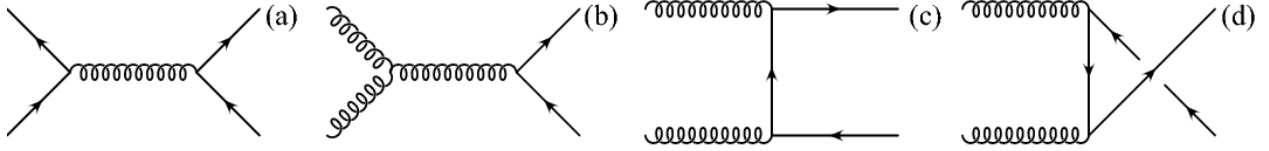
where ψ are colour triplets of quarks, t^a are the eight $SU(3)$ generators and $\kappa(x)$ is an eight component vector of arbitrary functions of spacetime. Imposing $SU(3)_C$ invariance necessitates an addition to the covariant derivative:

$$D_\mu\psi = (\partial_\mu - ig_1W_\mu^aT^a - ig_2Y(\psi)B_\mu)\psi - (ig_3G_\mu^at^a)\psi \quad (2.26)$$

where G_μ^a are the eight gauge fields whose particles carry a colour and anticolour charge, and g_3 is the strong coupling constant. Again, the physical bosons of the strong interaction - the gluons - are superpositions of G_μ^a , carrying superpositions of colour - anticolour charges. The new interaction terms in $\mathcal{L}_{Matter,int}$ mediated by gluons are between colour carrying particles, so quarks are the only strongly interacting fermions. The fact that gluons also carry colour means they are self-interacting. The kinetic term for the gluon fields is $-\frac{1}{4}F_{\mu\nu}^aF^{\mu\nu,a}$, where

$$F_{\mu\nu}^a = \partial_\mu G_\nu^a - \partial_\nu G_\mu^a + g_3\epsilon^{abc}G_\mu^bG_\nu^c. \quad (2.27)$$

The theory of strong interactions is known as Quantum Chromodynamics (QCD). In QCD, the distance behaviour of the coupling constant, α_S , leads to a phenomenon called quark confinement. The gluon self-interaction term drives the effective coupling constant up as the distance scale increases (this is in contrast to the effective electromagnetic coupling constant, for example, which decreases and then levels off as the distance scale increases). At very short distances, such as immediately after a quark-antiquark pair is produced in a high energy collision, quarks act as if they are free, and can be treated perturbatively (this is called asymptotic freedom). However, as pair produced quarks or bound quarks move away from each other, the potential energy between them quickly increases to the point that the probability of quark pair production approaches 1. This means that free quarks are never directly detected. It is the bound states - mesons and hadrons - that are detected, and they are always observed to be colourless. Long range QCD processes are known as hadronisation and are discussed in Chapter 4.

Figure 2.2: Feynman diagrams for the main $t\bar{t}$ production processes at the LHC [16].

2.2.4 Standard Model $t\bar{t}$ production

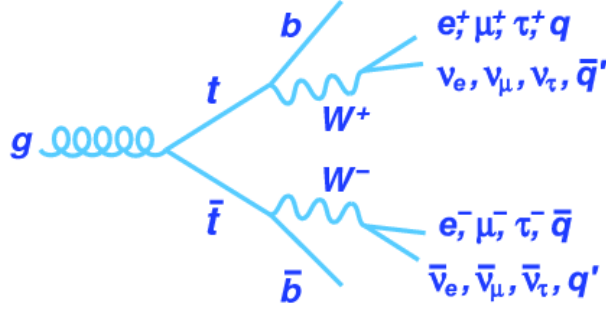
The top quark is the heaviest particle in the Standard Model. It is produced at the LHC mainly through the strong processes shown in Figure 2.2, with (b), (c) and (d) accounting for $\sim 90\%$ of the production [15].

The weak interaction couples up type quarks to the weak eigenstates of the down-type quarks, i.e. up to down, charm to strange and top to bottom, with the same interaction strength. The non-diagonality of the Yukawa coupling matrix, which gives the quark mass terms in \mathcal{L}_{Yukawa} , implies that the weak interaction eigenstates are mixtures of the mass eigenstates. The W^\pm bosons mediate interactions between linear combinations of the mass eigenstates. The weak eigenstates are related to the mass eigenstates by the Cabbibo-Kobayashi-Maskawa (CKM) matrix:

$$\begin{pmatrix} d' \\ s' \\ b' \end{pmatrix} = V_{CKM} \begin{pmatrix} d \\ s \\ b \end{pmatrix} = \begin{pmatrix} V_{ud} & V_{us} & V_{ub} \\ V_{cd} & V_{cs} & V_{cb} \\ V_{td} & V_{ts} & V_{tb} \end{pmatrix} \begin{pmatrix} d \\ s \\ b \end{pmatrix} \quad (2.28)$$

The elements of the CKM matrix give the branching fractions for W boson mediated transitions between up-type and down-type quarks. The fraction of times a top quark decays to a bottom quark is $|V_{tb}|^2$, where $|V_{tb}|$ is measured to be 1.019 ± 0.025 (averaged over Tevatron and LHC measurements) [17]. $t \rightarrow Wb$ is often assumed to be the exclusive decay mode in physics analyses because $t \rightarrow Ws$ and $t \rightarrow Wd$ are very rare. The top quark is the only quark that does not undergo hadronisation. With a lifetime around of 5×10^{-25} s, it decays via the weak interaction before confinement takes effect [4]. This leaves three decay modes available for study, shown in Figure 2.3, whose branching ratios are determined by the branching ratios of the W boson decays [4]:

Dileptonic: $t\bar{t} \rightarrow W^+bW^- \bar{b} \rightarrow \bar{\ell}\nu_\ell b\ell' b\ell' \bar{\nu}_{\ell'} \bar{b}$	BR=10.5%
Semileptonic: $t\bar{t} \rightarrow W^+bW^- \bar{b} \rightarrow q\bar{q}' b\ell^- \bar{\nu}_\ell \bar{b} + \ell^+ \nu_\ell b q'' \bar{q}''' \bar{b}$	BR=43.8%
All-hadronic: $t\bar{t} \rightarrow W^+bW^- \bar{b} \rightarrow q\bar{q}' b q'' \bar{q}''' \bar{b}$	BR=45.7%

Figure 2.3: Possible $t\bar{t}$ decay modes after $t \rightarrow Wb$ [18].

2.2.5 $t\bar{t}$ cross-section measurements

An accurate estimate of the $t\bar{t}$ cross-section, $\sigma_{t\bar{t}}$, is necessary for simulating the expected Standard Model background in a $t\bar{t}$ resonances search. Precision measurements of $\sigma_{t\bar{t}}$ have been made at the LHC [19]. These include the inclusive $t\bar{t}$ cross-section in all decay channels, differential cross-sections, and the cross-section of $t\bar{t}$ plus additional jets. The $t\bar{t}$ cross-section can be calculated from:

$$\sigma = \frac{N_{\text{total}} - N_{\text{background}}}{A\epsilon \int \mathcal{L}} \quad (2.29)$$

where N_{total} is the number of selected $t\bar{t}$ events, $N_{\text{background}}$ is the estimated number of non- $t\bar{t}$ events that pass the selection, A is the fraction of $t\bar{t}$ events that are accepted by the detector, ϵ is the efficiency for selecting these events, and $\int \mathcal{L}$ is the total integrated luminosity from which the $t\bar{t}$ events were selected. A measurement performed on 3.2 fb^{-1} of $\sqrt{s} = 13 \text{ TeV}$ proton-proton collision data collected by the ATLAS detector reported the $t\bar{t}$ cross-section in the semileptonic decay channel to be $818 \pm 8 \text{ (stat)} \pm 27 \text{ (syst)} \pm 19 \text{ (luminosity) pb}$ [4]. This is consistent with the Standard Model prediction of $832^{+40}_{-46} \text{ pb}$ at next-to-next-to-leading order (NNLO) + next-to-next-to-leading logarithmic order (NNLL) [20]. The plot in Figure 2.4 summarises the latest $t\bar{t}$ production cross-section measurements made using $\sqrt{s} = 13 \text{ TeV}$ proton-proton collision data along with the Standard Model prediction of the cross-section calculated at NNLO.

2.3 Beyond the Standard Model

Theories of physics Beyond the Standard Model, or BSM theories, are a set of theories that make similar predictions to the Standard Model at energy scales and precision levels already

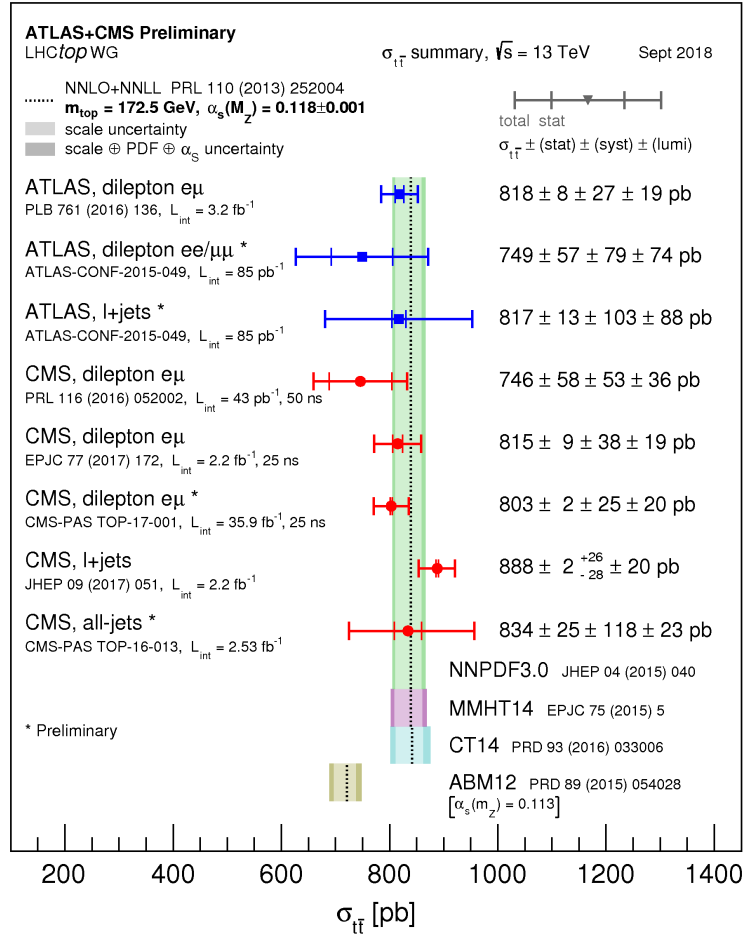


Figure 2.4: A summary, taken from [21], of the latest $t\bar{t}$ production cross-section measurements made by ATLAS and CMS at $\sqrt{s} = 13$ TeV, with their uncertainties, compared to the Standard Model prediction calculated at NNLO and its theoretical uncertainty.

probed by experiments, but make diverging predictions in other scenarios. BSM theories contain a range of new physics including new fields, interactions and dimensions. They are often extensions of the SM, reducing the SM to a low energy approximation and unifying the strong and electroweak interactions. BSM theories are regarded as well-motivated if they solve known SM problems. Of particular interest are the ones that predict new phenomena potentially accessible at the LHC. A possible approach to BSM searches is to look for $t\bar{t}$ resonances, which can arise in a range of models such as Topcolour-assisted Technicolour (TCT) [5] and Randall-Sundrum (RS) models. TCT extends the Standard Model gauge group, leading to a new gauge interaction and a spin-1 gauge boson, Z' , which decays to a top-antitop quark pair. TCT explains electroweak symmetry breaking (EWSB) dynamically, with a bound state performing the function of the Higgs boson. RS models include gravity and posit a warped extra dimension, with the SM particles existing on a three dimensional brane. RS models explain the scale difference between gravity and the SM interactions; gravity is not significantly weaker but its effects are observed to be weaker on the brane. RS models contain spin-2 Kaluza-Klein gravitons and spin-1 Kaluza-Klein gluons which both decay to a top-antitop quark pair.

2.4 Theory and the LHC

In order to ascertain whether any BSM physics has been observed in LHC collision data, it is necessary to have a reliable prediction of what SM physics would look like in data. QFT provides the tools to calculate interaction cross-sections and decay rates inside the SM. A good theoretical understanding of proton-proton collisions, which involve interactions over a range of energy scales, is also required so that the cross-sections can be calculated in the correct context. SM pseudodata is generated by simulating collisions, and the subsequent hadronisation and decays of outgoing particles, using Monte Carlo techniques. Interactions between long-lived simulated particles and the detector are modelled so that they have as close an experience as possible to the real particles. Physics analyses are applied to the real and simulated data, revealing any differences between observation and SM prediction. BSM pseudodata can be generated according to a chosen model in the same way.

2.4.1 Proton-proton Collisions

Protons are comprised of a stable combination of two up quarks and one down quark, called valence quarks, plus transitory sea quarks and gluons which arise as gluons mediating the interactions between the valence quarks split, resulting in the production and annihilation of off-shell quark pairs. A proton's momentum is shared between its valence and

sea partons. Parton distribution functions, $f_q(x, Q^2)$, give the probability of a parton with flavour q to carry a fraction $x \in [0, 1]$ of the proton's momentum at an energy scale Q . They parameterise the non-perturbative interactions between the partons inside the proton. High energy interactions between colliding partons are perturbative. These perturbative and non-perturbative elements are combined in proton-proton cross-section calculations by using the factorisation theorem. The factorisation theorem states that the cross-section of a collision to produce a particular final state X , $pp \rightarrow X$, is given by the following expression:

$$\sigma_{pp \rightarrow X}(Q^2) = \sum_{i,j}^{\text{parton flavours}} \int_0^1 \int_0^1 dx_1 dx_2 f_i(x_1, Q^2) f_j(x_2, Q^2) \hat{\sigma}_{ij \rightarrow X}(Q^2) \quad (2.30)$$

where f_i, f_j are the parton distribution functions, x_1, x_2 are the momentum fractions and $\sigma_{ij \rightarrow X}$ are the parton-level perturbative cross-sections for the process. An inelastic, perturbative parton-parton interaction during a proton-proton collision is referred to as a hard-scatter, and additional non-perturbative interactions are called soft-scatters.

2.4.2 Monte Carlo Event generation

Samples of proton-proton collision pseudodata are generated using Monte Carlo (MC) techniques. Incoming partons are selected from the parton distribution functions. The parton level cross-sections in equation 2.30 are obtained by calculating the matrix elements (ME) using perturbation theory to a predecided order. Partons emerging from the simulated hard-scatter simulation undergo parton showering. DGLAP equations [22] give probabilities for quark and gluon emissions of initial and final state partons. This stage approximates higher order corrections to the ME calculation. The cascade of decreasing energy parton emissions ceases when colour confinement takes effect. At this point hadronisation - the process of partons becoming confined in bound states - is simulated with phenomenological models such as the cluster model [23] and the string model [24]. Decays of certain hadrons before they reach the detector are also simulated. In addition to the hard scatter, the remainder of an LHC collision, called the underlying event, must be modelled. The underlying event comprises soft-scatter interactions between the remaining partons in the colliding protons. There are also instances where more than one hard parton-parton scatter occurs in the same proton-proton collision. Proton-proton collisions involving more than one hard-scatter are called multiple parton interactions [25]. The modelling of the underlying event is informed by data collected during minimum bias events (events collected with no high momentum final state filter applied), most of which do not contain a hard-scatter. Jet data is also used to parameterise the underlying event in the hard scatter. The diagram in Figure 2.5 visualises the different stages of simulating a proton-proton collision.

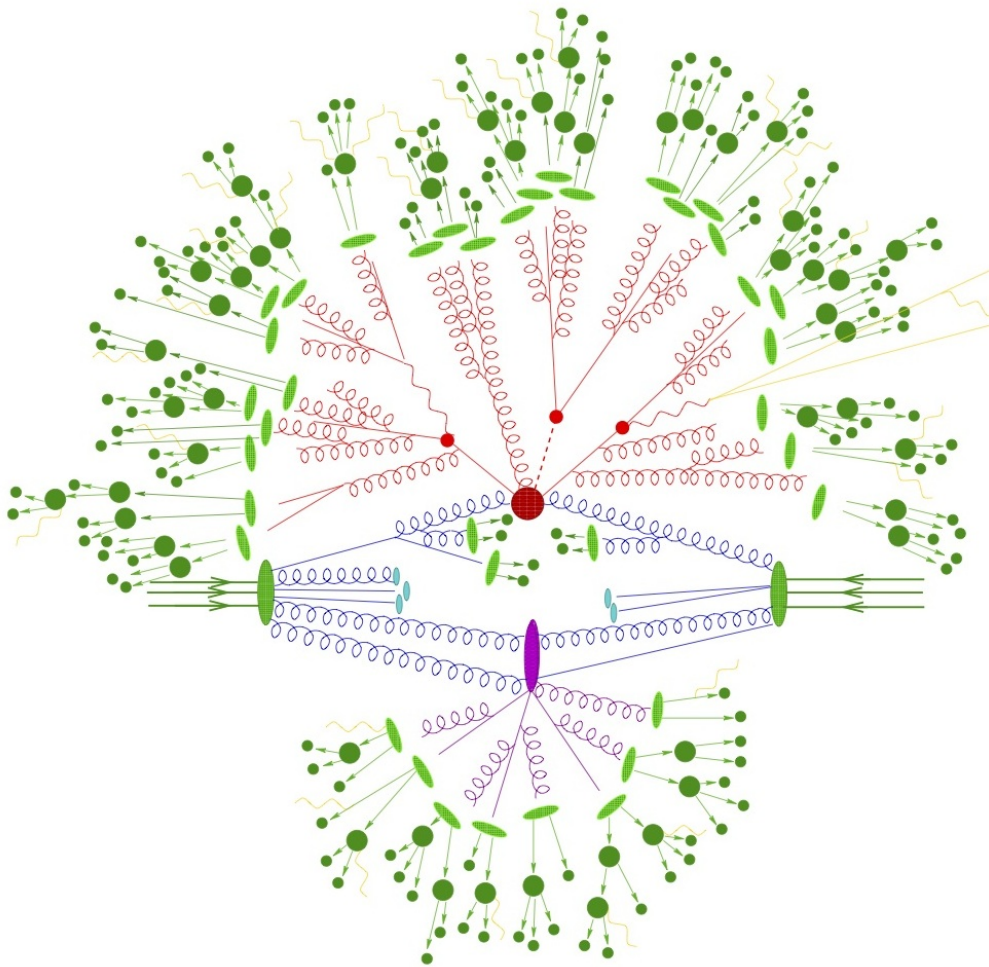


Figure 2.5: A diagram from [26] representing the simulation of a proton-proton collision. The incoming partons are shown in blue, with the location of the hard scatter marked by the red circle. The parton shower initiated by the hard scatter is shown in red; as the energy decreases, hadrons (in green) form. The underlying event is shown in purple and also results in outgoing hadrons.

2.4.3 Detector Simulation

Interactions between particles that reach the detector and the detector material are modelled for simulated particles using GEANT4 [27] software. This stage is referred to as *full simulation* because all sensing material and non-sensing material in the detector is modelled. The simulation of particles interacting with the active material, of signal generation in the detector and of the read out of those signals lead to energy and momentum measurements of simulated particles that reflect measurements made by the real detector. Full simulation is designed to make the simulated data look like the raw data obtained from the real detector, so that reconstruction procedures for physics objects and events can be used both for real and simulated data. This process is computationally intensive and time consuming. A faster method [28], sometimes used to complement GEANT4, employs full simulation except for interactions with the calorimeters where parameterised models are used. Differences between reconstructed physics objects in data and simulation which are a result of deficiencies in the detector simulation are corrected by applying scale factors to the simulated events, ensuring the same average performance of the detector for data and simulation.

Chapter 3

The LHC and the ATLAS Experiment

3.1 Introduction

In the era of the Standard Model, particle collider experiments are considered to be a promising way to directly observe signature of new physics such as new particles. They allow BSM models to be tested directly, by probing interactions at previously untested energy scales, and indirectly, through precise measurements of processes which have so far proved to be consistent with the Standard Model. They are the only known means of systematic exploration of high energy particle interactions¹ and can produce huge amounts of statistics for stress-testing the SM to an unprecedented degree.

With current collider technology it is possible to accelerate and collide combinations of protons, anti-protons, electrons, positrons and heavy ions e.g. gold or lead nuclei². Lepton-lepton colliders are useful for precision measurements because the colliding particles are fundamental; the centre of mass energy is known and can be finely tuned to maximise the rate of the physics process being studied, and hence there is relatively little background. However, synchrotron radiation - electromagnetic radiation emitted by charged particles when their paths are bent by a magnetic field - is a limiting factor in the energy that can be achieved and is experienced more severely by lighter particles. Composite particles are collided in hadron-hadron colliders; the energies of the interacting partons are varying and unknown, but greater energies can be reached due to less synchrotron radiation and there is more scope for producing new particles. Processes of interest must be deciphered from a large background in hadron colliders. The Large Hadron Collider was constructed with the aim of discovering the Higgs boson, and TeV scale physics beyond the Standard Model. Therefore protons are collided in the LHC, giving access to a myriad of physics processes at high energies.

¹Cosmic rays reach higher energies but are unpredictable and rare so limited knowledge can be gained from studying them.

²Depending on technological developments, muon colliders may be a future possibility.

Particle accelerators come in three main types: linear accelerators, cyclotrons, and synchrotrons, all of which operate on the same principle: energy is imparted to charged particles when they are accelerated through an electric field. The electric fields are normally generated by applying an alternating voltage to electrodes that the particle travels between and through, the particle's energy increasing in steps with each cycle. The energy that can be achieved by accelerating a particle through successive electric fields inside a linear accelerator is limited by the accelerator's length, while cyclotrons use a magnetic field to bend the particle's path, enabling it to return to, and repeatedly undergo acceleration through, the sole alternating electric field, as it travels outwards from the centre in a spiral path. Synchrotrons are specially designed to accelerate particles to relativistic speeds around a circular path. The frequency of the alternating fields must be synchronised and the strength of the path-bending magnetic field must be increased as the particle accelerates around the synchrotron, to account for the fact that the particle's motion follows relativistic equations, and keep the radius of the path constant.

3.2 LHC

3.2.1 The Collider

The Large Hadron Collider (LHC), located 100 m underground beneath the Franco-Swiss border, is the world's most powerful particle collider at the time of writing. An accelerator complex [29] comprising various stages, illustrated in Figure 3.1, is required to achieve the final LHC collision energy. Hydrogen atoms inside a storage cylinder are released in groups and make their way to the source chamber of a linear accelerator called LINAC2 where they undergo ionisation. The resulting protons are accelerated inside LINAC2, reaching an energy of 50 MeV, before they are delivered to the Proton Synchrotron Booster (PSB) - four synchrotron rings 157 m in circumference - which accelerates four groups simultaneously until they reach 1.4 GeV. From the PSB the protons are sent to the Proton Synchrotron (PS), where they are accelerated around the 628 m circumference - here they acquire the well-defined bunch structure that the LHC is designed to work with. Upon exiting the PS, the 25 GeV proton bunches are injected into the Super Proton Synchrotron (SPS), almost 7 km in circumference, where they reach 450 GeV before finally graduating to the LHC - a synchrotron of circumference ~ 27 km.

Inside the LHC, bunches are sent down one of two evacuated beryllium pipes until there are two beams filled with 2808 bunches³, one circulating clockwise and one anticlockwise.

³The LHC filling scheme (number of bunches in a train, bunch spacing etc.) is intended to achieve the desired luminosity while accounting for the LHC's design (e.g. it ensures that the bunches do not pass through the LHC's kicker magnets - which accelerate the bunches as they enter and leave the ring - while

Superconducting dipole electromagnets cooled with liquid helium keep the beams on their circular path. A variety of other electromagnets are used for beam manipulation. The bunches experience accelerating boosts inside 16 radio frequency (RF) cavities (chambers containing an oscillating electromagnetic field) around the LHC until they reach 6.5 GeV. The frequency of the oscillations is such that when the protons that have reached the target energy they no longer undergo acceleration, while protons with lower (higher) energy arrive outside the expected time and are accelerated (decelerated), helping to maintain the bunch structure.

The beams are made to collide at interaction points (IP) inside four caverns which house the main LHC experiments: ATLAS, CMS, LHCb and ALICE. Bunches containing up to 10^{11} protons are collided every 25 ns by squeezing them down to a width of 16 microns and crossing them, a configuration that corresponds to the design instantaneous luminosity: $L = 10^{34} \text{ cm}^{-2}\text{s}^{-1}$. This results in ~ 20 proton-proton interactions per bunch crossing. Colliding bunches are left largely intact and can be circulated for many hours until the intensity of the bunches degrade enough that the beams are dumped. The time it takes for the intensity of the beam to decrease to $1/e$ of its initial value is called the lifetime of the beam and is usually around ten hours [30].

3.2.2 The Collisions

The physics of proton-proton (p - p) collisions is covered in Chapter 2, but there are some terms and concepts particular to LHC collisions, and relevant to the analysis of the data, that should be introduced. As of run 2, the centre of mass energy of LHC p - p collisions is $\sqrt{s} = 13 \text{ TeV}$, with the interacting partons each carrying some fraction of the nominal 6.5 TeV proton energy. Run 1 saw collisions with $\sqrt{s} = 7 \text{ TeV}$ and $\sqrt{s} = 8 \text{ TeV}$; the final target is $\sqrt{s} = 14 \text{ TeV}$ which should be achieved in 2021. The parton-parton centre of mass energy dictates the cross-section of each type of interaction; it is hoped that increasing \sqrt{s} will bring about the production of particles with masses $\mathcal{O}(\text{TeV})$. In addition to high energy interactions, a large number of interactions may be necessary for access to new physics because the highest energy parton-parton interactions are rare. This is accomplished by optimising the rate of interactions over the available time. Given an interaction i with a fixed cross-section σ_i , its rate (number of interactions per second) is $L \times \sigma_i$, where the proportionality factor L is the instantaneous luminosity - the number of particles travelling through unit area (cm^2) per unit time (s). While many interesting processes are abundant at the LHC due to the collision energy, some kinematically allowed processes are suppressed by dynamical mechanisms. Instantaneous luminosity is then the means by which rare processes they ramp up).

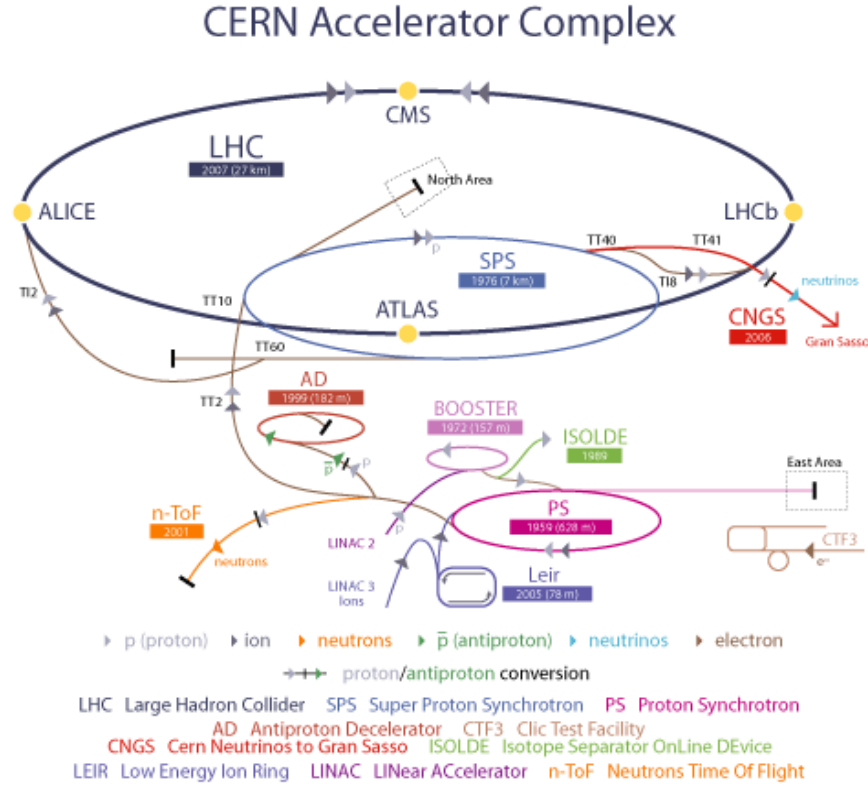


Figure 3.1: A schematic of the LHC accelerator complex taken from [31].

are amplified, and it can be modified via the beam configuration [32]:

$$L = \frac{n_p^2 n_b f}{4\pi\sigma_x\sigma_y} F \quad (3.1)$$

This luminosity equation assumes two identical colliding beams, whose densities have a Gaussian distribution in the x-y plane, comprised of n_b bunches and n_p protons per bunch, with revolution frequency f , and gaussian widths σ_x and σ_y . F is a factor that accounts for the reduction in luminosity, compared to a head-on collision, due to the crossing angle of the beams. *Total integrated luminosity*, $\mathcal{L} = \int L dt$, is the measure of the amount of data delivered by the LHC over a given time dt . The total number of occurrences of a process i , n_i , is given by $n_i = \mathcal{L} \times \sigma_i$. Larger instantaneous luminosities yield more integrated luminosity over a fixed time, which translates to more statistics for physics analyses. However, increasing the instantaneous luminosity comes at a cost: more p - p interactions in the same bunch crossing. Ideally, one bunch crossing would correspond to one high energy parton-parton interaction, referred to as the *event* and classified by the type of interaction that occurred. All the information collected by the detector during a bunch crossing could be used to reconstruct the event. In reality, hard-scatter events suffer contamination from other soft p - p interactions in the same bunch crossing, known as *in-time pile-up*, and from p - p interactions in adjacent

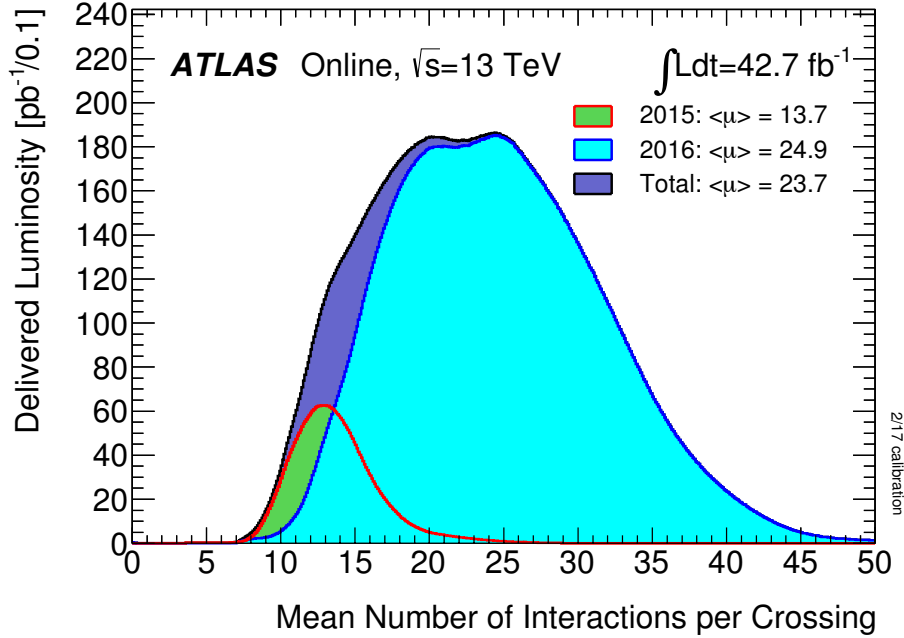


Figure 3.2: A plot taken from [33] showing the luminosity contribution and mean number of interactions per crossing of LHC runs in 2015 and 2016. The average in-time pile-up $\langle\mu\rangle$ (i.e. the delivered luminosity weighted average mean number of interactions per crossing) over each year, and over both years combined, are labelled.

bunch crossings, known as *out-of-time pile-up*. At current LHC luminosities, there are an average of around 23.7 proton-proton interactions per bunch crossing, denoted $\langle\mu\rangle = 23.7$. Figure 3.2 shows the luminosity contribution and average in-time pile-up of 2015 and 2016 LHC runs. There are also soft interactions in the proton-proton collision that contains the hard scatter; the soft part is known as the underlying event. *Vertices* are the locations of the proton-proton interactions that take place during a bunch crossing, and are used as a tool for deciphering the hard-scatter from pile-up.

3.3 ATLAS Detector

3.3.1 Introduction

The ATLAS detector resides inside a cavern at LHC Point 1 and occupies a cylindrical volume 25 m in diameter and 45 m long. It is oriented along the beam axis with the nominal interaction point at its centre. ATLAS is a general purpose detector in the sense that it is intended to search for any manifestations of new physics whether it be heavy particles that are produced directly or more subtle BSM processes whose effects may only be detected through precision measurements. ATLAS fulfils its purpose by collecting as much information

as possible from the output of collisions, namely the type and kinematics of particles that interacted with the detector, so that a full picture of the physics processes that occurred can be built. The features that allow ATLAS to do this well include:

- **Geometry:** ATLAS covers as much of the solid angle around the interaction point as is practical so that almost all particles produced in a hard-scatter must traverse the detector. This is important for a reliable calculation of missing transverse energy from which the presence of non or very weakly interacting particles can be inferred (see Chapter 4).
- **Subdetectors and magnet system:** three subdetectors - the inner detector, the calorimeters, and the muon spectrometer - are designed so that the presence and properties of different types of particles can be determined. The subdetectors operate in parallel with a magnet system which bends the trajectories of charged particles allowing their momenta to be calculated.
- **Proximity to beam pipe:** the first layer of the detector is 33.25 mm from the beam axis; this is crucial for distinguishing between primary, pile-up and secondary vertices in a busy environment.
- **High granularity:** small sensor elements provide good 2D position (ATLAS' first layer has a spatial resolution of 40 μm in z and 8 μm in $R\phi$), momentum and energy resolution, and control occupancy in high multiplicity collisions (there are ~ 1000 outgoing particles per bunch crossing within the inner detector coverage).
- **Minimal material:** the material encountered by particles before they reach the calorimeters is kept to a minimum so that the inner detector can track particles without compromising their energy measurement.
- **Radiation hardness:** sensors and readout electronics that are able to withstand LHC running conditions without significant deterioration so that good data quality can be maintained throughout the experiment's lifetime.
- **Trigger system:** allows the ATLAS readout system to cope with extremely large data rates by selecting a subset of interesting events to record; the rest are discarded.

The ATLAS subdetectors are arranged as a series of concentric cylindrical barrels and disk-shaped end-caps of increasing radius from the interaction point. A schematic is shown in Figure 3.3. The ATLAS coordinate system and subsystems are described in the following subsections.

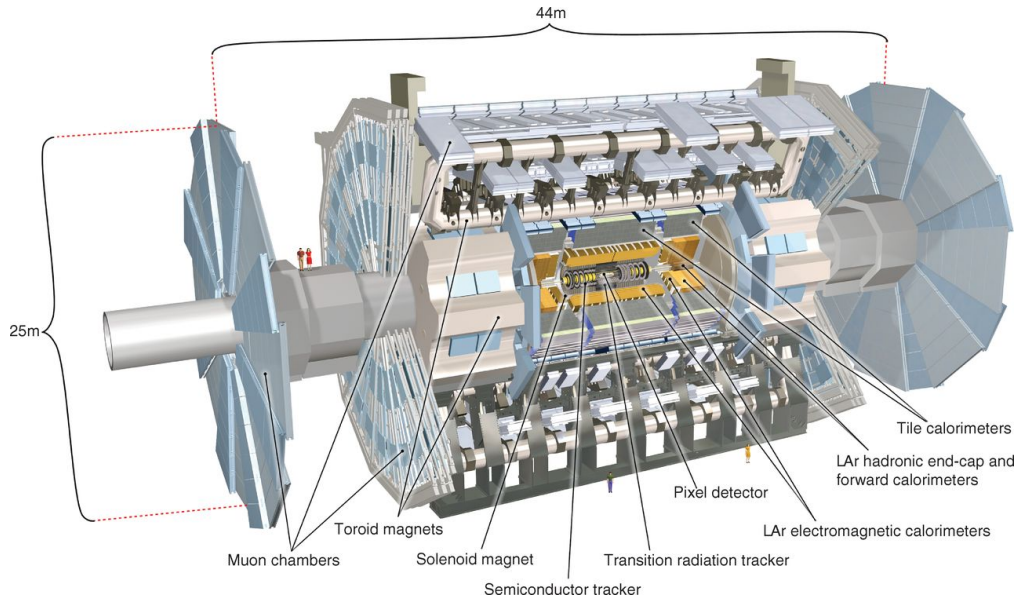


Figure 3.3: A schematic of the ATLAS detector taken from [34], showing the location of the subdetectors and the magnet systems.

3.3.2 Notes on the Coordinate System

Spatial positions in ATLAS are specified using a right-handed coordinate system with the nominal interaction point as the origin, the z -axis oriented along the beam axis and the x -axis and y -axis pointing to the centre of the LHC ring and upwards respectively. The azimuthal angle ϕ is measured in the $x - y$ plane around the z -axis and the polar angle θ is measured from the beam axis in the $y - z$ plane. Another measure of angular direction in the $y - z$ plane is the pseudorapidity $\eta = -\log_e(\tan \frac{\theta}{2})$ (starting at $\eta = 0$ perpendicular to the z -axis and tending to $\pm\infty$ moving towards the $\pm z$ -axis). A combination of spatial position and energy measurements are used to establish a four-momentum for each particle, (p_x, p_y, p_z, E) , or, equivalently, (p_T, η, ϕ, E) . The transverse momentum, $p_T = \sqrt{p_x^2 + p_y^2}$, is useful because it is invariant with respect to Lorentz boosts along the z -axis and balanced in p - p collisions. η tends to be used in favour of θ because it approximates to rapidity:

$$y = \frac{1}{2} \log_e \left(\frac{E + p_z c}{E - p_z c} \right)$$

, and differences in rapidities are invariant with respect to boosts along the z -axis, in the relativistic limit. Rapidity differences, Δy , and pseudorapidity differences, $\Delta \eta$, between particles emitted in a collision are therefore invariant with respect to boosts along the beam axis. This kind of Lorentz invariance is useful because the centre of mass frames of collisions travel with different velocities with respect to the rest frame of the experiment; these quantities can be used as they are measured in the ATLAS coordinate system without having to account for

boosts along the z -axis. A commonly used observable is the separation between the direction of two objects in (η, ϕ) space, ΔR :

$$\Delta R = \sqrt{\Delta\eta^2 + \Delta\phi^2} \quad (3.2)$$

which has the Lorentz invariance of $\Delta\eta$ and $\Delta\phi$. Transverse quantities, such as transverse momentum p_T and transverse energy E_T , from projections onto the $x - y$ plane are indicated with a subscript T .

3.3.3 Inner Detector

After exiting the interaction point and crossing the beam pipe, particles encounter the inner detector (ID) which comprises (in order of increasing distance from the interaction point) the pixel detector, the semi-conductor tracker (SCT) and the transition radiation tracker (TRT), and is immersed in a uniform 2 T solenoidal magnetic field provided by the thin superconducting solenoid magnet which encompasses it. It covers a pseudorapidity region $|\eta| < 2.5$; the layout is shown in Figure 3.4. The function of the inner detector is to track charged particles - record their trajectories as they traverse the detector - without impeding them so that their energies can be measured at a later stage. The magnetic field bends charged particles' trajectories so that their momentum and charge can be calculated from the curvature of their track. Interactions between particles and the inner detector are known as hits; the pixel detector and the SCT have very small, discrete sensor elements so that each recorded hit corresponds to precise spatial information that can be combined to reconstruct a trajectory. The TRT provides additional spatial information for tracking and contributes to electron identification. In addition to performing high precision momentum measurements, the inner detector is central to the reconstruction of vertices, as these are obtained by projecting tracks backwards towards the collision point.

Pixel Detector

There are four barrel and three end-cap layers of pixel detector. The innermost layer, the Insertable B-layer (IBL), lies 33.25 mm from the beam axis and plays a vital role in the location of vertices. Pixel sensors are finely segmented in $(z, r - \phi)$ in the barrel and $(\phi - z, r)$ in the end-caps. IBL pixels have area $50 \mu\text{m} \times 259 \mu\text{m}$ and intrinsic spatial resolution $8 \mu\text{m} \times 40 \mu\text{m}$, and the rest have area $50 \mu\text{m} \times 400 \mu\text{m}$ and intrinsic spatial resolution $10 \mu\text{m} \times 115 \mu\text{m}$. Sensor elements are bump-bonded to readout electronics and mounted on rectangular modules. Particles incident on the depletion region around a sensor's p-n junction generate a number of electron-hole pairs (proportional to the particle's energy) that drift towards

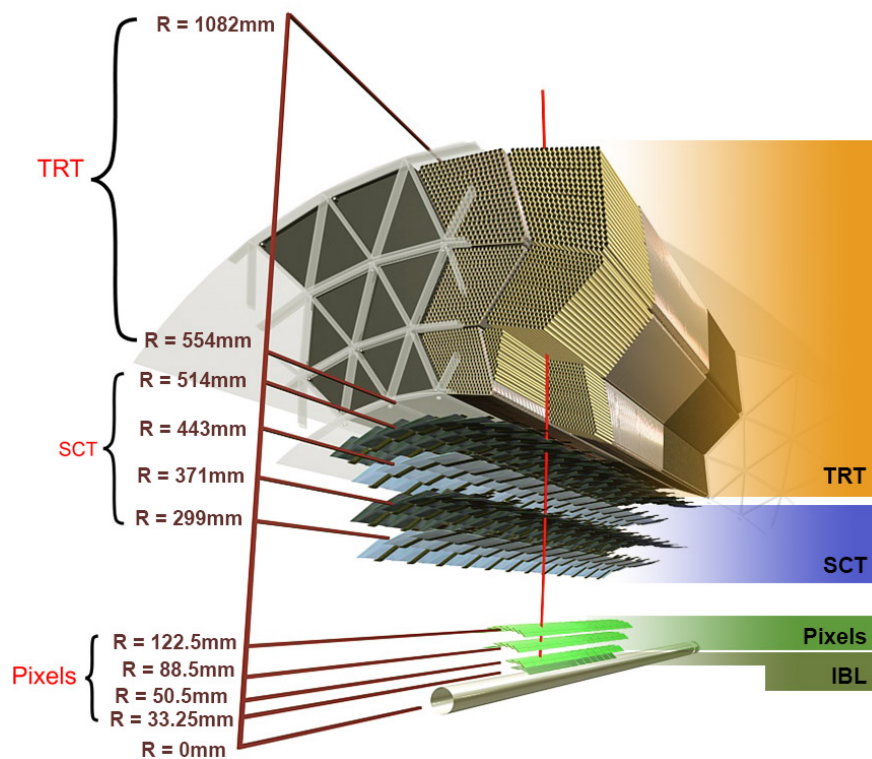


Figure 3.4: A diagram from [34] showing the layout of the ATLAS inner detector barrel sections and the radius of each layer from the centre. Closest to the beam is the insertable b-layer (IBL) followed by the rest of the pixel detector layers, the semiconductor tracker (SCT) and the transition radiation tracker (TRT).

opposite ends of the sensor causing a signal current which is amplified by a preamplifier then digitised in the readout chip. All particles should cross at least three layers of pixel detector.

Semiconductor Tracker (SCT)

The SCT is based on the same sensor technology as the pixel detector but with $\sim 80 \mu\text{m} \times 6.4 \text{ cm}$ silicon microstrips instead of pixels due to the larger area it has to cover. SCT modules are double-sided; the strips are arranged in pairs, one on each side, oriented at a stereo angle of 40 mrad with respect to each other so that a measurement in the longitudinal direction can be made. SCT strips have an intrinsic resolution of $17 \mu\text{m} \times 580 \mu\text{m}$. There are four barrel layers and nine end-cap disks on each side ensuring that particles cross at least four SCT layers.

Transition Radiation Tracker (TRT)

The TRT contains 370,000 drift tubes - cylinders 4 mm in diameter with a thin gold-plated tungsten wire running through the centre, filled with a gas mixture (mainly xenon or argon). The walls of the tube are held at negative potential and the wire at ground. In the barrel, the tubes are 144 cm long and positioned parallel to the beam axis, in the end-caps they are 37 cm long and arranged radially like wheel spokes. The area between the tubes is filled with polypropylene. Transition radiation is produced by relativistic charged particles as they pass between materials of different dielectric constants. In the TRT charged particles continually encounter the tube/filler boundaries, generating photons which accompany the original particle through the tubes, ionising the gas inside. Liberated electrons drift towards the anode causing a signal current to flow in the wire which is amplified and read out as a hit. The path of the incident particle through the tube can be calculated from the drift time of the electrons; the intrinsic resolution of the position measurement is $130 \mu\text{m}$ in ϕ . The wires are divided into two at the centre of the tubes with an independent readout system at each end for a more precise z (or r) measurement. The time over threshold of the straw signals depend on the amount of energy deposited, and the dependence is strongest for $p_T \leq 10 \text{ GeV}$. Since the amount of transition radiation produced by a particle depends on the γ factor (E/m), TRT measurements help to distinguish between low momentum electrons and pions. The TRT returns an average of 36 measurements per track over the region $|\eta| < 2.0$.

3.3.4 Calorimeters

The calorimeter layer lies directly outside the solenoid that surrounds the inner detector and extends out to $|\eta| = 4.9$. The calorimeters are used to measure the energies of neutral and charged particles; in contrast to the inner detector, they are designed to interact with

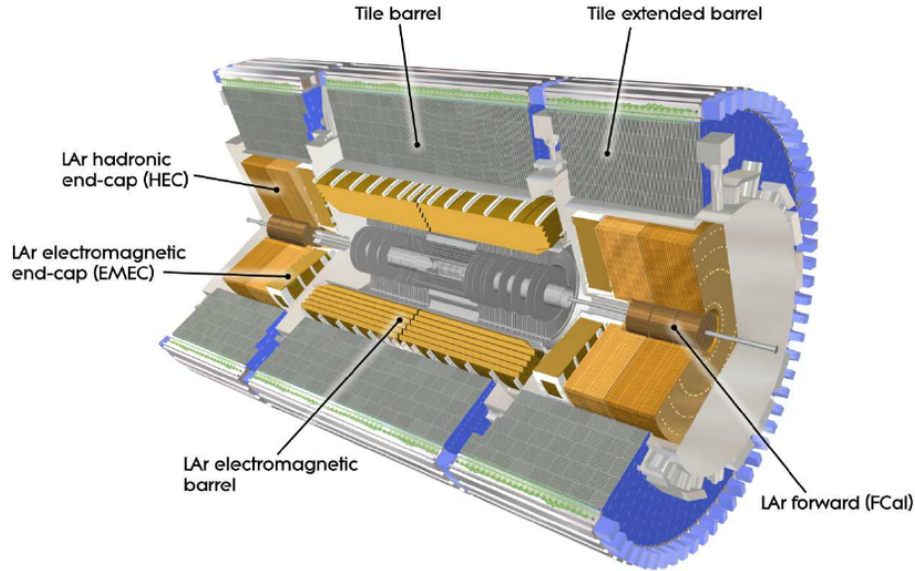


Figure 3.5: A digagram from [35] showing the layout of the ATLAS calorimeter system.

particles as much as possible so that all of the particle's energy is transferred to the calorimeter material and a full energy measurement can be made. They are sampling calorimeters; alternating layers of an absorber material with which the particle is likely to interact, instigating a shower of secondary particles carrying between them the energy of the original particle, and an active material which interacts with the secondary particles and generates the signal that is read out. Absorbing materials are characterised by their radiation length (X_0), the average distance an electromagnetically interacting particle must travel through the material for its energy to be reduced by a factor of e , or their nuclear interaction length (λ_0), the average distance a hadron travels through the material before it undergoes an inelastic nuclear interaction. The absorbers must present a sufficient number of radiation/nuclear interaction lengths to particles in order to prevent a significant amount of their energy escaping the calorimeter. The layout of the calorimeters is shown in Figure 3.5. The subsystems are based on different methods of calorimetry suitable for measuring different types of particle, and can be categorised into an electromagnetic (EM) calorimeter and a hadronic calorimeter. The electromagnetic calorimeter primarily measures the energies of electrons and photons; it comprises Liquid Argon (LAr) calorimeters in the barrel, end-cap and forward regions. The hadronic calorimeter primarily measures the energies of hadrons; it comprises the Tile calorimeter in the barrel and LAr calorimeters in the end-cap and forward regions. Three aluminium cryostats house the calorimeter subsystems - one for the barrel region and one for each end-cap/forward region.

Electromagnetic Calorimeters

The LAr electromagnetic calorimeters have lead as the absorbing material and cooled liquid argon, lying between copper electrodes, as the active material. Electromagnetic showers initiated by a particle incident on the lead ionise the liquid argon, causing a current proportional to the energy of the original particle to flow between the electrodes. This signal is read out and converted to an energy measurement. The calorimeter is segmented into cells of dimension $\Delta\eta \times \Delta\phi$, and the absorber and active layers are arranged with an accordion geometry as shown in Figure 3.6 to achieve a uniform response in ϕ . Positioned directly before the LAr electromagnetic calorimeters is a LAr presampler which is used to obtain an estimate of the amount of energy lost upstream of the calorimeters by particles with $|\eta| < 1.8$. The LAr electromagnetic calorimeter has barrel, end-cap and forward sections. The barrel section extends out to $|\eta| < 1.475$ and is divided into three longitudinal layers: strip, middle, and back. The strip layer has the finest granularity: $\Delta\eta \times \Delta\phi = 0.003 \times 0.01$. This makes it possible to differentiate between showers from single photons and showers from highly boosted π^0 decays. and to make a primary vertex measurement for trackless photon energy deposits. The middle layer has granularity 0.025×0.025 . It is the thickest and is where the majority of the energy of high energy particles is measured. The back layer has granularity 0.05×0.025 , collects most of the remaining energy, provides an estimate of how much energy escapes, and helps to distinguish between electromagnetic and hadronic showers. The end-cap sections have two wheels each: inner wheels that cover $1.375 < |\eta| < 2.5$ and outer wheels that cover $2.5 < |\eta| < 3.2$. In a similar way to the barrel, these wheels are separated into layers with different granularities, thicknesses, and primary functionalities. Finally, the first layer of the LAr forward calorimeter⁴ which extends out to $|\eta| < 4.9$ has copper as an absorber and is considered part of the electromagnetic calorimeter. The LAr electromagnetic calorimeter has degraded performance in the region $1.37 < |\eta| < 1.52$ due to necessary non-active material; this region is generally excluded from electron reconstruction in analyses.

Hadronic Calorimeters

In general, hadronic particles deposit some but not all of their energy inside the electromagnetic calorimeters. A layer of hadronic calorimeters surrounding the electromagnetic calorimeters is required to obtain a full energy measurement for these particles. Encompassing the LAr calorimeter in the barrel section there is a Tile calorimeter comprising a central and two extended barrels, covering the region $|\eta| < 1.7$. It has steel as an absorber and scintillating tiles as the active material. Photons generated when hadronic showers interact with

⁴The forward calorimeters are there to intercept the large rate of very far forwards particles with $|\eta| \in [3.1, 4.9]$.

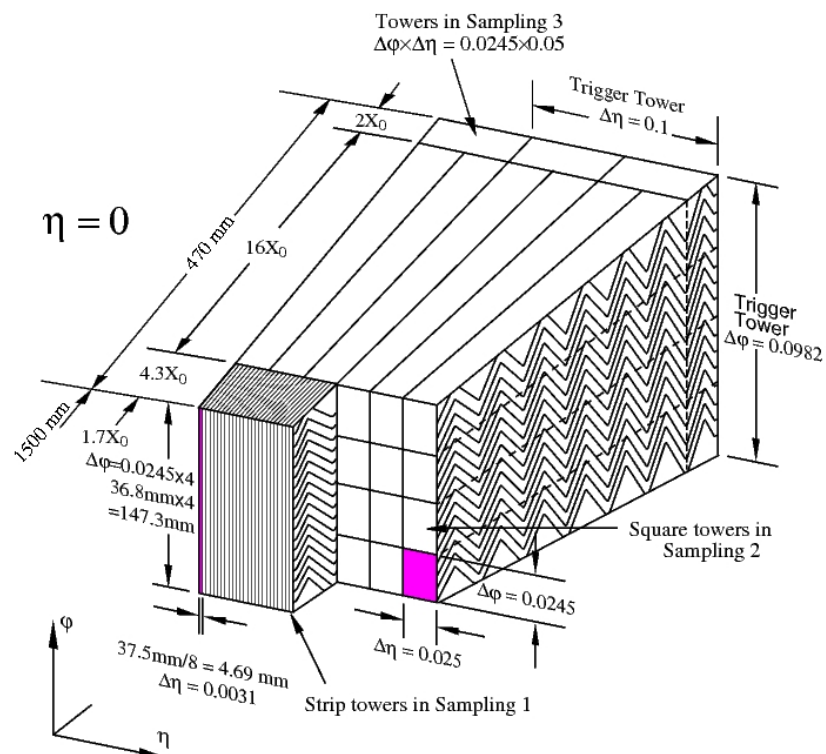


Figure 3.6: A figure from [36] showing the accordion geometry of the absorber and active layers in calorimeter cells.

the tiles are collected by wavelength shifting fibres and directed to photomultipliers where they are converted to an electronic signal. The barrels are segmented in ϕ into 64 modules (an example module is shown in Figure 3.7) and into three longitudinal layers, the first two with granularity $\Delta\eta \times \Delta\phi = 0.1 \times 0.1$ and the third with $\Delta\eta \times \Delta\phi = 0.2 \times 0.1$. The hadronic end-cap calorimeters have copper as the absorbing material and LAr as the active material. They comprise two wheels in each end-cap providing coverage in the $1.5 < |\eta| < 3.2$ region. The outer two layers of the LAr forward calorimeters use a tungsten absorber and extend hadronic calorimetry out to $|\eta| < 4.9$.

Performance

Good calorimetry is important for analyses that reconstruct short-lived particles from jets and electrons. The energy resolution of a calorimeter can be expressed as:

$$\frac{\sigma_E}{E} = \frac{a}{\sqrt{E}} \oplus b \quad (3.3)$$

where a is the *sampling term*, a result of the statistical nature of showering, and b is the *constant term*, a result of inhomogeneities in detector response and energy lost outside of the calorimeters. Test beam studies have shown that the calorimeters have achieved their design resolutions: $\sigma_E/E = 10\%/\sqrt{E} \oplus 0.7\%$ for the electromagnetic calorimeter (this is dominated by the constant term at high energies) [38], and $\sigma_E/E = 50\%/\sqrt{E(\text{GeV})} \oplus 3\%$ for hadronic jets [39].

3.3.5 Muon Spectrometer (MS)

Muons are the only particles expected to traverse the calorimeters relatively unimpeded (aside from neutrinos which escape ATLAS altogether); a dedicated subdetector is required to measure their tracks and momenta. The muon spectrometer (MS) is the final layer of ATLAS, built around three superconducting toroids which provide a magnetic field of average strength 0.5 T that bends muons' tracks in the r-Z plane, allowing their momentum to be calculated. One barrel and two end-cap toroids are required to provide the full magnetic field coverage: the barrel toroid field bends muon tracks inside $|\eta| < 1.0$, the end-cap toroid fields bend tracks inside $|\eta| \in [1.4, 2.7]$, and the combined fields bend tracks inside $|\eta| \in [1.0, 2.5]$. There are three tracking layers extending out to $|\eta| < 2.7$ instrumented primarily with monitored drift tubes (MDT), and with Cathode Strip Chambers (CSC) which comprise the innermost layer in the region $2.0 < |\eta| < 2.7$. The MDTs and CSCs are designed to make precision measurements; as a side effect they are slow to read out a muon signal. Three layers of fast-tracking detectors - Resistive Plate Chambers (RPC) covering $|\eta| < 1.05$ and Thin

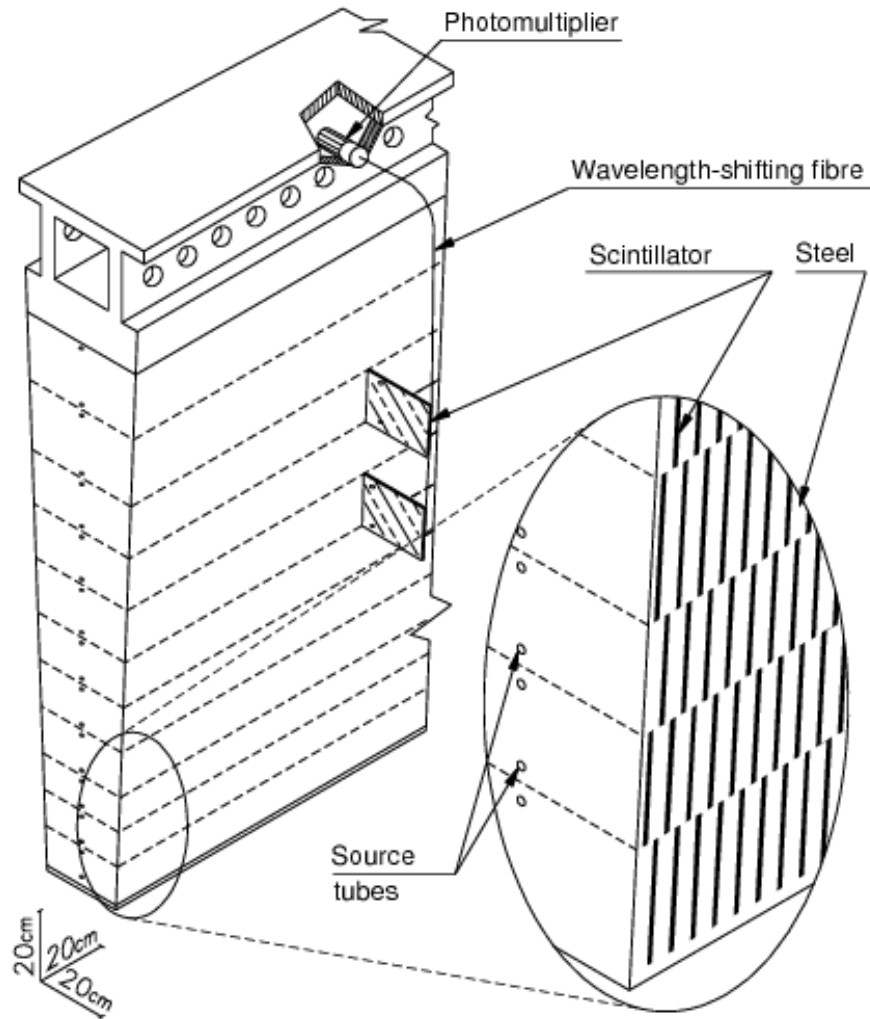


Figure 3.7: A diagram from [37] showing a tile calorimeter module. The tile calorimeter comprises 64 of these modules, segmented in ϕ and arranged in three longitudinal layers. The source tubes allow movable radioactive ^{137}Cs sources to pass through the calorimeter: the γ rays emitted by the sources have a well known energy, allowing the response of the scintillator tiles to be calibrated.

Gap Chambers (TGC) covering $|\eta| \in [1.0, 2.4]$ - carry out quick, less precise measurements that are used by the Trigger system discussed in the next section. The layout of the muon spectrometer is shown in Figure 3.8.

MDTs are 30mm diameter aluminium tubes with a tungsten-rhenium central anode wire, containing a pressurised Ar/CO₂ mixture. They are separated into chambers; a muon will cross multiple MDTs inside a chamber and the individual measurements, which have an intrinsic resolution of 80 μm in z , are combined into one measurement per chamber with a resolution of 35 μm in z . Muons cut a chord across the tubes, freeing electrons which drift towards the anode and arrive at a time dependent on their starting position. The gas mixture is chosen so that the electron drift velocity is strongly anti-correlated with radial distance from the anode. The current in the anode is read out as a pulse that reflects the difference in drift time of the first and last electrons arriving at the anode, allowing the muon's path to be calculated. The maximum drift time in MDTs is 700 ns, so CSCs, which have a faster readout time (the electron drift time is ~ 40 ns) and finer granularity, are used in the forward region where occupancy is higher. CSCs are filled with an Ar/CO₂ gas mixture and contain anode wires running in the z direction and cathode strips running perpendicular to the wires, sliced to give a resolution of 40 $\mu\text{m} \times 5$ mm in $r \times \phi$. The fast-tracking chambers have response times of 15-25 ns, allowing some information about muons to be read out for every event.

The momentum resolution of the muon spectrometer can be parameterised, for each η range, as:

$$\frac{\sigma(p)}{p} = \frac{p_0^{MS}}{p_T} \oplus p_1^{MS} \oplus p_2^{MS} \cdot p_T \quad (3.4)$$

where p_0^{MS} accounts for energy lost upstream of the spectrometer, p_1^{MS} for multiple scattering, and p_2^{MS} for intrinsic resolution of the measuring components [40]. These parameters were measured using 2011 p - p collision data [41]. In the barrel, they were found to be: $p_0^{MS} = 0.25$ TeV, $p_1^{MS} = 0.0327$, $p_2^{MS} = 0.168$ TeV⁻¹.

3.3.6 Trigger System

The LHC's design luminosity corresponds to an event rate of 40 MHz. It is not feasible to read out, process and store data from every single event and in any case most are soft-scattering events that are unlikely to be used in physics analyses. ATLAS uses a Trigger system to examine event data as it is read out and select events it considers interesting enough to be stored. The Trigger system has two levels: a hardware-based Level 1 (L1) Trigger and a software-based High Level Trigger (HLT). The L1 Trigger makes decisions about whether to discard an event based on signals from the calorimeters and the muon spectrometer, reducing the event rate to 100 kHz. It uses limited detector information and has simple selection criteria to keep the decision time under 2.5 μs . Regions of Interest

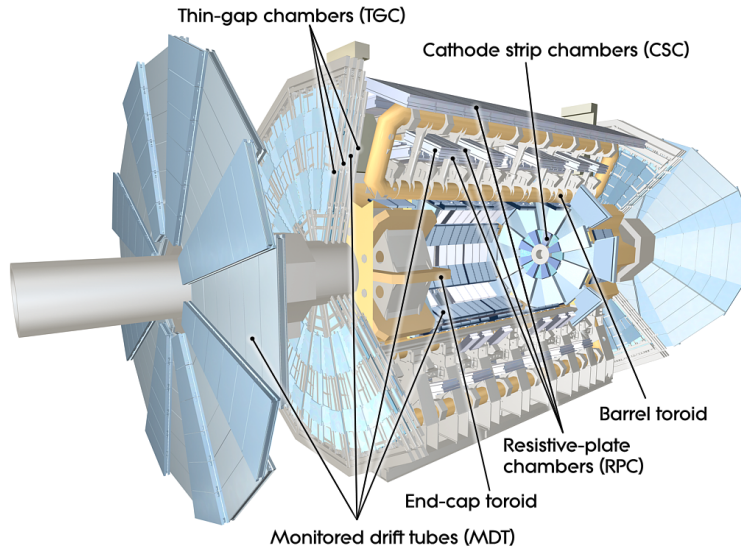


Figure 3.8: A diagram from [42] showing the layout of the subsystems inside the muon spectrometer.

(RoIs) in the detector are flagged by the L1 Trigger if signals indicate the presence of high p_T leptons, jets, photons, or large missing transverse energy; they are sent to the HLT for further inspection. The HLT performs a more sophisticated analysis of events that pass the L1 trigger, focusing on the RoIs for efficiency and using more detailed detector data including precision tracking information from the inner detector and the muon spectrometer, and higher granularity calorimeter information. Typically this is done in under 300 ms. The HLT reduces the event rate to 1 kHz; output events are stored to be analysed fully offline. There are multiple trigger criteria for each physics object. The set of criteria is known as the trigger menu. Analyses can require events to pass a combination of triggers based on their needs. For example, analyses looking at $t\bar{t}$ events may require events to pass at least one of two possible lepton triggers with different p_T and lepton identification criteria, plus a missing transverse energy trigger. This has the effect of instantly removing a lot of background from the analysis without forfeiting too much efficiency (the trigger that accepts lower p_T leptons would have stricter lepton identification criteria). The collision luminosity means that even high p_T objects are produced abundantly. If the p_T threshold of a particular trigger results in an output rate that is too high then it is prescaled: every n^{th} event that meets the criteria is kept, the rest are discarded.

Chapter 4

Physics Objects

Physics objects are the means by which a proton-proton collision is reconstructed. Outgoing particles that live long enough to interact with the detector are electrons, muons, photons and hadrons, and are known as final state particles. Each produces a distinctive signature in the detector; a combination of signals read out from the ID, calorimeters and MS. Physics objects are built using these signals, and are defined with the reconstruction of the hard-scatter physics process in mind. They can correspond to final state particles (leptons and photons), or, if it is more useful, to collections of final state particles. Collections of hadrons are used to build objects called jets, which can be associated with colour charged particles produced in the hard-scatter. One physics object, missing transverse energy, is made using all other physics objects in an event in order to reconstruct the kinetics of any particles that escape the detector leaving no physical trace. The only Standard Model particles to do this are neutrinos.

Physics objects associated with final state particles can be used to reconstruct heavier, short-lived mother particles, and, ultimately, infer which kind of physics process occurred during the hard-scatter and its kinematics. However, even if the reconstruction of physics objects was perfectly accurate, there is always some level of ambiguity since different processes can result in identical final state particles. When selecting one type of event from data, based on the physics objects present, a fraction of the selected events will be of another type, and this background must be estimated.

There are three steps involved in creating a physics object: trigger, reconstruction and identification. The trigger system flags signatures compatible with different types of objects using limited information that can be analysed quickly. Reconstruction algorithms build, if possible, a candidate physics object with full kinematic information (a four-momentum); these algorithms have access to the full information from the event. Finally, identification algorithms are applied to the reconstructed candidate objects to produce the final set of objects.

Each stage introduces an efficiency, since there will be signal objects which fail each stage, and a fake rate, as there will be background objects that pass each stage. Fakes for a particular type of object include objects not from the hard scatter, objects of a different type, and objects of the same type but originating from an in-flight decay. The trigger and reconstruction stages tend to be fixed in analyses. The identification stage is more adaptable and can usually be modified to meet the requirements of the analysis. There are various commonly used “working points” of identification algorithms which are designed to achieve the best background rejection for a desired efficiency. The identification for different objects will be discussed below.

Outlined in this section are the physics objects used in the analysis described in Chapter 6, i.e. those that are expected from a $t\bar{t}$ decay. They are electrons, muons, jets and b -jets, and missing transverse energy.

4.1 Tracks and Vertices

A track is a reconstruction of the path a charged particle took as it travelled outward from the interaction point and through the detector, and is an integral component of object reconstruction. Tracks may originate in the hard-scatter, another interaction in the bunch crossing, or the point at which an outgoing particle decays. Run 2 collision conditions are accompanied by denser distributions of tracks and interaction vertices, with track separations as small as the granularity of the inner detector [43], necessitating a rigorous track reconstruction procedure. Separate algorithms are used so that tracks from both primary and secondary tracks can be efficiently reconstructed¹. Primary tracks are reconstructed using an inside-out algorithm which builds on initial seeds: sets of three space-points in separate layers of the inner detector (pixel detector or SCT). A space-point is defined as the location where a particle passed through the detector layer and is calculated using a cluster of hits. Sensor elements (pixels or strips) are arranged in a grid, and any group of elements that have each registered an energy deposit above a certain threshold and are topologically connected by shared edges or corners comprise a cluster. In the pixel detector, one cluster corresponds to one space-point and in the SCT clusters on both sides of a strip layer are merged into one space-point. A rough estimate of momentum, impact parameter² and particle trajectory is

¹Primary tracks are the tracks of primary particles: those produced in p - p collisions with a mean lifetime greater than 3×10^{-11} s, or those that result from decays or interactions of particles produced in p - p collisions with a lifetime less than 3×10^{-11} s [44]. Secondary tracks are the tracks of secondary particles, or non-prompt particles, which are the result of particles decaying once they have left the interaction point.

²The impact parameter is a measure of how close the track origin (point of closest approach to the IP when the track is traced back to the centre of the detector) is to the IP. z_0 is the longitudinal impact parameter, the distance between the track origin z -position and the IP. d_0 is the transverse impact parameter, the distance between the x - y position of the track origin and the IP.

calculated for each seed. In order to select seeds likely to yield a good quality track and reject random combinations of three space-points, seeds are required to pass momentum and impact parameter cuts as well as fulfil the requirement of there being at least one additional space-point consistent with the extrapolated particle trajectory, where the extrapolation takes into account interactions with the detector and expected energy losses. Successful seeds are fed to a Kalman fitter [45], which generates track candidates from each seed by adding space-points from pixel and SCT layers at increasing radius from the interaction point, which are compatible with the trajectory of the seed, and adapting the trajectory in response to the incorporated space-points. There can be multiple track candidates built on a single seed if there are multiple compatible space-points on the same layer. The fitter achieves a good efficiency in generating tracks that go on to be used in successful particle reconstruction [43]. However, there are cases where track candidates share space-points or incorrect space-points have been included in the track; a technique called ambiguity solving [43] is used to improve purity. First, merged clusters - the result of energy deposits from more than one particle - are identified. Merged clusters are allowed to be shared between tracks, but tracks sharing single clusters must be limited (to not occur much more often than would be expected). Each track candidate is assigned a score, based on properties such as χ^2 of the track fit, p_T , and present and missing clusters compared to expectation, which reflects how likely the track is to match the path of a charged particle. Tracks with a higher score are prioritised when deciding which tracks are permitted to share single clusters. The track candidates are required to meet certain criteria based on p_T , $|\eta|$, impact parameter, number of clusters, number of shared clusters and missing clusters. Finally, tracks are extended to the TRT; if there are suitable space-points, they are added and the trajectory is re-fit accordingly. An outside-in algorithm reconstructs secondary tracks. The reconstruction follows a similar procedure as before but begins in the TRT and works inwards, avoiding space-points already assigned in the initial round of track reconstruction. Tracks with no matching space-points in the SCT or pixel detector are known as TRT standalone tracks.

Tracks are used to reconstruct the positions of primary vertices - parton-parton interactions inside the proton-proton collision - and secondary vertices, which are due to subsequent decays of outgoing particles and have the signature of being displaced from the interaction point. A longitudinal impact parameter z_0 is found for each track by calculating the z -position of the track origin with respect to the IP; the seed for the iterative vertex finding algorithm is the maximum of the z_0 distribution. Tracks close to the seed are weighted according to their level of compatibility with the seed, which modifies the seed position. This procedure is performed iteratively, with the IP providing a three dimensional constraint, and eventually assigns weights of either 1 or 0 to tracks, determining which tracks are matched to the vertex and a final vertex position. The same procedure is then repeatedly applied to

tracks unmatched to a vertex until all vertices have been reconstructed. The nominal primary vertex in the event is the vertex with the largest sum of associated tracks' p_T^2 , and must have at least two matched tracks. This primary vertex is chosen with the aim of extracting the most interesting physics in the collision to study, the result of the hard-scatter, known as the event, and relegates other primary vertices to pile-up.

Vertex reconstruction performance is sensitive to the number of interactions per bunch crossing and suffers as a result of the increased instantaneous luminosity in run 2. A balance must be struck between erroneously matching tracks from a single parton-parton interaction to different vertices (splitting) and matching tracks from different parton-parton interactions to the same vertex (merging), the latter occurring more often as pile-up increases. The problem of merging derives from vertex seeds being created one at a time which automatically prevents the reconstruction of later vertices if their tracks are close enough to be matched to earlier seeds. Vertex reconstruction in run 2 makes use of an imaging algorithm [46] which considers different potential vertex locations simultaneously, testing tracks with multiple seeds, to avoid merging.

4.2 Electrons

Electrons leave a track in the inner detector followed by an energy deposit in the EM calorimeter which are both used in the triggering and reconstruction of electron candidates. For each reconstructed electron an associated four-momentum is obtained, along with some additional quantities used in electron identification (described in section 4.2.3.).

4.2.1 Trigger

Before they undergo reconstruction, electron-like signals are flagged by the electron trigger, which comprises an L1 stage and a HLT stage. The L1 electron trigger selects 4×4 calorimeter towers as regions of interest (RoIs) if there is a high energy, isolated deposit in the EM calorimeter with limited energy deposited in the corresponding region of the hadronic calorimeter. The HLT then attempts a fast reconstruction, loosely matching tracks to EM clusters in the RoI, and applies some quality cuts to reduce data rates by rejecting some background.

4.2.2 Reconstruction

There are three stages in the reconstruction of electron candidates: calorimeter cluster finding, track matching and energy reconstruction. Only clusters with $|\eta| < 2.47$ are considered as they can go on to be matched to ID tracks. First, a sliding window algorithm scans the

EM calorimeter in windows of 3×5 calorimeter towers (where each tower is 0.025×0.025 in (η, ϕ) space), selecting towers with $E_T > 2.5$ GeV that are also local maxima as seeds for building energy clusters. A clustering algorithm includes surrounding towers with sufficient energy deposits while removing nearby seeds to avoid overlapping clusters. Once a cluster has been established, a larger window whose size depends on the position of the cluster is applied around the cluster to capture remaining towers with energy deposited by the electron. This algorithm is almost 100% efficient at finding clusters with $E_T > 15$ GeV [47].

Next, an attempt is made to match tracks to clusters. Tracks are reconstructed as in Section 4.1, however the standard trajectory extrapolation assumes that the charged particles are pions when accounting for energy loss. To recover efficiency for electron tracks, track seeds with $p_T > 1$ GeV that failed the track extension stage but are close in (η, ϕ) to an EM energy cluster, and full track candidates that failed the fitting stage, are reconsidered. An extension and fitting procedure that assumes the charged particles are electrons is applied. The tracks then have their trajectory extended to the middle layer of the EM calorimeter. If the (η, ϕ) position of the extended track is sufficiently close to that of the centre of a cluster then the track and cluster are matched and the track is refit, accounting for non-linear Bremsstrahlung losses. The track-cluster matching procedure can lead to several scenarios. If more than one track is matched to a cluster then the best track is chosen based on $\Delta R(\text{track}, \text{cluster})$ and the track quality. If a cluster has no matched track it is assumed to be from a photon. If the matched track is one of a pair of tracks bending in opposite directions that can be traced back to a vertex displaced from the primary vertex, and that have missing clusters early in the track, this is an indication of photon conversion [48]. Reconstructed electron candidates are successfully matched track-cluster pairs. A calibration procedure is applied to the measured energy to obtain the expected energy of the electron. The cluster energy is corrected for the fraction of energy lost upstream of the EM calorimeter as evaluated by the presampler, an estimate of the amount of energy deposited by the electron outside of the cluster (both in the EM calorimeter and in subsequent detector layers), and the response of the calorimeter (measured energy given true energy), which depends on η . The four-momentum uses the calibrated cluster energy, and the track η and ϕ .

4.2.3 Identification

Reconstructed electrons are tested against identification criteria. An electron identification algorithm is applied to each candidate to decide whether it is a real electron or another physics object that has been reconstructed as an electron. Common background objects include jets and photon conversions. There are also genuine electrons from the decays of heavy flavour particles, known as non-prompt electrons, which are regarded as background. The identification algorithm adopts a multivariate analysis approach when evaluating electron candidates.

More details on the signal-background discriminating variables can be found here [47]. The algorithm makes decisions based on a discriminant, $d_{\mathcal{L}}$ (equation 4.1), which depends on the likelihood that a candidate is signal, \mathcal{L}_S , and the likelihood that it is background, \mathcal{L}_B . The likelihoods are obtained by comparing each discriminating variable, x_i , calculated for the electron candidate, to the corresponding variable PDFs for signal and background, which are generated using simulated objects. Discriminating variables include a likelihood based on transition radiation in the TRT, $\Delta\eta$ between the extrapolated track and the middle layer cluster position, and the ratio of E_T in the first hadronic calorimeter layer to E_T of the EM cluster.

$$d_{\mathcal{L}} = \frac{\mathcal{L}_S}{\mathcal{L}_S + \mathcal{L}_B} \quad \mathcal{L}_{S(B)}(\vec{x}) = \prod_{i=1}^n P_{s(b),i}(x_i) \quad (4.1)$$

The cut applied to $d_{\mathcal{L}}$ determines the purity of the identified electrons. There are three commonly used working points: *loose*, *medium* and *tight*. The *tight* working point has the best background rejection, followed by *medium* and then *loose*. Therefore the *tight* working point, which is used in the analysis described in Chapter 6, yields the purest sample of electrons but has the lowest efficiency. Some of the variables that go into the identification algorithm are E_T and η dependent, therefore the cut applied to $d_{\mathcal{L}}$ for any given working point is optimised for different (E_T, η) ranges. Figure 4.1 shows the efficiencies and fake rates achieved by operating the identification algorithm at each working point. The performance improves with increasing E_T .

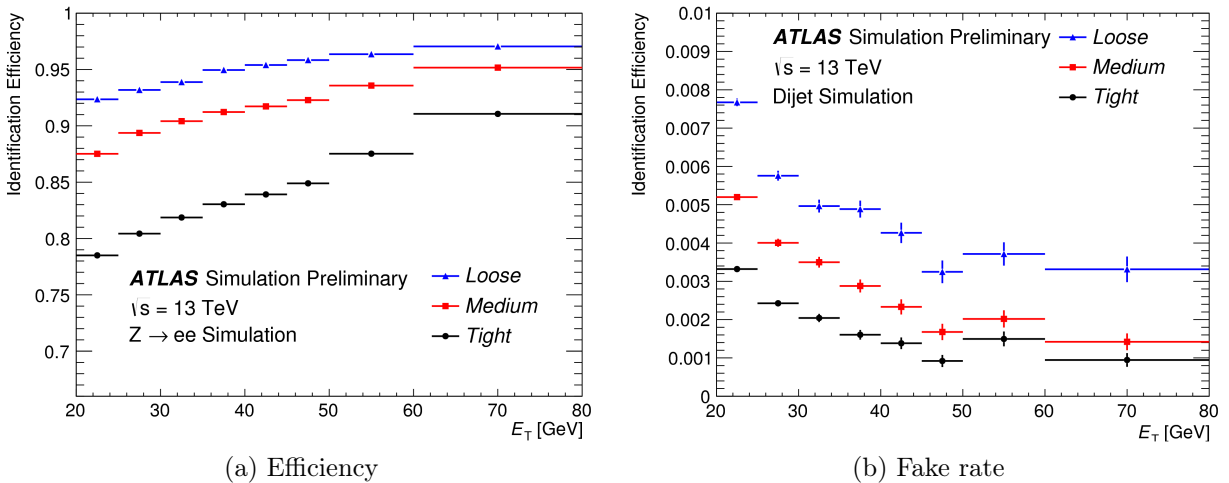


Figure 4.1: Plots from reference [47] that show the fraction of electrons reconstructed from (a) simulated $Z \rightarrow ee$ events and (b) simulated dijet events that were identified as electrons by the loose, medium and tight identification algorithms. (a) shows the identification efficiencies with respect to reconstructed electrons, and (b) shows the misidentification rates with respect to reconstructed electrons. (In (b) the identification efficiency in the y axis refers to the probability to falsely identify a jet as an electron.)

Efficiency Measurements

The overall³ electron efficiency ϵ_{total} has three components:

$$\epsilon_{\text{total}} = \epsilon_{\text{trigger}} \times \epsilon_{\text{reconstruction}} \times \epsilon_{\text{identification}} \quad (4.2)$$

Efficiencies are measured using a tag and probe method which is carried out as follows. Events in which pairs of prompt electrons are produced, for example $Z \rightarrow ee$ or $J/\psi \rightarrow ee$ decays, are selected from data and simulated events. The type of event used should be well-modelled, with a distinctive signature, low background and large cross-section. The objective is to create a sample of electron candidates that are reliably genuine electrons, but without using one of the trigger, reconstruction or identification algorithms (whichever efficiency is being measured), so that the efficiency of the particular algorithm can be calculated using these electrons. A selection is defined for the desired type of event, for example requiring the presence of at least two electron candidates with invariant mass $\sim m_Z$ when selecting $Z \rightarrow ee$ events. A large background contamination of the electron candidates is expected as no trigger/ reconstruction/ identification is applied (again, depending on which efficiency is being measured). Therefore in each event, at least one electron is required to meet strict identification criteria (referred to as a tag). Any electron that can be paired to the tag to reconstruct the mother particle, e.g. the Z boson in $Z \rightarrow ee$ decays, is referred to as a probe and is regarded as a real electron because of the circumstantial evidence. Additionally, an estimate of the background contamination of probes is made and subtracted from data. This is unnecessary for the simulated probes as it is possible to select from a sample only one type of event, and use truth-level information to remove background.

The total electron efficiency is defined to be the fraction of all probes which go on to be triggered, reconstructed and identified. The efficiency of each algorithm (trigger, reconstruction or identification) is measured using the probes that pass the previous algorithm. For example, the identification efficiency is defined as the fraction of reconstructed probes that go on to be identified.

There are often small differences between the efficiencies measured in data, ϵ_{data} , and in simulation, ϵ_{MC} . The efficiency ratio $\epsilon_{\text{data}}/\epsilon_{\text{MC}}$, known as a scale factor, is used to derive corrections that are made to simulated events via event weights so that efficiencies in simulation reflect efficiencies in data. The corrections, like the efficiencies, are E_T and η dependent.

³Often another adaptable set of criteria, called isolation criteria, are applied to electrons after they have passed identification criteria.

4.2.4 Energy scale and resolution

After the energy cluster calibration described previously, there can still be small, η dependent differences in energy measurements between data and simulation. Differences in calorimeter response for data and simulation translate to disparate energy scales (the ratio of measured energy to true energy). This is known as energy miscalibration, and is parameterised as:

$$E_i^{\text{data}} = E_i^{\text{MC}}(1 + \alpha_i) \quad (4.3)$$

for each η range i , where E_i^{data} is the electron energy measured in data, E_i^{MC} is the electron energy measured in simulation, and α_i represents the miscalibration [49]. The value of α_i is determined using $Z \rightarrow ee$ events, as it can be inferred from the shift in the invariant mass peak going from data to simulation [50]. Corrections to the energy scale are then applied using α_i .

The electron energy resolutions in data and simulation differ by a constant term c_i (energy independent to first order) [49]:

$$\left(\frac{\sigma(E)}{E}\right)_i^{\text{data}} = \left(\frac{\sigma(E)}{E}\right)_i^{\text{MC}} \oplus c_i \quad (4.4)$$

c_i is also obtained from $Z \rightarrow ee$ events using a method described in [50]. Corrections to the simulated resolution are implemented by smearing the electrons; modifying the kinematics of each by a random amount depending on the corrected resolution.

4.3 Muons

In general, muons traverse the inner detector and calorimeter layers relatively unimpeded before their momenta are measured in the muon spectrometer. The muon reconstruction and identification algorithms make use of information from the inner detector, calorimeters and muon spectrometer.

4.3.1 Reconstruction

To begin with, information from the ID and the MS is considered separately. Tracks in the ID are reconstructed using the standard track building techniques described in Section 4.1. MS tracks are reconstructed in segments. In each MS chamber, partial tracks are reconstructed using an algorithm which recognises the hit pattern of a trajectory bending in the plane a charged particle would in response to the superconducting toroids. Compatible track segments are combined to build a full MS track.

A combined reconstruction is then performed, which uses the MS and ID tracks as well as other information from the detector. The reconstructed muons are divided into the following four types according to which subdetectors were used in the reconstruction. Combined (CB) muons are muon tracks that are created by refitting an ID track and compatible MS track. Segment-tagged (ST) muons are ID tracks that have no compatible MS track but do have at least one compatible segment of an MS track. This can occur when muons do not pass through the entire MS. Calorimeter-tagged (CT) muons are ID tracks that have a minimum-ionising particle like matching energy deposit in the calorimeter as a substitute for a missing MS track. They allow for some reconstruction efficiency to be recovered in regions of limited muon spectrometer capability. Extrapolated (ME) muons are MS tracks with no associated ID track which when extrapolated backwards (accounting for energy losses in the calorimeters) are compatible with the IP [40].

4.3.2 Identification

Reconstructed muon candidates are required to meet additional quality criteria to be identified as prompt muons. The background objects most frequently reconstructed as muon candidates are non-prompt muons from charged hadron decays, whose tracks usually have a kink at the location of the decay. There is often a greater mismatch between ID and MS information associated to non-prompt muons compared to prompt muons. The variables used to discriminate between signal and background muon candidates include the χ^2 of the combined track (with respect to the measured hits in the ID and MS that the best fit combined track was fit to) and the difference between the transverse momentum of the muon measured in the ID and the MS. More details about the discriminating variables can be found in reference [40]. As was the case for electron identification, there are three standard sets of identification criteria, labelled *tight*, *medium* and *loose*, with *medium* being used in most ATLAS analyses. The systematic uncertainties arising from muon reconstruction and calibration are smallest when the *medium* criteria is used.

4.3.3 Efficiency Measurements

Reconstruction and identification efficiencies for muons in the range $|\eta| < 2.5$ are determined using a tag and probe method with $Z \rightarrow \mu\mu$ and $J/\psi \rightarrow \mu\mu$ events, detailed in reference [40]. In the range $2.5 < |\eta| < 2.7$, where the ID has no coverage, a different method described in [51] is used. The efficiency for *medium* muons, which are used in the analysis described in Chapter 6, is shown in Figure 4.2. The p_T and η dependent efficiency scale factor, $\epsilon_{\text{data}}/\epsilon_{\text{MC}}$, is used to weight simulated events in order to reconcile data and simulation efficiencies.

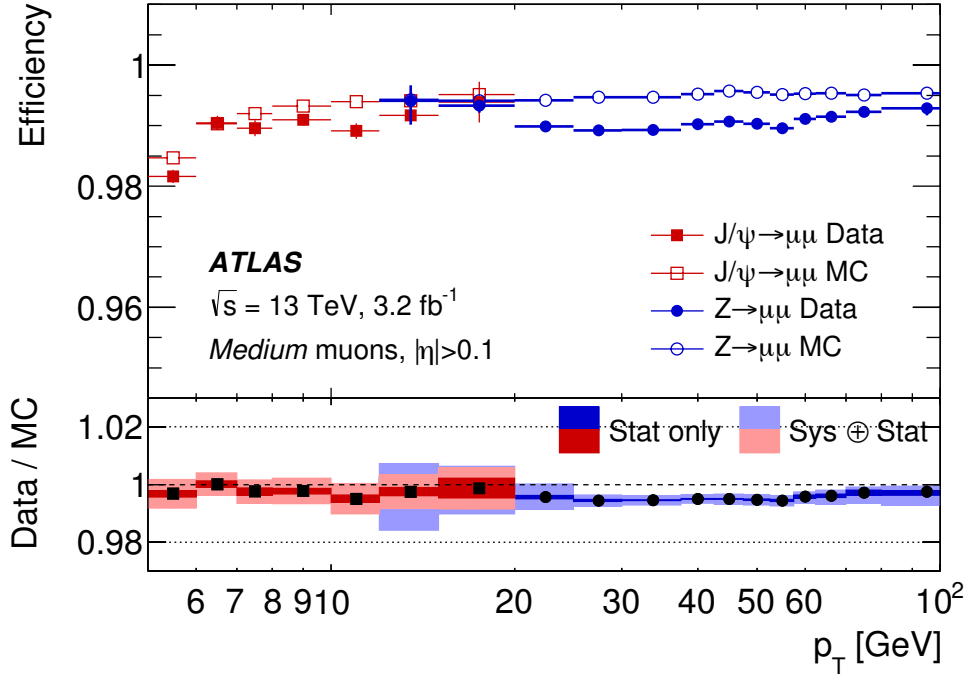


Figure 4.2: A plot from [40] showing the efficiency of selecting muons from $Z \rightarrow \mu\mu$ events and $J/\psi \rightarrow \mu\mu$ events using the medium identification criteria in data and simulation.

4.3.4 Momentum scale and resolution

Various deficiencies in detector simulation lead to p_T and η dependent data/simulation differences in muon momentum scale and resolution. The p_T of simulated muons is corrected so that they resemble data more closely. The p_T of ID and MS tracks are corrected individually: $p_T^{\text{MC,ID}} \rightarrow p_T^{\text{corr,ID}}$, $p_T^{\text{MC,MS}} \rightarrow p_T^{\text{corr,MS}}$. Divergences in momentum scale between data and simulation arise from the effects of the simulated detector not exactly replicating the effects of the real detector, resulting in an altered track curvature and therefore momentum measurement. Descriptions of the magnitude of the magnetic field, hit position and energy loss estimate in simulation all contribute to this. Another consequence is a narrower resolution in simulation compared to data prior to the correction.

4.4 Jets

4.4.1 Jet formation

Perturbative QCD interactions that occur during proton-proton collisions result in the production of high p_T colour-carrying particles: quarks and gluons. As they travel outward from the interaction point, the quarks and gluons continue to undergo perturbative interactions,

spawning more partons⁴, until colour confinement takes effect. At this point QCD bound states are formed from the free partons, a process known as hadronisation. The hadrons tend to be collimated due to conservation of the original hard parton momentum. It is the collimated streams of hadrons, initiated by partons, that are observed in the detector, and are therefore the proxy by which the interaction of quarks and gluons is studied. This is where jets come in. A jet is an object created out of localised groups of hadrons (and their decay products) in a way that causes it to acquire properties related to the instigating parton, for example a four-momentum. Hadrons can be neutral or charged, so jets can be built using signals from the ID, the EM and hadronic calorimeter. The series of events that leads to jet formation is depicted in Figure 4.3.

Jets emerge through a complex series of interactions that take place between the physics of interest at the interaction point and the observed physics at the detector, which can begin with initial state radiation, final state radiation, hadronic decays of heavy particles etc. Consequently, there is an inherent element of ambiguity when associating specific physics processes to jets, and there is not a reliable one-to-one correspondence between parton and jet kinematics. The best that can be done is to choose a method of jet construction, called a jet algorithm, that produces useful objects from which information about the hard-scatter can be inferred.

The task of a jet algorithm is to take a set of four-momenta, called constituents (they can be from tracks, clusters, simulated hadrons etc., as long as there is associated kinematic information), and cluster them into jets. Jets are defined by the algorithm used to create them: the algorithm decides which constituents to include in each jet and how to combine the constituents' kinematics to obtain the kinematics of the final jet (the recombination scheme). It is important to consider the behaviour of jet algorithms carefully; choices at the jet building level propagate backwards to the reconstruction of the event. Output jets should be insensitive to small, random variations in the chain of interactions that produce the input to the jet algorithm. In particular, the output object of a jet algorithm should be the same regardless of whether a hadron inside the jet radiates a soft (infrared) gluon, or a gluon parallel to its own direction (collinear). This is because theoretical calculations that account for these cases diverge and produce infinities, which are not observable, so a jet algorithm should not be sensitive to whether they occur. Together these properties are known as infrared and collinear safety (IRC safety).

⁴This is called perturbative parton showering.

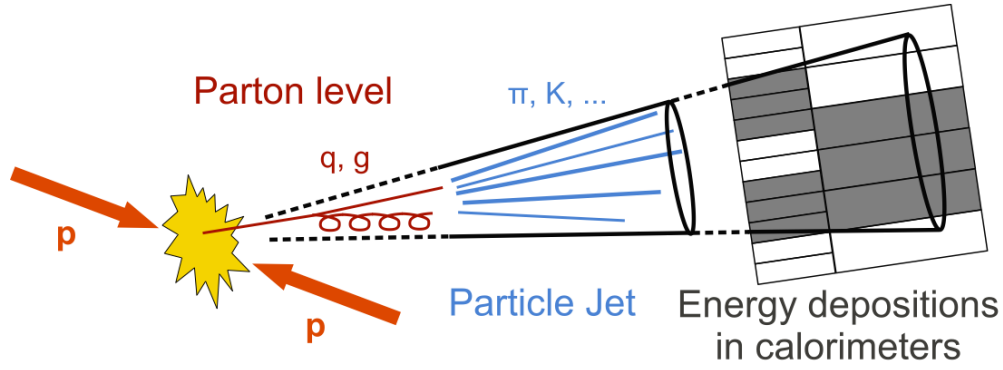


Figure 4.3: A diagram from [52] showing the stages of jet formation from the hard-scatter to energy deposits in the calorimeters.

4.4.2 Jet reconstruction: the anti- k_T algorithm

The anti- k_T algorithm [53] is a member of a genre of jet algorithm called sequential recombination algorithms which share a jet building technique and are characterised by the parameters they use. A benefit of sequential recombination algorithms is that they deal directly with the four-momenta of constituents and so can be applied directly to different types of input constituent in the same way. This makes them useful for testing theoretical models of jet formation because the output of the algorithm applied to, for example, simulated hadrons and calorimeter clusters can be readily compared. They also exhibit IRC safety.

The anti- k_T algorithm calculates a distance, d_{ij} , for each pair of constituents i and j with four-momenta $(k_{T,i}, \eta_i, \phi_i, E_i)$ and $(k_{T,j}, \eta_j, \phi_j, E_j)$, and a beam distance, d_{iB} , for every constituent i :

$$d_{ij} = \min\left(\frac{1}{k_{T,i}^2}, \frac{1}{k_{T,j}^2}\right) \frac{\Delta_{ij}^2}{R^2} \quad (4.5)$$

$$d_{iB} = \frac{1}{k_{T,i}^2}$$

where $\Delta_{ij} = \sqrt{(\eta_i - \eta_j)^2 + (\phi_i - \phi_j)^2}$ and R is a fixed number (for a given jet collection) that determines the radius of the jet in (η, ϕ) space. The smallest value of d_{ij} is identified, and the constituents i and j are combined by adding their four momenta to form a new single constituent if $d_{ij} < d_{iB}$, otherwise d_{iB} is declared a jet and removed from the procedure. The process is repeated until there are no constituents (i,j) such that $d_{ij} < d_{iB}$, i.e. all the constituents are jets.

The anti- k_T algorithm behaves in the following way with respect to hard and soft constituents.

Case 1: a single hard constituent, isolated from other hard constituents by $> 2R$, surrounded by soft constituents. In this case d_{ij} will be smaller for hard-soft pairings compared to soft-soft pairings, so soft constituents will be combined with the hard constituent before they get the chance to be combined with each other, and the momentum of the hard constituent will dominate the final jet. Soft constituents j are added to the growing jet i only if $\Delta_{ij} < R$, so the resulting jet will have a regular cone shape of radius ΔR around the original hard constituent.

Case 2: two hard constituents with $\Delta_{ij} < R$, surrounded by soft constituents. If one hard constituent has significantly larger p_T , then it dominates the jet momentum as the other hard and soft constituents are added to it, resulting in a jet with a regular cone shape around the hardest constituent. If the hard constituents have similar p_T , cones begin to form around each of them individually and are eventually combined, causing the final jet shape to be more irregular.

Case 3: two hard constituents separated by $R < \Delta_{ij} < 2R$, surrounded by soft constituents. The soft constituents will be divided between two jets built around the hard constituents. If one hard constituent has much larger p_T , it will be assigned most of the soft constituents from the overlapping radial area and the jet will have conical shape, while the other jet will be conical except with the overlapping area cut out. If the p_T are similar then there will be two irregularly shaped jets with the boundary inside the overlapping area about equidistant from the hard constituents.

The various scenarios are demonstrated in Figure 4.4. The advantage of the anti- k_T algorithm over other sequential recombination algorithms is that the jet boundaries are sensitive to hard constituents but not soft constituents, a consequence of the algorithm prioritising the hardest constituents. This means high p_T , isolated partons result in regular, cone shaped jets, allowing a 1-1 mapping between hard partons and jets, with a faithful representation of the parton kinematics.

4.4.3 Types of Jet

Anti- k_T jets are classified by the nature of the input constituents to the anti- k_T algorithm. Jets built using detector-level information, namely calorimeter jets and track jets, are called *reconstructed jets*, and can be made with data or simulated events. Jets can also be built from simulated final state particles with no detector effects applied; these are called *truth jets*. Calorimeter jets are made from topologically clustered calorimeter cells (topo-clusters). Topo-clusters are created by an algorithm which locates seed cells with energy above a threshold defined with respect to expected background noise, and adding topologically connected

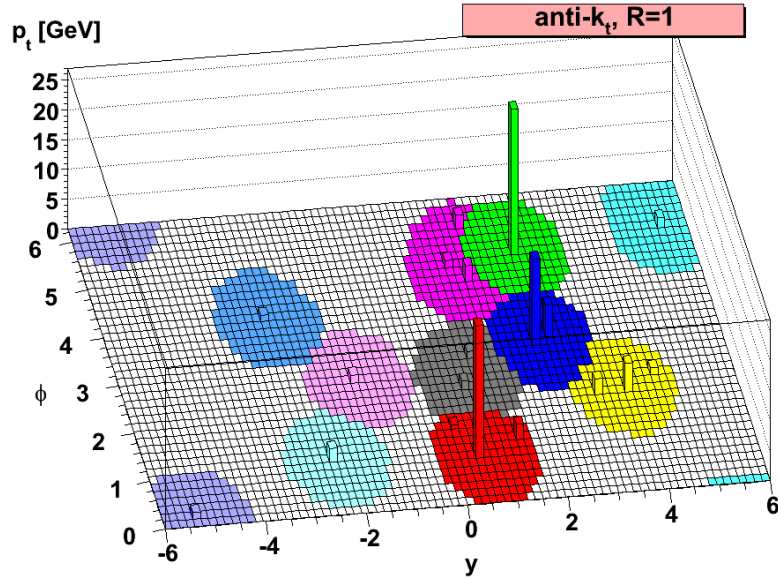


Figure 4.4: A plot from [53] showing the shapes of jets clustered using the anti- k_T algorithm with $R=1.0$. The shapes are regular and centred around the largest energy deposit. The red jet is an example of the anti- k_T algorithm applied to case 1 - a single hard constituent, isolated from other constituents by $> 2R$, surrounded by soft constituents - which results in a regular cone shape of radius ΔR around the original hard constituent. The blue jet is an example of case 2 - two hard constituents i and j with $\Delta_{ij} < R$, surrounded by soft constituents - which results in a slightly more irregularly shaped jet centred around the two hard constituents. The green and purple jets are an example of the algorithm applied to case 3 - two hard constituents i and j separated by $R < \Delta_{ij} < 2R$ - which results in two jets, the one centred on the hardest constituent having the most regular shape as the surrounding soft constituents are added to that jet first, and the one centred on the second hardest constituent having a more irregular shape as it loses some nearby constituents to the harder jet.

cells, working outwards and reducing the energy threshold as the displacement from the seed increases. The algorithm then separates large clusters with multiple local maxima into individual clusters [54]. A four-momentum is obtained by summing the energies of all the cells in the topo-cluster, and taking the energy-weighted average of the η and ϕ positions of the cells. It is assumed the topo-clusters originated at the centre of ATLAS (the origin of the coordinate system). Track jets, constructed from ID tracks with $p_T > 0.5$ GeV and $|\eta| < 2.5$, are less susceptible to pile-up contamination, because only tracks matched to the primary vertex are accepted by the jet algorithm. Simulated particles with lifetime $\tau > 10$ ps, except muons and neutrinos, are used to construct truth jets. Three collections of anti- k_T jets are used in the $t\bar{t}$ resonances search: R=0.4 anti- k_T calorimeter jets (called small-R jets), R=1.0 anti- k_T calorimeter jets (called large-R jets) and R=0.2 track jets.

4.4.4 Jet calibration

The discrepancy between the energy of the jet measured by the detector and the true energy⁵, called the jet energy scale (JES), which necessitates a calibration of the reconstructed jets. This discrepancy is much more significant for jets than for electrons and muons. A number of factors contribute to the JES that the calibration must account for: energy deposited outside of the calorimeters or in inactive calorimeter material, energy lost as a consequence of jet reconstruction (clusters of cells that didn't pass the topo-cluster signal-above-noise threshold, or weren't clustered by the jet algorithm), energy deposits due to pile-up, and the response of the calorimeter, which is non-uniform and lower for hadronic showers than electromagnetic showers [54].

The first calibration is applied directly to the topo-clusters, before the jet algorithm is applied, and results in two different jet collections. The initial energy measurement is performed at the electromagnetic scale (EM scale), which assumes the topo-clusters are made from energy deposited by electromagnetic showers, and so returns a correct value for that scenario. Jets built from these topo-clusters are called EM scale jets. Another collection of jets is created after local cluster weighting (LCW) is applied to the EM-scale topo-clusters. In this procedure, topo-clusters are identified as being a result of electromagnetic or hadronic showers, and cells in the latter are calibrated to account for the calorimeter response to hadrons. The energy deposited outside the clusters and in inactive material is also corrected for. In the $t\bar{t}$ resonances search, small-R jets are built using EM-scale topoclusters, and large-R jets are built using LCW topoclusters. The corrections applied to each EM-scale small-R

⁵The true energy is defined to be the energy of the corresponding truth jet. In simulation, truth jets are obtained by applying the jet algorithm to the final state particles in hadron showers. Reconstructed jets are obtained by applying the same algorithm to simulated detector signals that result from the same showers. Truth jets and reconstructed jets caused by the same hadron shower are usually close together in $\eta \times \phi$ space ($\Delta R < 0.4$). The truth jet energy is said to be at the particle-level scale.

jet to convert its four-momentum to the expected four-momentum of the particle responsible for the jet are described in this section. Since large-R jets tend to contain multiple particles, LCW topoclusters are used to give a more accurate energy measurement for the jet. Further corrections applied to large-R jets are also described in this section.

Corrections to small-R jets

Corrections to EM-scale small-R jets are applied in several stages, outlined in Figure 4.5. First, the jets' directions are modified so that they originate from the primary vertex instead of the detector's centre. Then the effect of pile-up on the EM-scale jet p_T , p_T^{reco} , is evaluated and removed on a per-event basis. The corrected jet p_T , p_T^{corr} , is obtained with the equation:

$$p_T^{\text{corr}} = p_T^{\text{reco}} - \rho \times A - \alpha \times (N_{PV} - 1) - \beta \times \mu \quad (4.6)$$

The $\rho \times A$ term removes most of the impact by subtracting the average p_T contribution from pile-up to a jet of area⁶ A . ρ is the average p_T density of jets in the event, taken from the median p_T/A of the jets. The terms $\alpha \times (N_{PV} - 1)$ and $\beta \times \mu$ remove a residual p_T dependence on the number of reconstructed primary vertices in the event (N_{PV}) and the pile-up (μ) and are determined from simulated events.

Once the effects of pile-up have been removed, the jets are ready to have their four-momentum altered to resemble that of a truth jet. This involves using the jet energy scale to obtain the particle-level energy, and correcting the η measurement, which is susceptible to biases arising from inhomogeneities in calorimeter material and granularity [56]. The jet energy scale is ascertained as follows. Truth jets and EM-scale jets are reconstructed from simulated events, and the EM-scale jets undergo origin and pile-up corrections. Isolated EM-scale jets are matched to truth jets if $\Delta R(\text{truth jet}, \text{EM-scale jet}) < 0.3$. Matched pairs are used to plot the ratio of reconstructed energy to truth energy, $E^{\text{reco}}/E^{\text{truth}}$, in bins of E^{truth} and η_{det} , the η coordinate of the detector (as opposed to the jet itself). The mean of the Gaussian fitted to an $E^{\text{reco}}/E^{\text{truth}}$ distribution is taken to be the average energy response in that bin. The response can then be expressed as a function of E^{reco} and determines the correction applied to a given E^{reco} . A similar method is used to analyse the remaining difference in η^{reco} and η^{truth} and prescribe a final calibration of jet p_T and η .

After the simulation-based energy calibration, the JES is found to have residual dependencies on certain jet properties. In particular, the calorimeter response and jet reconstruction are sensitive to the types of particles and energy distribution inside a jet, which are both properties related to the type of initiating particle. The global sequential calibration is a

⁶The area of a jet is defined in $y \times \phi$ space. It is calculated by imposing a uniform distribution of infinitesimally soft particles throughout the detector and clustering them into jets, then finding the $y \times \phi$ area within the jet that contains all the clustered soft particles [55].

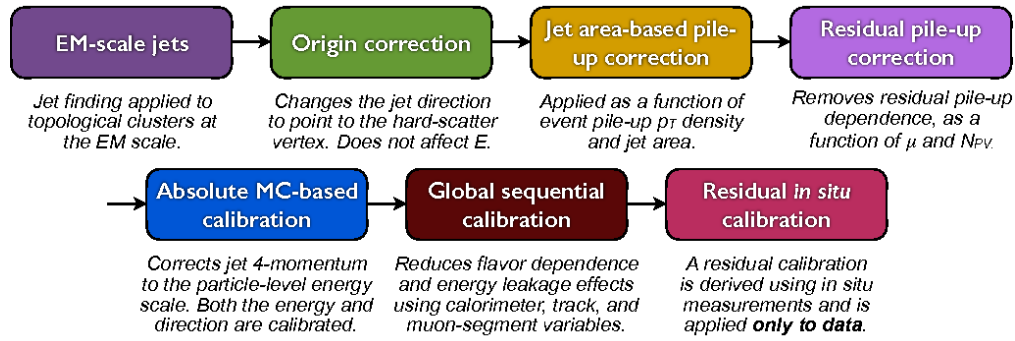


Figure 4.5: A schematic from [56] showing the series of calibrations applied to EM scale jets.

series of corrections based on five observables that the JES is independently sensitive to, which are applied to the jet four-momentum in order to mitigate JES bias in these observables. The five observables are: the fraction of the jet’s energy measured in the first layer of the hadronic calorimeter, the fraction of the jet’s energy measured in the third layer of the EM calorimeter, the number of tracks with $p_T > 1$ GeV matched to the jet, the average p_T weighted transverse distance in the η - ϕ plane between the direction of the jet and all tracks with matched to the jet, and the number of muon track segments matched to the jet. Lastly, the difference in jet response between data and simulation is evaluated and a final calibration is applied only to data. η dependent differences in response are determined by looking at dijet events with one jet in the forward region and one jet in the central region; the energy of the forward jet is corrected to that of the central jet whose energy measurement is more accurate. The difference in response to central jets between data and simulation is estimated using events where a jet recoils off a well-measured reference object such as a Z boson; in theory, the p_T of the jet and the reference object should be balanced. The difference between the average of the ratio $p_{T,\text{jet}}^{\text{data}}/p_{T,\text{ref object}}^{\text{data}}$ and the average of the ratio $p_{T,\text{jet}}^{\text{MC}}/p_{T,\text{ref object}}^{\text{MC}}$ is the JES ratio from which the data correction is derived.

The collection of reconstructed, calibrated small-R jets originate either in the hard-scatter or in pile-up interactions. Jet vertex tagger (JVT) [57] is a multivariate algorithm devised to reject jets that are likely a result of pile-up by considering how much of a jet’s momentum comes from tracks matched to the primary vertex.

Corrections to large-R jets

Large-R jets are usually associated with heavy, short-lived, hadronically decaying particles, namely high p_T top quarks, vector bosons and Higgs bosons. The ΔR separation of the decay products of one of these particles when $p_T \gg m_{\text{particle}}$ is approximately 1.0, so large-R jets in the $t\bar{t}$ resonances search are built using the anti- k_T with $R=1.0$. They are a more efficient means of gathering all the clusters associated with a heavy particle decay, compared to a

collection of several small-R jets [58], and therefore have the potential to return a better mass resolution (mass being a useful variable for signal/background discrimination). Due to their area, however, large-R jets are especially susceptible to contamination from clusters that are a result of initial state radiation, multiple parton interactions and pile-up. A trimming procedure [58] based on the assumption that clusters not from the hard scatter will be softer than clusters from the hard scatter is implemented with the aim of improving the large-R jet mass resolution. Constituents inside a large-R jet are reclustered into subjets with radius R_{sub} and are removed if they have $p_{T,\text{subjet}} < f_{\text{cut}} \times p_{T,\text{original large-R jet}}$. The values of the parameters optimised for mass resolution using anti- k_T jets are $R_{\text{sub}} = 0.2$, $f_{\text{cut}} = 0.05$.

The energy and η of trimmed large-R jets are then calibrated to the particle-level using the same simulation-driven procedure that is applied to small-R jets. Finally, a mass calibration [59] is applied to the calorimeter-based jet mass, m^{calo} , which for a jet J is defined to be:

$$m^{\text{calo}} = \sqrt{\left(\sum_{i \in J} E_i\right)^2 - \left(\sum_{i \in J} \vec{p}_i\right)^2} \quad (4.7)$$

where the jet constituents i have energy E_i and momentum \vec{p}_i . With the energy and mass calibrations applied, the distributions of the ratios $E_{T,\text{reco}}/E_{T,\text{truth}}$ and $m_{\text{reco}}^{\text{calo}}/m_{\text{truth}}^{\text{calo}}$ are on average equal to 1. The calibrations were developed for large-R jets with $p_T > 200$ GeV and $|\eta| < 2.0$.

4.5 b -tagging

b quarks initiate jets that contain a b hadron. The unique properties of b hadrons are exploited in order to identify so-called b -jets and distinguish them from jets initiated by lighter quarks, jets containing a charm hadron (c -jets), and jets initiated by hadronic τ decays. The abnormally long lifetime of b hadrons ($\simeq 1.5$ ps) compared to other unstable hadrons means that they travel on average a few mm from the interaction point before decaying, far enough that their decay products leave tracks with a significantly larger impact parameter than tracks originating at the primary vertex, and that the point of decay can be reconstructed as a secondary vertex. b -tagging is performed on track jets by a multivariate algorithm, MV2 [60], which makes decisions based on the outputs of other algorithms that can be classified into three separate types: impact parameter, secondary vertex reconstruction and decay chain multi-vertex reconstruction algorithms.

4.5.1 Impact-parameter based algorithms

There are two algorithms that assess how likely a track jet is to be a b -jet based on the impact parameters of its tracks: IP2D and IP3D. A sign is allocated to the transverse and longitudinal impact parameters of tracks, d_0 and $z_0 \sin \theta$, depending on whether the secondary vertex is in front of or behind the primary vertex relative to the jet direction. A large fraction of a b -jet's tracks are expected to originate at a vertex in front of the primary vertex. To differentiate between b -jets and other jets, the IP2D algorithm uses the transverse impact parameter significance, d_0/σ_{d_0} , while the IP3D uses the transverse and longitudinal parameter significance, $z_0 \sin \theta/\sigma_{z_0 \sin \theta}$. PDFs of the impact parameter significances for signal (tracks inside b -jets) and background (tracks inside light jets and c -jets) are generated using simulated events. The signal PDF is expected to be asymmetric compared to the more Gaussian-like background PDFs since background secondary vertices are more evenly distributed behind and in front of the primary vertex. Two log-likelihood ratio discriminants, $\sum_{i=1}^N \log(\frac{p_b}{p_l})$ and $\sum_{i=1}^N \log(\frac{p_b}{p_c})$, are calculated by each algorithm for each jet, where N is the number of tracks inside the jet, p_b is the likelihood of the track belonging to a b -jet track and p_l and p_c are the likelihoods of the track belonging to a light and c -jet respectively.

4.5.2 Secondary Vertex Finding Algorithm

The secondary vertex finding algorithm tests the hypothesis that a large fraction of the jet's tracks originate at a secondary vertex by attempting to reconstruct a secondary vertex using only tracks inside the jet. First, every pair of tracks is used to reconstruct its own two-track vertex. Two track vertices must be sufficiently displaced from the primary vertex, and must not look like a background secondary vertex, such as the point of decay of a long-lived particle. A new vertex is then created with a fitting method described in Section 4.1, using tracks from the successful two-track vertices. Several signal/background discriminating observables are calculated for the secondary vertices. For example, the mass of the tracks associated with the secondary vertex will be larger in the case of a b -hadron decay compared to other hadrons.

4.5.3 Decay Chain Multi-Vortex Algorithm

The most probable decay chain of a b quark is $b \rightarrow Wc$ then $c \rightarrow Ws$, resulting in multiple vertices associated with the jet. A decay chain multi-vertex reconstruction algorithm called JetFitter tries to find a line connecting the primary vertex to the b hadron and c hadron decay vertices that is consistent with the hadron lifetimes. Observables related to the decay

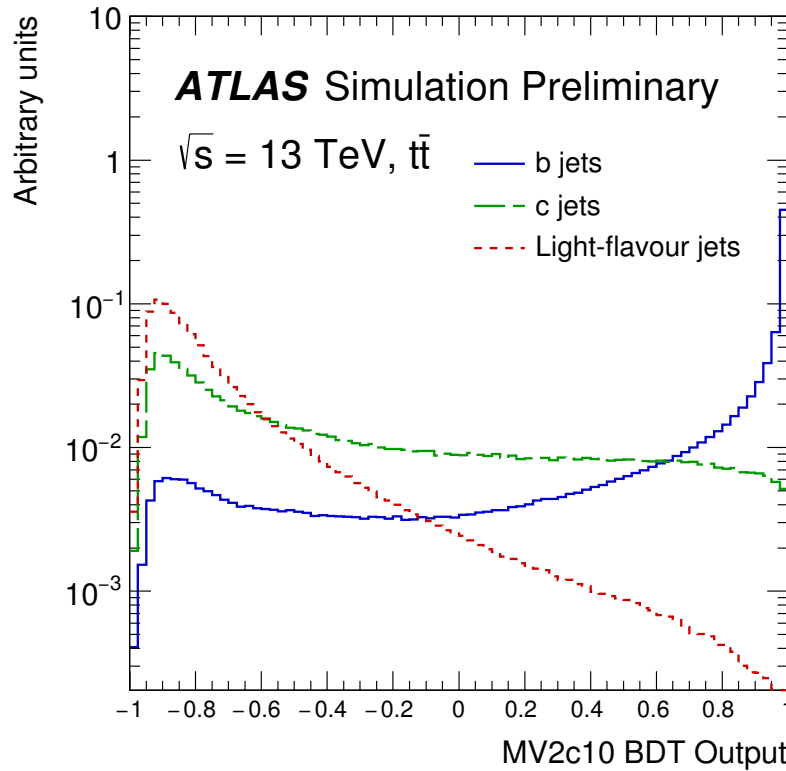


Figure 4.6: A plot from [60] showing the output of the MV2c10 BDT for b -jets, c -jets and light jets in simulated $t\bar{t}$ events.

chain that are useful for identifying b -jets are calculated.

4.5.4 Multivariate Algorithm

A Boosted Decision Tree (BDT) [60] combines the outputs of the algorithms into a single discriminant. The BDT was trained on $t\bar{t}$ events with b -jets labelled as signal and c -jets and light jets labelled as background. The distribution of the output discriminant, mv2c10, is shown in Figure 4.6. In the $t\bar{t}$ resonances search, the b -tagging algorithm is applied to $R=0.2$ track jets. Small- R jets are considered to be b -tagged if they fall within $\Delta R < 0.4$ of a b -tagged track jet. The cut placed on mv2c10 corresponds to a 70% working point, where the efficiency is defined to be the fraction of jets containing a b hadron that are b -tagged. At this working point, rejection rates of 17, 120 and 7 are achieved for τ -jets, light jets and c -jets respectively.

4.6 Top Tagging

LHC collision energies produce very high p_T top quarks, referred to as boosted top quarks, whose decay products have small ΔR separation in the detector. If a top quark decays hadronically and has sufficiently high p_T , its decay products are often found inside a single $R=1.0$ anti- k_T jet (a large- R jet). In a lower p_T decay, the kinematics of the individual quarks that decay from the top (b, q, q') can be reconstructed as they produce their own distinct small- R jets. As the top quark becomes more boosted, this information is lost. If the objective is to reconstruct the top quark, however, the ability to identify top quark decays in large- R jets means the kinematics of top can be determined without the intermediate step of reconstructing its individual decay quarks. A top-tagging algorithm [61] is a tool for identifying large- R jets that are the result of hadronically decaying top quarks. The top-tagging algorithm used in the $t\bar{t}$ resonances search [62] makes decisions based on two large- R jet variables: the invariant mass, defined in equation 4.7, and the N-subjettiness ratio τ_{32} . The N-subjettiness variable τ_N can be defined once N subjets are reconstructed from the large- R jet constituents using the k_t algorithm⁷. It is defined as:

$$\tau_N = \frac{1}{\sum_k p_{Tk} \times R} \sum_k p_{Tk} \times \min(\delta R_{1k}, \delta R_{2k}, \dots, \delta R_{Nk}) \quad (4.8)$$

where p_{Tk} is the p_T of constituent k , and $\delta R_{ik} = \Delta R(\text{constituent } i, \text{constituent } k)$. τ_N is a measure of how well the large- R jet can be broken down into N subjets. τ_{32} is defined as the ratio $\tau_{32} = \tau_3/\tau_2$; higher values of τ_{32} indicate that the large- R jet substructure can be better described by three separate subcomponents than two. Therefore, τ_{32} can be used to discriminate between, for example, large- R jets resulting from top quark decays and those resulting from W boson decays. The algorithm is available with a 50% and 80% working point and the latter is used for the $t\bar{t}$ resonances search.

4.7 Missing Transverse Energy

Conservation of momentum implies that the x and y components of the momentum of all final state particles in an event should sum to zero. Any deviation from zero indicates that particles that do not interact with the detector have been produced. Assuming Standard Model final state particles only, this means neutrinos. The missing momentum in the x (y) direction, E_x^{miss} (E_y^{miss}), is defined to be the negative of the sum of reconstructed objects' x (y) component of momentum. Electrons, photons, jets and muons are included in the sum,

⁷A sequential recombination algorithm as described in Section 4.4.2. It follows the same procedure as the anti- k_T algorithm, except $d_{ij} = \min(k_{T,i}, k_{T,j}) \frac{\Delta_{ij}^2}{R^2}$ and $d_{iB} = k_{T,i}^2$ in equation 4.5.

plus a soft component $E_{x,y}^{\text{soft}}$ built using tracks that are not associated with any object but are matched to the primary vertex and have $p_T > 400$ MeV:

$$E_{x,y}^{\text{miss}} = E_{x,y}^{\text{electrons}} + E_{x,y}^{\text{photons}} + E_{x,y}^{\text{jets}} + E_{x,y}^{\text{muons}} + E_{x,y}^{\text{soft}} \quad (4.9)$$

The missing transverse momentum is then defined as:

$$E_T^{\text{miss}} = \sqrt{(E_x^{\text{miss}})^2 + (E_y^{\text{miss}})^2} \quad (4.10)$$

4.8 Lepton Isolation

A standard requirement of electrons and muons used in physics analyses is that they are isolated. This is useful because an isolated energy deposit is a strong indication of a prompt non-hadronic particle; adding isolation criteria to the object selection helps to reject background jets without significantly degrading the identification efficiency. Isolation criteria need to be flexible to accommodate high p_T events. For example, a lepton from a high p_T leptonic top quark decay is expected to be less isolated than one from the same decay at low p_T due to the proximity of the W decay products. Isolation criteria is implemented as follows. The variable MI_R is calculated for each lepton ℓ using all tracks except the lepton's own track:

$$MI_R = \sum_{\Delta R(\text{track},\ell) < R_{\text{cut}}} p_T^{\text{track}} \quad (4.11)$$

where $R_{\text{cut}} = \min(10 \text{ GeV} / p_{T,\ell}, R_{\text{max}})$ ($R_{\text{max}} = 0.2$ for electrons and 0.3 for muons). To be considered isolated, leptons must have $MI_R < 0.06 \times p_{T,\ell}$. The cut on MI_R loosens with increasing p_T .

4.9 Overlap Removal

It is possible for the same detector signal, such as a calorimeter cluster or a track, to be used in the reconstruction of multiple physics objects. An overlap removal procedure is applied to nearby objects to ensure that a single signal does not result in two separate objects. In the $t\bar{t}$ resonance search, a standard overlap removal is applied to nearby lepton - small-R jet pairs. Calorimeter jets and electrons can share electromagnetic calorimeter clusters. The ΔR distance is calculated for all electron-jet pairs in the event. If $\Delta R(\text{electron},\text{jet}) > 0.2$, the jet is assumed to have been constructed from the electron energy deposit and is removed from the event. Then, if $\Delta R(\text{electron},\text{jet}) < 0.4$ for any remaining pairs, the electron is assumed to be from a decay inside the jet and is removed. Jets can occasionally leave signals in the muon

spectrometer. If any muon-jet pair has $\Delta R(\text{muon, jet}) < 0.04 + 10 \text{ GeV} / p_{\mu, T}$, then the muon is rejected from the event, as long as the jet has more than two associated tracks matched to the primary vertex. Otherwise it is the jet that is rejected. Additionally, R=0.2 track jets with $\Delta R(\text{lepton, track jet}) < 0.2$ are removed.

Chapter 5

Statistical Methods

5.1 The Role of Statistics in Searches for New Physics

In a search for new physics, two possibilities are considered: background-only (SM), and signal-plus-background (BSM+SM)¹. The aim is to compare data with background-only expectation, which is well understood, in a way that will reveal the most striking difference if a signal exists. This is done by considering observables with the greatest sensitivity to the new physics. A $t\bar{t}$ resonance signal would modify the mass distribution of $t\bar{t}$ pairs produced in collision events, causing a local excess or deficit with respect to expectation around the mass of the new particle. Therefore the number of $t\bar{t}$ events that fall inside an arbitrary local mass range is an observable sensitive to a new resonance. Predictions about this observable, which is a random variable, under background-only and signal-plus-background models can be encoded in probability density functions (PDFs). In a $t\bar{t}$ resonance search the relevant PDF is a Poisson distribution. Equation 5.1 describes the probability of finding n $t\bar{t}$ events in a given mass ($m_{t\bar{t}}$) bin, if ν is the known mean number of events in that bin. Since the masses of any new particles are unknown, the entire $t\bar{t}$ mass spectrum up to 6000 GeV is examined; equation 5.2 is the joint PDF describing the probability of finding $\mathbf{n} = \{n_i\}$ events over all the mass bins, if ν_i is the mean number of events in the i^{th} bin.

$$P(n; \nu) = \frac{e^{-\nu} \nu^n}{n!} \quad (5.1) \quad P(\mathbf{n}; \boldsymbol{\nu}) = \prod_{i=1}^{N_{bins}} \frac{e^{-\nu_i} \nu_i^{n_i}}{n_i!} \quad (5.2)$$

The data can be compared to a particular model by calculating the joint PDF in equation 5.2, with n_i set to the observed n_i , and ν_i set to the mean n_i according to that that model. The result is a measure of how likely it was to observe the data n_i if the model is true, and is known as the *likelihood*² of the model, \mathcal{L} .

¹Many different signal models affect the same observable and can be explored in the same search.

²The likelihood is not a true probability. It is a statement about the how likely a model is given observed data, rather than how probable a set of data is given a certain model.

Whether the data is described by the background-only hypothesis or a signal-plus-background hypothesis, it is subject to statistical fluctuations that may cause the data to appear consistent with a model that is false, or inconsistent with a model that is true. As the number of events collected increases, the data n_i will on average converge on the mean of the Poisson distribution that truly describes them, but there is an inherent statistical uncertainty that means rigorous statistical methods are required to draw conclusions about how well a model describes the data and, when comparing different hypotheses, which one is most supported by the data.

A frequentist approach to statistics is adopted in the methods described in the following chapters. Assuming that the correct type of PDF is chosen to describe the data, the unknown parameters in the PDF are considered to have true values which can, in theory, be ascertained from data as $N_{events} \rightarrow \infty$. However, in reality, finite data can be used to make statements about the true value with a degree of uncertainty related to N_{events} . The purpose of this section is to introduce the statistical methods that will be used in future chapters, described in the context of a search for a new heavy resonance.

5.2 Quantifying the agreement between data and prediction

In the statistical analysis of data collected for a new physics search it is standard to begin by assessing how compatible the observed data is with the Standard Model prediction by applying a hypothesis test. The hypothesis under scrutiny (the Standard Model) is called the null hypothesis, H_0 , and the contending BSM hypothesis is called the alternative hypothesis, H_1 . Each hypothesis corresponds to a PDF of the random variable or random vector being measured. For example, if the measurement is the number of events n_i in each of N bins, denoted \mathbf{n} , then the null and alternative hypotheses can be expressed as:

$$H_0 : f(\mathbf{n}; H_0) = \prod_{i=1}^{N_{bins}} \frac{e^{-B_i} B_i^{n_i}}{n_i!} \quad (5.3) \quad H_1 : f(\mathbf{n}; H_1) = \prod_{i=1}^{N_{bins}} \frac{e^{-(S_i+B_i)} (S_i + B_i)^{n_i}}{n_i!} \quad (5.4)$$

where B_i is the mean number of expected events in the i^{th} bin under the background-only hypothesis, and $S_i + B_i$ is the mean number of expected events in the i^{th} bin under the signal-plus-background hypothesis.

A test statistic t is calculated for the observed data and is designed to be a measure of the level of agreement between the data and H_0 . It can be as simple as one scalar number representing the whole dataset. A useful test statistic is optimised to be sensitive to the kind of deviation a signal is likely to cause. In the case of a $t\bar{t}$ resonance search where the events

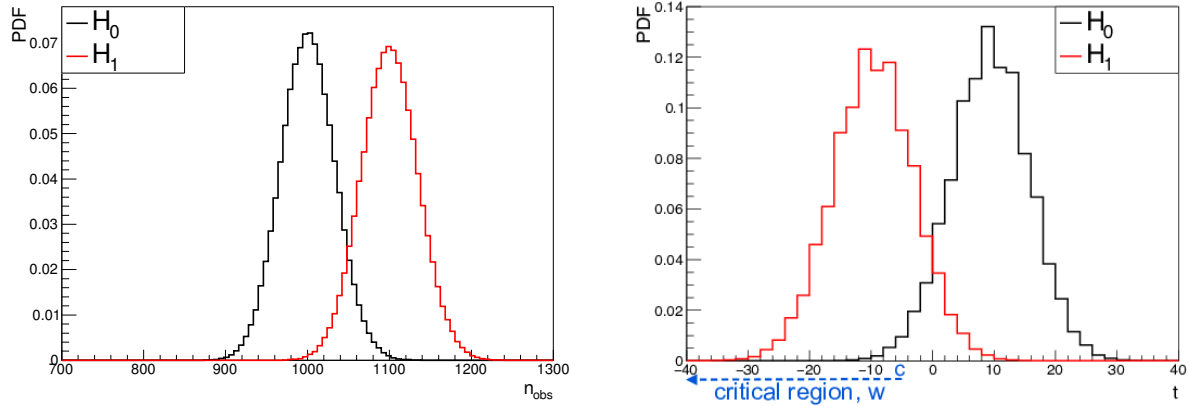


Figure 5.1: Events were generated randomly according to the PDFs in equations 5.3 and 5.4, where H_0 had 1000 expected background events and H_1 had 1000 expected background events plus 100 expected signal events. The left hand side plot shows the distribution of the number of observed events in a bin, n_{obs} , under H_0 and H_1 . The right hand side plot shows the distribution of a test statistic t calculated from the number of observed events. The test statistic used here is the log likelihood ratio, defined in equation 5.17. The test statistic distribution is shifted to the left for H_1 , so the critical region is defined beginning in the left tail of the H_0 distribution and extends out to negative infinity.

are binned in $m_{t\bar{t}}$, this would be a local excess of events with respect to the Standard Model prediction; the more extreme the excess, the larger the test statistic. Since the test statistic is a function of the observed data, it is a random variable itself and has a distinct PDF under H_0 and H_1 . A critical region, w , shown in Figure 5.1, is defined such that if $t \in w$ then H_0 is rejected. A hypothesis test can reject hypotheses in this way, but can never prove them to be true. If $t \notin w$ then H_0 is simply not rejected. The choice of w determines the confidence with which one can reject the hypothesis. The probability α that t will be observed in the critical region under H_0 is called the significance level of the hypothesis test. This is the probability that H_0 is rejected when true, and is known as a type-I error. The probability β that H_0 is not rejected in the case where H_1 is true is called a type-II error. The power of a test to reject H_0 when it is not true is defined to be $1 - \beta$, and depends on which alternative hypothesis H_1 is true. For the critical region chosen in the example in Figure 5.1, α and β are given by:

$$\alpha = P(t \in w; H_0) = \int_{-\infty}^c g(t; H_0) dt \quad (5.5) \quad \beta = P(t \notin w; H_1) = \int_c^{\infty} g(t; H_1) dt \quad (5.6)$$

The p-value of the observed data is the probability of obtaining data equally or less consistent with H_0 than the observed data was, as quantified by the test statistic. The smaller the p-value, the larger the discrepancy between the data and H_0 . The critical region represents a cut on the p-value of the data; when $t_{\text{obs}} \in w$, the p-value will be $\leq \alpha$, small enough

that the data is considered to be sufficiently incompatible with H_0 for H_0 to be rejected. It is conventional to formally reject H_0 , when H_0 is the Standard Model, when the p-value $\leq \alpha = 3 \times 10^{-7}$ [63]. The statement of rejection is: if H_0 were true, the probability that a measurement would yield the observed data is less than 3×10^{-7} , so H_0 is assumed to be untrue. The low value chosen for α is to ensure that H_0 is not rejected as a result of statistical fluctuations - the priority is to avoid a type-I error when testing against the null hypothesis.

5.2.1 Trials Factor

When quantifying the agreement between data and H_0 , resonance searches focus on a data excess in a group of adjacent bins. Equation 5.4 takes into account data deviations across all bins; if the test statistic was based on this PDF it would reduce the sensitivity of a resonance search. However, the group of bins that should be used to create the test statistic is ambiguous. The location of the excess is not predicted by signal models, and choosing the group of bins with largest excess of events after the data has been revealed corrupts the hypothesis test. It is possible that choosing the largest statistical fluctuation out of N independent groups of bins to create the test statistic will return a p-value $< \alpha$, causing H_0 to be ruled out when true. The larger N , the more likely this is to happen. A hypothesis test that uses a test statistic dependent on the outcome of the experiment no longer has type-I error α [64] because of the choice of test statistics that could be used in the experiment, the probability that any one of them returns a p-value $< \alpha$ is greater than the probability that a given one of them does the same:

$$P(\text{at least one p-value} \leq \alpha) = 1 - \prod_{i=1}^N P(\text{p-value} > \alpha) = 1 - (1 - \alpha)^N \quad (5.7)$$

To circumvent this issue, a *hypertest* is defined, based on the results of N independent hypothesis tests applied to the data, sampling all bins. Its test statistic is:

$$t = -\log_e(\min_i\{\text{p-value}_i\}) \quad (5.8)$$

the negative log of the smallest p-value out of the N tests. This hypertest considers all bin groups individually and has the desired type-I error probability α shown in equation 5.5.

5.3 Parameter Estimation in New Physics Searches

Another statistical challenge in the analysis of collision data is the estimation of an unknown parameter from a known PDF. In a new physics search, the parameter of interest is often the signal strength, μ . In a signal-plus-background model, the mean number of expected events in each bin ν_i can be parameterised as $\nu_i = B_i + \mu S_i$, with $\mu = 1$ corresponding to the nominal signal-plus-background model, $\mu = 0$ corresponding to the background-only model, and $\mu \in (0, 1)$ corresponding to a signal-plus-background model with a diminished signal cross-section. If a hypothesis test with significance α fails to reject H_0 , the next step is to consider the set of alternative hypotheses H_1 :

$$f(\mathbf{n}; H_1) = \prod_{i=1}^{N_{bins}} \frac{e^{-(\mu S_i + B_i)} (\mu S_i + B_i)^{n_i}}{n_i!} \quad (5.9)$$

where the signal strength μ is such that it would not have caused H_0 to be rejected. If the nominal signal and background rates S_i and B_i are known then μ can be inferred by estimating the parameter $\boldsymbol{\nu} = \mu \mathbf{S} + \mathbf{B}$ from the observed data. Since H_0 is not rejected, μ is generally estimated in terms of an upper limit on its value. Alternatively, if a hypothesis test with significance α rejects H_0 , the alternative hypotheses H_1 are considered in order to estimate the cross-section of the observed signal.

5.3.1 Confidence Intervals

Confidence intervals are a well-defined means of conveying the statistical uncertainty on an estimate of an unknown parameter ν . A confidence interval is constructed using the observed data in an experiment. It contains a range of possible parameter values and has the property that it contains the true value ν_t in a specified fraction of identical independent experiments as the number of experiments $N \rightarrow \infty$.

An estimator of a parameter is a function of the observed data. For example, the Maximum Likelihood Estimator $\hat{\nu}$ of the parameter ν , calculated from observed data n_{obs} when the PDF is a Poisson distribution of mean ν , is simply $\hat{\nu} = n_{obs}$. The PDF of the estimator then depends only on the value of the parameter: $f(\hat{\nu}; \nu)$, and can be used to find a value a (b) such that the estimator will be greater (less) than a (b) with probability α (β):

$$\alpha = P(\hat{\nu} \geq a(\nu)) = \int_{a(\nu)}^{\infty} f(\hat{\nu}; \nu) d\hat{\nu} \quad (5.10) \quad \beta = P(\hat{\nu} \leq b(\nu)) = \int_{-\infty}^{b(\nu)} f(\hat{\nu}; \nu) d\hat{\nu} \quad (5.11)$$

The probability that the estimator $\hat{\nu}$ lies in the interval $[b, a]$ is then:

$$P(\hat{\nu} \in [b(\nu), a(\nu)]) = 1 - \alpha - \beta \quad (5.12)$$

This can be manipulated to obtain information about ν . From 5.10 and 5.11, it follows that

$$\alpha = P(a^{-1}(\hat{\nu}) \leq \nu) \quad (5.13) \quad \beta = P(b^{-1}(\hat{\nu}) \geq \nu) \quad (5.14)$$

yielding an interval that contains ν with probability $1 - \alpha - \beta$:

$$P(\nu \in [a^{-1}(\hat{\nu}), b^{-1}(\hat{\nu})]) = 1 - \alpha - \beta \quad (5.15)$$

This holds true for all possible ν , but since the estimator is calculated with observed data, it is an estimator of ν_t , and so the constructed interval applies to ν_t . Thus from observed data and a known PDF of the estimator, it is possible to build an interval which contains the unknown parameter with a specified probability. To set an upper limit on a parameter, the lower bound of the interval is set to zero and the resulting upper bound is greater than the parameter with the chosen probability.

5.3.2 Log-likelihood Ratio

Before the method of creating a confidence interval for the signal strength is described, the log-likelihood ratio must be introduced. The method involves testing data against signal-plus-background hypotheses with increasing signal strength μ , using the log-likelihood ratio test statistic. For this reason, the roles of the hypotheses are reversed, with signal-plus-background becoming the null hypothesis H_0 and background-only becoming the alternative hypothesis H_1 . The conventional significance used in this case is $\alpha = 0.5$, making it much easier to reject a signal model than the Standard Model. Previously it was stated that the low value of α is chosen to avoid a type-I error. At the same time, it is desirable for the hypothesis test to be useful in the event that H_1 is true (the SM), with a minimal probability that it would accept H_0 (the signal model) in this case, i.e. the power of the test is maximised for any chosen α . There is a choice of critical regions w with the property $P(t \in w; H_0) = \alpha$. It follows from the Neyman-Pearson lemma [65] that the optimal power, $1 - \beta$, of a hypothesis test for a given significance α is achieved via the log-likelihood ratio method. In this method the test statistic is built by taking the ratio of the likelihoods of the hypotheses. Given a fixed set of data $\mathbf{n} = \{n_i\}$, generated according to a joint PDF f which depends on an unknown parameter $\boldsymbol{\nu} = \{\nu_i\}$, the likelihood of a particular $\boldsymbol{\nu}$ is defined as $\mathcal{L}(\boldsymbol{\nu}) = f(\mathbf{n}; \boldsymbol{\nu})$. Assuming H_1 and H_0 correspond to the PDFs in equations 5.3 and 5.4:

$$\mathcal{L}(\boldsymbol{\nu}) = \prod_{i=1}^{N_{bins}} f(n_i; \nu_i) = \prod_{i=1}^{N_{bins}} \frac{e^{-\nu_i} \nu_i^{n_i}}{n_i!} \quad (5.16)$$

where $\boldsymbol{\nu} = \mathbf{B} (= \{B_i\})$ for H_0 and $\boldsymbol{\nu} = \mathbf{S} + \mathbf{B} (= \{S_i + B_i\})$ for H_1 , and n_i are the observed data. Then the likelihood of H_0 , \mathcal{L}_0 , the likelihood of H_1 , \mathcal{L}_1 , and the log-likelihood ratio,

LLR , which is the test statistic, are given by:

$$\mathcal{L}_1 = \frac{e^{-B} B^n}{n!} \quad \mathcal{L}_0 = \frac{e^{-(S+B)} (S+B)^n}{n!} \quad LLR = -2 \log_e \left(\frac{\mathcal{L}_0}{\mathcal{L}_1} \right) \quad (5.17)$$

The test statistic used to illustrate the critical region w for the chosen α in Figure 5.1 is the LLR . Using the log-likelihood ratio method, the chosen α uniquely determines the upper limit c of the integral in equation 5.5, since the lower bound of the integral is $-\infty$. Then α and β can be unambiguously expressed as:

$$\alpha = \int_{-\infty}^c g(LLR; H_0) dLLR \quad (5.18) \quad \beta = \int_c^{\infty} g(LLR; H_1) dLLR \quad (5.19)$$

If the LLR calculated from the observed data, LLR_{obs} , falls below c , then the H_0 is rejected with significance α . If $g(LLR; H_0)$ and $g(LLR; H_1)$ cannot be determined analytically they can be obtained by generating many pseudo-datasets $\mathbf{n}_{gen} = \{n_{gen,i}\}$ for each hypothesis according to $f(\mathbf{n}; H_0)$ and $f(\mathbf{n}; H_1)$ then building the resulting LLR distributions. In this section it was assumed that the expected number of signal and background events, S and B , as well as the form of the PDF, are known exactly, and the only unknown parameter was the Poissonian mean ν . The modifications made to this method in order to account for systematic uncertainties are described in section 5.4.

5.3.3 Limit Setting with CL_s

The CL_s method is often used to prescribe a confidence interval to a signal cross section in a signal-plus-background model. CL_{s+b} and CL_b , given in equations 5.20 and 5.21, are calculated for each signal-plus-background hypothesis H_1 (H_1 's PDF is shown in equation 5.9) as the signal strength μ is increased from 0.

$$CL_{s+b} = \int_{LLR_{obs}}^{\infty} g(LLR; H_1) dLLR \quad (5.20) \quad 1 - CL_b = \int_{-\infty}^{LLR_{obs}} g(LLR; H_0) dLLR \quad (5.21)$$

CL_{s+b} is the p-value for H_1 ; the smaller it is, the less signal-like the data. Therefore for a fixed LLR_{obs} , calculated from a dataset consistent with the background-only hypothesis, CL_{s+b} calculated for each signal strength μ will decrease as μ increases. A cut α can be placed on CL_{s+b} to exclude with $1 - \alpha$ confidence level (CL) all signal strengths with $CL_{s+b} < \alpha$. This means that if the fraction of times the LLR under a given μ would be less signal-like than LLR_{obs} is smaller than α , then that value of μ is excluded with $1 - \alpha$ CL. The μ s with $CL_{s+b} \in [\alpha, 1.0]$ are not excluded; this range of μ values, $\mu \in [0, \mu_{upper\ limit}]$, comprises a confidence interval that contains μ_t a fraction $1 - \alpha$ of the time.

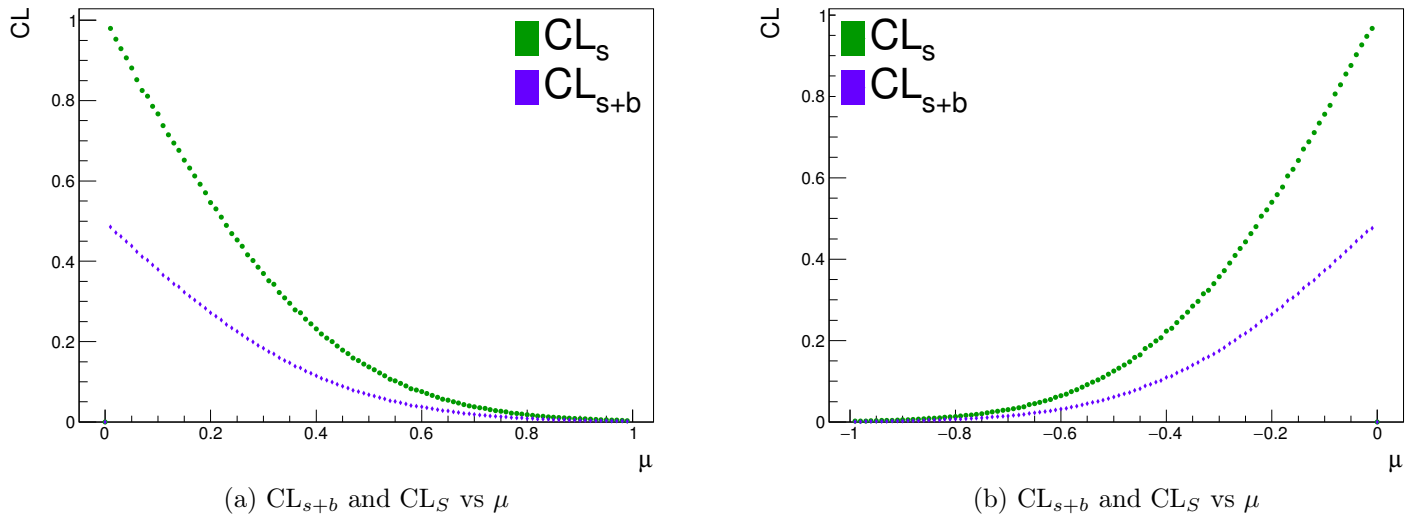


Figure 5.2: CL_{s+b} and CL_s plotted against signal strength for positive (a) and negative (b) signal strengths, where the background only and signal plus background models are represented by equations 5.3 and 5.4 respectively. When the signal strength is large, it is clearer whether the data is more compatible with signal or background. CL_{s+b} and CL_s converge. When the signal strength is small, data that is very incompatible with the signal will also be incompatible with the background. In this case it is harder to exclude μ using CL_s .

If the experiment has poor sensitivity, it is possible that when LLR_{obs} is very un-signal like, it is also very un-background like. It is not desirable to exclude signal strengths using CL_{s+b} when the data is also incompatible with background. CL_b can be used to modify the limit setting method in this scenario. $1-CL_b$ is the p-value for H_0 ; it is the probability that LLR would be more signal-like than LLR_{obs} under H_0 . CL_s is defined as:

$$CL_s = \frac{CL_{s+b}}{CL_b} \quad (5.22)$$

A cut α is applied to CL_s in the same way as it is to CL_{s+b} , in order to exclude a range of signal strengths. $CL_s \simeq CL_{s+b}$ when the experiment is sensitive to signal, since signal-like data will have $CL_b \simeq 1$. When data is incompatible with both signal and background, CL_b is low and boosts the CL_{s+b} value so that H_1 is not excluded so easily. The response of CL_{s+b} and CL_s to increasing signal strength is demonstrated in Figure 5.2. $CL_b < 1 \implies CL_s > CL_{s+b}$ so a quoted confidence interval derived using CL_s includes μ_t more than a fraction $1 - \alpha$ of the time, where $1 - \alpha$ is the stated CL.

5.3.4 Incorporating systematic uncertainties

Realistically, the signal strength, μ , cannot be inferred from the observed data and the signal and background models with only statistical uncertainty. Various elements that contribute to the signal and background estimation in H_1 and H_0 have an associated systematic uncertainty; changing them from their nominal values has an impact on the expected signal and background yields. There are various sources of systematic uncertainty. They can be a result of detector simulation, e.g. uncertainties in energy scales, efficiencies and resolutions, or of theoretical uncertainties, e.g. predicted cross-section uncertainties. Systematic uncertainties are accounted for in a hypothesis test by including them as additional parameters in the likelihood. We now consider the data PDF to depend on multiple unknown parameters: the parameter of interest, μ , and nuisance parameters $\{\theta_j\} = \boldsymbol{\theta}$, which represent the systematic uncertainties:

$$f(n_{obs}|\mu) \rightarrow f(n_{obs}|\mu, \boldsymbol{\theta}) \quad (5.23)$$

The nuisance parameters must be constrained in some way, otherwise a genuine excess in data could be explained away by modifying a nuisance parameter and keeping $\mu = 0$, while a false excess could be manufactured by modifying a nuisance parameter in a way that causes a deficit and allowing $f(n|\mu = 1)$ to fit the data.

Often, values with associated systematic uncertainties follow a Gaussian distribution centred on the nominal value. The quoted systematic uncertainty is the σ of the Gaussian. This can be encoded in the likelihood by introducing nuisance parameters, θ_j , for each uncertainty source, which follow a Gaussian distribution with mean 0 and $\sigma = 1$. The impact of deviation from nominal of the value the event yield for each uncertainty, parameterised by θ_j , is determined: $B \rightarrow B(\theta_j)$, and a Gaussian likelihood function of θ_j , $C(\theta_j)$, is used to multiply the model's likelihood, effectively constraining the nuisance parameter and therefore the value. For example, if some value has a systematic uncertainty of $\pm 5\%$, and increasing the nominal value by 5% results in a 10% increase in background yield, the likelihood becomes:

$$\mathcal{L}(\mu, \boldsymbol{\theta}) = P(n|\mu S + B(1 + 0.1 \times \boldsymbol{\theta})) \cdot C(\boldsymbol{\theta}) \quad (5.24)$$

Here the nominal value, which corresponds to $\theta_j = 0$, will reproduce the nominal expected background and maximise the Gaussian function. A large deviation from expectation in the value will return a small Gaussian value, reducing the likelihood. Taking into account all data bins and systematic uncertainties represented by $\boldsymbol{\theta}$, the likelihood becomes:

$$\mathcal{L}(\mu, \boldsymbol{\theta}) = \prod_{i=1}^N P(n_i|\mu, \boldsymbol{\theta}) C(\boldsymbol{\theta}) \quad (5.25)$$

From the modified likelihood, a new test statistic called the *profile likelihood-ratio* test statistic is defined:

$$\lambda(\mu) = \frac{\mathcal{L}(\mu, \hat{\boldsymbol{\theta}}(\mu))}{\mathcal{L}(\hat{\mu}, \hat{\boldsymbol{\theta}})} \quad (5.26)$$

where $\hat{\mu}$ and $\hat{\boldsymbol{\theta}}$ are the values of μ and $\boldsymbol{\theta}$ that maximise \mathcal{L} , and $\hat{\boldsymbol{\theta}}$ maximises \mathcal{L} for a given μ .

Chapter 6

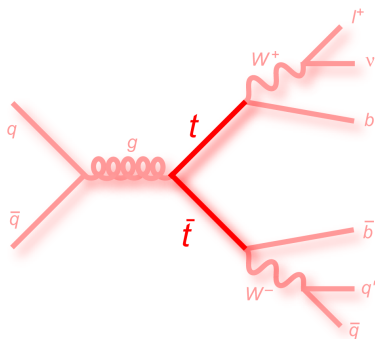
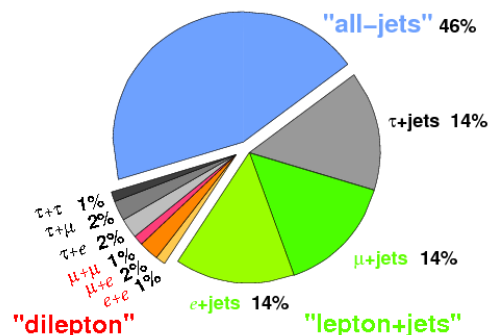
A Search for $t\bar{t}$ resonances

6.1 Introduction

This analysis searches LHC proton-proton collision data collected by ATLAS for deviations with respect to Standard Model expectation in $t\bar{t}$ production that may indicate the existence of a new particle that decays to a $t\bar{t}$ pair: a local excess or deficit in the $t\bar{t}$ invariant mass ($m_{t\bar{t}}$) spectrum. It is motivated by various BSM theories, some of which provide predictions for particle ($X \rightarrow t\bar{t}$) cross-sections, resonance widths and shapes that are used as reference signals in the search. The search is performed by constructing and comparing the $m_{t\bar{t}}$ spectrum in data and the expected SM background. In data, the $m_{t\bar{t}}$ spectrum is built by selecting events consistent with $t\bar{t}$ decay; the selected events will primarily be final state $t\bar{t}$ events, with a contribution from $t\bar{t}$ -like backgrounds. Therefore, the expected background $m_{t\bar{t}}$ spectrum is built by applying the same selection to simulated SM $t\bar{t}$ events as well as other non- $t\bar{t}$ SM processes that have a non-negligible chance of passing the selection criteria. When relevant SM processes are not reliably described by simulation, data-driven methods are used to estimate their contribution to the $m_{t\bar{t}}$ spectrum. It is impossible to distinguish between individual SM background and BSM signal $t\bar{t}$ final states, i.e. SM $t\bar{t}$ is an irreducible background. For the search method to remain agnostic of the signal model, $t\bar{t}$ events must be selected without bias, for example with no preference for a particular signal mass. Other SM final states which can, in principle, be distinguished from $t\bar{t}$ are reducible and are suppressed by the event selection. The result of the search is twofold. As discussed in Chapter 5, first a p-value is assigned to the data using a test statistic that is sensitive to a $t\bar{t}$ resonance but signal model independent, i.e. sensitive to the number of events that fall in an arbitrary $m_{t\bar{t}}$ range. This quantifies the level of agreement between data and expected background. The p-value that would constitute evidence for or a discovery of non-SM physics is predefined. Second, if no significant deviation is found, 95% CL upper limits are set on the cross-sections of signals in three benchmark models for a range of resonance masses and widths. The 95%

CL upper limit is the upper boundary of a confidence interval $[0, \text{upper limit}]$ that contains the true cross-section 95% of the time. Mass constraints can be placed on the particles in signal models by comparing the nominal theoretical cross section and the upper cross section limit for a series of signal masses. If the theoretical cross-section is higher than the upper limit for a particular signal mass, the signal is said to be excluded at that mass. The theoretical cross section decreases with increasing mass. At some point it will fall below the observed upper limit. It is concluded that the new particle is not produced at any mass below this point and the experiment is not sensitive to larger signal masses. The $\sqrt{s} = 13$ TeV collision energy will increase the mass reach of the search over earlier searches at lower centre of mass energies. The increased integrated luminosity - this search uses 36.1 fb^{-1} of p-p collision data - improves the power of the limit setting procedure, allowing smaller signal cross-sections to be ruled out.

The search is carried out in the semileptonic decay channel, shown in Figure 6.1; both tops decay to a W boson and a b quark, one of the W s then decays leptonically to a lepton and a neutrino while the other decays hadronically to two quarks ($t\bar{t} \rightarrow WbWb \rightarrow l\nu bqq'b$). This channel includes events where the initial lepton is a tau ($W \rightarrow \tau\nu_\tau$) that decays leptonically so that the final state is still an electron or muon and missing transverse energy. If the tau goes on to decay hadronically then the event is considered an all-hadronic $t\bar{t}$ decay, a reducible background. This channel is the most promising in terms of signal sensitivity, offering the best balance between cross section ($\sim 30\%$ of $t\bar{t}$ decays) and non- $t\bar{t}$ background contamination. The most frequent $t\bar{t}$ decay mode is all-hadronic but this channel suffers from a large multijet background. Dileptonic decay is the cleanest channel with two high p_T leptons but this decay is rarer and it is harder to reconstruct the $m_{t\bar{t}}$ variable due to the presence of one neutrino from each top decay. The branching ratios of the $t\bar{t}$ decay modes are shown in Figure 6.2.

Figure 6.1: Semileptonic $t\bar{t}$ decay.Figure 6.2: $t\bar{t}$ decay channel ratios.

Semileptonic $t\bar{t}$ decay has an experimental signature of a single, isolated high p_T lepton, missing transverse energy and jets, including a b -tagged jet. Events are selected using a high

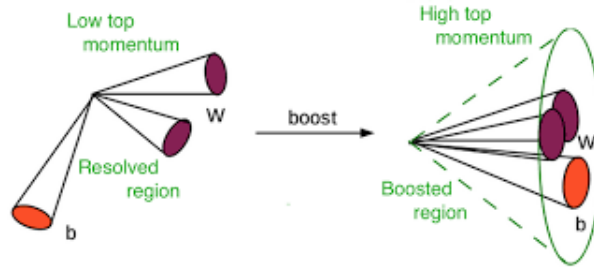


Figure 6.3: Depiction of the change in hadronic top decay topology as the top p_T increases.

p_T single lepton trigger and then a preselection is applied to identify possible $t\bar{t}$ events. Further kinematic and topological cuts are implemented to suppress the reducible backgrounds. Physics objects in data and simulated events are reconstructed as in Chapter 4, with additional object selection criteria applied. The $t\bar{t}$ invariant mass is reconstructed from objects in the event that have been identified as products of the $t\bar{t}$ decay. LHC collisions produce top quarks over a large p_T range, resulting in a variety of decay topologies. The calorimeter clusters from hadronic top decay that are input into the jet algorithm tend to go from being well separated in (η, ϕ) space to overlapping as the top p_T increases, as illustrated in Figure 6.3, and so the object(s) reconstructed from a high p_T top decay are likely to differ from those reconstructed from a low p_T top decay, making it impractical to use a single rigid event selection. The selection and reconstruction methods are adapted to different decay scenarios so that good selection efficiency and $m_{t\bar{t}}$ reconstruction can be achieved. Selected $t\bar{t}$ events are separated into four mutually exclusive decay channels based on lepton flavour (electron or muon) and top decay topology: *boosted* (high p_T) and *resolved* (low p_T), allowing the analysis to take advantage of the high collision energy and remain as sensitive to as wide a range of resonance masses as possible.

6.2 Object Definitions

The physics objects used in this analysis are leptons, jets (including b-tagged jets) and missing transverse energy. Each candidate object in simulation and data is required to pass quality cuts in order to achieve a desired efficiency/ fake rate balance, and undergo overlap removal if necessary. Details on how the candidate objects are reconstructed from detector-level information can be found in Chapter 4. This section describes the additional quality cuts applied to the candidate objects. The event selection, and all subsequent steps of the analysis, use only objects that have passed the quality cuts.

6.2.1 Leptons

Reconstructed electrons and muons are required to pass identification criteria as described in section 4.2. and 4.3 respectively. In this analysis electrons must pass tight likelihood criteria and muons must pass medium. Electrons and muons must have $p_T > 30$ GeV and $p_T > 25$ GeV respectively, and $|\eta|$ within the detector acceptance ($|\eta| \in [0, 1.37] \cup (1.52, 2.47]$ for electrons and $|\eta| < 2.5$ for muons). Cuts are applied to the lepton's impact parameters, d_0 and z_0 , to suppress pile-up. Leptons are also required to be isolated from other physics objects. Lepton isolation is quantified by a variable MI_R that measures the sum of p_T of tracks (excluding the lepton's own track) inside a cone of variable radius around the lepton direction.

$$MI_R = \sum_{\Delta R(\text{track}, \ell) < R_{\text{cut}}} p_T^{\text{track}} \quad (6.1)$$

where R_{cut} is the minimum out of 10 GeV/ p_T^ℓ and 0.2 if the lepton being considered is an electron, and the minimum out of 10 GeV/ p_T^ℓ and 0.3 if it is a muon. Leptons are isolated if they have $MI_R < 0.06$. The variable cone size effectively loosens the isolation requirement for high p_T leptons as the tracks included in the MI_R calculation come from a reduced volume. This allows leptons from high p_T W decays that are close to the other top quark decay products to be accepted. A lepton from an equivalent decay at low p_T is expected to be more isolated and must pass the same MI_R cut with a larger volume.

6.2.2 Jets and Missing Transverse Energy

Large-R jets are anti- k_T R=1.0 jets built from local-calibrated topoclusters and trimmed with parameters $R_{\text{sub}} = 0.2$ and $f = 0.05$. A top-tagging algorithm [62] is applied to large-R jets with $p_T > 300$ GeV and $|\eta| < 2.0$. The algorithm tags hadronic top quark decays based on the mass and n-subjettiness ratio τ_{32} variables. It is implemented at the 80% working point, which has a background rejection of 5.5 for large-R jet $p_T \in (200, 500)$ GeV and 5.2 for large-R jet $p_T > 500$ GeV [62].

Small-R jets (also referred to as jets) are anti- k_T R=0.4 jets built from EM-scale topoclusters. They must have $p_T > 25$ GeV and $|\eta| < 2.4$. A cut on the jet vertex tagger (JVT) output (defined in Chapter 4), $JVT > 0.59$, is applied to jets with $p_T < 60$ GeV and $|\eta| < 2.4$. The JVT accepts jets from the hard-scatter with 92% efficiency and rejects 98% of pile-up jets. Small-R jets are used to evaluate missing transverse energy, E_T^{miss} , which is calculated as in Chapter 4.

In the event selection, at least one b-tagged jet is required in the event. The MV2c20 b -tagging algorithm is applied to track jets: anti- k_T R=0.2 jets built from tracks with $p_T > 400$ MeV that are $> \Delta R=0.2$ from leptons. The track jets that undergo b -tagging are required

to have $p_T > 10$ GeV, $|\eta| < 2.5$ and at least two tracks. The MV2c20 algorithm operates at the 70% working point, which has a rejection rate of 17, 120 and 7 for τ -jets, light jets and c-jets respectively. Track jets are used because a better b-tagging efficiency can be achieved with track jets compared to calorimeter jets at high jet p_T .

6.2.3 Trimming parameters for large-R jets

The trimming procedure applied to large-R jets is described in section 4.4.4. This procedure uses parameters f_{cut} and R_{sub} when deciding how to cluster subjets inside the large-R jet, and which of these subjets to remove. Ideally all the subjets that are removed would be pile-up and those leftover would be the decay products of the hadronically decaying top quark. The trimming parameters can be tuned using simulated events to achieve as close to this scenario as possible. The figures of merit used to decide the best values of f_{cut} and R_{sub} are the mean and width of the large-R jet mass distributions obtained using each combination of the parameters. The best combination should give the mean of the large-R jet mass distribution closest to the mass of the top quark and the smallest spread in mass values. Optimisation studies were performed using simulated large-R jets reconstructed from hadronic top quark decays to tune these parameters. Gaussians were fitted to the peaks of mass distributions of top-tagged large-R jets that had been trimmed using different parameter combinations. Figure 6.4 shows the means and standard deviations (in GeV) of these Gaussians for each combination of trimming parameters applied to large-R jets in simulated samples of Z' events. Although these plots appear to indicate that the optimal parameters are $f_{\text{cut}} \simeq 0.05$ and $R_{\text{sub}} \simeq 0.3$, other aspects of the large-R jet mass distribution had to be taken into account. For example, Figure 6.5 shows the large-R jet mass distribution after trimming with parameters $f_{\text{cut}} = 0.05$ and $R_{\text{sub}} = 0.3$ was applied to top-tagged large-R jets in $Z' = 5$ TeV events: there is a distinct peak around the top quark mass but large tails on either side consisting of large-R jets with masses far from the top quark mass. The final recommendation for the parameters was $f_{\text{cut}} = 0.05$ and $R_{\text{sub}} = 0.2$, based on the combined results of different studies. These parameters were found to produce the best combination of large-R jet mass close to the expected top quark mass, and a narrow width of the mass peak, as well as other features of the reconstructed large-R jet that are sensitive to changes in the parameters.

6.2.4 Overlap Removal

Overlap removal is applied to pairs of objects that have otherwise passed the selection criteria but are close enough in (η, ϕ) space that one object may have been double-counted. Any jet with $\Delta R(\text{electron, jet}) < 0.2$ is assumed to be a fake and rejected. Any electron

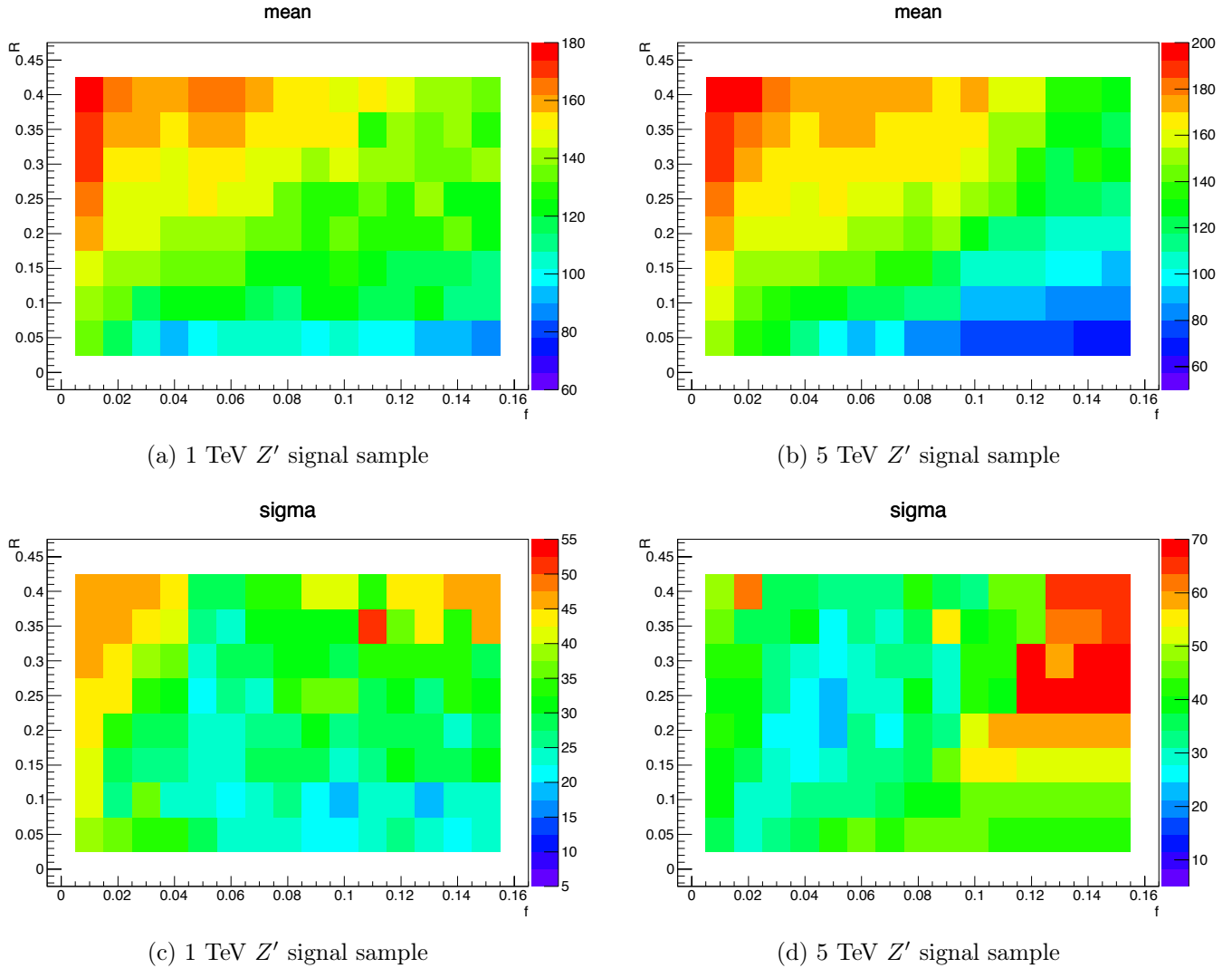


Figure 6.4: Mean and standard deviation (in GeV) of Gaussians fitted to the peaks of mass distributions of top-tagged large-R jets in Z' signal samples, for a range of combinations of the large-R jet trimming parameters f_{cut} (or f in the plots) and R_{sub} (or R in the plots).

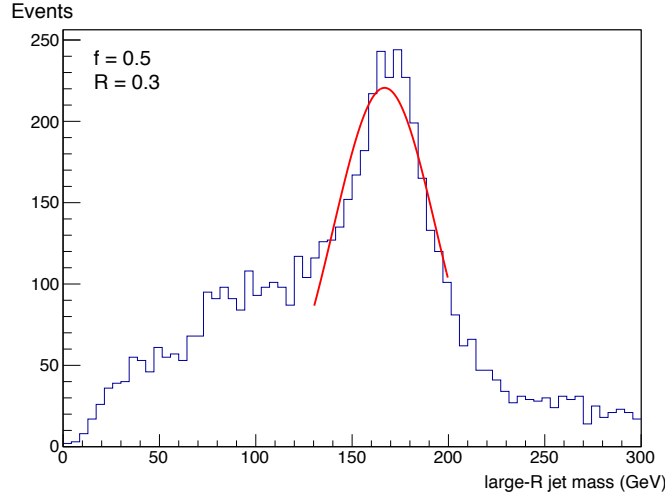


Figure 6.5: The large-R jet mass distribution after trimming with parameters $f_{\text{cut}} = 0.05$ and $R_{\text{sub}} = 0.3$ was applied to top-tagged large-R jets in $Z' = 5$ TeV events: the large tails on the distribution should be taken into account when tuning the parameters.

within $\Delta R < 0.4$ of a remaining jet is assumed to be a non-prompt electron from a b-jet decay and is also rejected. This is discussed in more detail in section 7.2. Muons with $\Delta R(\text{muon}, \text{jet}) < 0.04 + \frac{10 \text{ GeV}}{p_T^\mu}$ are removed as they are likely fakes, unless the jet has less than three tracks in which case the jet is removed instead.

6.3 Signal, Backgrounds and Data

6.3.1 Signal

Three benchmark signals are used in the limit setting stage of this analysis: a Z' boson, a Kaluza-Klein graviton and a Kaluza-Klein gluon. The parameters in the BSM models that determine the masses and widths of the signal particles are unknown. Signal samples for signal masses ranging from 0.4 TeV to 5 TeV are prepared for each model (the predicted cross-section of a given hypothesised particle decreases for increasing particle mass and the analysis is not expected to be sensitive to the benchmark signals considered beyond masses of 5 TeV). The three models' parameters are tuned to give different signal widths: the Z' boson is the narrowest and the Kaluza-Klein gluon is the widest. Smaller widths correspond to narrower peaks, which are easier to detect than a wider peak for a given cross-section.

Z'_{TC2} boson

Z'_{TC2} is a leptophobic spin-1 boson predicted by a topcolour-assisted-technicolour model [5]. Its production is associated with a narrow resonance. Z'_{TC2} events were generated using

Pythia 8 [66] with the NNPDF2.3 LO PDF set [67] and normalised to the NLO cross-section. Z'_{TC2} resonance widths are smaller than the detector resolution; samples were generated with widths of 1% and 3% of the particle's mass.

Kaluza-Klein graviton

The Kaluza-Klein graviton, G_{KK} , is a spin-2 graviton in a Randall-Sundrum model [68]. Its branching ratio to light fermions is suppressed because in this model Kaluza-Klein gravitons are localised near the TeV brane and the light fermions are localised near the Planck brane [69]. G_{KK} has a width between 3% and 6% of its mass for masses 0.4-3 TeV. MadGraph5_acMC@NLO [70] was used with the NNPDF2.3 LO PDF set to generate G_{KK} events. The parton showering was done with Pythia.

Kaluza-Klein gluon

The Kaluza-Klein gluon, g_{KK} , is a spin-1 boson in a Randall-Sundrum model [6] with a width between 10% and 40% of its mass. g_{KK} events were generated by the Pythia 8 generator at leading order with the NNPDF2.3 LO PDF set.

6.3.2 Standard Model Backgrounds

The main Standard Model backgrounds are $t\bar{t}$ production, a W boson produced alongside jets (W +jets), single top production, a Z boson produced alongside jets (Z +jets), multijets, and the production of two vector bosons (diboson). The W +jets and multijets backgrounds have data-driven elements that are described in the next section. The rest are simulated using Monte Carlo techniques.

$t\bar{t}$ and single top

$t\bar{t}$ and single top quark events were generated at NLO by the Powheg v2 [71] generator with the CT10 parton distribution function (PDF) [72] set. The parton shower and underlying event were simulated using Pythia v6.428 [73] with the CTEQ6L1 PDF set [74]. Heavy flavour hadron decays were modelled with EvtGen v1.2.0 [75]. Dedicated $t\bar{t}$ samples, sliced in $m_{t\bar{t}}$, are used for $m_{t\bar{t}} > 1.1$ TeV by applying a mass filter. This is done to obtain better statistics at high $m_{t\bar{t}}$ and reduce the statistical uncertainty when setting limits on the cross-sections of high mass particles. $t\bar{t}$ samples are normalised to the NNLO+NNLL cross-section [76], [77].

W +jets, Z +jets and diboson

W +jets and Z +jets events were generated using the Sherpa 2.2.1 generator [78] (matrix elements were calculated for up to two partons at NLO and four partons at LO) with the NNPDF30 NLO PDF set [67] and normalised to NNLO cross-sections. $W + b\bar{b}$ +jets, $W + c\bar{c}$ +jets, $W + b\bar{b} + c\bar{c}$ +jets, $W + c$ +jets, W + light jets samples are produced separately. Dedicated samples with vector boson p_T and heavy flavour content filters applied were used to ensure sufficient statistics even for high p_T events. Diboson events (WW , WZ , ZZ) were generated using the Sherpa 2.2.1 generator (matrix elements were calculated for up to one parton at NLO and up to three partons at LO) with the CT10 PDF set and normalised to the generator cross-sections.

6.3.3 Data

36.1 fb⁻¹ of $\sqrt{s} = 13$ TeV proton-proton collision data collected by the ATLAS detector in 2015 and 2016 is used in this search. The data was taken from a centrally produced good run list (GRL). To be included in the GRL, data must pass certain quality criteria. For example, the data must have been recorded during stable beams, and all ATLAS subdetectors had to be operational so that events can be properly reconstructed.

6.4 Data driven backgrounds

6.4.1 Multijets normalisation and kinematic distributions

Multijet events are events with a final state comprising several jets. They have a large cross-section [79] and are a dominant background in many new physics searches but are suppressed by the requirement of a high p_T , isolated lepton. If one of the jets is misreconstructed as an electron, the multijet event may pass the semileptonic $t\bar{t}$ selection. This process has large statistical and systematic uncertainties when modelled using Monte Carlo techniques, and so the multijet background is estimated from data using a matrix method [1].

$t\bar{t}$ events are selected from data, once using tight lepton identification and isolation criteria, yielding N_{tight} events, and once using loose lepton identification and no isolation criteria, yielding N_{loose} events. N_{loose} and N_{tight} can be broken down into signal and background components:

$$N_{\text{loose}} = N_{\text{prompt}} + N_{\text{multijet}} \quad (6.2)$$

$$N_{\text{tight}} = \epsilon \times N_{\text{prompt}} + f \times N_{\text{multijet}} \quad (6.3)$$

where N_{prompt} is the number of events with a prompt lepton¹, N_{multijet} is the number of multijet events, ϵ is the efficiency for selecting events with prompt leptons, and f is the misidentification rate for selecting multijets events.

f is established from data by defining a multijet background control region. $t\bar{t}$ events are selected using the resolved channel selection criteria, but with inverted cuts on missing transverse energy and transverse mass so that the data sample is dominated by multijet events. In this selection, objects are only required to satisfy loose lepton identification criteria and do not need to be isolated. The prompt lepton contribution to this multijet enriched sample, which can be modelled more easily, is estimated with simulated events and subtracted. The fake rate f is defined to be the fraction of objects in the control region that pass tight lepton identification and isolation criteria. The efficiency ϵ is defined to be the fraction of prompt leptons passing loose identification criteria that additionally pass tight identification and isolation criteria. It is calculated using simulated $t\bar{t}$ events. The simulation efficiency is converted to the corresponding data efficiency with a correction based on the difference between data and simulation efficiency in $Z \rightarrow \ell\ell$ events, by applying weights to the simulated events. Once f and ϵ are known, equations 6.2 and 6.3 can be solved to obtain N_{prompt} and N_{multijet} . The kinematic distributions of the multijet background are modelled by parameterising ϵ and f as functions of the kinematic variables of interest: lepton p_T , an isolation variable and $\Delta R(\text{lepton, nearest jet})$.

6.4.2 $W + \text{jets}$ normalisation and flavour components

The $W + \text{jets}$ background consists of $W + b\bar{b} + \text{jets}$, $W + c\bar{c} + \text{jets}$, $W + c + \text{jets}$ and $W + \text{light jets}$ events. Corrections to the simulated $W + \text{jets}$ samples, derived from data, are applied to correct the normalisation and flavour component fractions. The normalisation correction procedure uses the fact that more positively charged W^+ bosons than negatively charged W^- bosons are produced in $p-p$ collision due to the uud quark content of protons. This charge asymmetry is predicted more accurately by simulation than the overall rate of $W + \text{jets}$ events. Therefore, a more reliable estimate of the total number of $W + \text{jets}$ events in data, $N_{W,\text{data}}$, can be obtained using:

$$\frac{\Delta_{\text{data}}^{\text{charge}}}{N_{W,\text{data}}} = \frac{\Delta_{\text{MC}}^{\text{charge}}}{N_{W,\text{MC}}} \quad (6.4)$$

where $N_{W,\text{MC}}$ is the total number of $W + \text{jets}$ events in simulation and $\Delta_{\text{MC}}^{\text{charge}}$ ($\Delta_{\text{data}}^{\text{charge}}$) is the number of $W^+ + \text{jets}$ events minus the number of $W^- + \text{jets}$ events in simulation (data). A $W + \text{jets}$ control region is defined using $t\bar{t}$ selection criteria without the ≥ 1 b -tagged jet

¹A prompt lepton is a lepton that originates at or very close to the primary vertex e.g. from a vector boson or τ lepton decay. A non-prompt lepton originates away from the primary vertex e.g. from the in-flight decay of a hadron exiting the collision point.

requirement since this cut greatly reduces the W +jets acceptance. $N_{W,MC}$ and $\Delta_{MC}^{\text{charge}}$ are counted when the control region is applied to simulated W +jets events. To determine $\Delta_{\text{data}}^{\text{charge}}$ the control region is applied to data and the number of events with positive/negative leptons are counted. The observed $\Delta_{\text{data}}^{\text{charge}}$ will have contributions from charge symmetric processes like $t\bar{t}$ which will cancel out through approximately equal contributions to $N_{W^+, \text{data}}$ and $N_{W^-, \text{data}}$, and from charge asymmetric processes such as single top production which are evaluated using simulated events and subtracted from the data. The number of W +jets events in data before b -tagging, $N_{W^+} + N_{W^-}$, can be rewritten as:

$$N_{W^+} + N_{W^-} = \left(\frac{r_{MC} + 1}{r_{MC} - 1} \right) (N_{W^+, \text{obs}} - N_{W^-, \text{obs}}) \quad (6.5)$$

where $r_{MC} = N_{W^+, MC} / N_{W^-, MC}$, and $N_{W^+, \text{obs}} - N_{W^-, \text{obs}}$ is the observed difference between the number of events with a positively charged lepton and a negatively charged lepton (after subtracting the contribution from charge asymmetric processes). A scale factor C_A , parameterised as a function of jet multiplicity, is derived by taking the ratio $N_{W, \text{data}} / N_{W, MC}$ for each jet multiplicity separately (2, 3, 4 and ≥ 5). Simulated events are weighted by C_A so that the overall normalisation is modified to the expected number of W +jets events in data prior to b -tagging: $N_{W, MC} \rightarrow N_{W, \text{data}}$.

The flavour fractions, $f_{\text{flavour}} = \frac{N_{W, MC}^{\text{flavour}}}{N_{W, MC}}$, are not accurately predicted in simulation, so they are estimated from data. The four flavour fractions are $f_{b\bar{b}}$, $f_{c\bar{c}}$, f_c , and f_{light} . A scale factor for each flavour fraction, K_{flavour} , is determined by comparing data and simulation after the global scale factor C_A has been applied. A W +jets enriched control region is created by modifying the $t\bar{t}$ event selection to require exactly 2 jets instead of at least 3 jets. The number of multijet background events in this control region, N_{Q^\pm} , is non-negligible and must be accounted for². The system of linear equations:

$$C_A \sum K_{\text{flavour}} N_{W, MC^-}^{\text{flavour}} + K_Q N_{Q^-} = D_{W^-} + N_{Q^-} \quad (6.6)$$

$$C_A \sum K_{\text{flavour}} N_{W, MC^+}^{\text{flavour}} + K_Q N_{Q^+} = D_{W^+} + N_{Q^+} \quad (6.7)$$

$$\sum f_{\text{flavour}} K_{\text{flavour}} = 1 \quad (6.8)$$

can be solved to obtain the scale factors, K_{flavour} , where D_{W^\pm} is the observed number of W +jets events with a positively/negatively charged lepton, minus the background contribution estimated with simulated events, and K_Q corrects the normalisation of the multijet background. The K_{flavour} are $K_{b\bar{b}, cc}$, K_c and K_{light} , where $K_{b\bar{b}, cc}$ refers to both the $W + b\bar{b}$ +jets and $W + c\bar{c}$ +jets contributions, the $N_{W, MC^\pm}^{\text{flavour}}$ are N_{MC, W^\pm}^{bb} , N_{MC, W^\pm}^{cc} , N_{MC, W^\pm}^c , $N_{MC, W^\pm}^{\text{light}}$, and

² N_{Q^\pm} is evaluated using the previously described matrix method (section 6.4.1) but with the W +jets control region.

K_c is assumed to be 1³. The simulated W +jets charge asymmetry prediction used to determine C_A depends on the flavour fractions. This means that the procedure for estimating C_A followed by the procedure for estimating the flavour fractions must be repeated iteratively until the outputs are stable.

6.5 Event Selection

The event selection is a series of kinematic and topological cuts applied to data and simulated events to remove non- $t\bar{t}$ final states from the data sample while accepting different decay topologies and final state particles present in semileptonic $t\bar{t}$ decay. To achieve this, a loose preselection is applied to identify $t\bar{t}$ -like events, followed by a more rigorous selection that separates selected events into four orthogonal channels by decay topology (boosted or resolved) and lepton flavour (electron or muon).

6.5.1 Preselection

The event must contain at least one primary vertex, ensuring that it is a hard-scatter event. Events must pass one of a combinations of single lepton triggers⁴ (electron or muon) with the lowest p_T threshold at 24 GeV (20 GeV) for electrons (muons) in 2015 runs and 26 GeV (26 GeV) for electrons (muons) in 2016 runs. Additionally, exactly one lepton (electron or muon) must be present, and this lepton has to match the trigger that was fired⁵. This excludes many dileptonic final state $t\bar{t}$ events and other common backgrounds containing two leptons such as $Z \rightarrow ee$. Some missing transverse energy is expected from the leptonic W boson decay, so the cut $E_T^{\text{miss}} > 20$ GeV is applied, reducing the multijet background. Another test, which involves reconstructing a transverse mass variable, is carried out to assess whether the E_T^{miss} and the lepton are compatible with a leptonic W boson decay. The transverse mass of one particle, m_T , and of a two particle system, M_T , are defined by:

$$m_T^2 = m^2 + p_x^2 + p_y^2 = E^2 - p_z^2 \quad M_T^2 = (E_{T,1} + E_{T,2})^2 - (\mathbf{p}_{T,1} + \mathbf{p}_{T,2})^2. \quad (6.9)$$

³This is because the multijet background estimated by the procedure described in section 6.4.1 is not very precise, and so a scale factor K_Q is included in the linear equations and applied to the multijet estimate used in this method. The contributions of $W + c$ +jets and the multijet background are both charge symmetric, so since the multijet estimate is corrected for in this method, the data/simulation difference cannot be used to estimate K_c .

⁴The 2015 trigger menu was HLT_e24_lhmedium_L1EM20VH, HLT_e60_lhmedium_HLT_e120_lhloose for electrons and HLT_mu20_iloose_L1MU15, HLT_mu50 for muons. The 2016 trigger menu was HLT_e26_lhtight_nod0_ivarloose, HLT_e60_lhmedium_nod0, HLT_e140_lhloose_nod0 for electrons and HLT_mu26_ivarmedium, HLT_mu50 for muons.

⁵A lepton ℓ is matched to the trigger if $\Delta R(\ell, \text{lepton that fired the trigger}) < 0.1$.

When M_T^2 is constructed with a lepton and E_T^{miss} from a W decay, the M_T distribution represents the transverse mass of the W ; it will peak near the W boson mass then fall off, since $M_T < M$, the mass of the W boson. Assuming the E_T^{miss} represents a massless neutrino, M_T , or M_T^W , can be re-expressed as:

$$M_T^W = \sqrt{2p_T^\ell E_T^{\text{miss}}(1 - \cos \alpha)} \quad (6.10)$$

where p_T^ℓ is the lepton transverse momentum and α is the azimuthal angle between ℓ and \vec{E}_T^{miss} . A cut, $M_T^W + E_T^{\text{miss}} > 60$ GeV, is used to select events that contain a leptonic W decay, and consequently further suppresses multijet events. At least one b -tagged track jet is required in the event. The remaining events are now ready to be sorted into channels. First they are tested against the boosted selection (described in section 6.5.2), and only if they fail that are they tested against the resolved selection (described in section 6.5.3), so that there is no overlap in event content between the channels. The orthogonality in the electron and muon channels is already enforced by the preselection. In the case where an event would meet both boosted and resolved criteria, preference is given to the boosted channel since a better $m_{t\bar{t}}$ resolution can be achieved from reconstructing boosted events, and the boosted channel is more sensitive to high mass signals. Events that pass the preselection but fail the boosted and resolved selections are rejected as background.

6.5.2 Boosted Selection

An event has a boosted topology if the decay products of the hadronic top quark fall inside one large-R jet. This topology occurs frequently in the decays of top quarks with a sufficiently high p_T . Boosted events must contain at least one large-R jet that is top-tagged. Since the lepton and the the top-tagged large-R jet are products of different top quark decays in a boosted $t\bar{t}$ event, some (η, ϕ) separation is expected between them, and a cut $|\Delta\phi(\text{large-R jet}, \ell)| > 2.3$ is applied. One small-R jet, referred to as the selected jet, j_{sel} , that satisfies $\Delta R(j_{sel}, \text{lepton}) < 1.5$ and $\Delta R(\text{large-R jet}, j_{sel}) > 1.5$ is required. If there is more than one such jet then the one with the highest p_T is chosen to be j_{sel} . The first ΔR cut is for choosing a j_{sel} that is likely to share a mother particle with the lepton, and the second is to make sure it does not overlap with the large-R jet, since clusters inside the large-R jet can also be reconstructed as small-R jets. j_{sel} is identified with the b -jet from the leptonically decaying top. At least one b -tagged small-R jet is required in the event, however j_{sel} does not need to be b -tagged. Choosing j_{sel} as described, without requiring it to be b -tagged, gives a better $m_{t\bar{t}}$ resolution compared to using b -tagging information to choose it, and compared to using information about the reconstructed top quark candidate [1].

6.5.3 Resolved Selection

An event has a resolved topology if the hadronic decay products of the top quarks are reconstructed as four small-R jets that are well separated in (η, ϕ) . The majority of events fit this topology. Top quarks in resolved events have, on average, a lower p_T than in boosted events. Resolved events are required to have at least four small-R jets; three will be matched to the hadronic top decay products and one to the b -jet from the leptonic top. No ΔR requirement between the reconstructed objects is used to associate jets to theoretical decay products as in the boosted channel, instead a χ^2 algorithm, described in section 6.6, is used to select the best four jet combination in the event by comparing each jet mass to the expected mass of a jet that is correctly associated with the theoretical decay product; the combination that gives the lowest value of χ^2 is selected. A cut is placed on the minimum value of χ^2 to suppress backgrounds with many jets that otherwise meet the resolved criteria.

6.5.4 b -tag Categories

In order to improve the sensitivity of the search, selected events in each channel are further separated into four categories based on the b -tagged track jets:

- Category 0: no b -tagged jet matched to either of the top quark candidates.
- Category 1: a b -tagged jet is matched to the leptonic top candidate only.
- Category 2: a b -tagged jet is matched to the hadronic top candidate only.
- Category 3: Both the hadronic and leptonic top candidates have b -tagged jets matched to them.

Category 0 events are removed for the limit setting procedure; this channel is the most susceptible to non- $t\bar{t}$ background and it has the poorest reconstruction performance so the invariant mass of selected $t\bar{t}$ events is distorted; studies show that including this category degrades the sensitivity of the analysis [80]. In the boosted channel, a b -tagged jet is matched to the leptonic top if it lies within $\Delta R = 0.4$ of j_{sel} and matched to the hadronic top if it lies within $\Delta R = 1.0$ of the top-tagged large-R jet. In the resolved channel, a b -tagged jet is matched to the leptonic or hadronic top if it lies within $\Delta R=0.4$ of one of the small-R jets selected as b -jets by the χ^2 algorithm. Further dividing the four channels into three b -tag categories results in twelve final channels.

6.6 Event Reconstruction

Once $t\bar{t}$ events have been selected, the invariant mass of the $t\bar{t}$ pair, $m_{t\bar{t}}$, is reconstructed using only the objects in the event that have been associated with top quark decays. The four-momentum of the $t\bar{t}$ system is required to calculate the invariant mass and is obtained by summing together the four-momenta of each object matched to a $t\bar{t}$ decay product. This approach results in an offset between the mass of the produced $t\bar{t}$ pair and the reconstructed mass of the decay products, due to final state radiation.

6.6.1 Leptonically decaying W boson

The four-momentum assigned to the leptonically decaying W boson is that of the lepton plus neutrino system, however the information about this system is incomplete as the neutrino is not detected. The missing transverse energy is taken to be the neutrino p_T (or the summed p_T of two neutrinos in case of a tau decay). The initial p_z of the centre of mass of the parton-parton collision is not known, so missing p_z , and hence neutrino p_z , cannot be inferred from conservation of momentum like p_x and p_y . Instead, the invariant mass of the lepton plus neutrino system is constrained to be the on-shell W boson mass (PDG value):

$$p_{(\ell+\nu)}^i p_{(\ell+\nu)i} = m_W^2 \quad (6.11)$$

Expanding and rearranging this equation yields:

$$(E_\ell + \sqrt{|\mathbf{p}_{T,\nu}|^2 + p_{z,\nu}^2})^2 - |\mathbf{p}_{T,\ell} + \mathbf{p}_{T,\nu}|^2 - (p_{z,\ell} + p_{z,\nu})^2 - m_W^2 = 0 \quad (6.12)$$

which is quadratic in the unknown z component of neutrino momentum, $p_{z,\nu}$. The known quantities are $\mathbf{p}_{T,\nu}$ and $\mathbf{p}_{T,\ell}$, the transverse momenta of the lepton and neutrino, E_ℓ , the energy of the lepton, and $p_{z,\ell}$, the z component of the lepton momentum. There may be one real solution, two real solutions, no real solution for $p_{z,\nu}$. If there are two real solutions, the smallest is chosen as $p_{z,\nu}$ because on average this choice gives the best reconstruction [8]. If there is no real solution, the magnitude of $\mathbf{p}_{T,\nu}$ is rescaled and the orientation of $\mathbf{p}_{T,\nu}$ in the $x - y$ plane is adjusted by the smallest amount necessary to obtain one real $p_{z,\nu}$ solution. The assumption here is that the limitations of the detector resolution have caused no real solutions, and therefore a reliable $\mathbf{p}_{T,\nu}$ estimation can be made by selecting the closest value that comes with one real $p_{z,\ell}$. From this point on the reconstruction methods for boosted and resolved events diverge since different types of objects are involved.

6.6.2 Boosted Channel

The top-tagged large-R jet is identified as the hadronic top quark decay, while the leptonically decaying W boson and j_{sel} are taken to be the leptonic top decay. The $t\bar{t}$ system is reconstructed by adding together these four-momenta.

6.6.3 Resolved Channel

Three small-R jets must be associated with the hadronic top decay (t_{had}) and one small-R jet must be associated with the b -jet decay from the leptonic top t_{lep} . To do this, a χ^2 value is assigned to each possible combination of four jets in the event. The χ^2 value provides a measure of how compatible a particular combination of jets is with resolved $t\bar{t}$ decay by matching each jet to a theoretical $t\bar{t}$ hadronic decay product and comparing the masses of the resulting reconstructed objects, for example the W boson, to the expected mass of that object if it were built using correctly-matched jets.

$$\chi^2 = \underbrace{\left[\frac{m_{jj} - m_W}{\sigma_W} \right]^2}_{\text{W mass}} + \underbrace{\left[\frac{m_{jbb} - m_{jj} - m_{th-W}}{\sigma_{th-W}} \right]^2}_{\text{hadronic top mass}} + \underbrace{\left[\frac{m_{j\ell\nu} - m_{t\ell}}{\sigma_{t\ell}} \right]^2}_{\text{leptonic top mass}} + \underbrace{\left[\frac{(p_{T,jbb} - p_{T,j\ell\nu}) - (p_{T,th} - p_{T,t\ell})}{\sigma_{\text{diff}p_T}} \right]^2}_{\Delta_{p_T}(\text{hadronic top, leptonic top})} \quad (6.13)$$

The first term compares the invariant mass of the two jets matched to the W boson m_{jj} to the expected mass m_W . The second term is intended to compare the mass of the reconstructed hadronically decaying top to expectation. To avoid the effects the strong correlation between the mass of the reconstructed W and the reconstructed t_{had} , m_{jj} and m_{jbb} , m_{jj} is subtracted from m_{jbb} and this is compared to the expected mass of $t_{had} - W$, m_{th-W} . The third term compares the mass of the reconstructed t_{lep} , $m_{j\ell\nu}$, to the expected mass $m_{t\ell}$. If there were two real solutions for $p_{z,\nu}$ then both solutions are tested in addition to each permutation of jets. The fourth term compares the p_T difference between the two reconstructed tops, $p_{T,jbb} - p_{T,j\ell\nu}$, to the expected p_T difference, $p_{T,th} - p_{T,t\ell}$. The combination of jets (plus $p_{\nu,z}$ solution) with the smallest χ^2 is selected as the resolved $t\bar{t}$ decay provided $\log_{10}(\chi^2) < 0.9$, otherwise the event is discarded. Cutting on χ^2 effectively constrains the kinematics of the reconstructed objects to be close to the expected kinematics assuming correctly matched jets and so on average the correct combination returns the smallest χ^2 . The fixed parameters are $m_W = 80.51$ GeV, $m_{th-W} = 85.17$ GeV, $m_{t\ell} = 167.36$ GeV, $\sigma_W = 12.07$ GeV, $\sigma_{th-W} = 16.05$ GeV, $\sigma_{t\ell} = 25.41$ GeV, $p_{T,th} - p_{T,t\ell} = -0.23$ GeV and $\sigma_{\text{diff}p_T} = 18.85$ GeV. The simulation studies used to fit these parameters for the run 2 search can be found in [80]. The parameter values are obtained by correctly associating the jets to theoretical decay products using truth level information, and plotting the mass (Δp_T) distributions for each reconstructed object. Then the m and

Δp_T parameter values are the means of the Gaussians fitted to the distributions, and the σ values are the standard deviations. The parameter distributions were generated using a Z' sample ($m_{Z'} = 3$ TeV), therefore the fourth term gives preference to signal events where the p_T of both top quarks is more similar on average than in background events.

6.7 Corrections applied to simulated events

Some residual differences between data and simulation, which are a result of deficiencies in detector modelling, are corrected by applying scale factors to simulated events prior to the event selection stage of the analysis. Pile-up is especially difficult to simulate, and weights are required to correct the shape and normalisation of pile-up distributions in simulation to reflect those in data. Differences between data and simulation for b -tagging and lepton identification efficiencies are p_T and η dependent, and require p_T and η dependent weights to correct the simulation efficiency to the data efficiency. Finally, weights are applied to simulated $t\bar{t}$ events to account for higher-order electroweak effects in $t\bar{t}$ production that are not included in the event generator. This correction is calculated by theorists [81] and modifies the kinematic distributions p_T and $m_{t\bar{t}}$. The value of the correction increases with increasing $m_{t\bar{t}}$ and reaches $\mathcal{O}(10\%)$ at $m_{t\bar{t}} = 2.5$ TeV [80].

6.8 Systematic Uncertainties

There are various sources of systematic uncertainty that affect the shape and normalisation of the predicted signal and background $m_{t\bar{t}}$ distributions. For each source the size of the uncertainty and its impact on the event yield must be determined so it can be included as a nuisance parameter in the limit setting procedure. Systematic uncertainties include theoretical uncertainties, which derive from theory-based choices such as the Monte Carlo generator and the generator settings, and uncertainties related to detector simulation, such as the modelled efficiencies, calibrations and resolutions during object reconstruction. There are also uncertainties attached to the corrections applied to the energies of reconstructed simulated objects to correct them to the corresponding energies that would be expected in data. The main sources of systematic uncertainty affecting the simulated $m_{t\bar{t}}$ distribution are described in this section. Table 6.8 shows the impact of the most significant uncertainties on the total background yields in the boosted and resolved channels. The $t\bar{t}$ modelling and jet energy uncertainties contribute the most to the total uncertainty in the background yields.

Systematic Uncertainty	Background [$\pm\%$]	
	resolved	boosted
$t\bar{t}$ ISR/FSR	4.2	2.5
$t\bar{t}$ QCD NNLO	0.8	7.3
$t\bar{t}$ cross section	5.0	-
$t\bar{t}$ generator	1.2	3.4
$t\bar{t}$ parton shower	0.4	2.9
Multi-jet	2.9	3.1
Anti- k_T R=0.4 JER	1.1	0.2
Anti- k_T R=0.4 JES	5.8	0.9
Anti- k_T R=1.0 JER	0.1	4.0
Anti- k_T R=1.0 JES	0.3	6.0
b -tagging efficiency	3.2	1.8
b -tagging extrap.	2.4	2.3
luminosity	1.8	1.8
pile up	4.2	0.5
Total	11.5	12.6

Table 6.1: The systematic uncertainties on the background yields resulting from each source that are the most significant in terms of percentage uncertainty. The sources of smaller uncertainties are left out.

6.8.1 Luminosity and pile-up

The uncertainty on the total integrated luminosity of the data sample is 2.1%. It was determined from luminosity measurements made with van der Meer scans⁶ [83] in 2015 and 2016. The uncertainty attached to the pile-up weights applied to simulated events in order to improve the agreement between pile-up in data and simulated pile-up has a larger impact on the resolved channel due to the χ^2 algorithm selecting pile-up jets to reconstruct the $t\bar{t}$ system.

6.8.2 Leptons

The differences between lepton reconstruction in data and in simulation, which are a result of the mis-modelling of lepton efficiencies, energy scale and resolution, are estimated using $Z \rightarrow \ell\ell$ events so that corrections to be applied to simulation as event weights can be determined. The uncertainties associated with the corrections extracted from these studies translate to systematic uncertainties on the event yield.

⁶In van der Meer scans the beam, which is parallel to the z -axis, is displaced along the x -axis direction and the y -axis direction in turn until the collision rate reduces to zero. Plots of the luminosity against the beam displacement are made and used as a reference. More information can be found in reference [82].

6.8.3 Jets

Uncertainties in the small-R jet energy scale and jet energy resolution lead to uncertainties in the calibrations applied to jets described in section 4.4, and therefore to a systematic uncertainty on the $m_{t\bar{t}}$ distribution. The scales of the large-R jet variables energy, mass and τ_{32} have associated uncertainties, with the latter two contributing to an uncertainty in the top-tagging efficiency. There is also an uncertainty on the b -tagging efficiency correction applied to simulated events.

6.8.4 $t\bar{t}$ cross-section

The $t\bar{t}$ cross-section is calculated at NNLO (+NNLL) to be $\sigma_{t\bar{t}} = 832_{-52}^{+46}$ pb [76], [77], with the uncertainty corresponding to a systematic uncertainty in the overall $t\bar{t}$ normalisation. MC related choices in the $t\bar{t}$ sample creation lead to systematic uncertainties affecting both the shape and normalisation of the $t\bar{t}$ background. The impact of these choices are quantified by comparing the outcome of the chosen simulator/setting to the outcome obtained using an alternative simulator/setting. The uncertainty associated with the Powheg event generator was obtained by comparing a $t\bar{t}$ sample generated with Powheg+Herwig to one generated with aMC@NLO+Herwig. The uncertainty on parton showering with Pythia was obtained by comparing a Powheg+Pythia sample to a Powheg+Herwig sample, and the uncertainty attached to the chosen PDF set was obtained by comparing the resulting sample with one that was built using the PDF4LHC15 PDF set. QCD radiation in generated samples depends on the generator settings. The Powheg+Pythia parameters were varied within limits imposed by measurements and the impacts on the samples were quantified as systematic uncertainties.

6.8.5 Single top

The dominant systematic uncertainty associated with single top production is the uncertainty on an NNLO cross-section prediction, which translates to a 5.3% uncertainty on the single top background normalisation [1], followed by an uncertainty on the interference between single top and $t\bar{t}$ production.

6.8.6 W +jets

There are uncertainties attached to the W +jets normalisation and flavour fraction scale factors, C_A and K_{flavour} . Modifying the scale factors within their uncertainty affects the predicted W +jets event yield. The W +jets estimate also relies on object reconstruction and MC choices that have associated uncertainties. The combined impact of these uncertainties on the W +jets yield leads to a small uncertainty on the predicted W +jets background.

6.8.7 Multijets

The number of predicted multijet background events depends on the definition of the multijet control region used to extract the fake rate f . The control region is varied, and the resulting change in the multijet yield is converted to a systematic uncertainty. After accounting for the impact of systematic uncertainties attached to choices in object reconstruction and MC simulation used in the multijet estimation procedure, the total normalisation uncertainty of the multijet background is 50%.

6.9 Results

6.9.1 Compatibility of data with expectation

A hypothesis test is used to assess the compatibility of the data $m_{t\bar{t}}$ spectrum with SM prediction and determine whether there is any resonance like signal present in the data. Before this test is carried out, several other kinematic distributions are compared in data and simulated background. This is because regardless of whether there is signal in the data, each non- $m_{t\bar{t}}$ kinematic data distribution is expected to be consistent with the corresponding background prediction within the uncertainties; comparing these distributions in data and background establishes whether the background has been estimated well in a way that is independent of the existence of signal. Figures 6.6 - 6.10 show the data and background distributions for the lepton p_T , E_T^{miss} , large-R jet p_T , leptonic top mass, and hadronic top mass, with bands to represent the systematic and statistical uncertainties on the background. The distributions for the resolved selections agree within the uncertainties. The data and background $m_{t\bar{t}}$ spectra for b -tag categories 1, 2 and 3 are shown in Figures 6.11 and 6.12. For all of the kinematic distributions, there is a slight deficit of data compared to simulation in the boosted channels, and a slight excess of data compared to simulation in the resolved channels. Additionally, the data/simulation disagreement in the large-R jet p_T distributions increases with increasing p_T ; the data deficit is largest at high p_T . This disagreement at high top quark p_T has been observed [84] for several different event generators. Including higher order corrections is seen to improve the data/simulation disagreement at high top quark p_T [84]. This may explain the data deficit (excess) in the boosted (resolved) channels as events with a high p_T large-R jet are boosted, and there are more of these predicted by simulation than observed in data.

The level of agreement between data and expectation is evaluated using BumpHunter [64], a hypothesis testing tool which takes the Standard Model to be the null hypothesis, and which is sensitive to local deviations in the data $m_{t\bar{t}}$ spectrum. The BumpHunter algorithm scans the $m_{t\bar{t}}$ data distribution in each channel separately, calculating the Poisson probability of

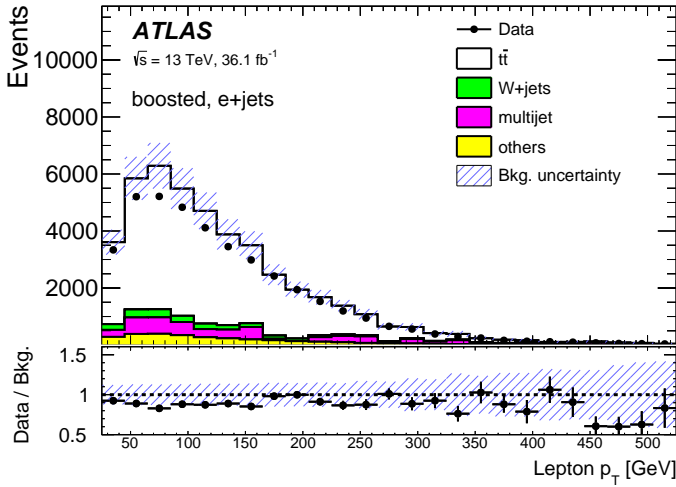
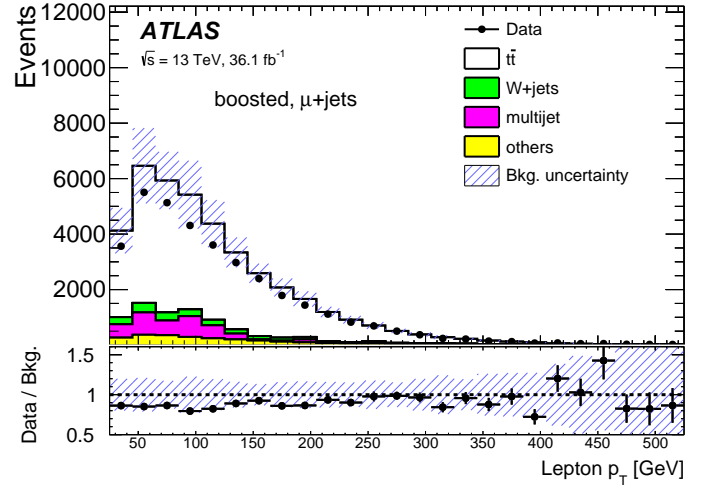
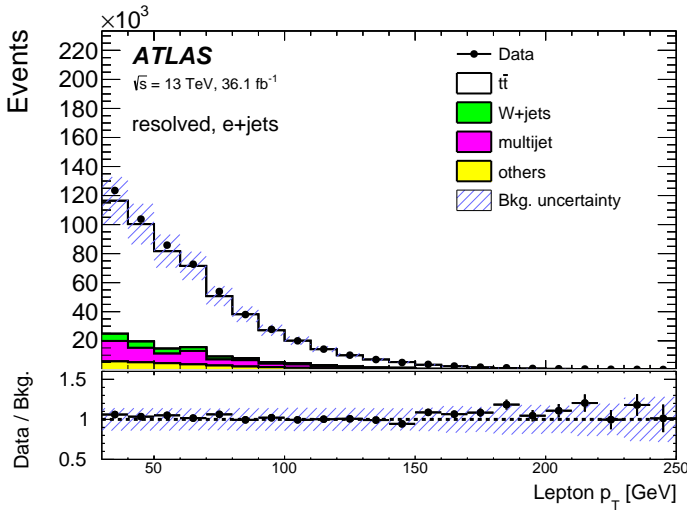
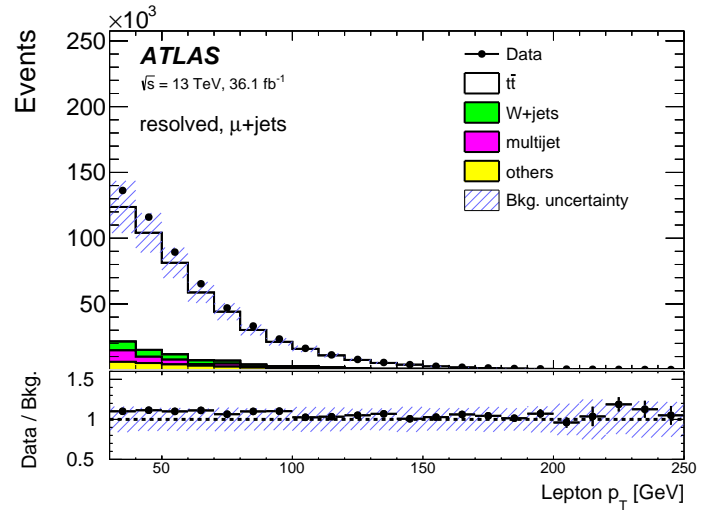
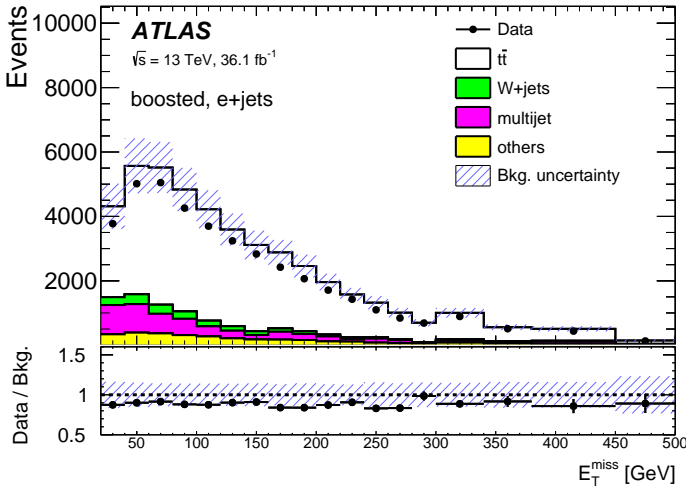
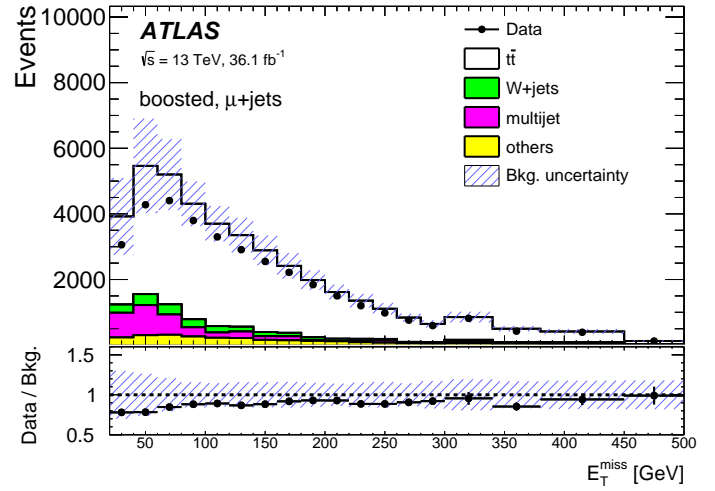
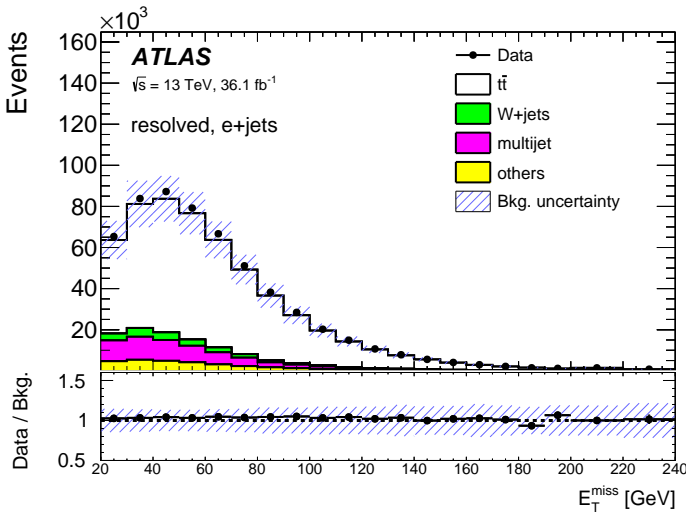
(a) e +jets, boosted selection(b) μ +jets, boosted selection(c) e +jets, resolved selection(d) μ +jets, resolved selection

Figure 6.6: Transverse momentum of the lepton. Data and simulation agree within the uncertainties. There is a small deficit of data events observed in the boosted channels and a small excess observed in the resolved channels, which may be explained by event generators predicting more $t\bar{t}$ events with high top quark p_T than are observed in data.



(a) e+jets, boosted selection

(b) μ +jets, boosted selection

(c) e+jets, resolved selection

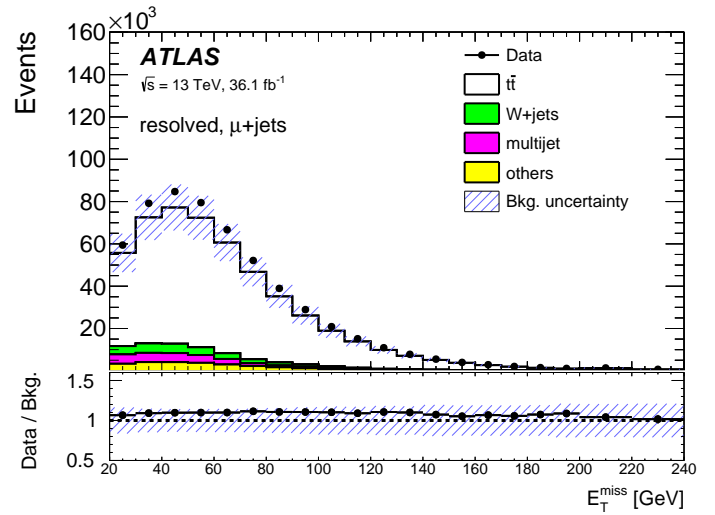
(d) μ +jets, resolved selection

Figure 6.7: Missing transverse energy. There is a small deficit of data events observed in the boosted channels and a small excess observed in the resolved channels, which may be explained by event generators predicting more $t\bar{t}$ events with high top quark p_T than are observed in data.

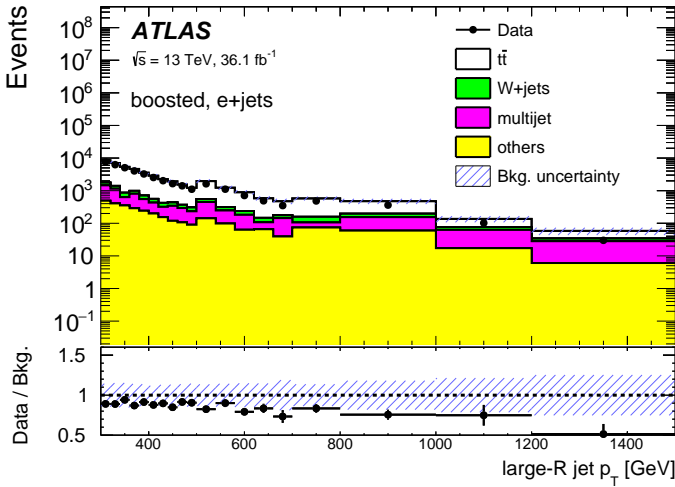
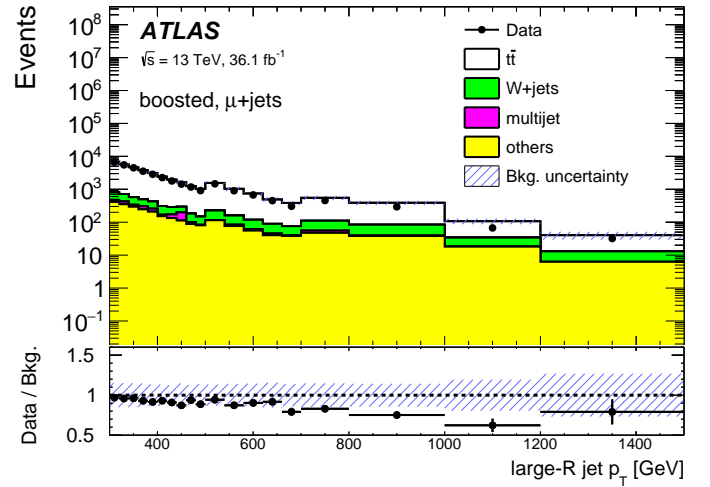
(a) e +jets, boosted selection(b) μ +jets, boosted selection

Figure 6.8: Transverse momentum of the top-tagged large-R jet. There are fewer data events compared to simulated events and this disagreement increases with increasing large-R jet p_T . This is a feature observed in different event generators [84].

the number of observed events windows of adjacent bins, starting with windows two bins wide and repeating the scan for windows of up to $\frac{N}{2}$ bins, where N is the total number of bins in the distribution. Bumhunter identifies the window with the largest excess compared to the expected background spectrum, which is the window with the smallest Poisson probability, and calculates a test statistic from this window while accounting for the look elsewhere effect⁷.

When searching for an excess, the Poisson probability of a window is defined to be:

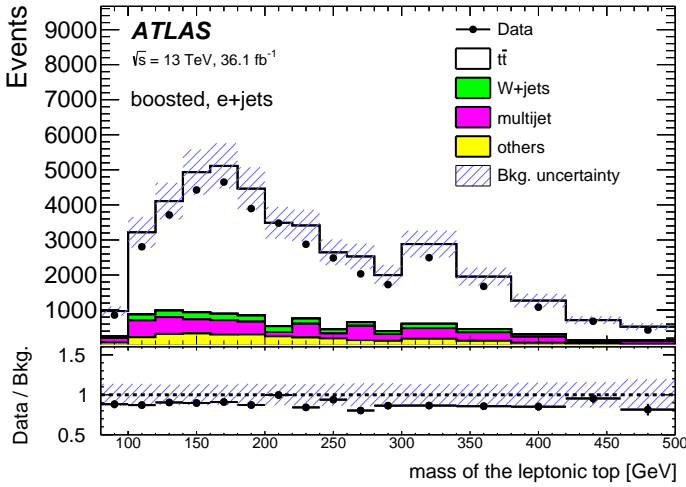
$$P(d_i, b_i) = \begin{cases} \sum_{n=d_i}^{\infty} \frac{b_i^n}{n!} e^{-b_i} & \text{if } d_i \geq b_i. \\ 1 - \sum_{n=d_i+1}^{\infty} \frac{b_i^n}{n!} e^{-b_i} & \text{if } d_i < b_i. \end{cases} \quad (6.14)$$

where d_i is the observed number of events in the window and b_i is the expected number of events in the window. The Poisson probability associated with the least likely window, P_i^{\min} , is used to calculate the Bumhunter test statistic:

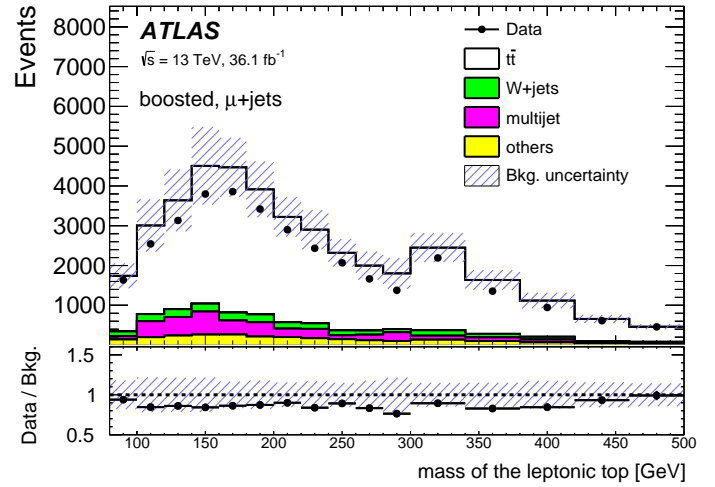
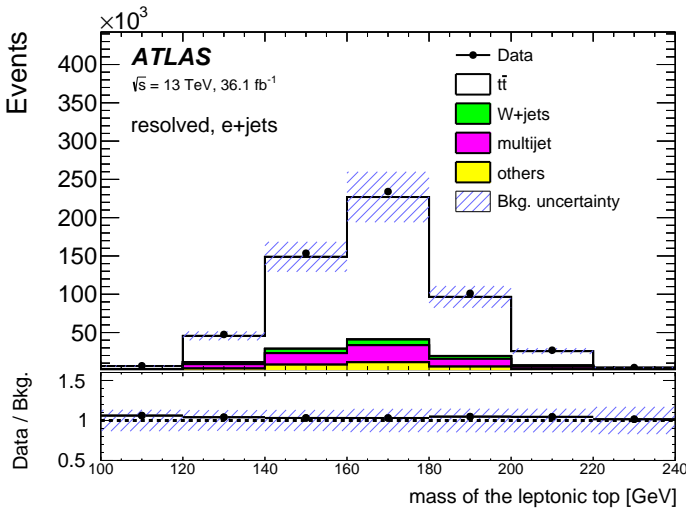
$$t = \begin{cases} 0 & \text{if } d_i \leq b_i \\ -\log P_i^{\min} & \text{if } d_i > b_i \end{cases} \quad (6.15)$$

and a p-value is calculated for the data in each channel. To account for the systematic uncertainty on the predicted background yield, the test statistic t is modified by redefining

⁷Bumhunter's test statistic makes it a hypertest (see section 5.2.1).



(a) e+jets, boosted selection

(b) μ +jets, boosted selection

(c) e+jets, resolved selection

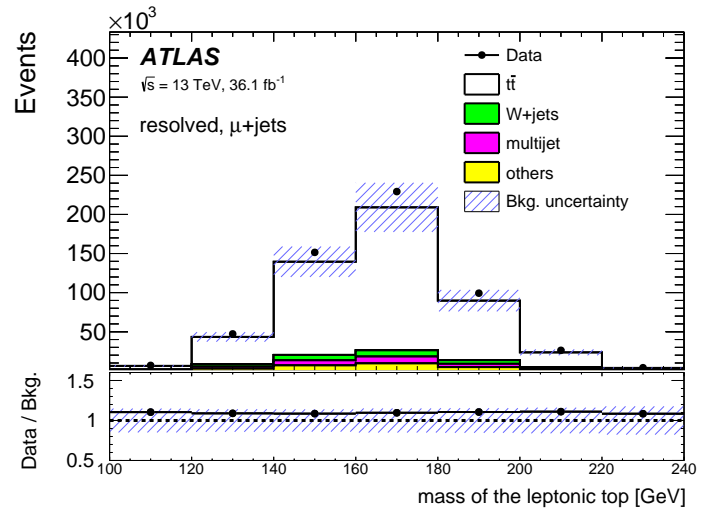
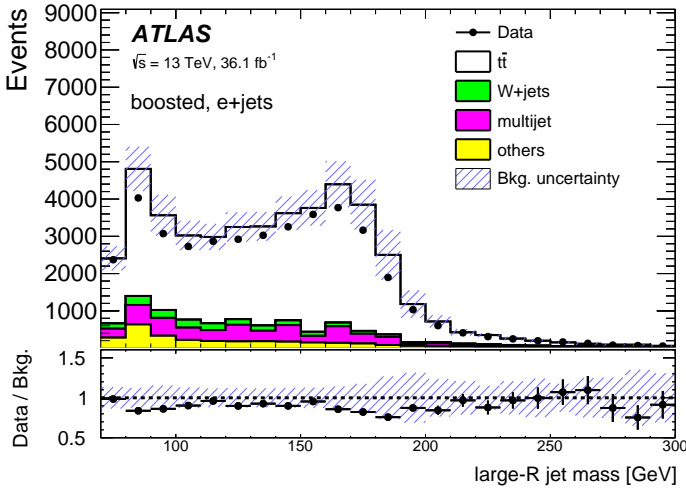
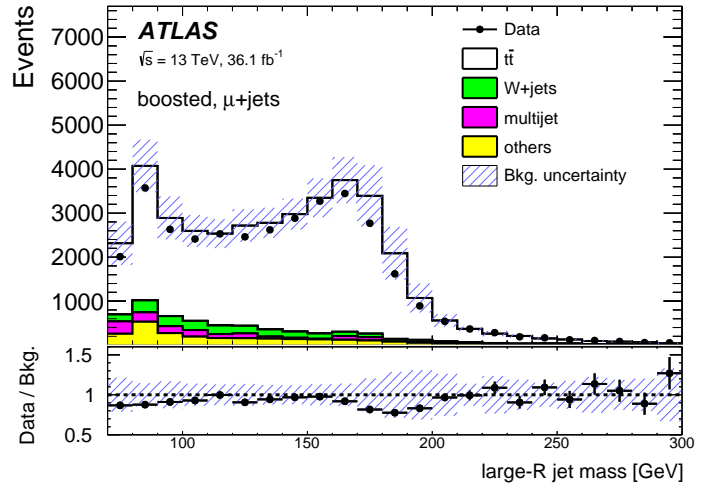
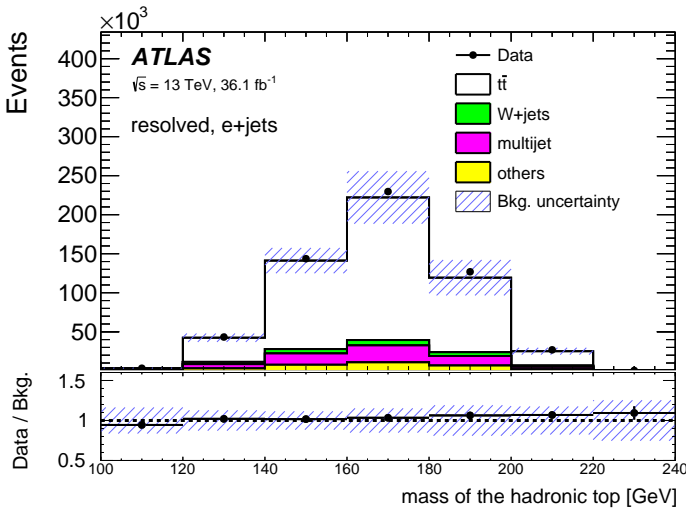
(d) μ +jets, resolved selection

Figure 6.9: Mass of the leptonic top. There is a small deficit of data events observed in the boosted channels and a small excess observed in the resolved channels, which may be explained by event generators predicting more $t\bar{t}$ events with high top quark p_T than are observed in data.



(a) e+jets, boosted selection

(b) μ +jets, boosted selection

(c) e+jets, resolved selection

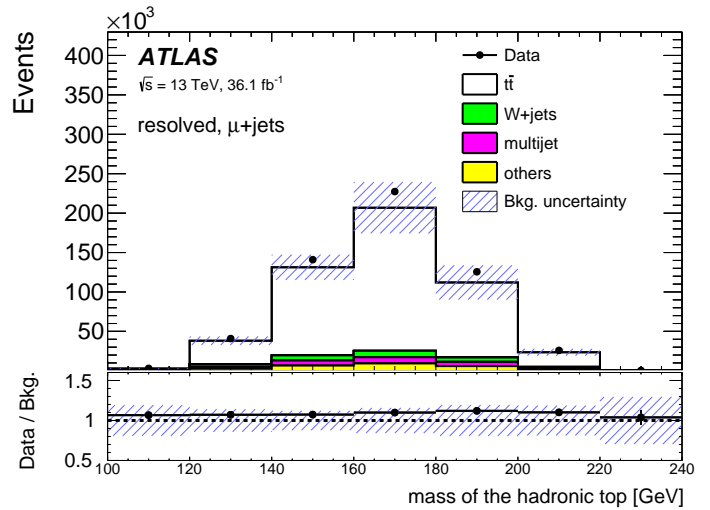
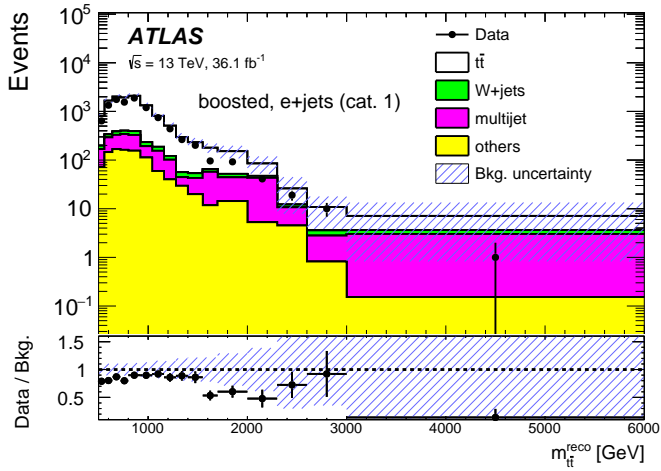
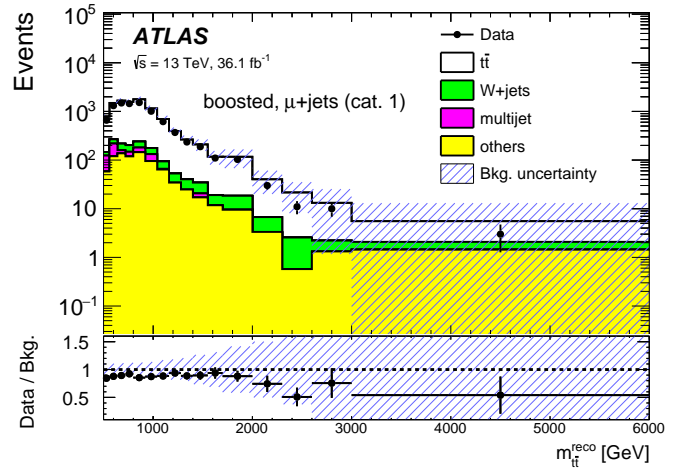
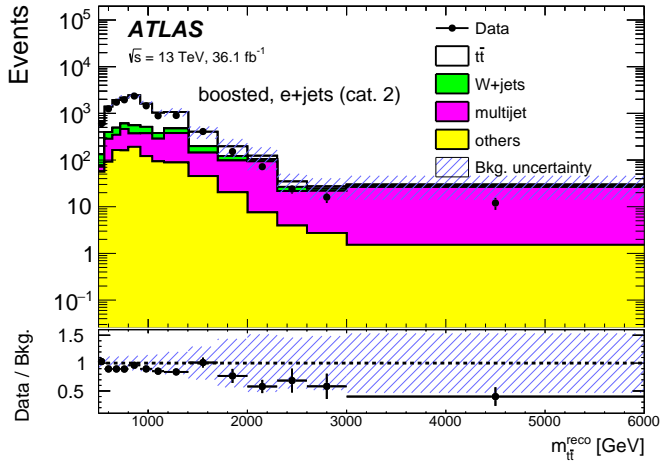
(d) μ +jets, resolved selection

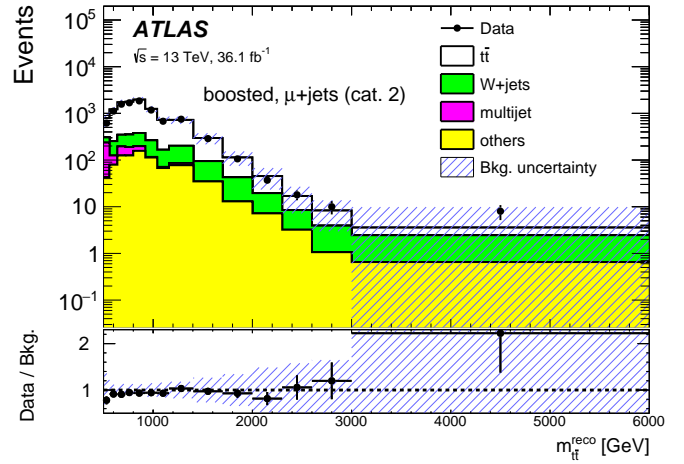
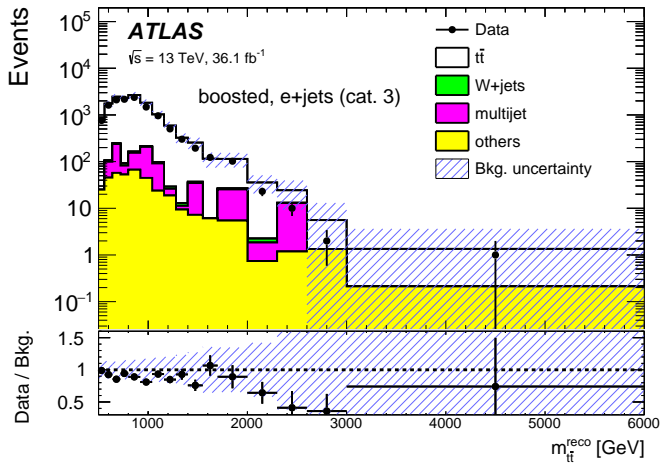
Figure 6.10: Mass of the hadronic top. There is a small deficit of data events observed in the boosted channels and a small excess observed in the resolved channels, which may be explained by event generators predicting more $t\bar{t}$ events with high top quark p_T than are observed in data.



(a) e+jets, btag category 1

(b) μ +jets, btag category 1

(c) e+jets, btag category 2

(d) μ +jets, btag category 2

(e) e+jets, btag category 3

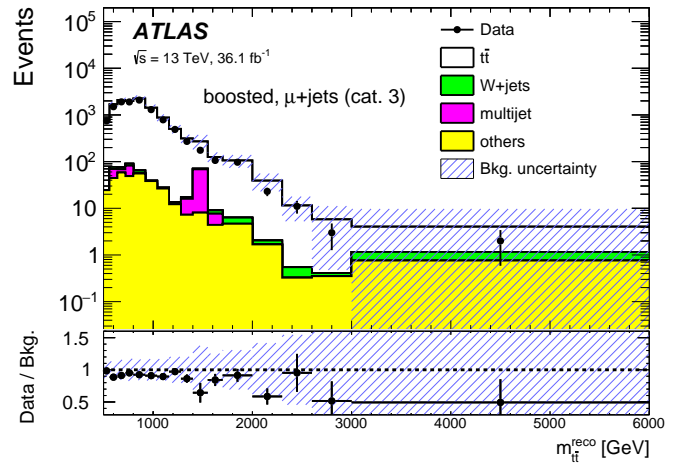
(f) μ +jets, btag category 3

Figure 6.11: Invariant mass of the $t\bar{t}$ system in the boosted channel. There tends to be a small deficit of data events in each boosted channel, which may be explained by event generators predicting more $t\bar{t}$ events with high top quark p_T than are observed in data.

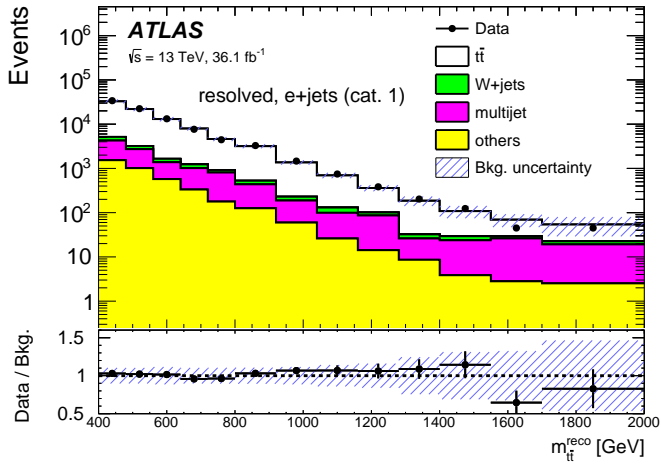
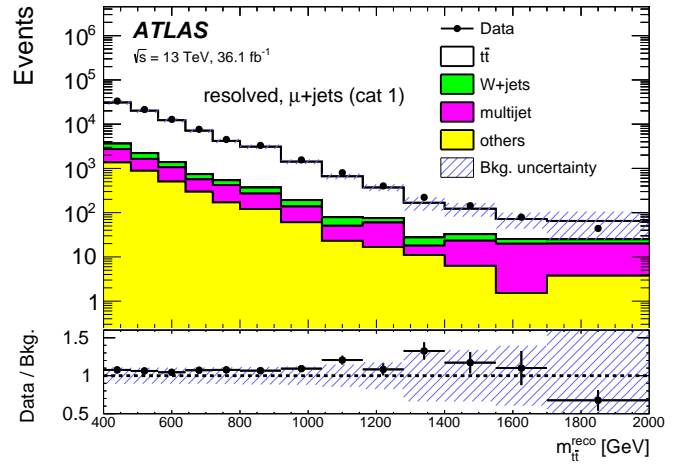
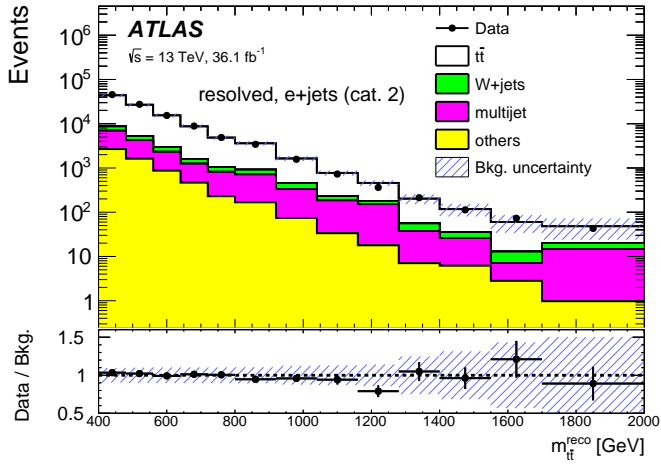
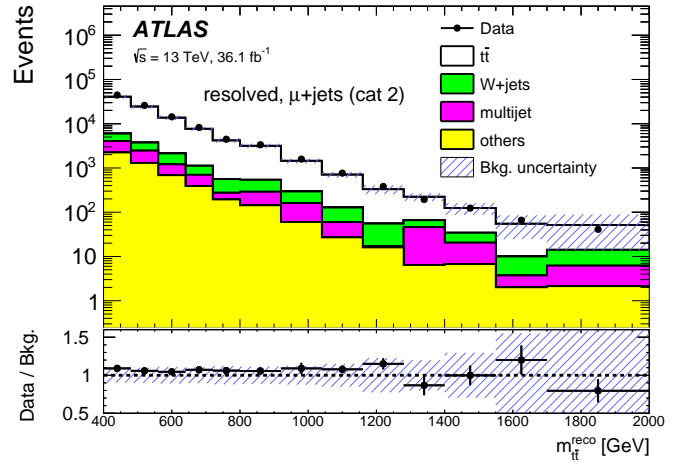
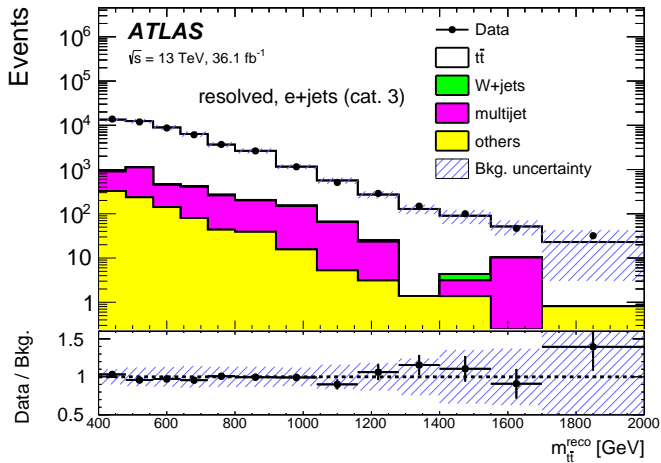
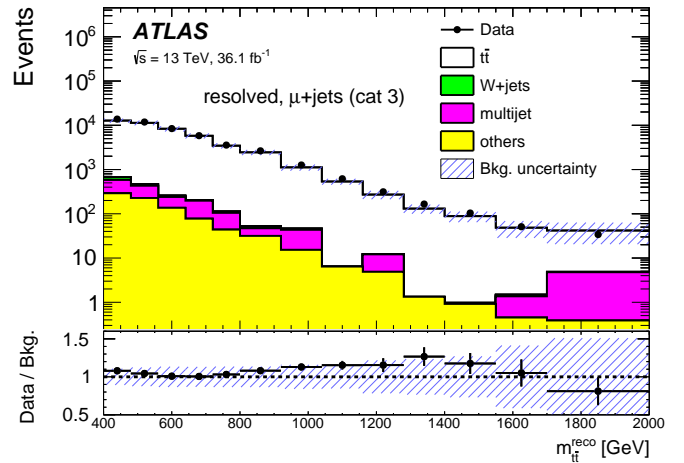
(a) e +jets, btags category 1(b) μ +jets, btags category 1(c) e +jets, btags category 2(d) μ +jets, btags category 2(e) e +jets, btags category 3(f) μ +jets, btags category 3

Figure 6.12: Invariant mass of the $t\bar{t}$ system in the resolved channel. There tends to be a small deficit of data events in each resolved channel, which may be explained by event generators predicting more $t\bar{t}$ events with high top quark p_T than are observed in data.

$P(d_i, b_i) \rightarrow P(d_i, b_i + \lambda_i \theta_i) e^{-\frac{\lambda_i^2}{2}}$, where θ_i is the uncertainty on the number of background events in window i , and $\lambda_i \in [-8, 8]$ maximises $\frac{(b_i + \lambda_i \theta_i)}{d_i!} e^{-(b_i + \lambda_i \theta_i)} e^{-\frac{\lambda_i^2}{2}}$. This means that in the case of a large data excess d_i with a large background uncertainty θ_i , λ_i can remain relatively small and cause $P(d_i, b_i + \lambda_i \theta_i)$ to be a large poisson probability (since $d_i \simeq b_i + \lambda_i \theta_i$) while not causing the factor $e^{-\frac{\lambda_i^2}{2}}$ to decrease too much (which would bring P_i closer to P_i^{\min}). A large data excess d_i with a comparably large uncertainty will not cause a significant deviation to be observed. However, in the case of a large data excess with small background uncertainty θ_i , λ_i would need to be larger to maximise $P(d_i, b_i + \lambda_i \theta_i)$, which would cause the factor $e^{-\frac{\lambda_i^2}{2}}$ to shrink, making P_i small and therefore the test statistic t large and more likely to be return a small p-value in a hypothesis test. If the windows with the smallest probability in each channel do not overlap in $m_{t\bar{t}}$, this is not consistent with a $t\bar{t}$ resonance. If they do overlap, a combined probability for the windows is found by taking the product of the Poisson probabilities in equation 6.14 (since the channels are independent), then a new test statistic is calculated according to 6.15 and used to determine a p-value for the combined channels. Taking systematic uncertainties into account, no significant differences between data and background are found.

6.9.2 Limit Setting

The CL_s method is used to set 95% CL upper limits on the cross-section times branching ratio of signals in a set of benchmark models. The profile likelihood-ratio test statistic is used, where the systematic uncertainties in the predicted $m_{t\bar{t}}$ distributions are included as nuisance parameters in the likelihood constrained by Gaussian PDFs with width equal to the size of the uncertainty considered. Correlations between different channels and bins are taken into account. The likelihood of a signal strength μ is defined to be:

$$\mathcal{L}(\mu, \boldsymbol{\theta}) = \prod_{i=0}^{\text{channels, bins}} \frac{e^{-\mu a_{Z',i}(\boldsymbol{\theta}) \sigma_{Z'} + b_i(\boldsymbol{\theta})} (\mu a_{Z',i}(\boldsymbol{\theta}) \sigma_{Z'} + b_i(\boldsymbol{\theta}))^{D_i}}{D_i!} C(\boldsymbol{\theta}) \quad (6.16)$$

where for each bin i , D_i is the observed number of events in data, b_i is the predicted number of background events, $a_{Z',i}$ is the signal acceptance, $\sigma_{Z'}$ is the predicted signal cross-section times branching ratio (for the Z' case), and $C(\boldsymbol{\theta})$ are the functions constraining the systematic uncertainties. The likelihood can be maximised by adjusting the signal strength μ and the nuisance parameters. An $m_{t\bar{t}}$ distribution is created by setting $\mu = 0$ and adjusting the nuisance parameters to maximise the likelihood. This post background-only fit $m_{t\bar{t}}$ spectrum is compared to the data spectrum. The expected and observed number of events in each channel after the background-only fit are shown in table 6.2.

	Boosted e	Boosted μ	Resolved e	Resolved μ
$t\bar{t}$	$28\,500 \pm 500$	$26\,000 \pm 400$	$231\,100 \pm 2\,000$	$225\,300 \pm 1\,700$
W+jets	$2\,200 \pm 250$	$2\,200 \pm 180$	$9\,400 \pm 1\,000$	$10\,300 \pm 900$
multi-jet	$2\,100 \pm 600$	800 ± 300	$8\,300 \pm 1\,400$	$7\,400 \pm 1\,500$
others	$2\,900 \pm 200$	$2\,400 \pm 200$	$13\,000 \pm 500$	$12\,000 \pm 500$
Total	$35\,700 \pm 600$	$31\,400 \pm 300$	$262\,200 \pm 1\,200$	$254\,600 \pm 1\,200$
Data	35 595	31 168	261 552	254 265

Table 6.2: Data and background yields in the boosted electron, boosted muon, resolved electron and resolved muons channel, and the systematic uncertainty on the background, after the background-only fit.

The profile likelihood ratio test statistic is $-2 \log_e(\Lambda(\mu))$, where

$$\Lambda(\mu) = \frac{L(\mu, \hat{\theta})}{L(\hat{\mu}, \hat{\theta})}. \quad (6.17)$$

Here, $\hat{\mu}$ and $\hat{\theta}$ are the unconditional maximum likelihood estimates of μ and θ , and $\hat{\mu}$ is the maximum likelihood estimate of θ for a given value of μ .

Observed and expected cross-section limits are calculated for several signal masses and interpolated between each mass point. Figure 6.13 shows that a 1% width Z' boson is excluded for masses less than 3.0 TeV (2.6 TeV expected). Figure 6.14 shows that a 15% width Kaluza-Klein gluon is excluded for masses less than 3.7 TeV (3.2 TeV expected) and a 30% width Kaluza-Klein gluon is excluded for masses less than 3.8 TeV (3.5 TeV expected). Figure 6.15 shows that a 3–6% width Kaluza-Klein graviton is excluded in the mass interval $0.45 < m_{G_{KK}} < 0.65$ TeV, as expected.

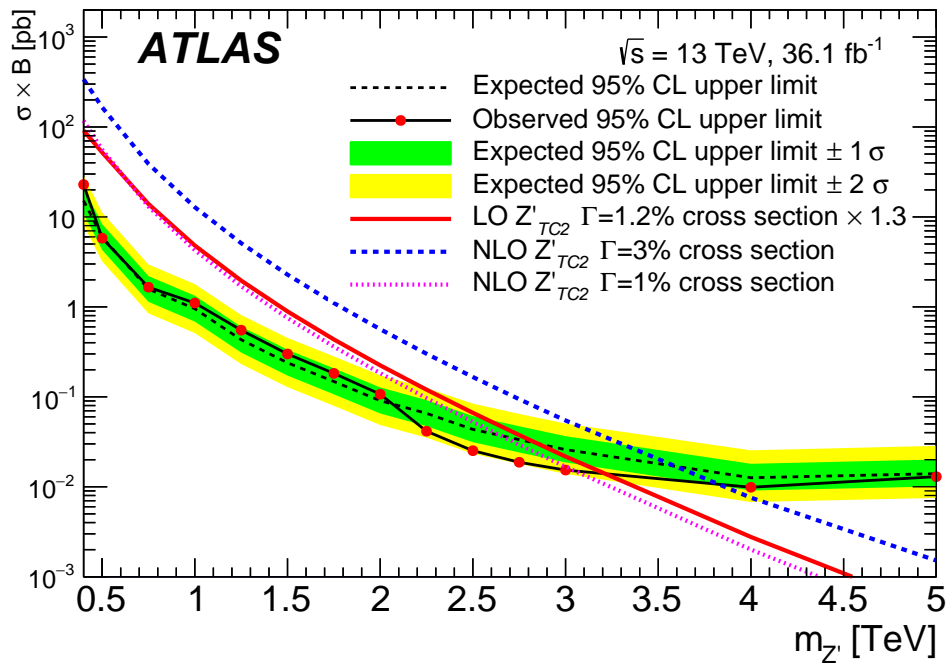


Figure 6.13: Observed and expected 95% CL limits on the cross-section \times branching ratio of the Z' boson for each signal mass point. The theoretical cross-sections are given to show the Z' masses that can be excluded: a 1% width Z' boson can be excluded for masses less than 3.0 TeV (2.6 TeV expected).

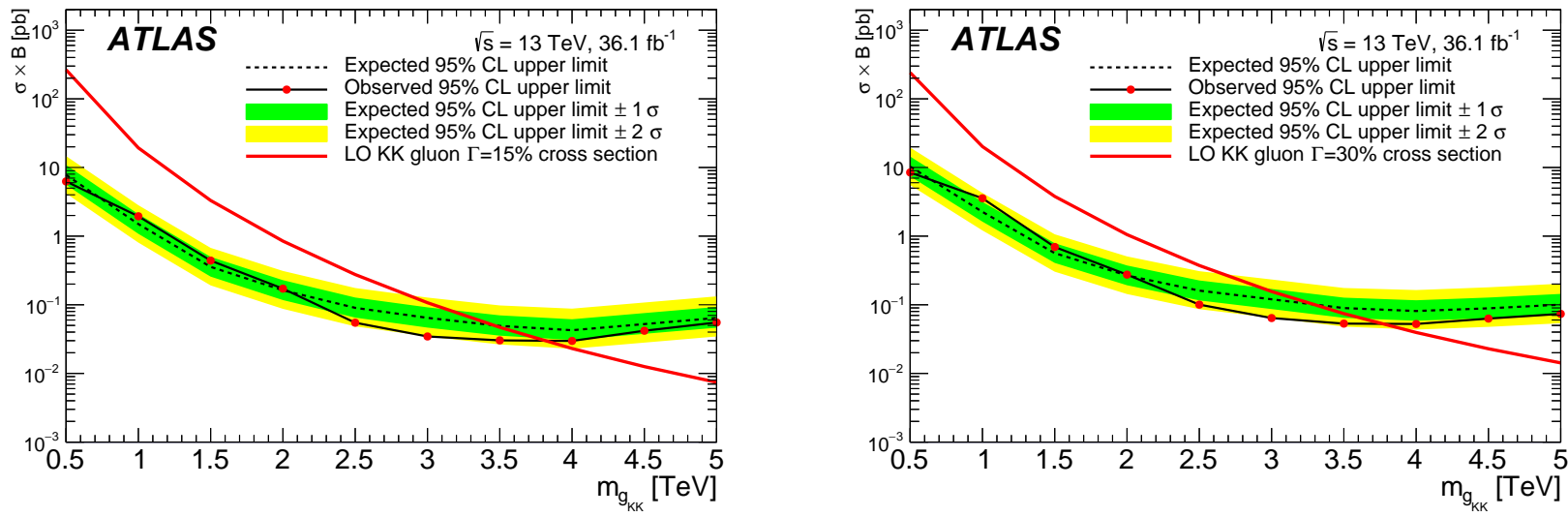


Figure 6.14: Observed and expected 95% CL limits on the cross-section \times branching ratio of the 15% width (left) and 30% width (right) Kaluza-Klein gluon for each signal mass point. The theoretical cross-sections are given to show the g_{KK} masses that can be excluded: a 15% width Kaluza-Klein gluon is excluded for masses less than 3.7 TeV (3.2 TeV expected) and a 30% width Kaluza-Klein gluon is excluded for masses less than 3.8 TeV (3.5 TeV expected).

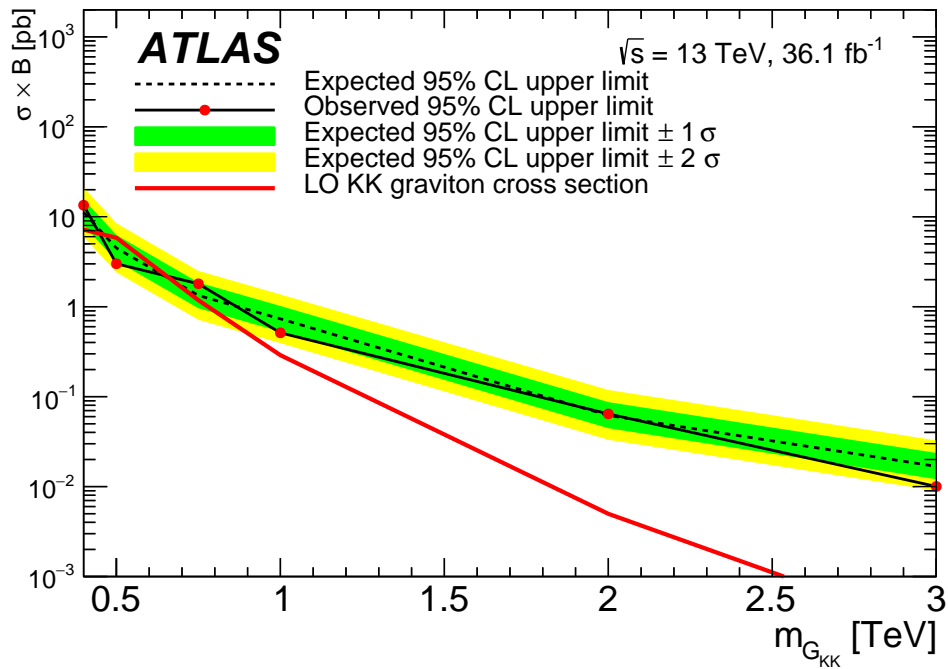


Figure 6.15: Observed and expected 95% CL limits on the cross-section \times branching ratio of the Kaluza-Klein graviton for each signal mass point. The theoretical cross-sections are given to show the G_{KK} masses that can be excluded: a 3 – 6% width Kaluza-Klein graviton is excluded in the mass interval $0.45 < m_{G_{KK}} < 0.65 \text{ TeV}$, as expected.

Chapter 7

Improving the sensitivity of the $t\bar{t}$ resonances search

7.1 Introduction

It is important that the $t\bar{t}$ resonances search is as sensitive as possible to signs of new particles, so that it has the best chance of detecting evidence of new physics in the available data. The sensitivity can be improved by finding ways to increase the number of signal events accepted by the event selection without a comparable increase in the number of background events. This section describes two methods that were developed to increase the acceptance of signal events: 1) an electron-in-jet overlap removal procedure and 2) the selection and reconstruction of final state $t\bar{t}$ events with decay topologies that do not fit the criteria of the boosted and resolved channels.

7.2 Electron in Jet Overlap Removal

When a jet and electron in a $t\bar{t}$ event are found very close together in $\eta \times \phi$ space, there are three possibilities:

- 1) An electron calorimeter deposit has been reconstructed once as an electron and once as a jet.
- 2) The b -jet and electron from the leptonic top decay have overlapping energy deposits in the calorimeters and the reconstructed jet contains the electron cluster.
- 3) A b -jet decay has produced a non-prompt electron.

An electron-jet overlap removal procedure, which aims to prevent the double counting of electrons as jets as well as remove non-prompt electrons, is carried out as follows. $\Delta R(\text{electron}, \text{jet})$

is calculated for all electron-jet combinations in an event. Jets with $\Delta R(\text{electron}, \text{jet}) < 0.2$ are removed, and then electrons within $\Delta R \in (0.2, 0.4)$ of remaining jets are removed. A consequence of this procedure is that the electron and b -jet from a leptonic top decay are both kept in the event only if $\Delta R(\text{electron}, \text{jet}) > 0.4$.

The ΔR separation of the top quark decay products is strongly correlated with the top quark p_T . Figure 7.1 shows the ΔR separation between the b -jet and electron (at truth-level) from the leptonically decaying top, plotted against top p_T , for SM $t\bar{t}$ events and a Z' sample with $m_{Z'} = 3$ TeV. The current overlap removal procedure hinders the efficient

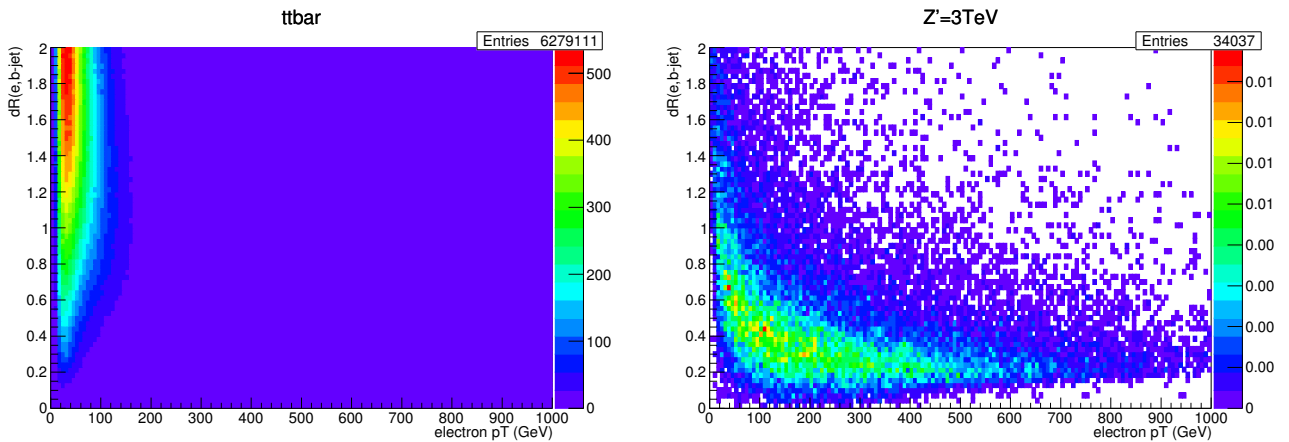


Figure 7.1: $\Delta R(\text{truth electron}, \text{truth } b\text{-jet})$ plotted against top quark p_T for simulated $t\bar{t}$ events and a 3 TeV Z' sample.

reconstruction of high p_T leptonically decaying top quarks, and disproportionately affects high mass signal events. A large fraction of high p_T $t\bar{t}$ events will have either a b -jet or electron removed, potentially causing it to fail the selection. If it does pass the selection, the kinematic information about the event will be distorted.

An improved overlap removal procedure would be able to examine nearby jet-electron pairs and distinguish between the three possible scenarios. In the first case, the fake jet should be removed from the event. In the second case, the jet should be kept but with the electron cluster contamination removed. In the third case, the non-prompt electron should be removed from the list of electrons in the event, so it doesn't cause the event to fail the single electron requirement.

7.2.1 Modified Overlap Removal Procedure: Electron-in-jet Subtraction

First it is necessary to establish a variable that decides whether nearby electron-jet pairs have been reconstructed from the same object. This is done by examining $Z \rightarrow ee$ events: if

$\Delta R(\text{electron}, \text{jet}) < 0.4$ in a $Z \rightarrow ee$ event, it is highly likely that the jet has been reconstructed from an electron cluster. Plotting the p_T difference of electrons and jets reconstructed from the same electron cluster should yield a Gaussian distribution where the mean reflects any difference in the electron and jet energy calibrations. These Δp_T Gaussian distributions are generated, using $Z \rightarrow ee$ events, for different jet p_T ranges to develop a p_T dependent cut that can be used to differentiate between real and fake jets found close to electrons. The cut is defined to be the Gaussian mean $+ 2\sigma$; if the p_T difference between a nearby electron and jet is less than the Gaussian mean $+ 2\sigma$ (using the Δp_T Gaussian corresponding to the jet p_T), then this indicates that the jet is probably a result of the electron cluster. Otherwise, there is likely to be a significant contribution from hadronic clusters in addition to the electron cluster. The Δp_T cut must be determined for different jet p_T ranges because the calibration difference and Gaussian width changes with the p_T of the objects.

The new overlap removal procedure uses this cut to decide whether to keep electrons and jets with $\Delta R < 0.4$ in $t\bar{t}$ events. For each jet in the event, if there is one electron within a radius of $\Delta R < 0.4$, that electron four-momentum is subtracted from the jet four-momentum to obtain the subtracted-jet four-momentum. A p_T cut is applied to the subtracted-jet (which depends on the p_T of the original jet). If the subtracted-jet fails the p_T cut, it is assumed to have been constructed from the electron cluster and is removed. Otherwise, $\Delta R(\text{electron}, \text{subtracted jet})$ is calculated. If $\Delta R(\text{electron}, \text{subtracted jet}) > 0.2$ then both the electron and the jet are recognised as independent objects in the event; the subtracted jet is considered to be a genuine jet, now with the electron energy contribution removed. If $\Delta R(\text{electron}, \text{subtracted jet}) < 0.2$, then it is assumed that the electron is a b -jet decay product; its four-momentum is added back to the subtracted jet and it is not counted as a prompt electron.

7.2.2 Determining the p_T cut with $Z \rightarrow ee$ events.

Events with exactly two electrons and at least one jet are selected from simulated $Z \rightarrow ee$ events with no electron-jet overlap removal carried out. A cut, $\Delta R(\text{electron 1}, \text{electron 2}) > 0.5$, is applied to veto events where a Z boson recoils at high p_T from a jet, since in those events the two electrons from the Z boson are very close together and one jet is often found to overlap with both electrons, and this isn't expected to happen in $t\bar{t}$ events which are single lepton events. Jet p_T - electron p_T is plotted for selected pairs with $\Delta R(\text{jet}, \text{electron}) < 0.4$, with the plots separated by jet p_T range. Gaussians are fitted to the peaks of the $\Delta p_T(\text{jet}, \text{electron})$ distributions, shown in Figure 7.2. The right hand side tails are the result of events where an electron falls within $\Delta R = 0.4$ of a real jet, so they are not included in the fit. The Δp_T cuts (Gaussian mean $+ 2\sigma$) are shown in Table 7.1.

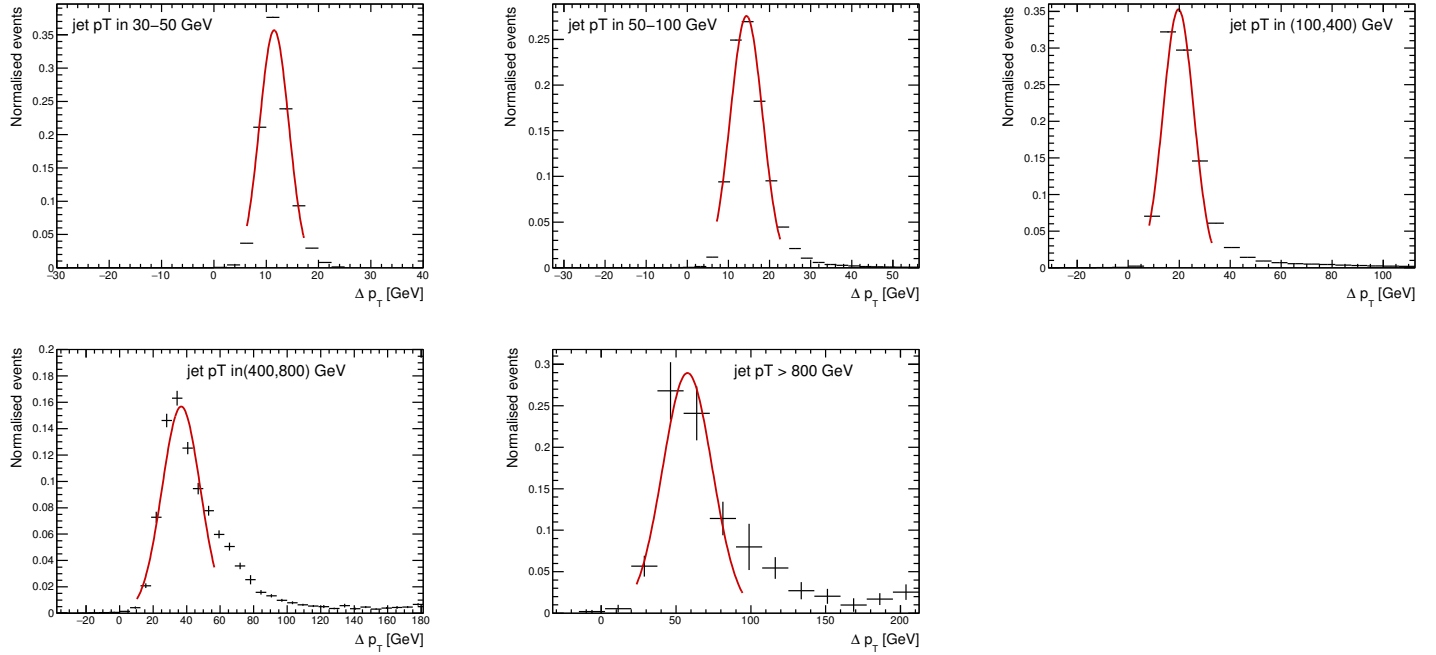


Figure 7.2: $\Delta p_T(\text{electron}, \text{jet})$ distributions (normalised to 1), where $\Delta R(\text{electron}, \text{jet}) < 0.4$, in simulated $Z \rightarrow ee$ events. The plots are separated by jet p_T range: 30-50 GeV, 50-100 GeV, 100-400 GeV, 400-800 GeV, > 800 GeV. It is assumed that the electron-jet pairs plotted here are reconstructions from the same (electron) energy cluster.

7.2.3 Impact on Signal Acceptance

The new overlap removal technique is expected to increase the acceptance of $X \rightarrow t\bar{t}$ events. High p_T $t\bar{t}$ final states often have $\Delta R(\text{electron}, b\text{-jet}) < 0.4$ due to the high p_T leptonically decaying top. With the new overlap removal procedure, fewer b -jets < 0.2 from electrons in $t\bar{t}$ final states will be rejected, and fewer electrons < 0.4 from remaining b -jets will be removed, making the event more likely to pass the selection, compared with the old procedure where all $t\bar{t}$ final states with $\Delta R(\text{electron}, b\text{-jet}) < 0.4$ would have one of the objects removed. This benefits the analysis if signal sensitivity is improved, i.e. if the signal acceptance increases at least as much as the background acceptance. Implementing the new overlap removal

jet p_T range	30-50 GeV	50-100 GeV	100-400 GeV	400-800 GeV	> 800 GeV
Δp_T cut	17 GeV	22 GeV	32 GeV	60 GeV	90 GeV

Table 7.1: Values of Gaussian mean $+ 2\sigma$ from the Δp_T plots in Figure 1.2. These values - “cuts 1” - are used to indicate what p_T cut should be applied to the subtracted jet in the new overlap removal procedure. A default cut > 25 GeV is applied to all jets, including subtracted jets. A higher p_T cut is applied to the subtracted jet if the p_T of the original jet is sufficiently high.

jet p_T range	30-100 GeV	100-200 GeV	200-400 GeV	400-600 GeV	600-800	800-1200	1200-1600	1600-2000	> 2000 GeV
Δp_T cut	30 GeV	70 GeV	90 GeV	120 GeV	130 GeV	230 GeV	700 GeV	1250 GeV	1350 GeV

Table 7.2: Final p_T cuts (“cuts 3”) applied to subtracted jets to decide whether they will be removed from the event.

with initial Δp_T cuts taken from table 7.1 (referred to as “cuts 1”) causes fewer events to be accepted than with the old overlap removal. Upon inspection of the $t\bar{t}$ event cutflows in Figure 7.3, it seems that in the electron channels more events are lost with cuts 1 compared to old overlap removal at the point in the selection where they are required to have at least one electron. This suggests that fake jets from electron energy deposits that would originally have been removed are now passing the subtracted jet p_T cut and causing the nearby electron to be removed. To combat this, the subtracted jet p_T cuts are increased (in new versions of the cuts, referred to as “cuts 2” and “cuts 3”) so it is harder for fake jets to pass. The electron channel event cutflows for cuts 2 and cuts 3 show that this is successful in keeping prompt electrons in the events. The event cutflow for a Z' signal sample is shown in Figure 7.4. For the signal sample, the number of events in the boosted electron channel passing the ≥ 1 electron cut with the new overlap removal is greater than with the old overlap removal, and this improvement is maintained through the rest of the cuts. For the $t\bar{t}$ sample, the number of selected events with new overlap removal drops below the number with old overlap removal at the cut which requires events to have a jet < 1.5 from the electron¹. However, the next event selection cut asks for at least one top-tagged large-R jet, and this restores the improvement of the new method. The extra events that pass with the new overlap removal are more likely to be boosted events. Even though more events pass the jet < 1.5 from electron cut with old overlap removal, the majority of them do not have a top-tagged large-R jet and fail the boosted selection. The muon channel cutflows show that the new overlap removal loses events at the cut which requiring a certain number of jets (resolved channel), and at the cut requiring a jet < 1.5 from the lepton (boosted channel). The final cuts, shown in Table 7.2, are optimised for boosted and high $m_{t\bar{t}}$ events where signal is expected, resulting in a large gain in the boosted electron channel, approximately no change in the boosted muon channel, and losses in the resolved channels.

The impact of the new overlap removal on signal acceptance is quantified by the event selection ratio:

$$\frac{\text{number of accepted signal events under new overlap removal}}{\text{number of accepted signal events under old overlap removal}} \quad (7.1)$$

This ratio is plotted for $t\bar{t}$ events and two Z' samples (2 TeV and 3 TeV) in Figure 7.5 and

¹In lower p_T events, the p_T cut may be too tight, causing subtracted jets which are real b -jets to fail the cut and be rejected.

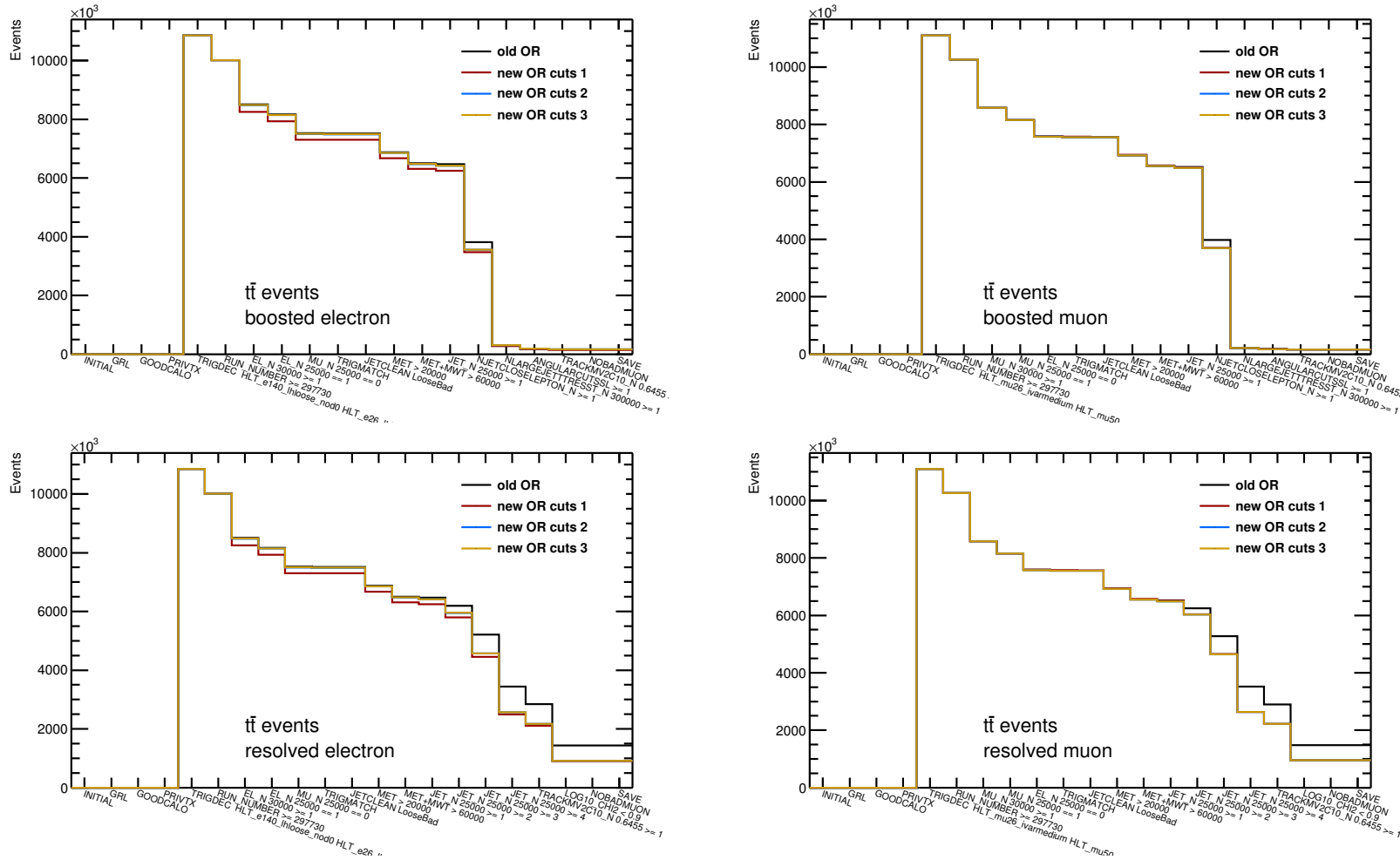


Figure 7.3: Event selection cutflows in the boosted electron, boosted muon, resolved electron and resolved muon channels, for each overlap removal method, with simulated SM $t\bar{t}$ events.

shows a significant improvement in the boosted electron channel, especially at high $m_{t\bar{t}}$.

7.2.4 Jet Performance

Subtracted jets saved by the new overlap procedure are taken to be real jets with the electron energy contribution removed. If this is the case then it should be reflected in the p_T resolution of the subtracted jets. The jet p_T resolution is defined to be:

$$\frac{\text{truth jet } p_T - \text{jet } p_T}{\text{truth jet } p_T} \quad (7.2)$$

The closest truth jet to a jet is matched to it if the truth jet $p_T > 15$ GeV, and $\Delta R(\text{jet}, \text{truth jet}) < 0.2$. Jets for which no truth jet meets this criteria are not used. The truth jets are taken from the ‘‘Truth WZ jets’’ collection - they are made using all final state truth particles except leptons. The jet p_T resolution is compared for subtracted jets that pass the

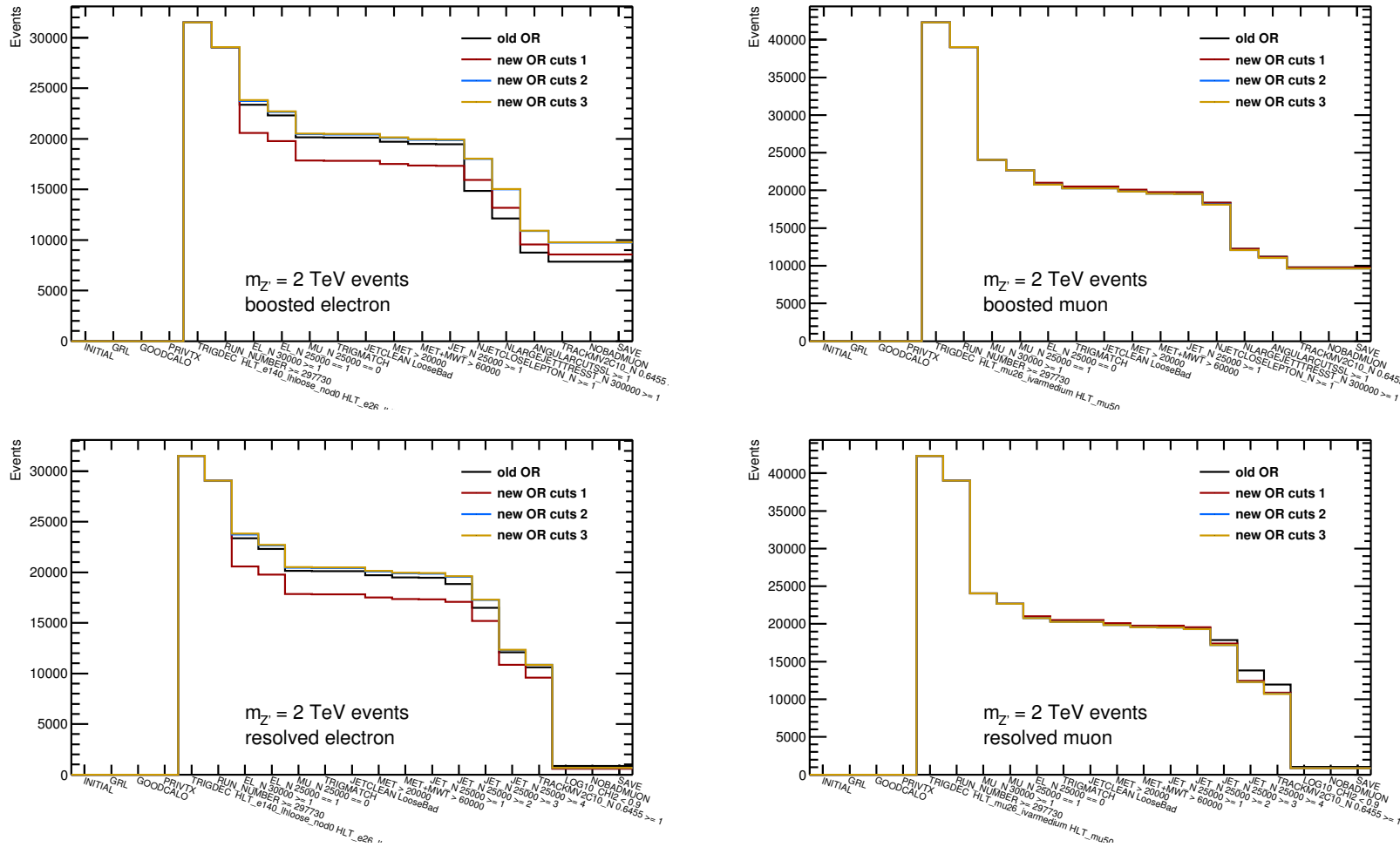


Figure 7.4: Event selection cutflows in the boosted electron, boosted muon, resolved electron and resolved muon channels, for each overlap removal method, with simulated Z' at 2 TeV events.

overlap removal p_T cut, the same jets before the electron four-momentum was subtracted, and for jets that do not have an electron four-momentum subtracted from them. Figure 7.6 shows the jet p_T resolution of simulated $t\bar{t}$ events in each case. Subtracted jets that pass the new overlap removal p_T cut are observed to have a similar p_T reconstruction performance to non-subtracted jets.

7.2.5 Electron Performance

The electron p_T resolution, $(p_T^{reco} - p_T^{truth})/p_T^{truth}$, for electrons with $\Delta R(\text{electron, nearest jet}) \in (0.2, 0.4)$ and for electrons with $\Delta R(\text{electron, nearest jet}) > 0.4$ is shown in Figure 7.7. These distributions are similar, indicating that relaxing the minimum ΔR cut between electrons and jets from 0.4 to 0.2 does not lead to a significant contamination of fake or non-prompt electrons being selected as the single lepton, but does allow prompt electrons < 0.4 from jets

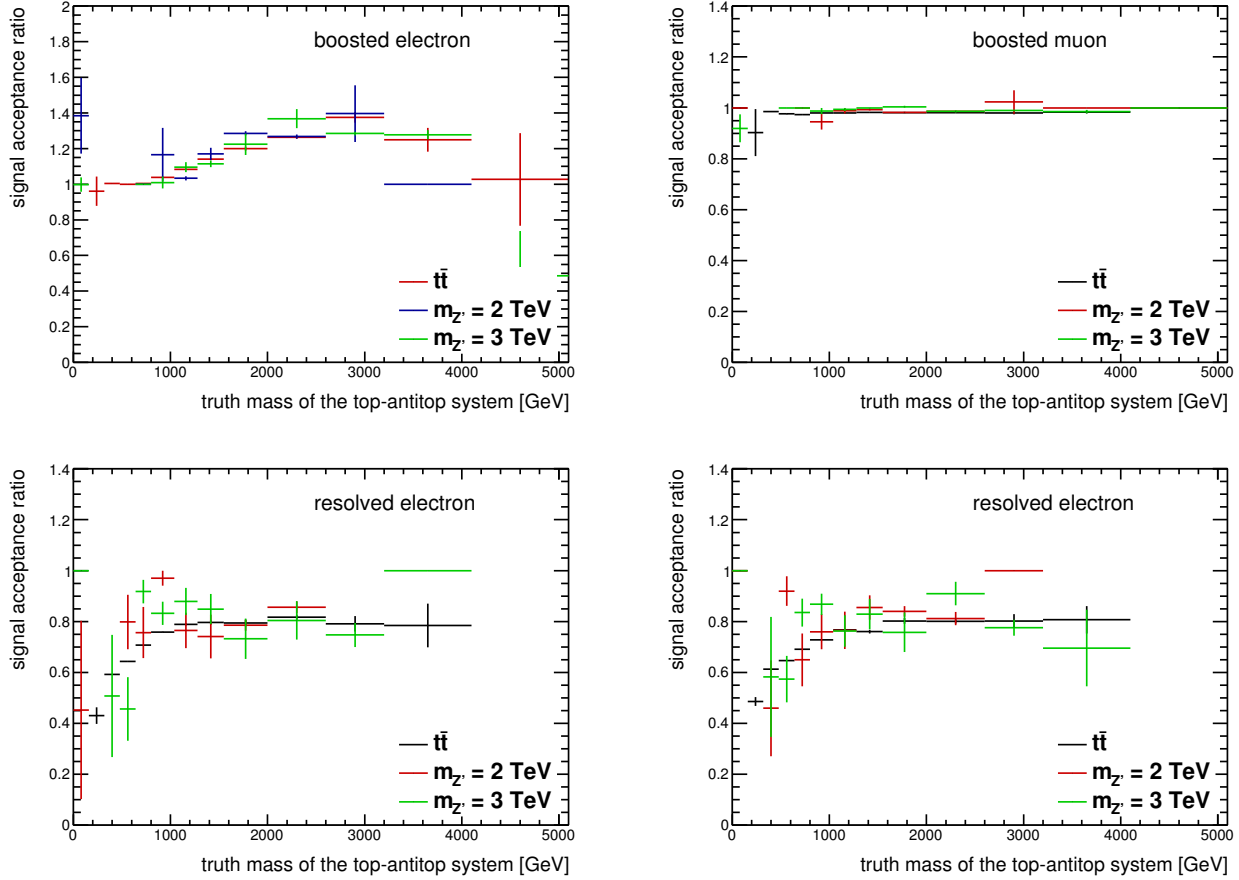


Figure 7.5: New/old signal acceptance ratio (equation 7.1) plotted against truth $m_{t\bar{t}}$ in each channel, shown for SM $t\bar{t}$ and two Z' samples.

to be accepted.

7.2.6 Scale factor for electrons near jets

Corrections to simulated events to account for known differences between data and simulation are implemented as event weights applied to simulated events. In this analysis a scale factor is used to correct for differences in electron identification between data and simulation. This scale factor is defined as:

$$\text{scale factor} = \frac{\text{electron identification efficiency in data}}{\text{electron identification efficiency in simulation}} \quad (7.3)$$

and it has been established only for electrons with $\Delta R(\text{electron}, \text{nearest jet}) > 0.4$; a scale factor appropriate for electrons with $\Delta R(\text{electron}, \text{nearest jet}) < 0.4$ must also be calculated to be used with the new overlap removal procedure. A $Z \rightarrow ee$ tag and probe method based on reference [85] is used to find the scale factor for electrons close to jets.

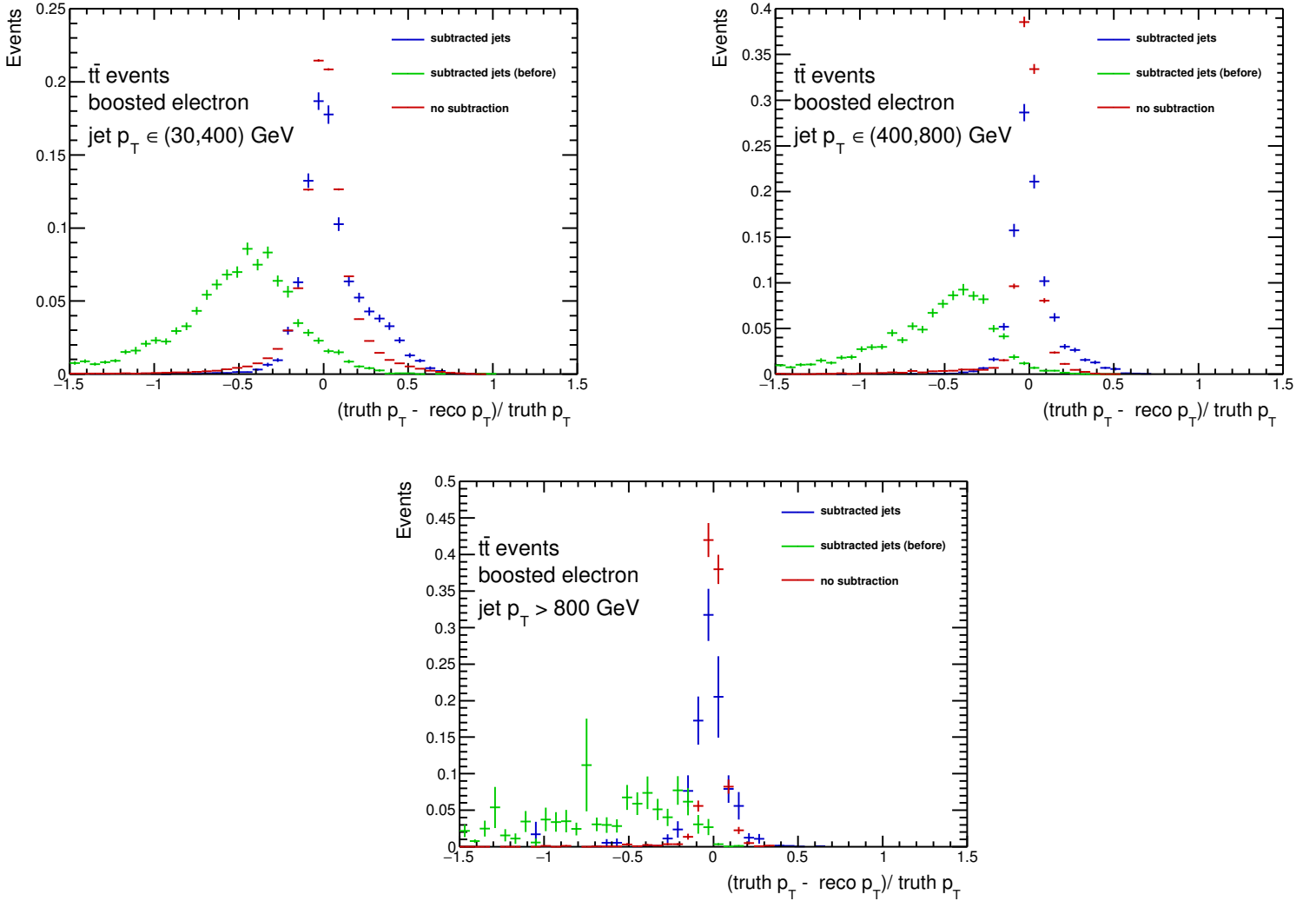


Figure 7.6: Jet p_T resolutions plotted for subtracted jets, the same jets with no electron subtracted, and jets not involved in overlap removal.

Electron identification efficiencies arise when the electron identification algorithm is applied to reconstructed electron candidates. Only candidates that pass the cuts are counted as electrons, the others are discarded as background. The efficiency depends on the identification criteria, which can be tight, medium or loose. The tight criteria has the best background rejection and the poorest efficiency, while the reverse is true for the loose criteria. The fraction of reconstructed electrons that pass a certain identification criteria is the efficiency of that criteria.

The idea of the tag and probe method is to build a sample of objects that are extremely likely to be reconstructed electrons without applying identification cuts to them, and find what fraction passes additional identification criteria. This is done by selecting $Z \rightarrow ee$ events from data and simulated events with minimal identification criteria placed on the

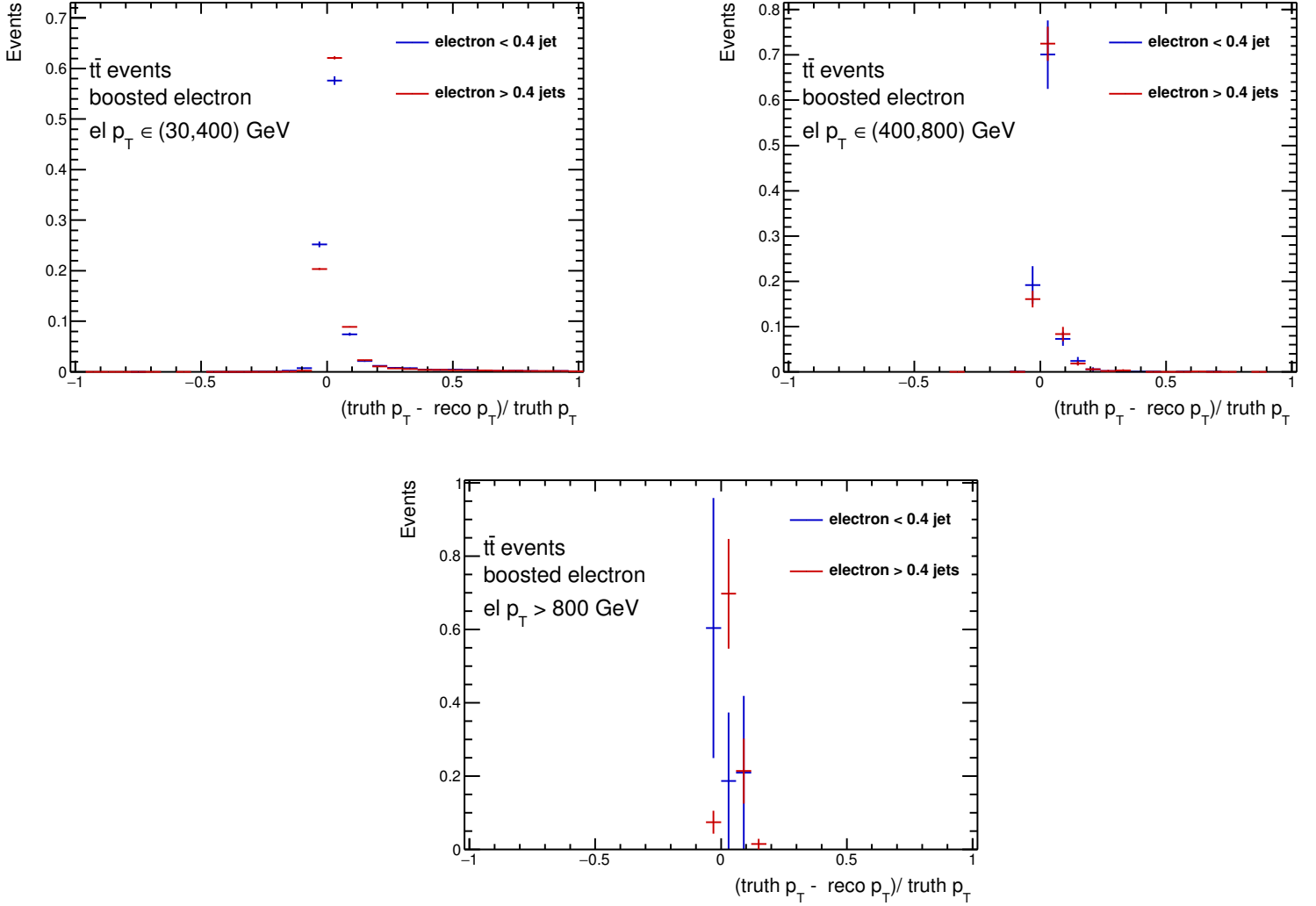


Figure 7.7: Electron p_T resolution for electrons with $\Delta R(\text{electron}, \text{nearest jet}) \in (0.2, 0.4)$ and for electrons with $\Delta R(\text{electron}, \text{nearest jet}) > 0.4$.

electron candidates, which are referred to as base electrons. Tag and probe pairs are selected from these events; pairs of opposite sign base electrons with invariant mass m_{ee} close to the Z boson mass, one of which (the tag) must meet tight identification criteria while the other (the probe) has no additional requirements placed on it. All possible tag and probe pair combinations in an event are considered, including the same pair twice if both electrons meet the tag criteria, so that the probes constitute an unbiased sample of reconstructed electrons. The tight requirement on the tag along with the m_{ee} mass cut is meant to ensure that the probe object is really a reconstructed electron (from the Z boson decay), so that the fraction of base electrons passing for example tight identification criteria will reflect the

real identification efficiency:

$$\text{tight electron identification efficiency} = \frac{n_{\text{tight probes}}}{n_{\text{base probes}}} \quad (7.4)$$

$Z \rightarrow ee$ events are ideal for this measurement: they are a large cross-section source of isolated pairs of electrons suitable for tag and probe pairs. The minimal initial requirements on the base electrons rejects the majority of jets faking electrons in the probe sample. In simulated $Z \rightarrow ee$ events, truth-level information is used to ensure that the objects used in the efficiency calculation are reconstructed electrons from the Z decay. When selecting $Z \rightarrow ee$ events from data, a certain number of non $Z \rightarrow ee$ events will be chosen, and the base electrons sample will contain fake and non-prompt electrons. The background contribution must be estimated and subtracted. Electron identification efficiencies are p_T and η dependent, so a separate efficiency calculation is done for a set of (p_T, η) regions. The p_T bins are $p_T \in (25,30), (30,35), (35,40), (40,45), (45,50), (50,60), (60,80), 80+$ GeV. Coarser η bins are used for sufficient statistics: $\eta \in (-2.5,-1.5), (-1.5,-0.5), (-0.5,0.5), (0.5,1.5), (1.5,2.5)$.

Selecting tag and probe events

Events must pass a single electron trigger², and contain at least two base electrons, no muons and at least one jet. Any base electron pair with $m_{ee} \in [70, 110]$ GeV, opposite sign and $\Delta R(e, e) > 0.6$ is a tag and probe pair candidate³. If there is more than one such pair in the event, every candidate pair is tested against the full tag and probe criteria. To be a tag, a base electron must pass tight likelihood identification criteria, match the single lepton trigger, have $p_T > 25$ GeV, $|\eta|$ within the inner detector acceptance and $\Delta R(\text{electron, nearest jet}) > 0.4$. To be a probe, a base electron must have $p_T > 25$ GeV and $|\eta|$ within the inner detector acceptance. At least one of the electrons in the candidate pair must pass the tag criteria. If only one electron passes the tag criteria, the other electron is used as the probe and this pair will count once towards the efficiency calculation. If both electrons pass the tag criteria, each electron in turn is used as the probe, and this pair will count twice towards the efficiency calculation. The probes used in the calculation are separated into two categories, A and B, based on whether $\Delta R(\text{probe, nearest jet}) > 0.4$ (category A) or $\Delta R(\text{probe, nearest jet}) < 0.4$ (category B). The efficiencies are calculated separately for each category so that any difference in scale factor is visible.

²HLT_e26_lhtight_nod0_ivarloose, HLT_e60_lhmedium_nod0 HLT_e140_lhloose_nod0

³The $\Delta R(e, e) > 0.6$ cut is used to remove Z boson recoil events.

Background subtraction from data

The electron selection efficiency in data is defined to be:

$$\text{tight electron identification efficiency in data} = \frac{n_{\text{tight}} - n_{\text{tight}}^{\text{fake}}}{n_{\text{base}} - n_{\text{base}}^{\text{fake}}} \quad (7.5)$$

The number of $Z \rightarrow ee$ tag and probe events selected from data with (a) fake tight probe electrons, $n_{\text{tight}}^{\text{fake}}$, and (b) fake base probe electrons, $n_{\text{base}}^{\text{fake}}$, i.e. background events, must be estimated. This is done in two steps: 1) estimating the shape of the tag and probe m_{ee} distribution for background events, and 2) estimating the total number of background events that pass the tight and base criteria. For each (p_T, η) range, the m_{ee} background shape can be normalised to the expected number of background events (tight or base) and subtracted from the corresponding data m_{ee} distribution, which can then be compared to the signal-only m_{ee} distributions in simulation to check how well they agree. The background estimation method makes use of tag and probe m_{ee} distributions in the Z boson mass window 70-110 GeV referred to as the peak, as well as in the range 120-240 GeV, referred to as the sideband.

Templates derived from data are used to describe the m_{ee} shape of the background for each (p_T, η) range. They are constructed by selecting tag and probe events from data, in which the probe fails additional quality cuts: it must fail loose likelihood identification criteria and tight isolation criteria. The fake templates are contaminated with signal ($Z \rightarrow ee$) tag and probe events in which the probe electron fails the additional quality cuts. The $Z \rightarrow ee$ contribution is estimated by selecting from simulation $Z \rightarrow ee$ events that pass the background template criteria, and correcting the normalisation of the resulting signal contamination template using a scale factor⁴. The corrected signal contamination template is then subtracted from the data fakes shape template to yield the corrected fakes shape template.

The same templates are used for the tight background and the base background as there is assumed to be no significant difference in the shape of the m_{ee} distribution using fake probes that fail loose criteria and using fake probes that pass tight criteria. Initially the fake shape templates are normalised to the number of fakes that fail loose criteria and tight isolation, but a non-negligible amount of fake probes also pass loose, medium and even tight identification criteria. The shape templates are normalised to the expected number of fake base and fake tight probe events using sideband techniques.

In order to estimate the number of fake tight probes in the data, same-sign electron pairs with $m_{ee} \in (120, 250)$ GeV which otherwise satisfy the tag and probe criteria, with the probe also passing tight identification criteria, are selected from the data. The number of such sideband pairs is expected to be about the same as the number of tight, opposite

⁴The scale factor is the global ratio of tight tag and probe pairs in the data m_{ee} peak to tight tag and probe pairs in the MC m_{ee} peak.

sign tag and probe sideband pairs that do not come from a $Z \rightarrow ee$ decay, and so is an estimate of $n_{\text{tight}}^{\text{fake}}$ in the m_{ee} sideband. The same-sign requirement is to prevent the selection of $Z \rightarrow ee$ signal events that fall in the sideband. The background m_{ee} peak shape template is normalised to $n_{\text{tight}}^{\text{fake}}$ using:

$$[n_{\text{fake}}]_{\text{peak}} = \left[\frac{n_{\text{same sign, tight}}}{n_{\text{template}}} \right]_{\text{tail}} \times [n_{\text{template}}]_{\text{peak}} \quad (7.6)$$

The ratio of template peak to template tail tag and probe pairs is expected to be the same as the ratio of fake tight peak to fake tight tail tag and probe pairs, so this ratio is used to translate the estimated number of fake tight pairs in the tail to the expected number of fake tight pairs in the peak. However, in some (p_T, η) bins the statistics are poor and there can be no events in one or both of the peak and tail shape template, so there is no usable ratio. In these cases, the $n_{\text{template, peak}}/n_{\text{template, tail}}$ ratio is plotted against p_T for each η range and the ratio is extrapolated from this plot. For each (p_T, η) bin, the estimated fake tight m_{ee} distribution is subtracted from the tight data m_{ee} distribution.

The number of fake base probes is estimated by first selecting opposite sign electron pairs with $m_{ee} \in (120, 250)$ GeV which otherwise satisfy the tag and probe criteria; this accepts a considerable amount of signal from the m_{ee} tail, which must be subtracted. The signal contamination is estimated by selecting tight opposite sign tag and probe pairs in the sideband (to gather tight signal events), subtracting tight same sign tag and probe pairs (to account for fake tight) and dividing the resulting number by the tight efficiency, since:

$$\frac{n_{\text{tight}, Z \rightarrow ee}}{n_{\text{base}, Z \rightarrow ee}} = \frac{n_{\text{tight, identified}}}{n_{\text{tight, all}}} = \epsilon_{\text{tight}} \quad (7.7)$$

The background shape template is normalised to $n_{\text{base}}^{\text{fake}}$ using:

$$[n_{\text{fake}}]_{\text{peak}} = \left[\frac{n_{\text{opposite sign}} - (n_{\text{opposite sign, tight}} - n_{\text{same sign, tight}})/\epsilon_{\text{tight}}}{n_{\text{template}}} \right]_{\text{tail}} \times [n_{\text{template}}]_{\text{peak}} \quad (7.8)$$

For each (p_T, η) bin, the estimated fake base m_{ee} distribution is subtracted from the data base distribution.

Electron selection efficiency in data and simulation

The tight electron identification efficiencies for data and simulation, and their ratio, plotted against probe p_T and η are shown in Figures 7.8, 7.9, 7.10. The efficiencies for two example η bins plotted against probe p_T are shown in Figure 7.11. The identification efficiencies of electrons > 0.4 from jets are similar to the efficiencies produced by the egamma group as a

reference for ATLAS analyses in both data and simulation [85]. The identification efficiencies of electrons < 0.4 from jets resemble the reference efficiencies at electron $p_T < 50$ GeV, but suffer from large statistical fluctuations at higher p_T , due to the lack of electrons overlapping with real jets in $Z \rightarrow ee$ events. The data/simulation efficiency ratios for electrons > 0.4 and < 0.4 from jets are similar to the reference ratios, except for the statistical fluctuations in the latter. Further studies have been performed on efficiencies for electrons < 0.4 from jets using dileptonic $t\bar{t}$ events [86], which have better statistics for high p_T electrons overlapping with real jets, but other complications arise in these studies due to the high fake electron rate that arises from relaxing the electron identification criteria.

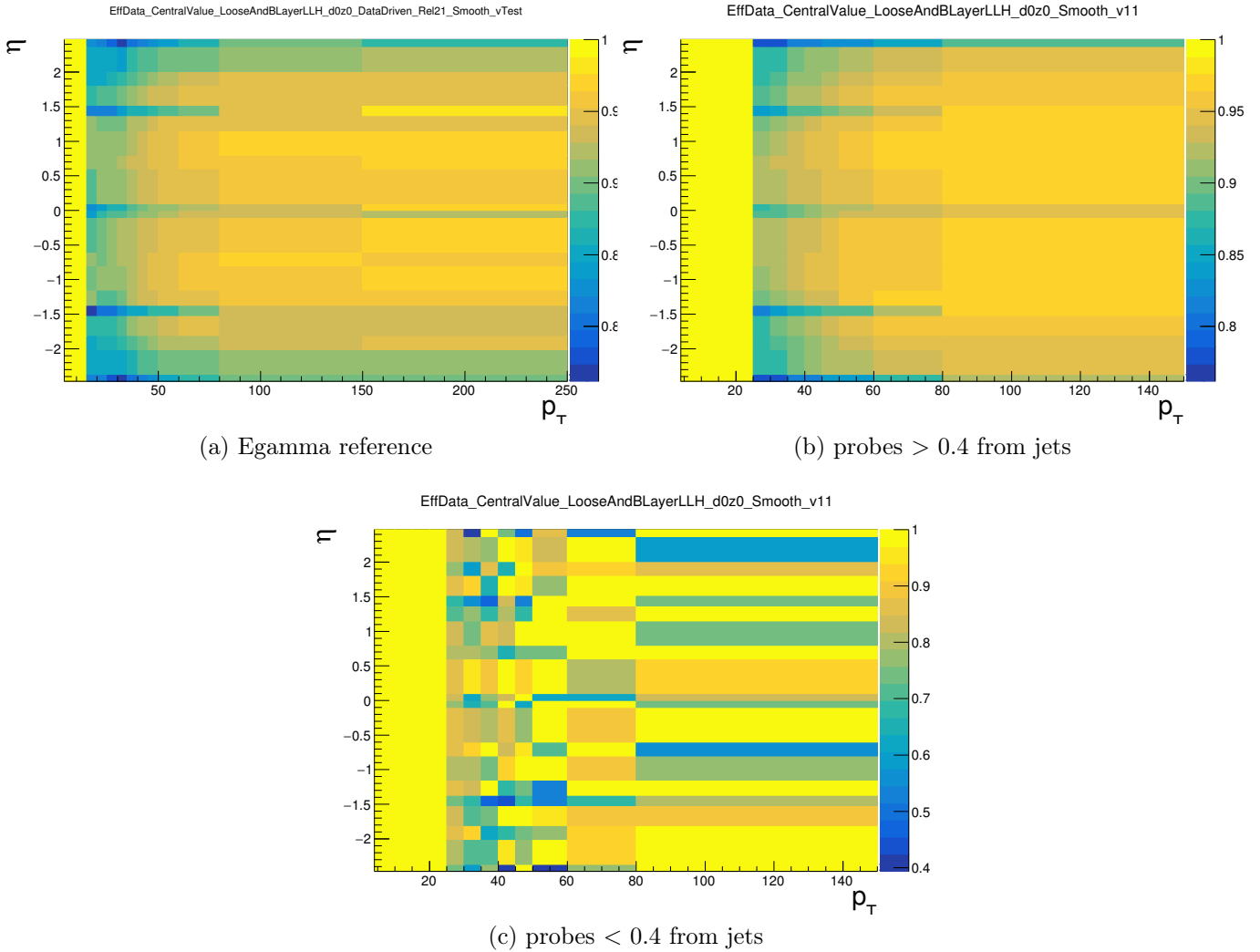


Figure 7.8: Electron identification efficiency in data for (a) egamma reference, (b) probes > 0.4 from jets and (c) probes < 0.4 from jets.

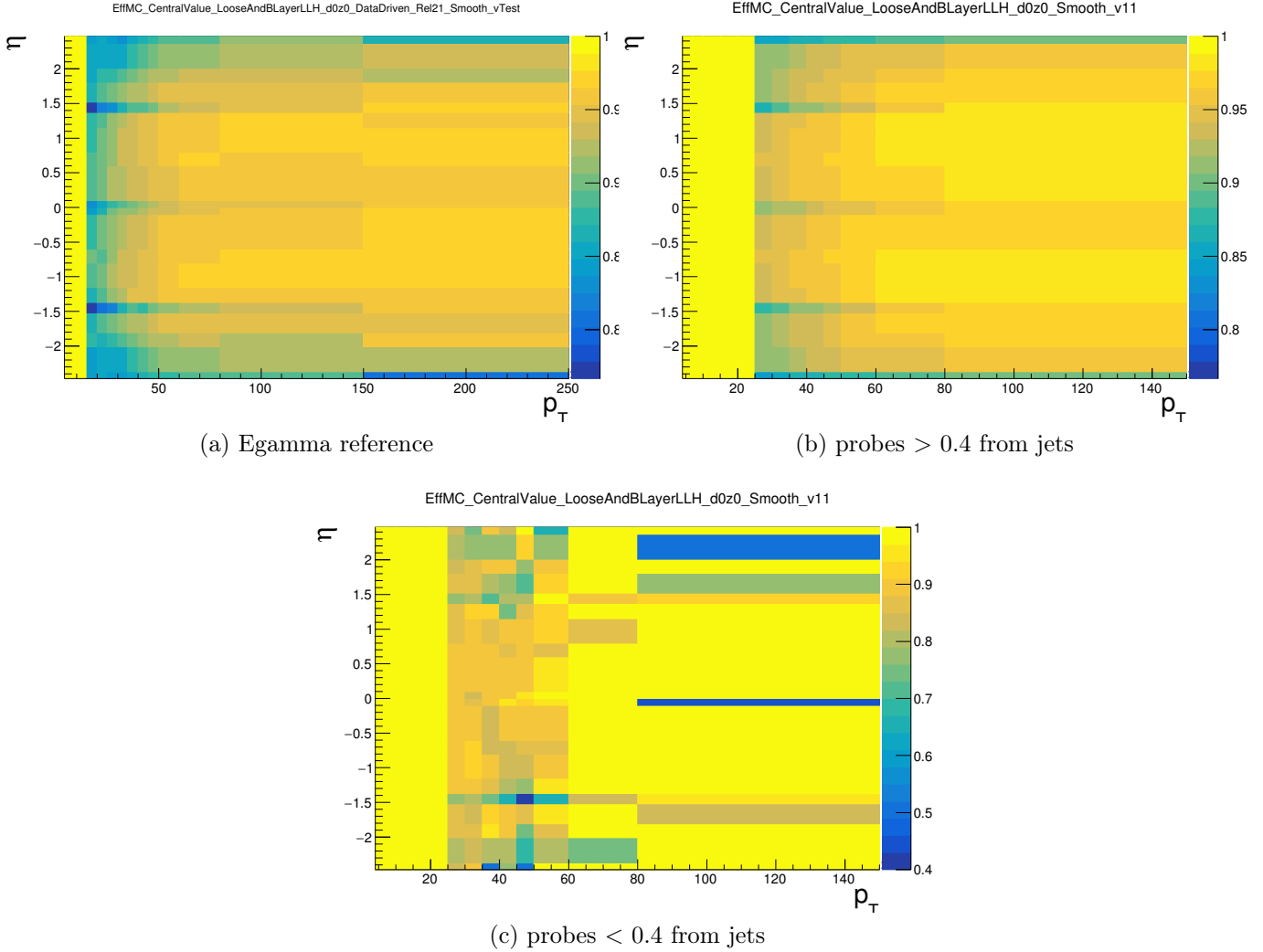


Figure 7.9: Electron identification efficiency in simulation for (a) egamma reference, (b) probes > 0.4 from jets and (c) probes < 0.4 from jets.

7.2.7 Impact on Sensitivity of the Search

The impact of this method on the sensitivity of the search is quantified by comparing the expected upper limits, assuming no signal, that can be set on the Z' boson cross-section with the standard overlap removal procedure applied and with the electron subtraction procedure applied. The multijet background is not included here as it is estimated from data and is sensitive to the definition of leptons which would change if the subtraction procedure was used. Dedicated studies would be required to assess the change in this background. Figure 7.12 shows the expected upper limits using standard overlap removal (in black) and the subtraction method (in red) for the boosted electron channel only and for all channels. For the boosted electron channel only, the subtraction methods improves the Z' mass exclusion limit by 0.1-0.2 TeV. Including all channels, the improvement is smaller (due to the new

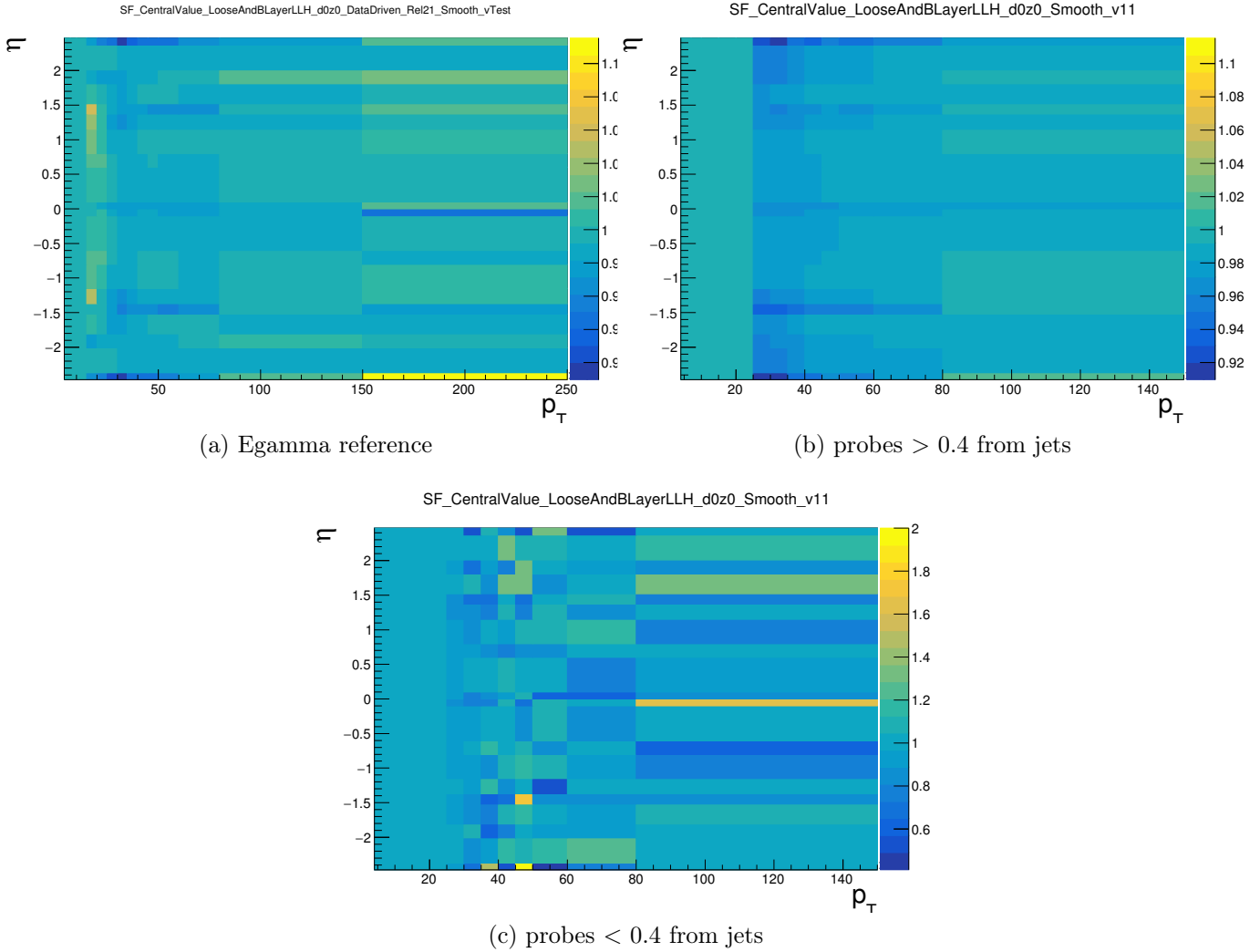


Figure 7.10: Data efficiency/ simulation efficiency for (a) egamma reference, (b) probes > 0.4 from jets and (c) probes < 0.4 from jets.

method leading to a small degradation in the sensitivity of the resolved channels and no change in boosted muon channel), but the subtraction method results in better cross-section limits at high signal masses.

7.3 Other Decay Topologies

7.3.1 Motivation

The $t\bar{t}$ selection efficiency in this analysis is highly dependent on the $t\bar{t}$ decay topology. Figures 7.13 and 7.14 show the selection efficiency for boosted events, resolved events and events that pass neither channel but do pass a preselection which comprises a subset of the boosted and resolved cuts up to where the two selections diverge, plus additional requirements

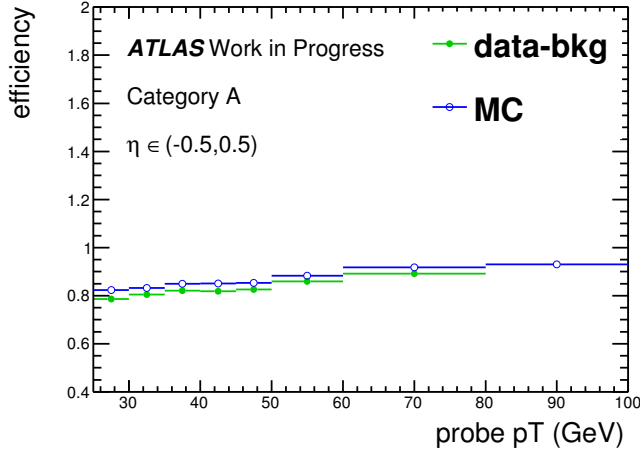
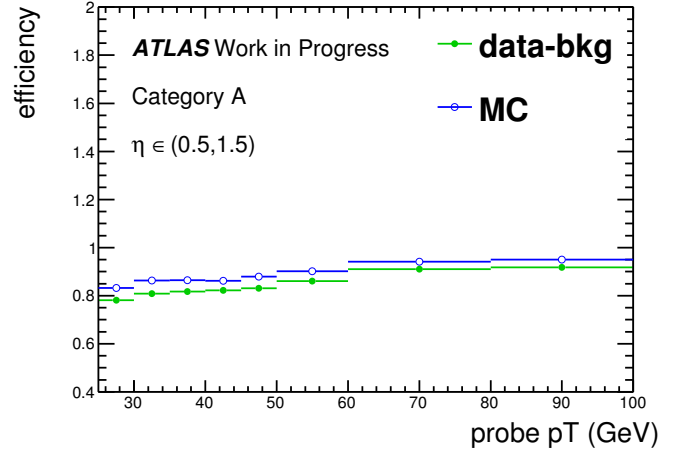
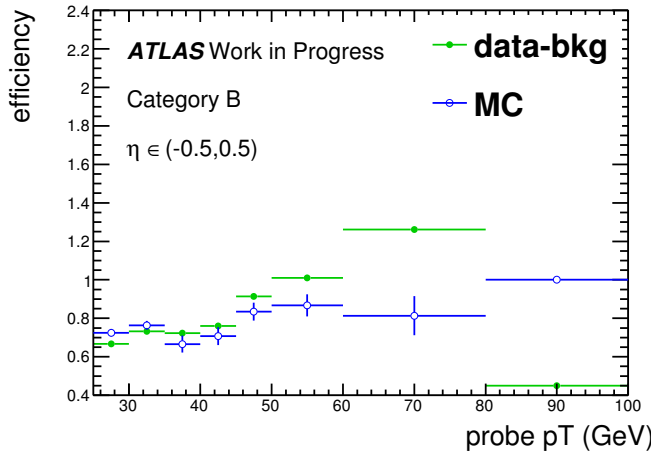
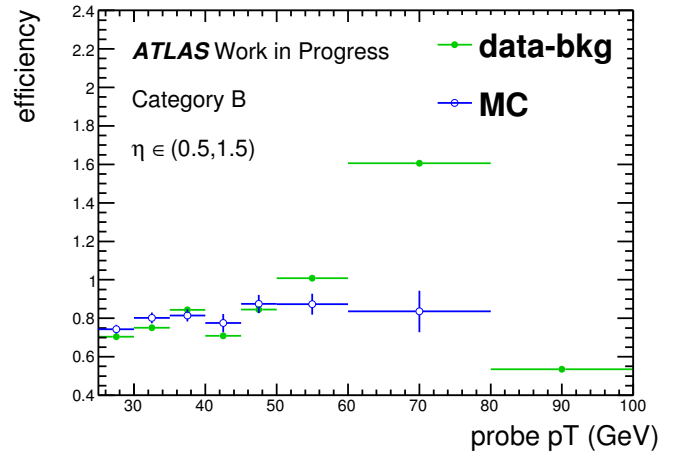
(a) probes > 0.4 from jets(b) probes > 0.4 from jets(c) probes < 0.4 from jets(d) probes < 0.4 from jets

Figure 7.11: The efficiency of probes > 0.4 from jets ((a), (b)) and probes < 0.4 from jets ((c), (d)) plotted against probe p_T in two example η bins.

of ≥ 2 small-R jets and $\Delta R(\ell, \text{small-R jet}) < 1.5$. The ‘neither’ selection is:

- At least one primary vertex.
- Passes single lepton trigger.
- Exactly one lepton that matches the trigger.
- $E_T^{\text{miss}} > 20$ GeV and $M_T^W + E_T^{\text{miss}} > 60$ GeV.
- At least one b -tagged track jet.
- At least two small-R jets.

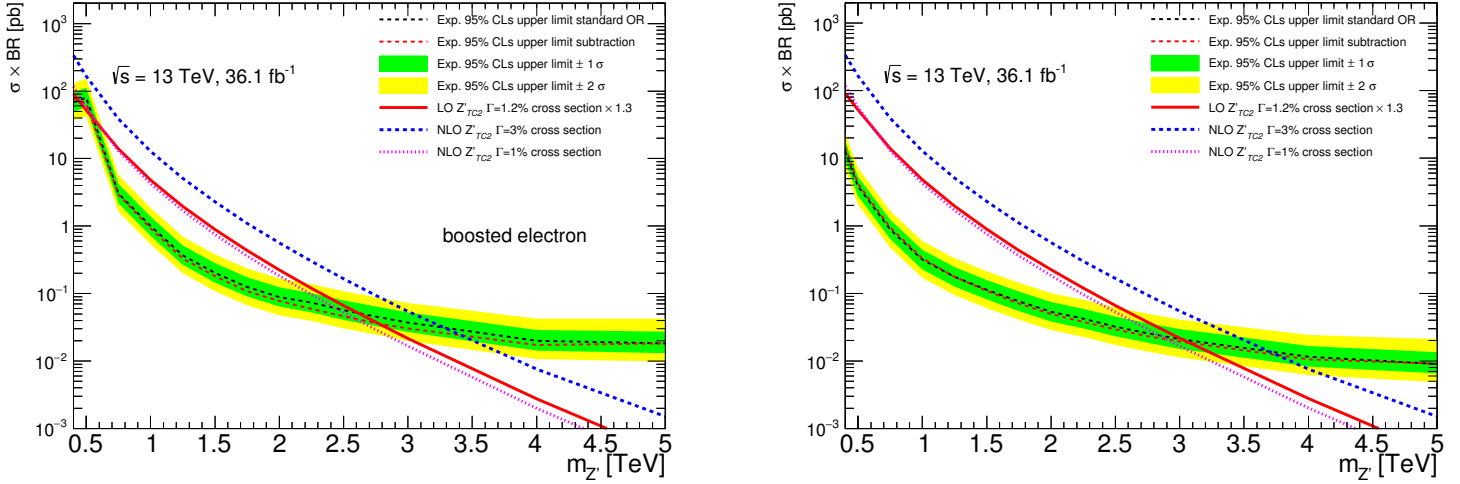


Figure 7.12: Expected 95% CL upper limits set on a Z' boson using standard overlap removal (black dashed line) and the subtraction method (red dashed line), shown for the boosted electron channel only on the left hand side and all channels on the right hand side.

- $\Delta R(\ell, \text{small-R jet}) < 1.5$.

The efficiency is defined to be:

$$\frac{\text{number of selected } t\bar{t} \text{ events}}{\text{total number of } t\bar{t} \text{ events in the sample}} \quad (7.9)$$

for each selection. Of the established channels, the resolved channel has the best efficiency for selecting SM $t\bar{t}$ events with truth $m_{t\bar{t}} \lesssim 900$ GeV, with the boosted channel taking over at higher masses.

At truth $m_{t\bar{t}} > 1400$ GeV, only about half of the preselected events are accepted into a channel (mainly the boosted channel). There is also a middle mass range, 600-1200 GeV, after the point where the resolved channel efficiency begins to decrease, but before the boosted channel efficiency reaches its maximum, where a significant proportion of preselected events do not fit the criteria for either channel.

This section investigates whether it is feasible to use a new selection and reconstruction procedure to recover preselected events that do not pass the boosted or resolved selections in the two identified $m_{t\bar{t}}$ regions: middle-range mass and high mass. The drop off in selection efficiency in the middle mass region indicates that there is a certain p_T range where the boosted and resolved selections fail to recognise the topology of hadronic top decays; a “semi-boosted” channel is postulated. Additionally, signatures of very high p_T hadronic top decays are investigated in order to determine other ways of capturing very high $m_{t\bar{t}}$ events that fail the boosted selection.

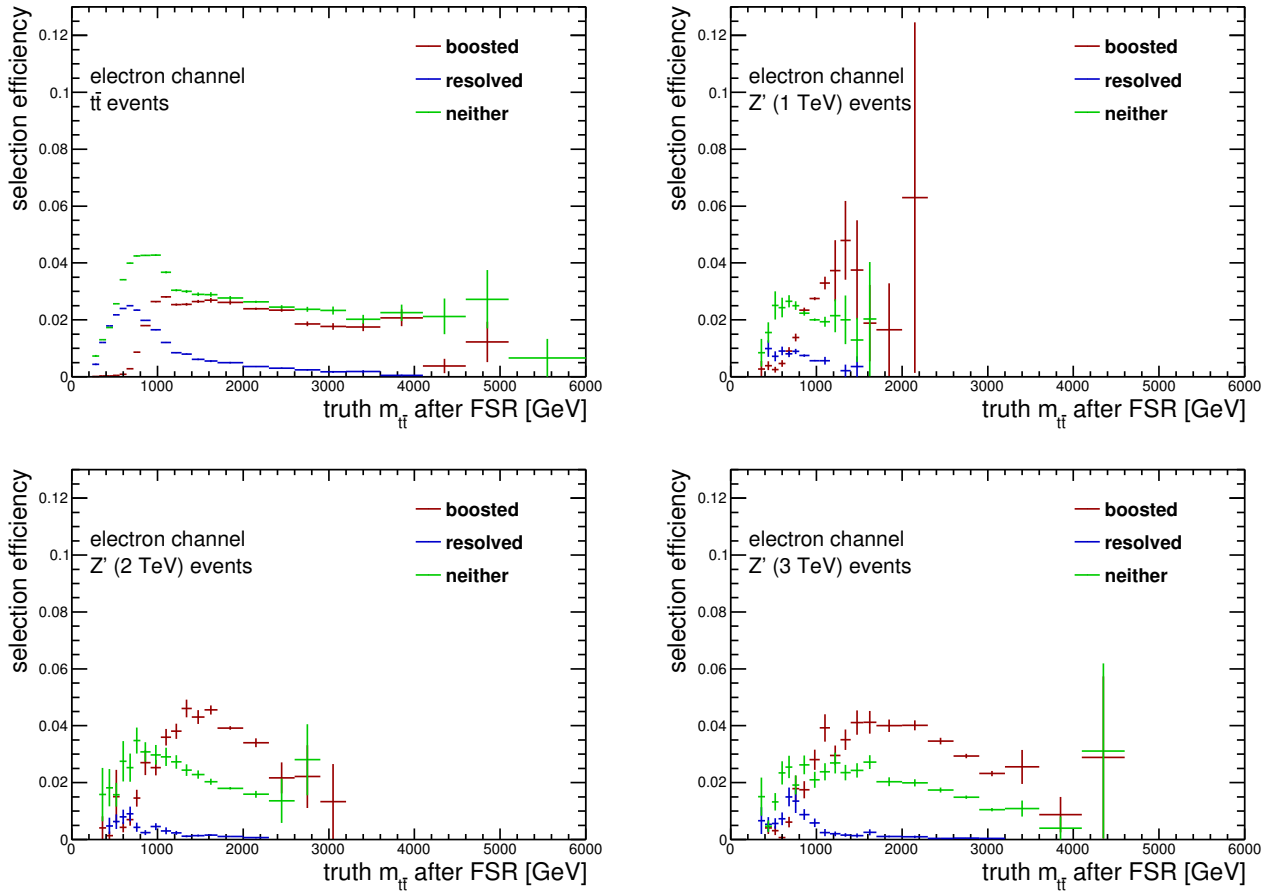


Figure 7.13: $t\bar{t}$ event selection efficiency for the boosted electron channel, resolved electron channel, and events that pass neither channel but do pass an electron channel preselection. The selection efficiency is shown in bins of truth $m_{t\bar{t}}$ after final state radiation (FSR).

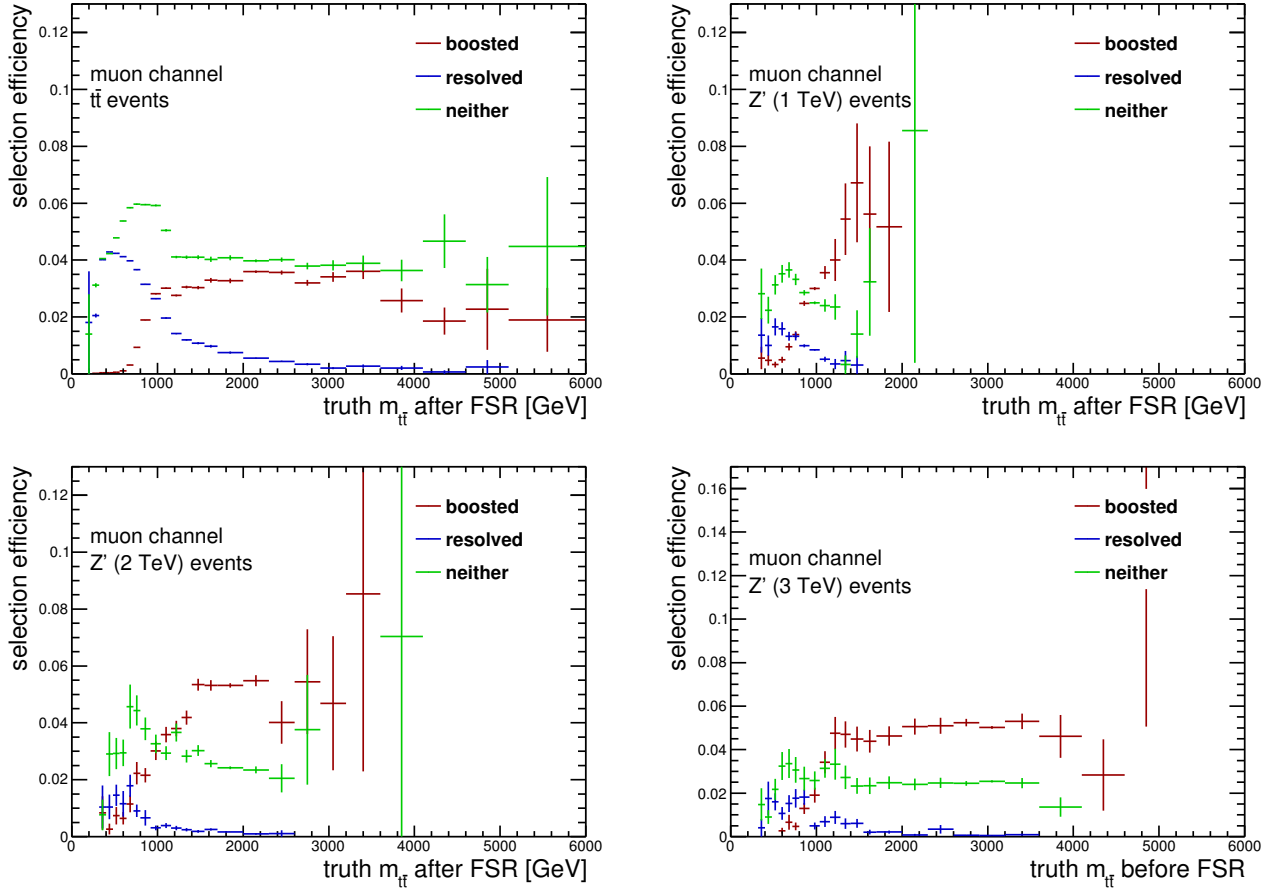


Figure 7.14: $t\bar{t}$ event selection efficiency for the boosted muon channel, resolved muon channel, and events that pass neither channel but do pass a muon channel preselection. The selection efficiency is shown in bins of truth $m_{t\bar{t}}$ after final state radiation (FSR).

Two cases of hadronic top decay are considered: very boosted events in which the t_{had} is detected as two separate small-R jets instead of a large-R jet, one of which has a high mass as it captures the entire W boson decay, as shown in Figure 7.15, and semi-boosted events in which the t_{had} is detected as one large-R jet and one small-R jet, as shown in Figure 7.16.

7.3.2 Very boosted events

Events that pass the preselection (fully described in Section 6.5.1) and that contain at least two small-R jets, one with mass greater than 60 GeV, but do not pass the boosted or resolved channels, are selected from a SM $t\bar{t}$ sample and Z' (1-3 TeV) samples. Of the small-R jets, one is required to satisfy $\Delta R(\ell, \text{small-R jet}) < 1.5$, so that t_{lep} can be reconstructed, and the one with mass greater than 60 GeV, known as j_{hm} , is associated with the t_{had} decay. These events are called very boosted events. The truth $m_{t\bar{t}}$ distributions of very boosted, boosted and resolved events are shown in Figures 7.17 and 7.18. The proportion of very boosted

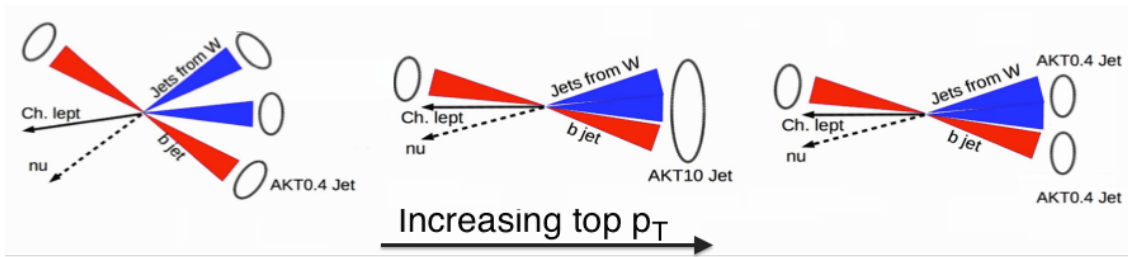


Figure 7.15: “Very boosted” scenario (right): the W_{had} decay and the b_{had} decay are detected inside two separate small-R jets. The small-R jet containing the W boson decay is expected to have mass > 60 GeV.

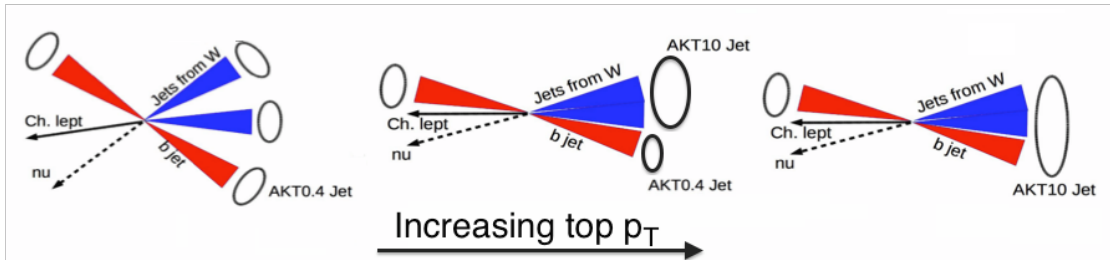


Figure 7.16: “Semi-boosted” scenario (middle): The W_{had} decay is detected inside one large-R jet, and the b_{had} decay is detected inside a nearby small-R hjet.

events is greatest for the $m_{Z'} = 3$ TeV sample. It can be seen in Figures 7.19 and 7.20 that many boosted channel events also possess the very boosted topology; in high mass Z' samples, the majority of boosted events contain one small-R jet with mass greater than 60 GeV.

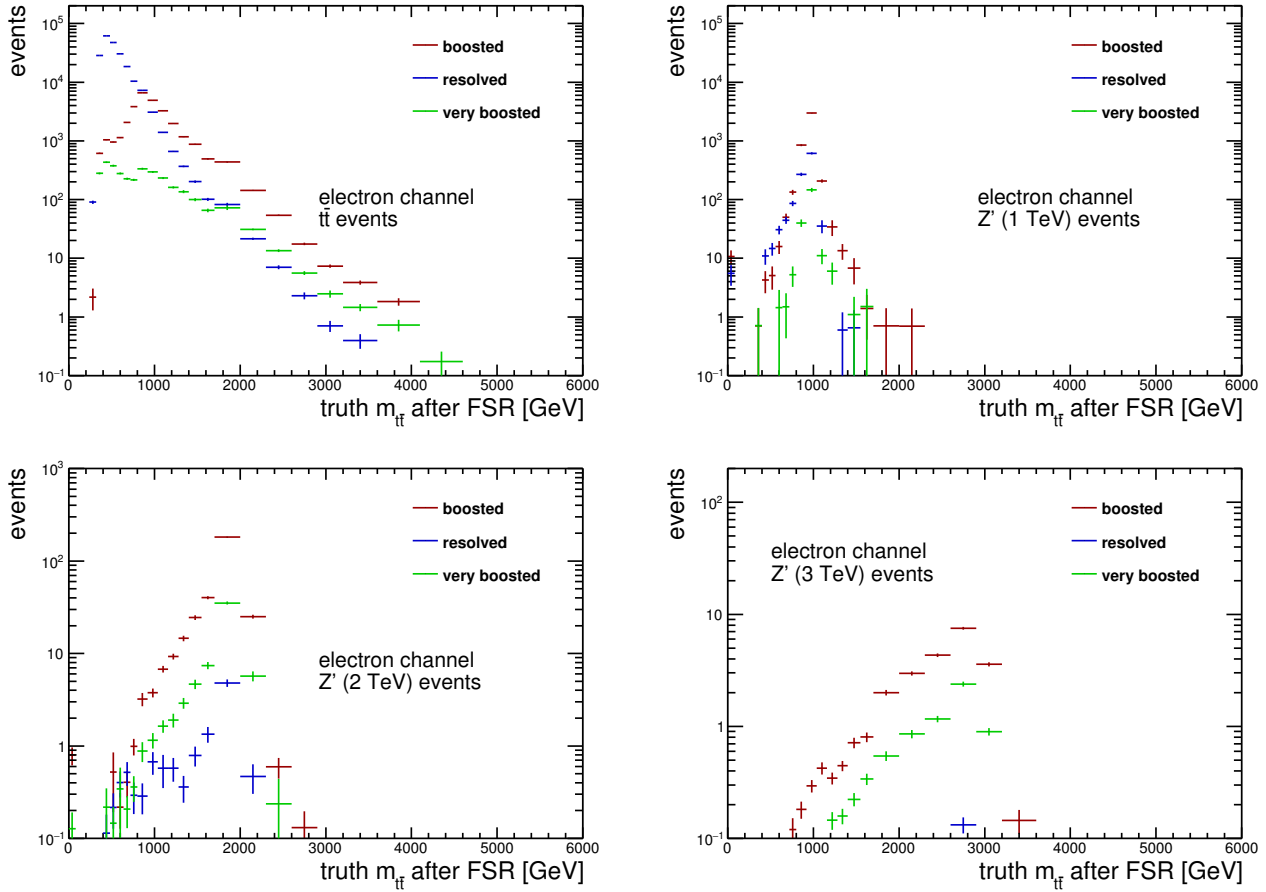


Figure 7.17: Truth $m_{t\bar{t}}$ distribution (after final state radiation) in the boosted electron, resolved electron and very boosted electron channel for SM $t\bar{t}$ and Z' samples. The proportion of very boosted events increases with Z' mass.

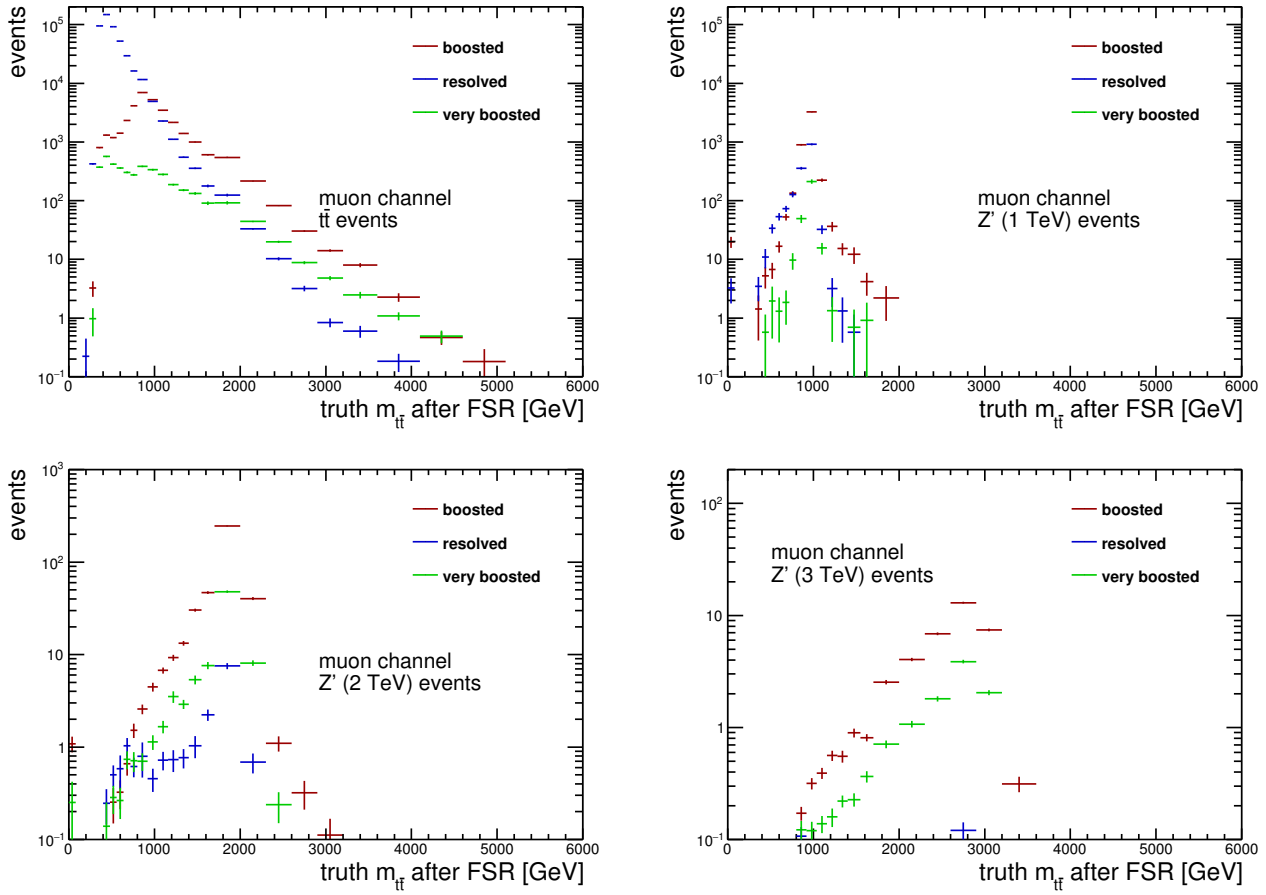


Figure 7.18: Truth $m_{t\bar{t}}$ distribution (after final state radiation) in the boosted muon, resolved muon and very boosted muon channel for SM $t\bar{t}$ and Z' samples. The proportion of very boosted events increases with Z' mass.

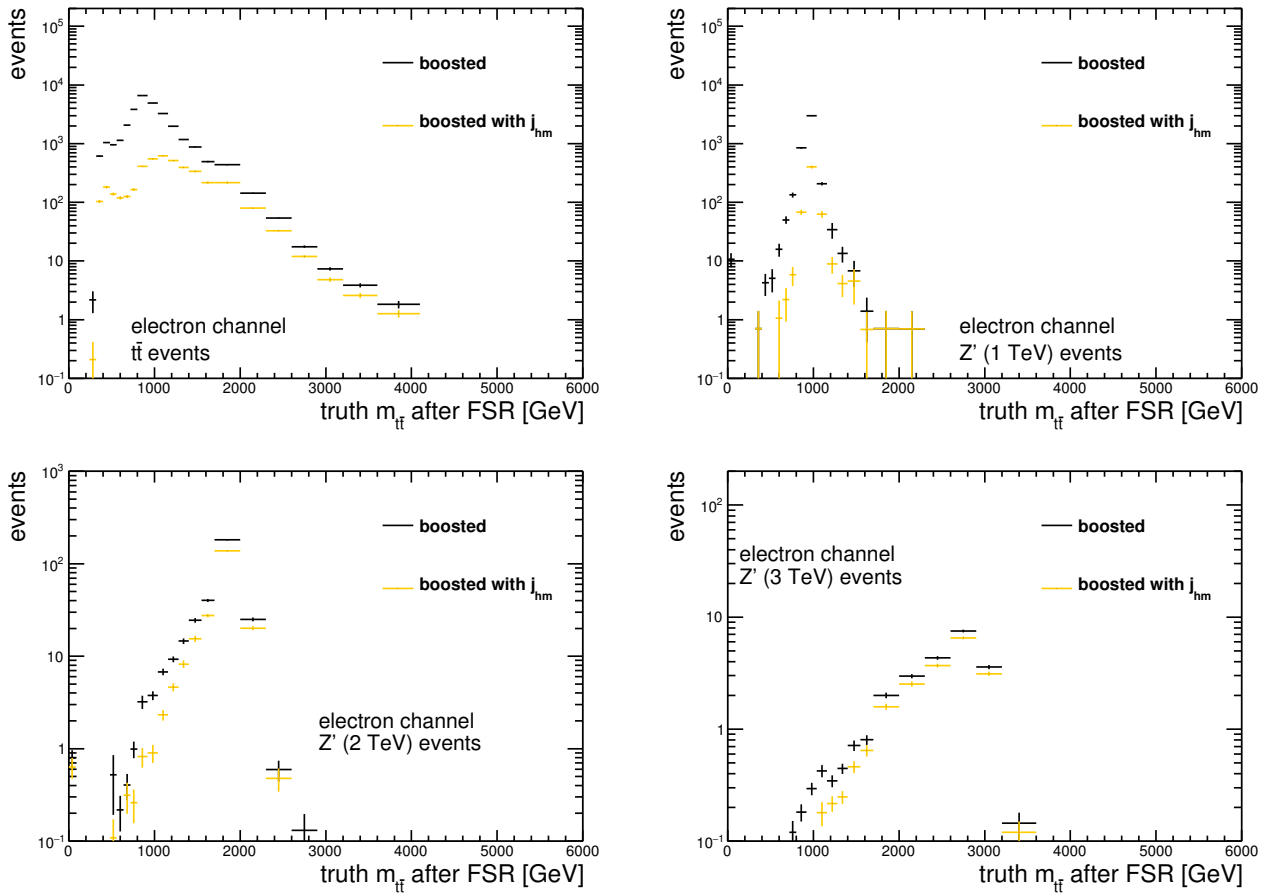


Figure 7.19: Truth $m_{t\bar{t}}$ distribution (after final state radiation) for boosted electron events, and boosted electron events that also meet the very boosted criteria (a small-R jet with mass > 60 GeV). The majority of boosted events from the $m_{Z'} = 2$ TeV and $m_{Z'} = 3$ TeV sample are also very boosted.

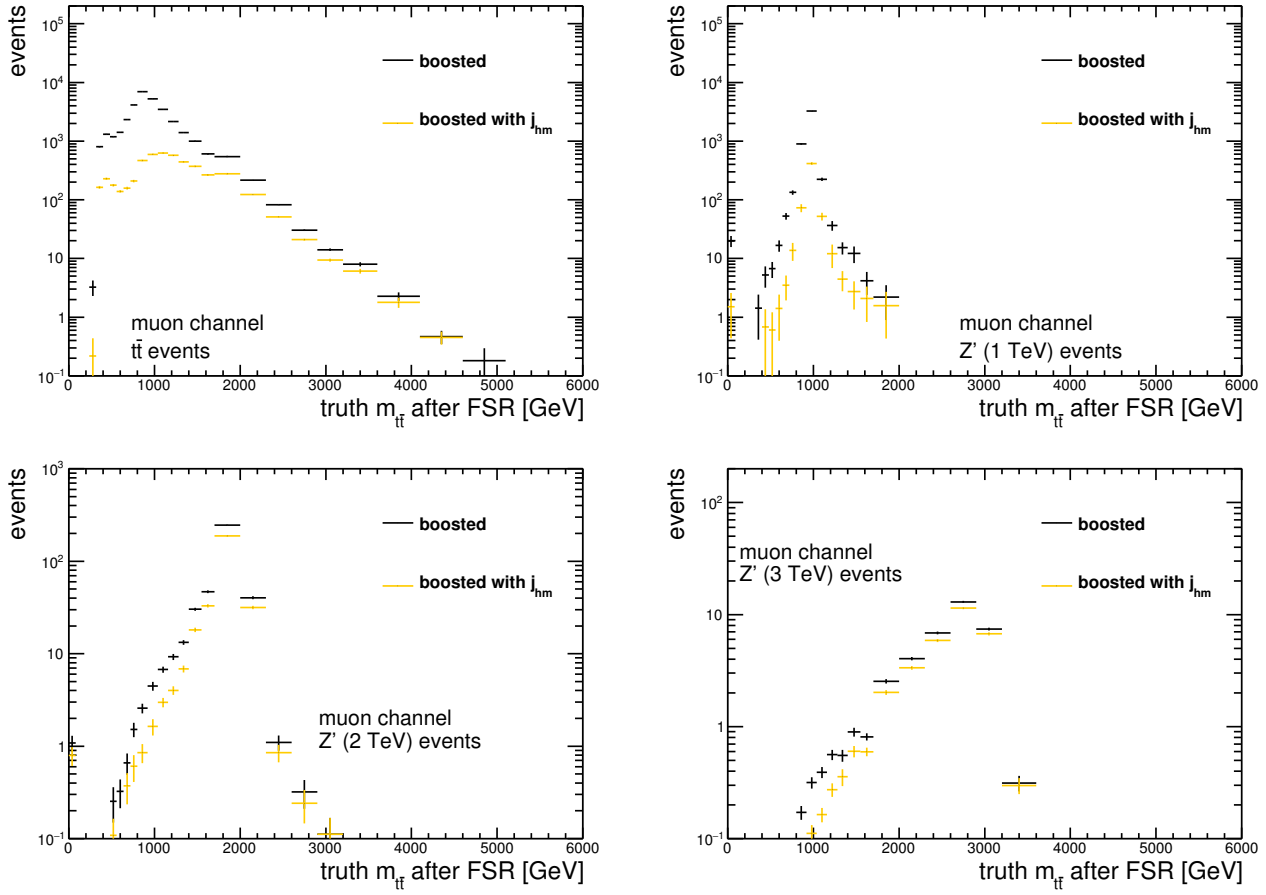


Figure 7.20: Truth $m_{t\bar{t}}$ distribution (after final state radiation) for boosted muon events, and boosted muon events that also meet the very boosted criteria (a small-R jet with mass > 60 GeV). The majority of boosted events from the $m_{Z'} = 2$ TeV and $m_{Z'} = 3$ TeV sample are also very boosted.

Reconstructing very boosted events

For the very boosted events that fail the boosted selection, an alternative reconstruction method is developed. t_{lep} is reconstructed as in the boosted channel, but there is no clear prescription for how to reconstruct t_{had} using j_{hm} (the small-R jet with mass > 60 GeV associated with part or all of the hadronic top quark decay). It is expected that if the W decay is responsible for j_{hm} ⁵, as depicted in Figure 7.15, then an additional small-R jet containing the rest of the t_{had} decay should be in the vicinity. Alternatively, a large-R jet close to j_{hm} may have caught the whole t_{had} decay without being top-tagged, causing the event to fail the boosted selection. To test these hypotheses, the mass of j_{hm} and the mass of

⁵The plots in Figure 7.27 show that there is a range of topologies present in very boosted events, including the W_{had} decay contained inside j_{hm} , the b_{had} decay and part of the W_{had} decay contained inside j_{hm} , as well as the whole t_{had} decay merged inside j_{hm}

the closest large-R jet (if there is one within $\Delta R < 0.8$) are plotted in Figures 7.21 and 7.22 for very boosted events where a) there is another small-R jet within $\Delta R < 2.0$ of j_{hm} and b) there is no other small-R jet in this radius. In the case where there is no other suitable small-R jet, both j_{hm} and the large-R jet mass distributions peak below 100 GeV (and also around m_{top} for the Z' samples); either the whole t_{had} decay is encapsulated by j_{hm} , or the remainder of the decay is not reconstructable with the default small-R or large-R jet algorithm. In the case where there is a suitable small-R jet, the j_{hm} and large-R jet distributions peak below 100 GeV, with another peak in the large-R distribution around m_{top} suggesting that the large-R jet contains j_{hm} and the other t_{had} decay jet in these cases.

The mass distribution of t_{had} when it is reconstructed using (a) j_{hm} only, (b) j_{hm} + small-R jet, and (c) the large-R jet, is shown in Figures 7.23 and 7.24. The high mass tail on the j_{hm} + small-R jet distribution following the m_{top} peak indicates that in some cases it is more appropriate to use j_{hm} or the large-R jet only to reconstruct t_{had} . A hybrid reconstruction method is employed where method (a), (b) or (c) is chosen based on which of the possible options gives a reconstructed t_{had} with mass closest to m_{top} . The resulting t_{had} mass distribution is shown in Figures 7.25 and 7.26. The performance of this reconstruction method is evaluated in Figures 7.28, 7.29, 7.30 and 7.31 through the $m_{t_{\text{had}}}$ resolution and $p_{T,t_{\text{had}}}$ resolution. The $p_{T,t_{\text{had}}}$ resolution is similar for each of the reconstruction methods. Regarding the $m_{t_{\text{had}}}$ resolution: reconstruction methods (a) and (c) give a $m_{t_{\text{had}}}$ resolution peak shifted above zero, as they often don't include the whole t_{had} decay in the reconstruction. Method (b) gives a peak around zero, with a long negative tail due to events where the whole t_{had} decay is contained in j_{hm} , so adding another small-R jet is superfluous. The combined reconstruction method produces a peak around zero, plus a peak above zero which cannot be totally avoided since sometimes there is no suitable small-R jet available and method (a) or (c) must be used even when they do not contain the entire t_{had} decay.

Performance of the very boosted channel

The final $m_{t\bar{t}}$ resolutions for the very boosted, boosted and resolved channels are shown in Figures 7.32 and 7.33. The performance of the very boosted channel is similar to the boosted channel for the Z' samples. It is also similar for the SM $t\bar{t}$ events, except the negative $m_{t\bar{t}}$ resolution tail is more prominent than in the other channels, likely because of events where t_{had} is reconstructed using j_{hm} and the wrong extra small-R jet. This would happen less in the Z' channel when j_{hm} or the large-R jet more frequently catch the whole t_{had} decay and are used for the reconstruction. Another check on the very boosted combined reconstruction method is done by selecting boosted channel events which meet the very boosted criteria and reconstructing them once using the standard boosted method, and once using the very boosted method. Figures 7.34 and 7.35 show that both methods result in a similar $m_{t\bar{t}}$

resolution when applied to the same events.

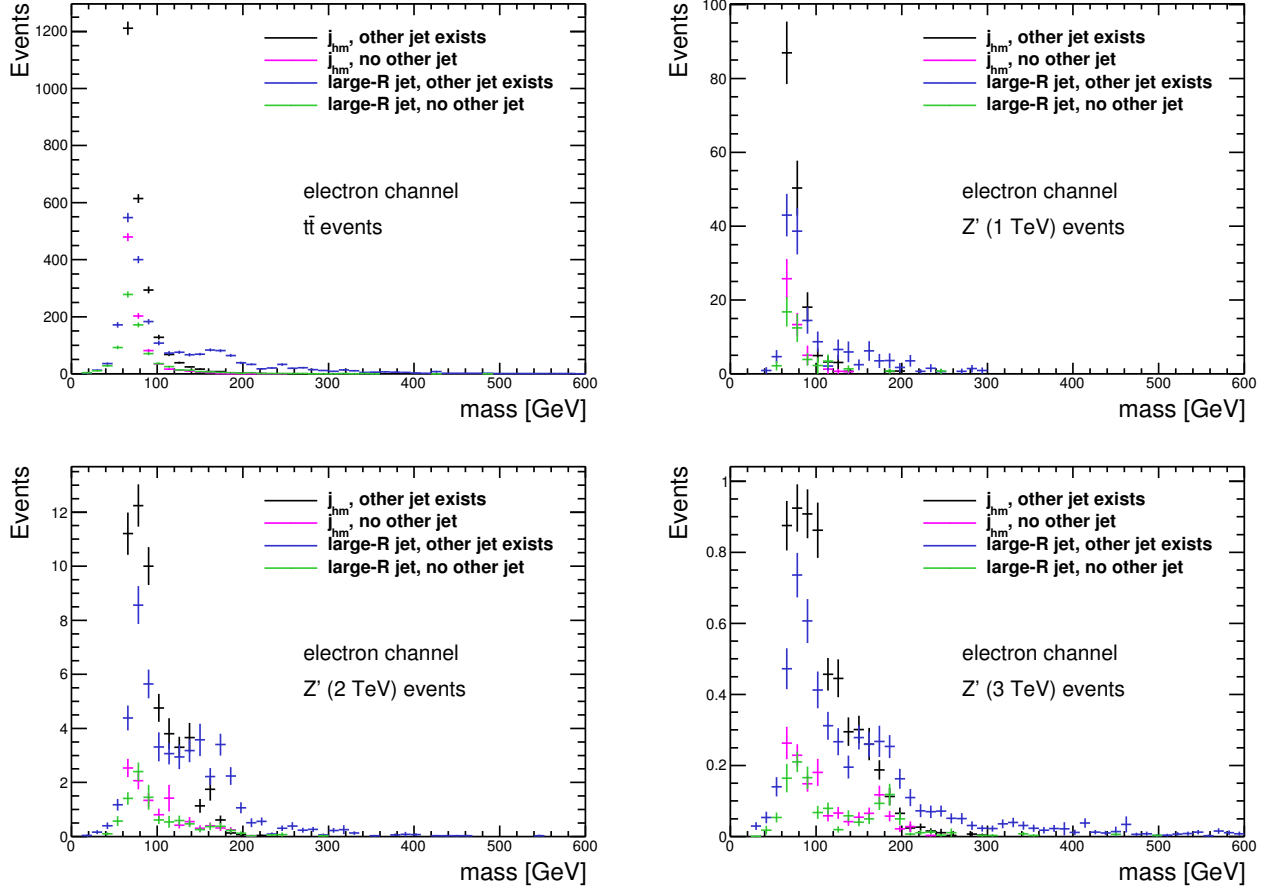


Figure 7.21: These plots show the masses of objects assumed to be part of the hadronic top quark decay: the high mass small-R jet (j_{hm}) and the large-R jet. These objects may be used alone or combined with another object in order to reconstruct t_{had} . The masses of these objects are considered in different scenarios to help understand which combination of objects should be used to reconstruct t_{had} . For example, if the j_{hm} (or the large-R jet) mass distribution peaked around m_{top} when there was no other nearby small-R jet to add to it, and peaked around m_W when there was, this would indicate how to reconstruct t_{had} in each scenario. For $t\bar{t}$ and $Z' = 1, 2, 3$ TeV events, these plots show the masses of j_{hm} and the closest large-R jet (if there is one within $\Delta R < 0.8$) in very boosted events in the case where there exists another small-R jet within $\Delta R < 2.0$ of j_{hm} (in black and blue respectively) and in the case where there is not (in pink and green respectively) (electron channel).

The event selection efficiency for the finalised very boosted channel, along with the boosted and resolved channels, is shown in Figures 7.36 and 7.37. The very boosted channel has a higher selection efficiency than the resolved channel at high truth $m_{t\bar{t}}$ for SM $t\bar{t}$ and Z' samples, as expected. Figures 7.38 and 7.39 show the sensitivity of each channel to a 2 TeV and 3 TeV Z' signal. The very boosted channel is more sensitive to high mass signals than the resolved channel. Figures 7.40 and 7.41 compare the combined channel sensitivity

with and without including the very boosted channel. Including the very boosted channel increases both signal/background and signal/ $\sqrt{\text{background}}$ for high mass Z' signals. It appears to be worth attempting to reconstruct preselected $t\bar{t}$ events that contain a high mass small-R jet, even if they fail the boosted selection, because they are likely to be high p_T $t\bar{t}$ events, and an excess of these events could indicate a high mass Z' signal.

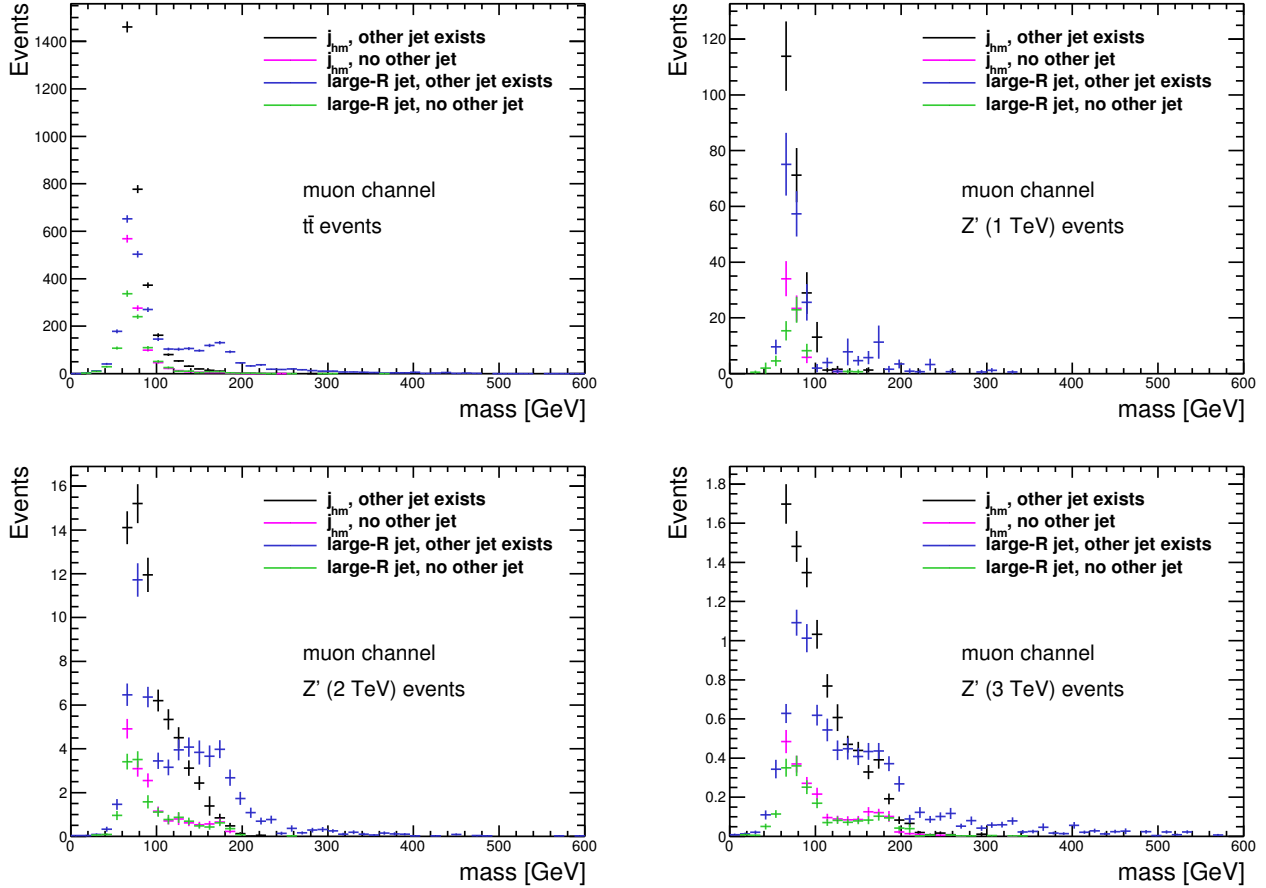


Figure 7.22: These plots show the masses of objects assumed to be part of the hadronic top quark decay: the high mass small-R jet (j_{hm}) and the large-R jet. These objects may be used alone or combined with another object in order to reconstruct t_{had} . The masses of these objects are considered in different scenarios to help understand which combination of objects should be used to reconstruct t_{had} . For example, if the j_{hm} (or the large-R jet) mass distribution peaked around m_{top} when there was no other nearby small-R jet to add to it, and peaked around m_W when there was, this would indicate how to reconstruct t_{had} in each scenario. For $t\bar{t}$ and $Z' = 1, 2, 3$ TeV events, these plots show the masses of j_{hm} and the closest large-R jet (if there is one within $\Delta R < 0.8$) in very boosted events in the case where there exists another small-R jet within $\Delta R < 2.0$ of j_{hm} (in black and blue respectively) and in the case where there is not (in pink and green respectively) (muon channel).

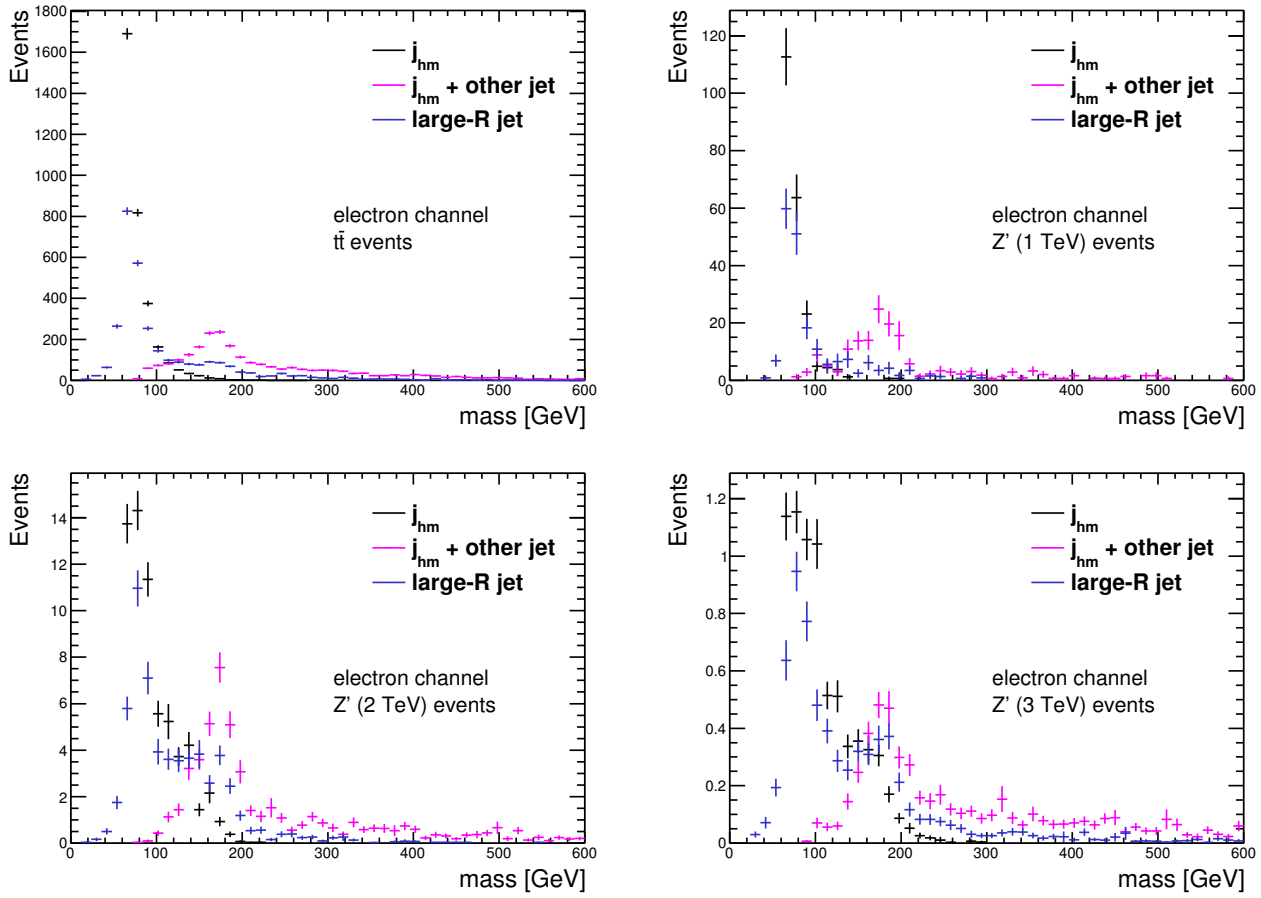


Figure 7.23: Mass distributions of j_{hm} , j_{hm} plus nearby small-R jet and large-R jet (electron channel). There is a peak in the mass distribution of the $j_{hm} + \text{other small-R jet}$ system around m_{top} as well as a long high mass tail indicating that the small-R jet need not always be added, and sometimes j_{hm} or the large-R jet should be used to reconstruct t_{had} instead.

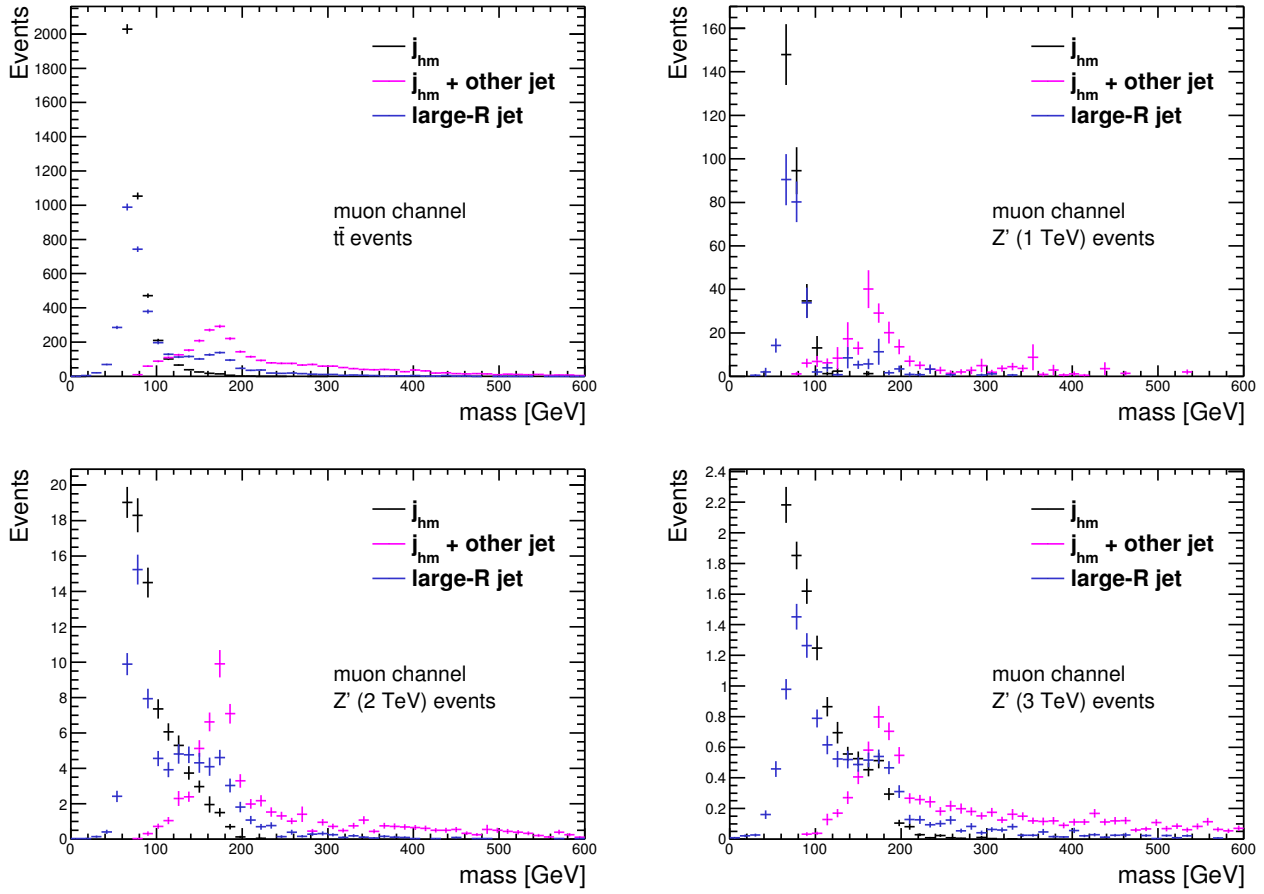
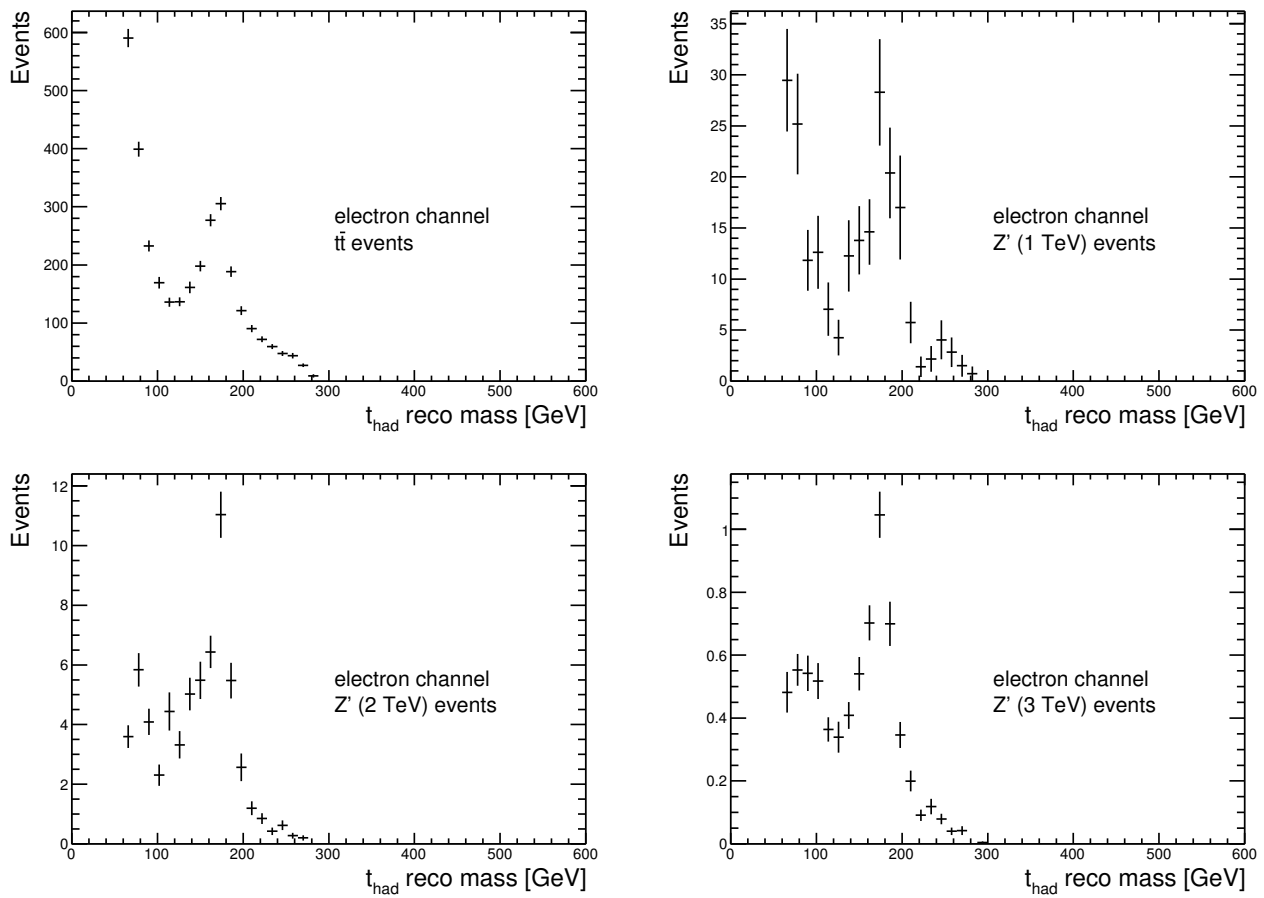
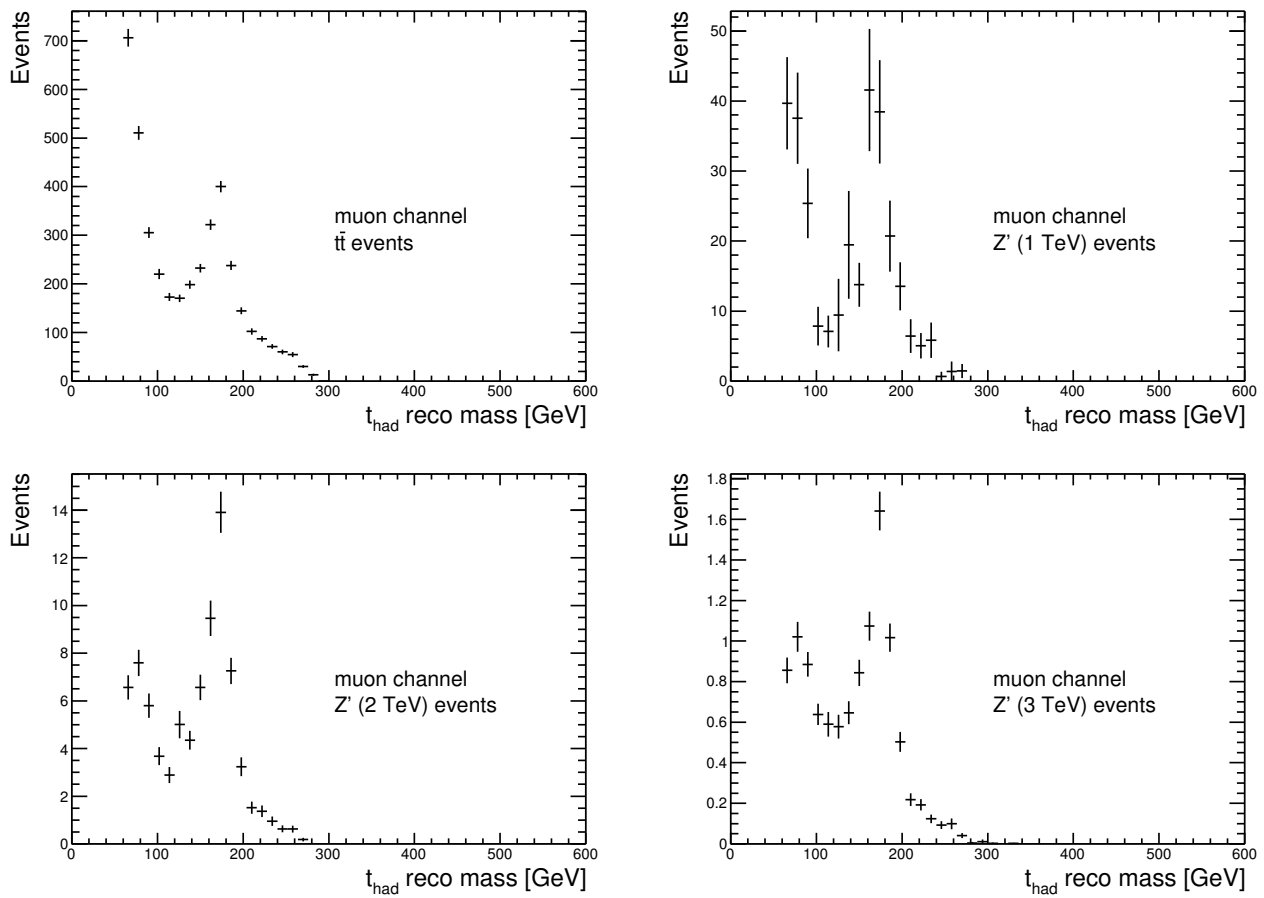


Figure 7.24: Mass distributions of j_{hm} , j_{hm} plus nearby small-R jet and large-R jet (muon channel). There is a peak in the mass distribution of the $j_{hm} + \text{other small-R jet}$ system around m_{top} as well as a long high mass tail indicating that the small-R jet need not always be added, and sometimes j_{hm} or the large-R jet should be used to reconstruct t_{had} instead.

Figure 7.25: Mass distributions of the reconstructed t_{had} in the very boosted electron channel.

Figure 7.26: Mass distributions of the reconstructed t_{had} in the very boosted muon channel.

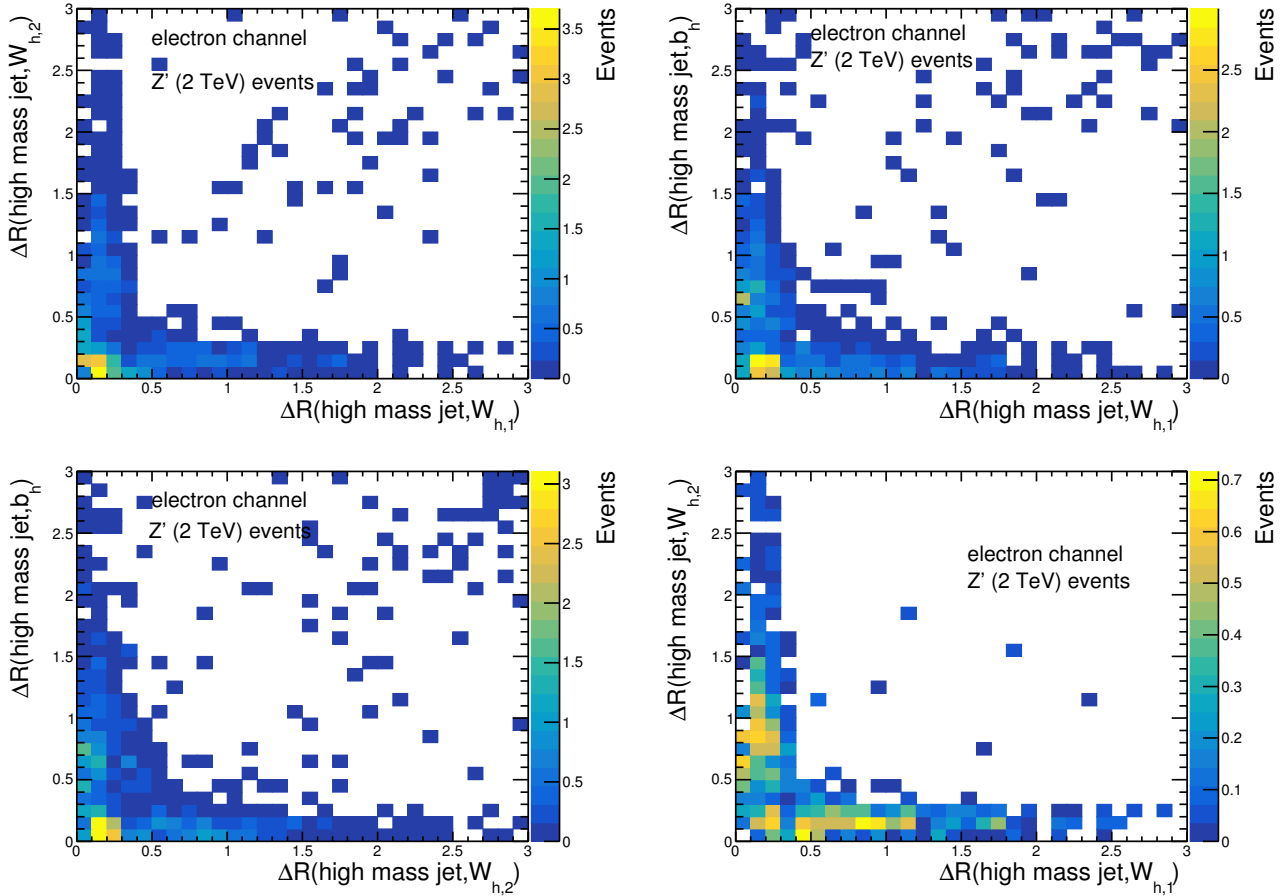


Figure 7.27: These plots explore the topology of very boosted events selected from a Z' at 2 TeV sample. They show the ΔR separation between j_{hm} and the truth-level quantities: the b quark decaying from t_{had} (b_h) and the two quarks decaying from W_{had} ($W_{1,h}$ and $W_{2,h}$). The top left hand side plot shows that many very boosted events do have the whole W_{had} decay inside j_{hm} . The top right and bottom left plots show that there are also events where the b_{had} decay and at least part of the W_{had} decay fall inside j_{hm} . The bottom right plot shows $\Delta R(W_{1,h}, W_{2,h})$ for events where $\Delta R(j_{hm}, b_h) < 0.4$, suggesting that sometimes j_{hm} contains the entire top quark decay.

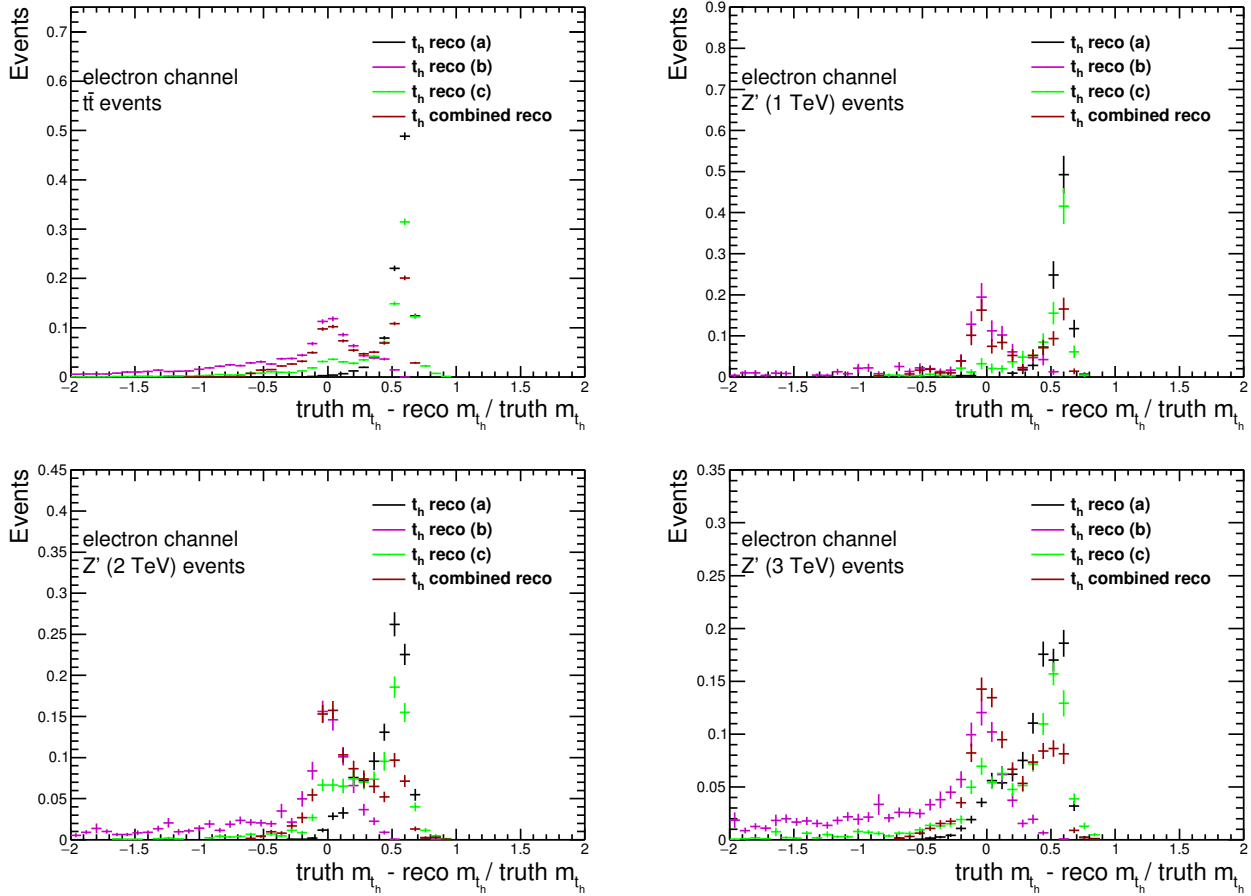


Figure 7.28: t_{had} mass resolution for reconstruction methods (a) j_{hm} , (b) j_{hm} +small-R jet, and (c) large-R jet, and the final hybrid reconstruction method (electron channel).

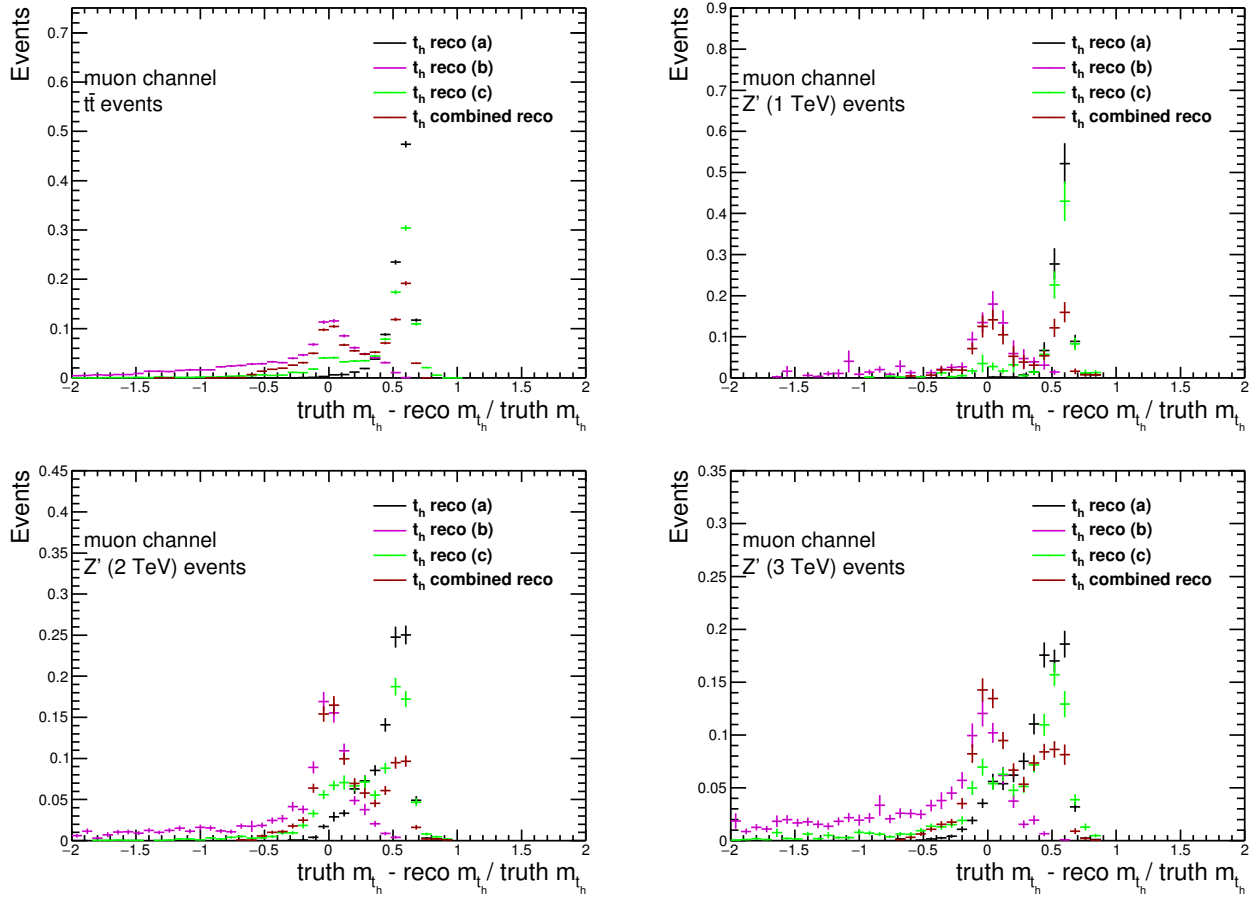


Figure 7.29: t_{had} mass resolution for reconstruction methods (a) j_{hm} , (b) $j_{\text{hm}} + \text{small-R jet}$, and (c) large-R jet, and the final hybrid reconstruction method (muon channel).

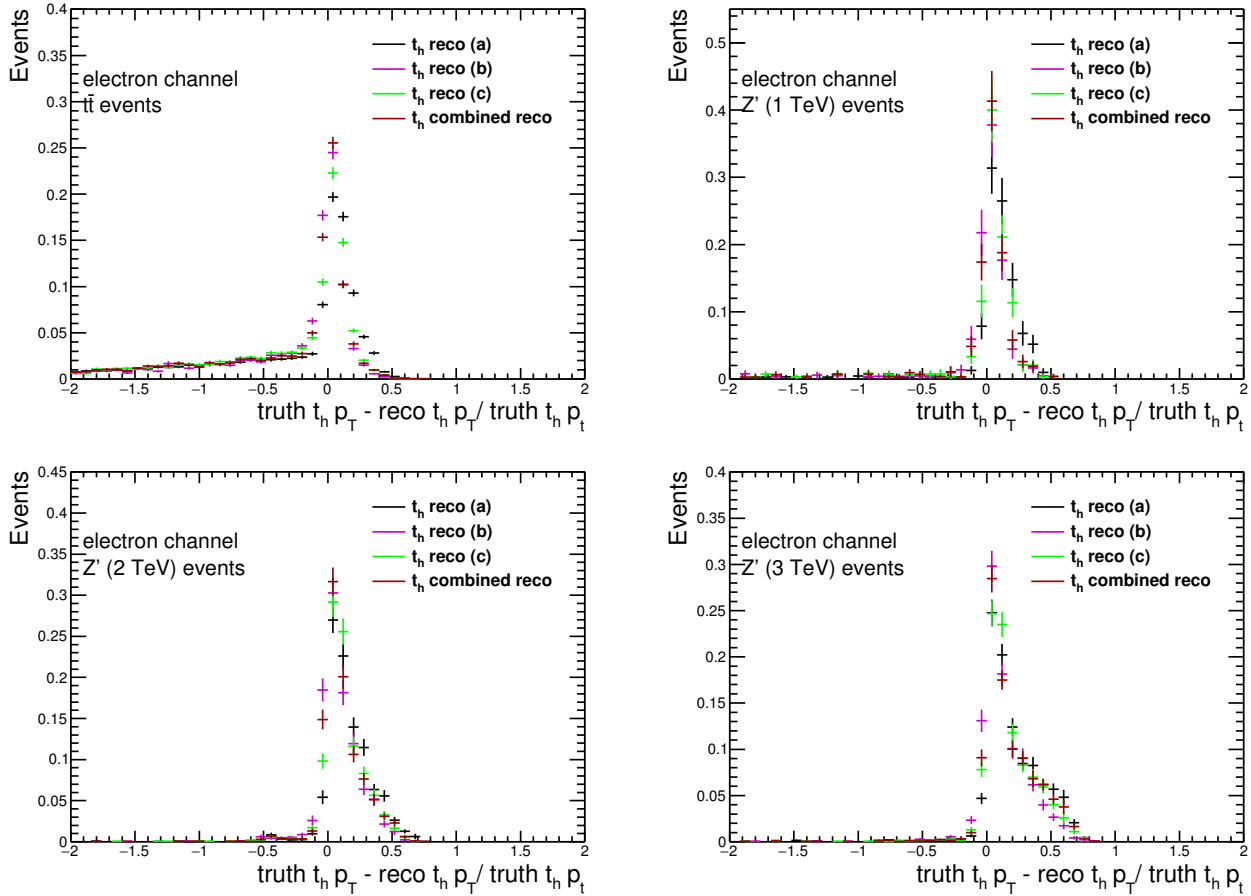


Figure 7.30: $t_{\text{had}} p_T$ resolution for reconstruction methods (a) j_{hm} , (b) j_{hm} +small-R jet, and (c) large-R jet, and the final hybrid reconstruction method (electron channel).

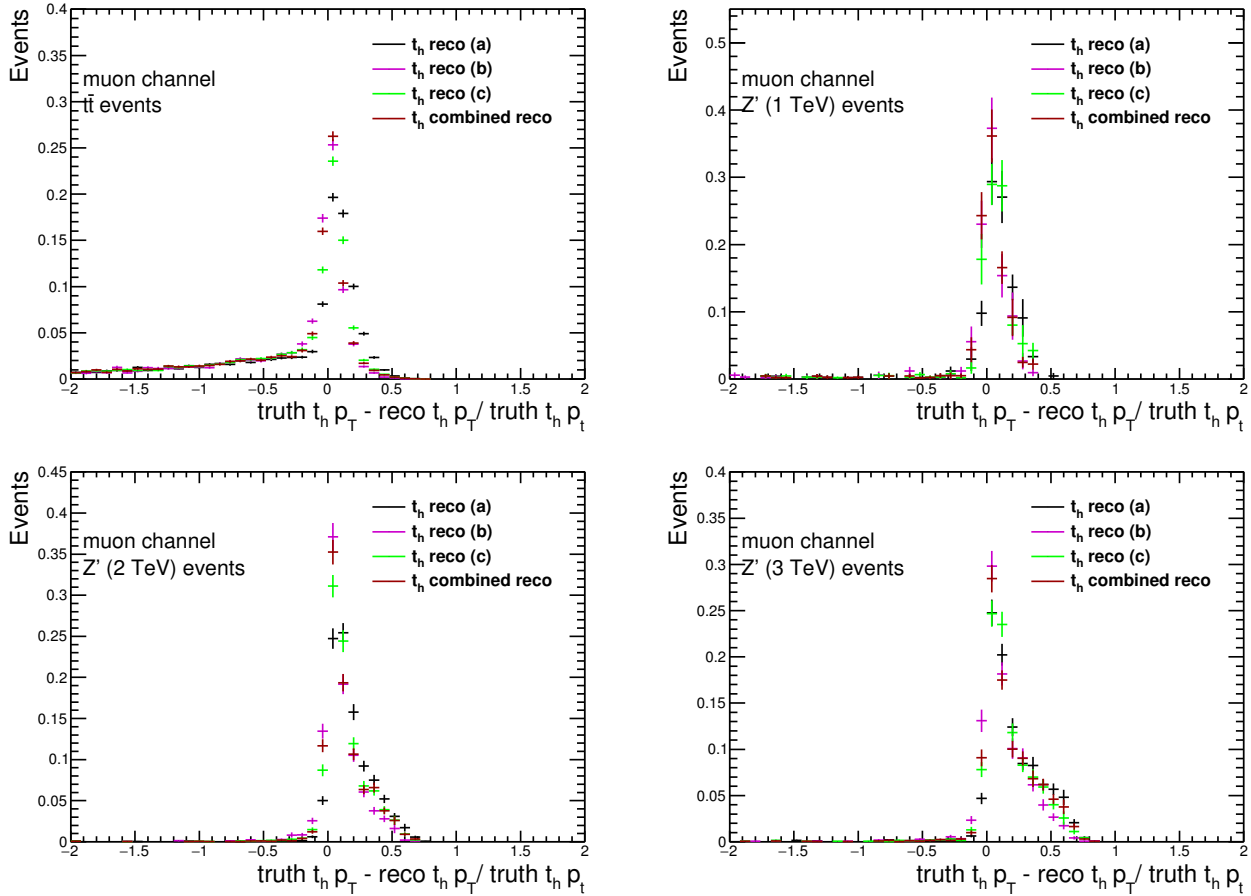


Figure 7.31: $t_{\text{had}} p_T$ resolution for reconstruction methods (a) j_{hm} , (b) $j_{\text{hm}} + \text{small-R jet}$, and (c) large-R jet, and the final hybrid reconstruction method (muon channel).

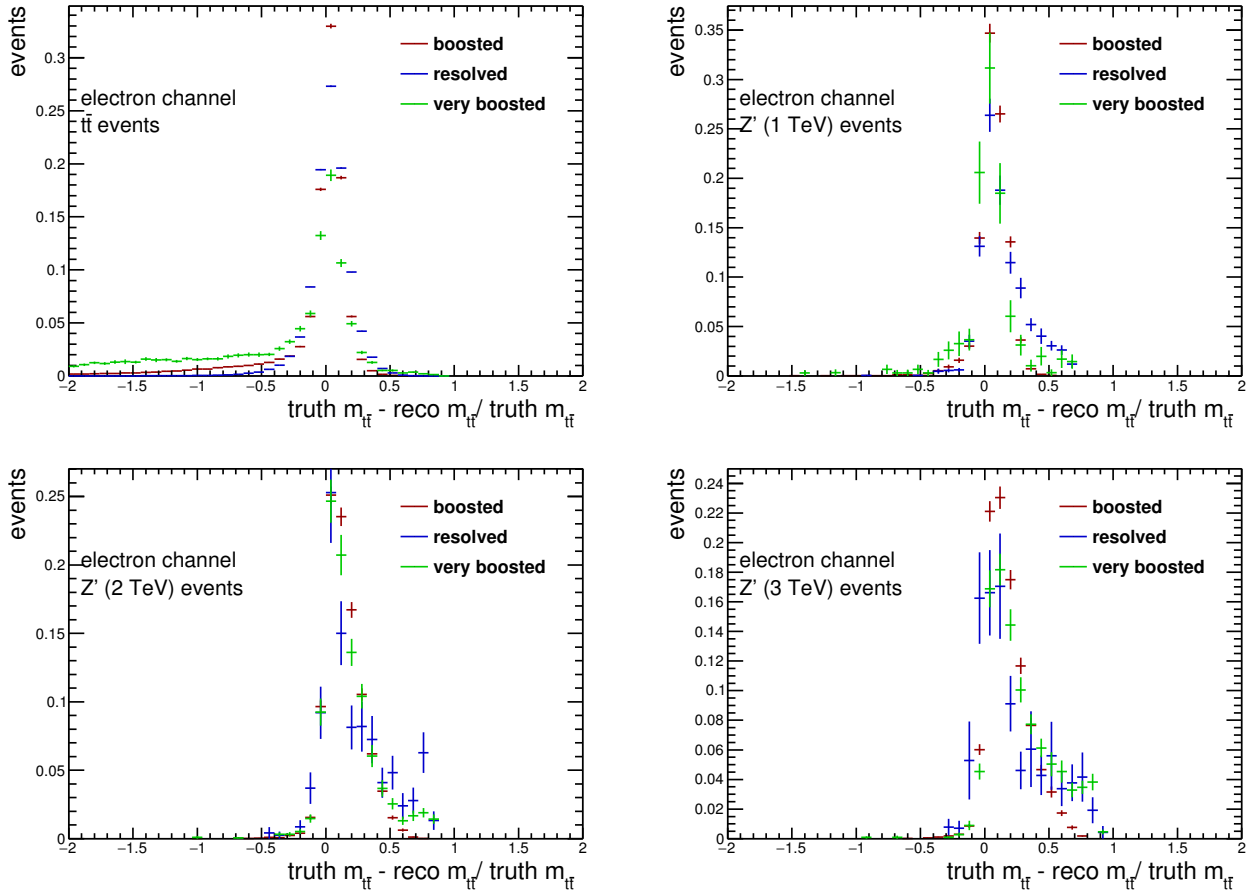


Figure 7.32: $m_{t\bar{t}}$ resolution in the very boosted electron, boosted electron and resolved electron channels.

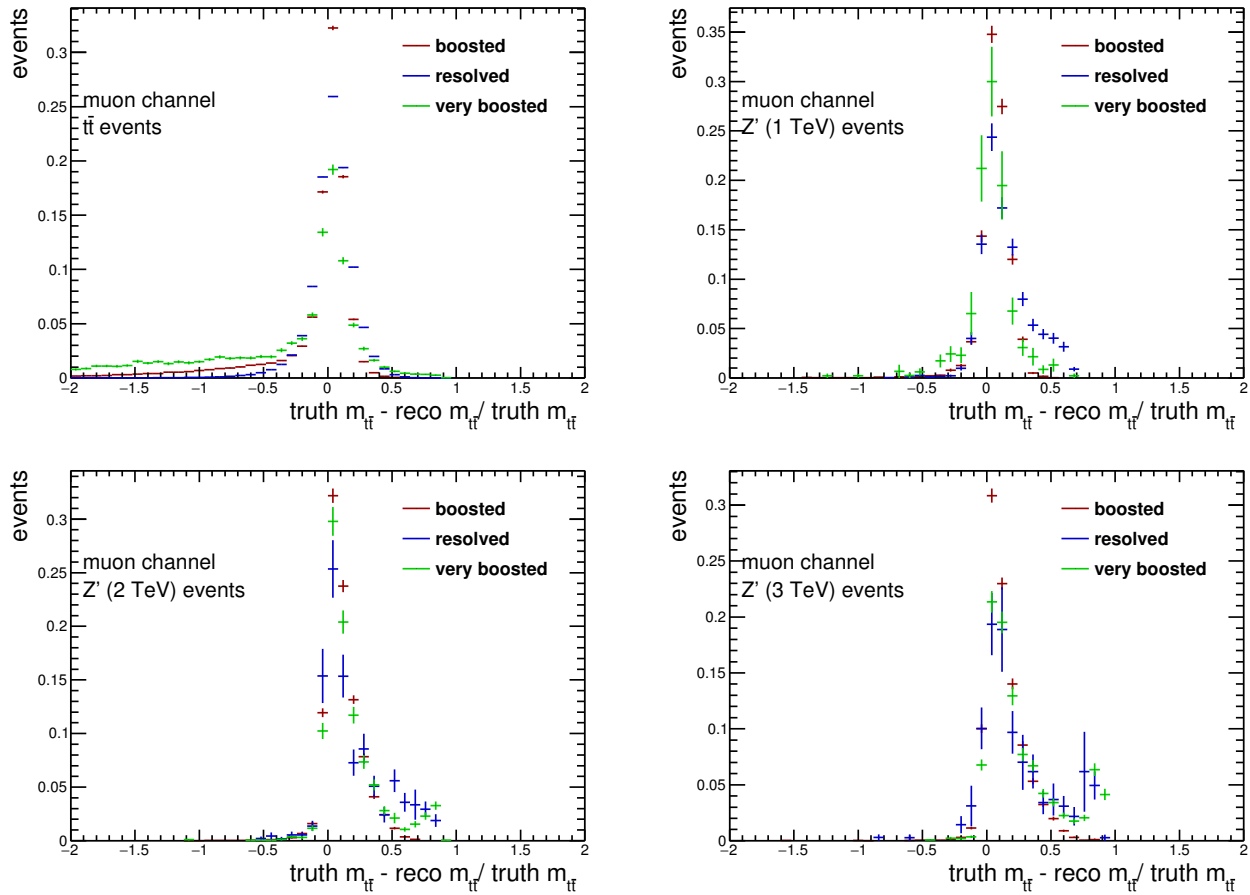


Figure 7.33: $m_{t\bar{t}}$ resolution in the very boosted muon, boosted muon and resolved muon channels.

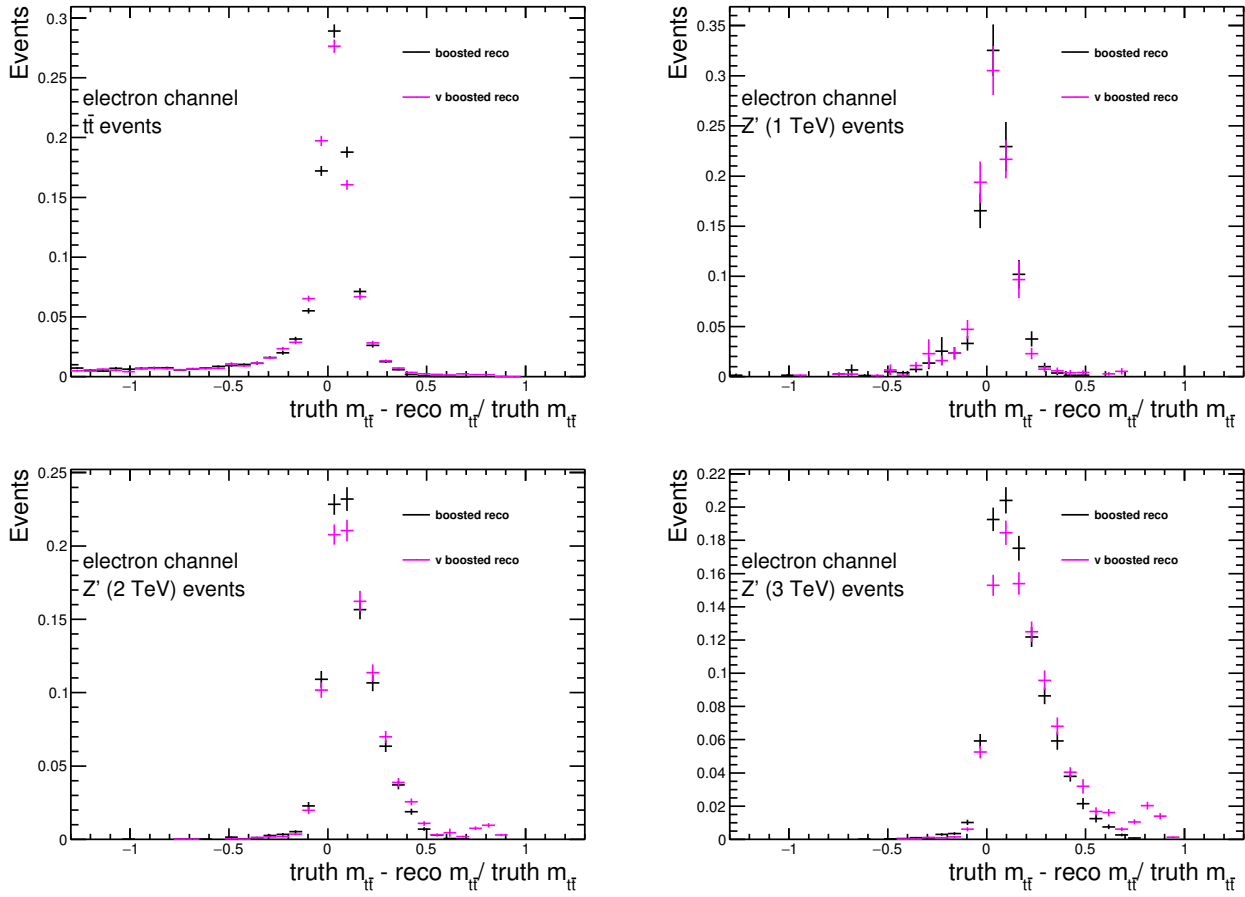


Figure 7.34: $m_{t\bar{t}}$ resolution in the boosted electron channel for boosted events that also meet the very boosted criteria, using the standard boosted $m_{t\bar{t}}$ reconstruction method and the reconstruction method used in the very boosted channel.

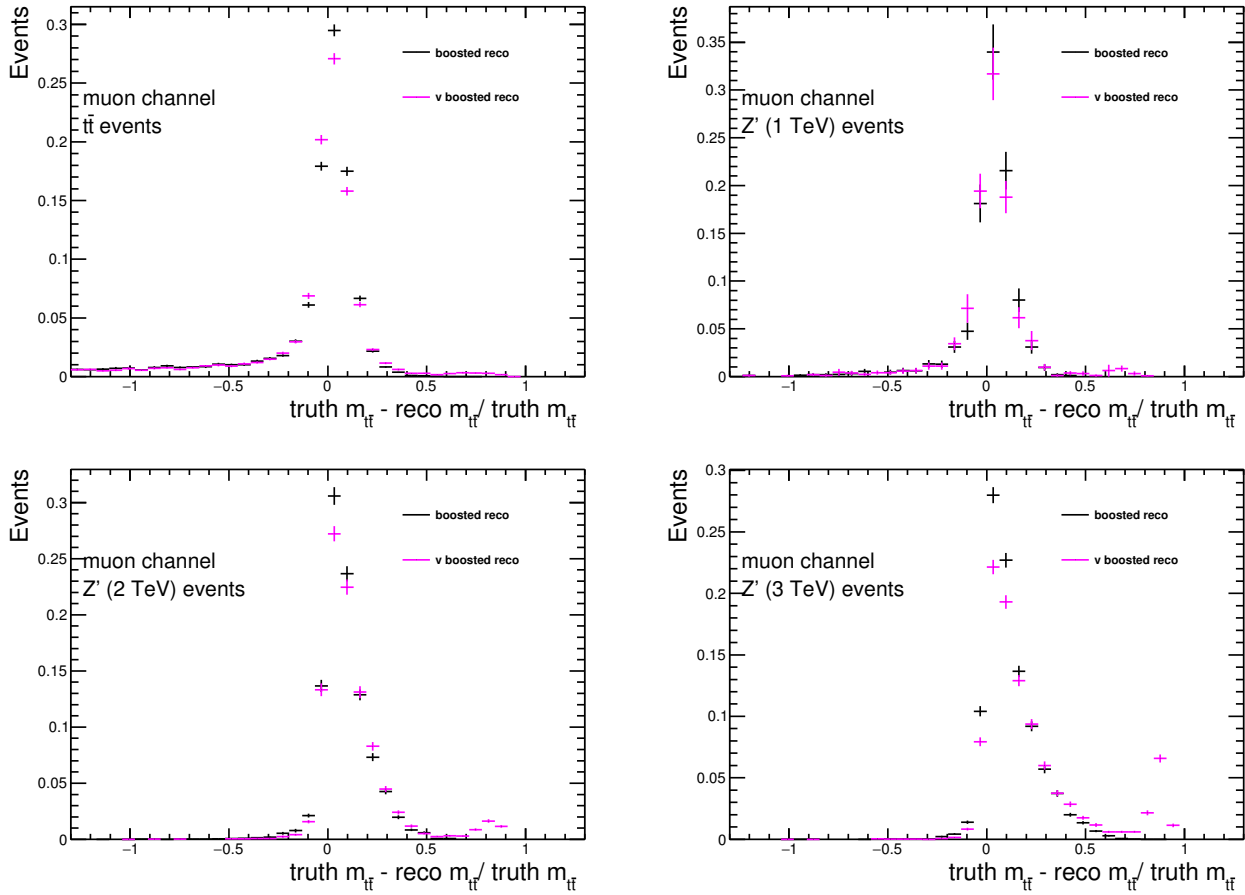


Figure 7.35: $m_{t\bar{t}}$ resolution in the boosted muon channel for boosted events that also meet the very boosted criteria, using the standard boosted $m_{t\bar{t}}$ reconstruction method and the reconstruction method used in the very boosted channel.

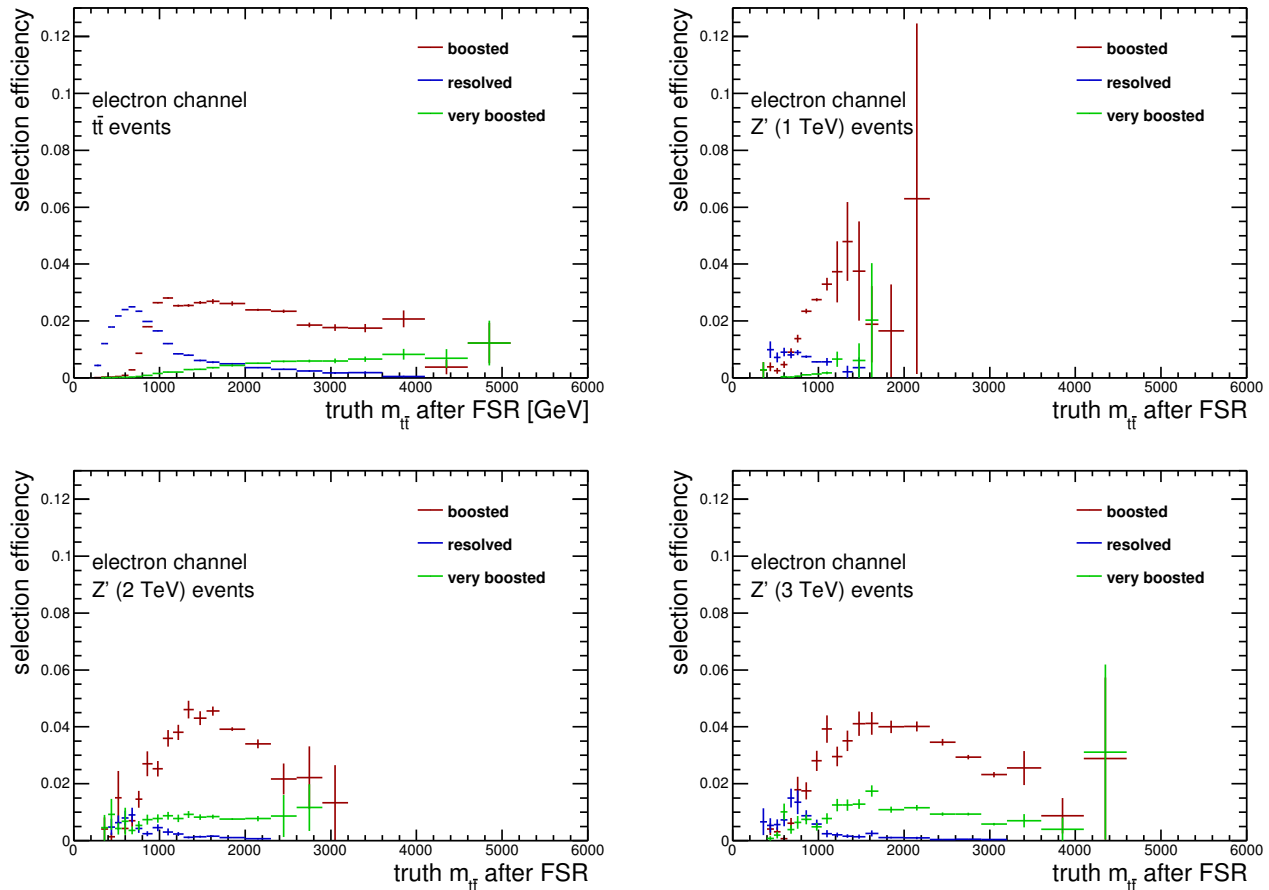


Figure 7.36: Event selection efficiency of the very boosted electron, boosted electron and resolved electron channels.

7.3.3 Semi-boosted events

This channel targets events in the $m_{t\bar{t}}$ range where the selection efficiency of the resolved channel begins to decrease and the selection efficiency of the boosted channel begins to increase - around 700 GeV to 1100 GeV. Preselected⁶ events that do not pass the boosted, resolved or very boosted channels are examined to see if many of them possess a semi-boosted decay topology. This is when a large-R jet contains part of the hadronic top decay with the remainder being detected in a small-R jet, as depicted in Figure 7.16. Events with this topology may fail the boosted selection due to the large-R jet failing the top-tagging requirements. If a preselected event contains a large-R jet that satisfies the kinematic criteria $p_T > 250$ GeV, $|\eta| > 2.0$, mass > 65 GeV and the topological criteria $\Delta R(\text{large-R jet}, j_{sel}) > 1.5$, $\Delta\phi(\text{large-R jet}, \ell) > 2.3$, then it is a candidate for the semi-boosted channel

⁶Events which pass the standard preselection described in section 6.5.1, plus have at least two small-R jets and one small-R jet with $\Delta R(\text{lepton}, \text{jet}) < 1.5$.

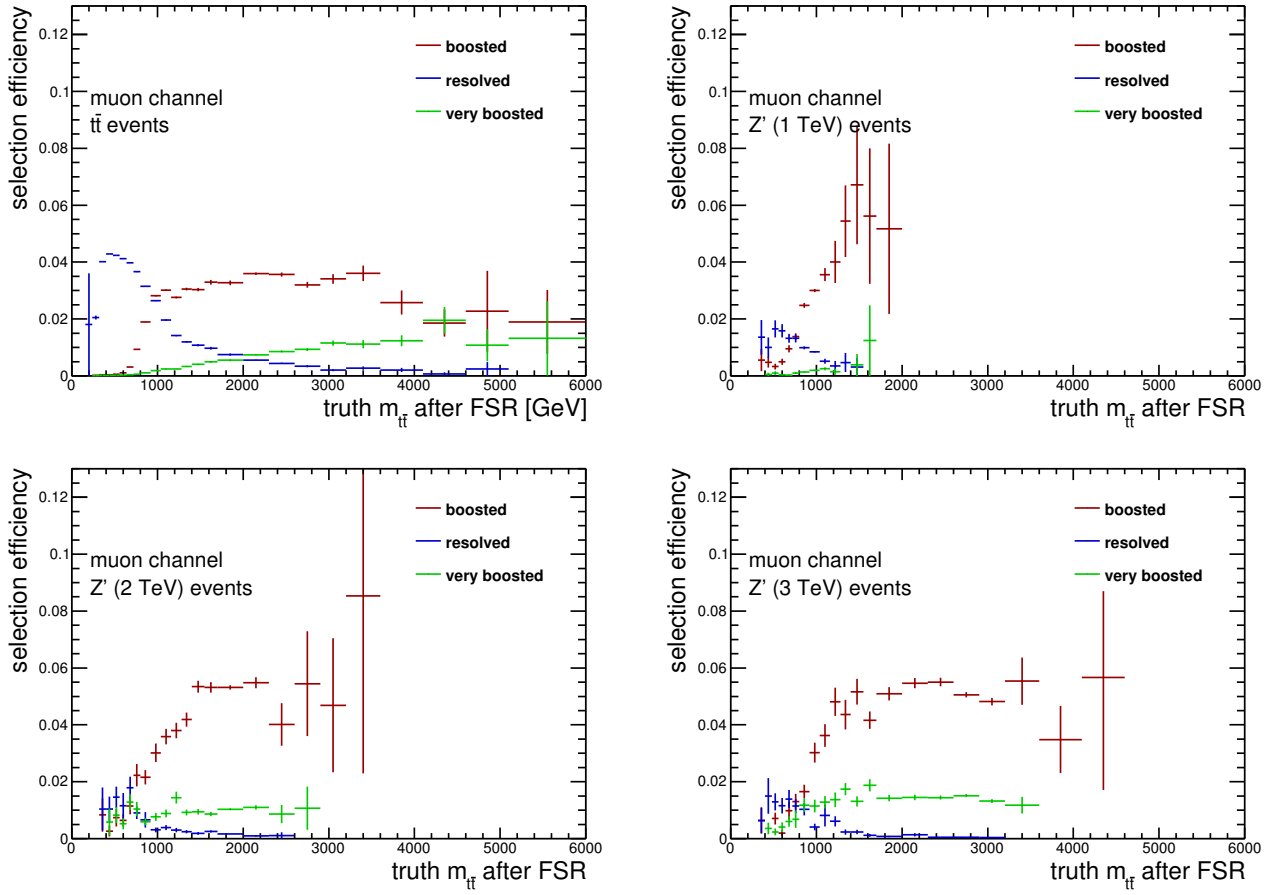


Figure 7.37: Event selection efficiency of the very boosted electron, boosted electron and resolved muon channels.

(provided it has not been accepted into any of the other three channels). This selection essentially comprises a looser boosted channel; large-R jet mass and τ_{32} (defined in section 4.6) distributions are compared for boosted events and semi-boosted candidate events in Figure 7.42 to determine why the semi-boosted candidates do not make it into the complete boosted channel. While the boosted large-R jet 2D (mass, τ_{32}) distribution has two peaks, one at $\sim m_W$ and high τ_{32} , corresponding to a partial top decay, and one at $\sim m_{top}$ and low τ_{32} , corresponding to a full top decay, the semi-boosted candidate distribution only has the former peak. The spread in mass of the high τ_{32} peak (60-150 GeV) indicates that the two-jet substructure of the large-R jet is not necessarily always due to the W boson decay. Further decay topology investigations support the hypothesis that the candidate events exhibit a semi-boosted topology where the large-R jets contain a mixture of W boson decays, and partial W boson plus b -jet decays.

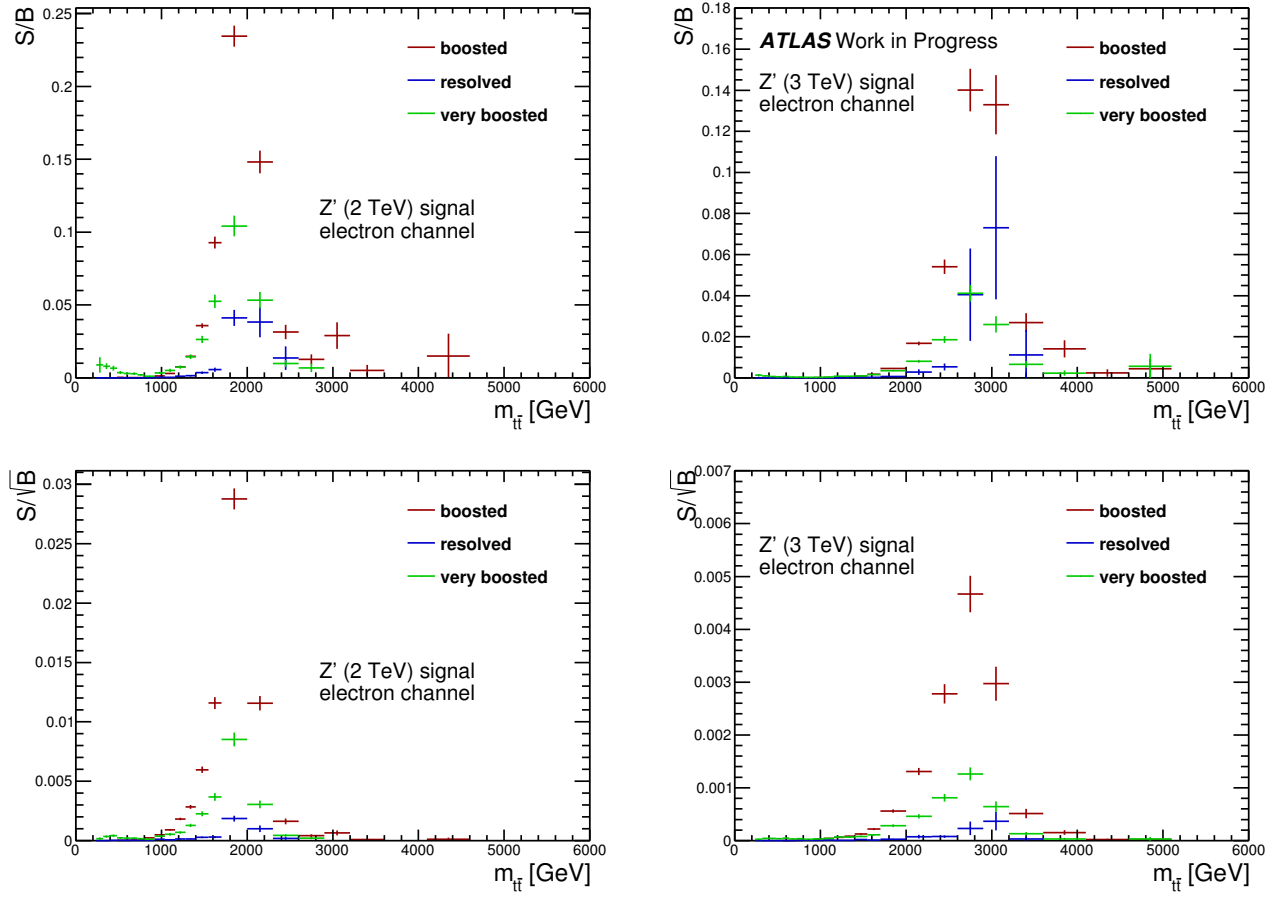


Figure 7.38: Signal sensitivity (signal/background and signal/ $\sqrt{\text{background}}$) in the electron channels.

Reconstructing semi-boosted events

The reconstruction of t_{had} is done by summing the four-momenta of the large-R jet and a suitable nearby small-R jet likely to contain the rest of the t_{had} decay. The small-R jet must be within $\Delta R \in (1.1, 2.3)$ of the large-R jet, and have $\Delta R(\text{small-R jet}, j_{\text{sel}}) > 1.0$. Often there is more than one suitable small-R jet. First, truth-level information is used to select the “correct” small-R jet - the one that is $\Delta R < 0.4$ from the parton that is the furthest in ΔR from the large-R jet - and if it exists it is added to the large-R jet. The resulting reconstructed $m_{t_{\text{had}}}$ distribution is shown in Figure 7.43. Although this reconstruction method yields a clear $m_{t_{\text{top}}}$ peak, the correct small-R jet is only found in a minority of events; extracting reconstruction-level information about these jets and using it to create a selection for the suitable small-R jet would be inefficient. Therefore, to perform the t_{had} reconstruction, the suitable small-R jet that brings $m_{t_{\text{had}}}$ mass closest to $m_{t_{\text{top}}}$ is selected. Finally, a mass cut $m_{t_{\text{had}}} \in (140, 190)$ GeV is applied to suppress events where an incorrect or superfluous small-R jet has been added; this would degrade the $m_{t\bar{t}}$ resolution if the event was $t\bar{t}$, and is also a

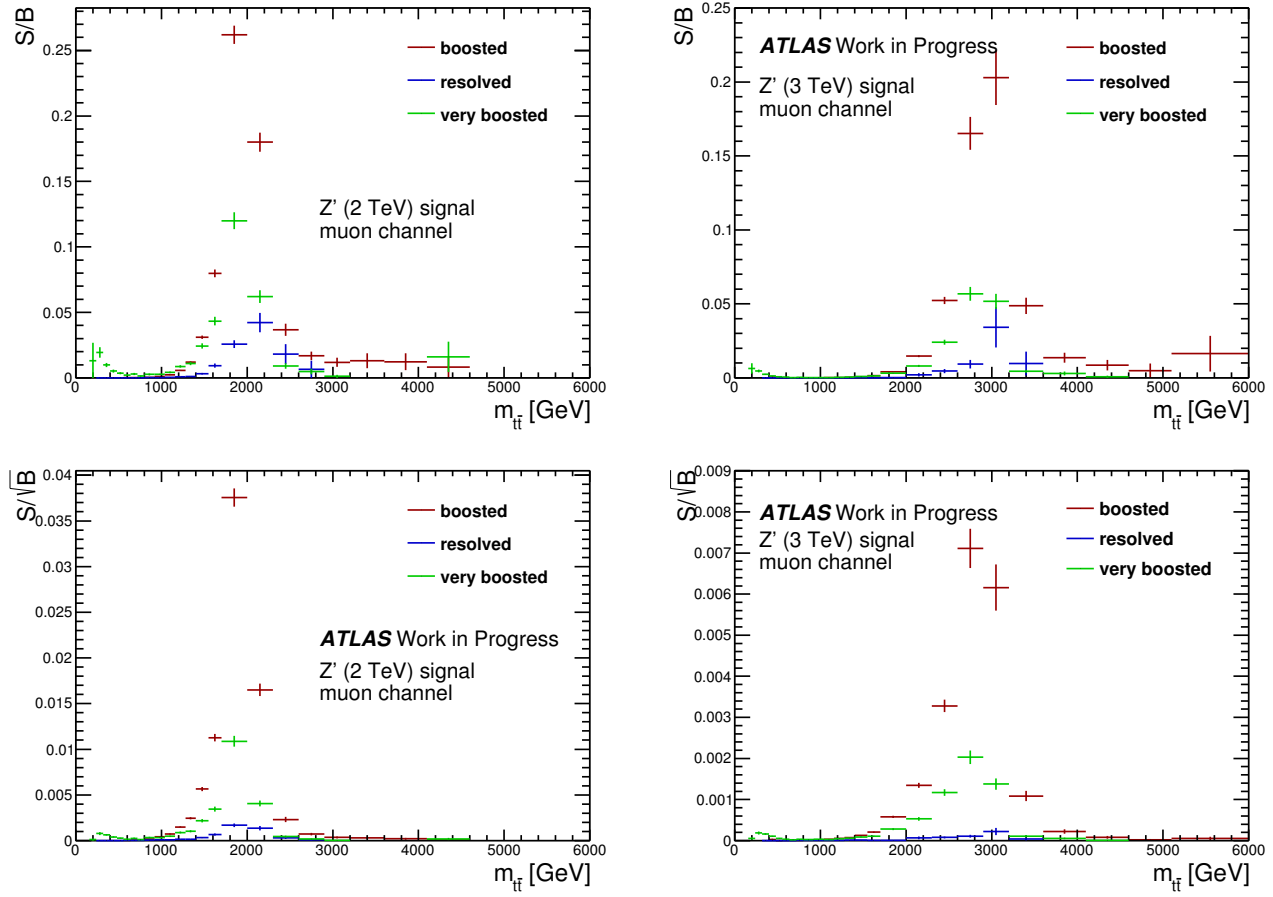


Figure 7.39: Signal sensitivity (signal/background and signal/ $\sqrt{\text{background}}$) in the muon channels.

feature of the W +jets background which is the most likely to contaminate the semi-boosted channel. The resulting $m_{t_{\text{had}}}$ distributions before and after the mass cut are also shown in Figure 7.43. Candidate events that pass the $m_{t_{\text{had}}}$ cut comprise the finalised semi-boosted channel.

Performance of the semi-boosted channel

The performance of the $m_{t_{\text{had}}}$ reconstruction method is evaluated in Figures 7.44 and 7.45 through $m_{t_{\text{had}}}$ and $p_{T,t_{\text{had}}}$ resolutions. While the mass resolution is narrow and centred on zero (which is expected given the reconstruction method), the p_T resolution demonstrates that a significant number of $t\bar{t}$ events have been reconstructed poorly, specifically the selected small-R jet should not have been added. The $m_{t\bar{t}}$ resolution is shown for each channel in Figure 7.46; the resolution in the semi-boosted channel is poorer than in the other channels due to the t_{had} reconstruction. The truth $m_{t\bar{t}}$ distributions and selection efficiencies for each channel are shown in Figures 7.47 and 7.48. The semi-boosted channel has a truth $m_{t\bar{t}}$ and selection

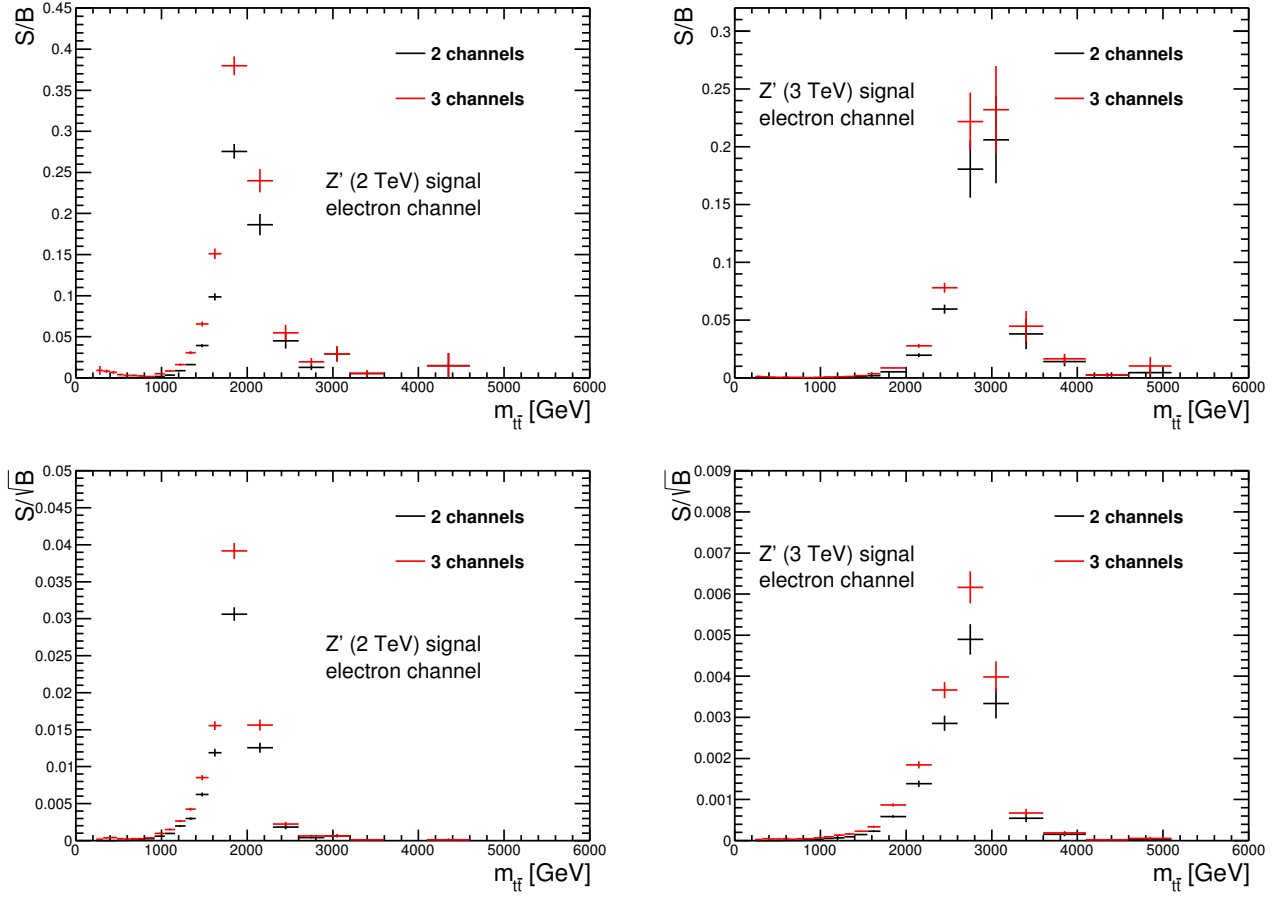


Figure 7.40: Comparing electron channel signal sensitivity (signal/background and signal/ $\sqrt{\text{background}}$) with (3 channels) and without (2 channels) including the very boosted channel.

efficiency peak between that of resolved and boosted $m_{t\bar{t}}$ and selection efficiency peaks, as expected. Figures 7.49 and 7.50 show the signal sensitivity of each channel; it can be seen that the semi-boosted channel is most sensitive to the lowest mass Z' signal: 1 TeV. Including the semi-boosted channel in the analysis improves the overall sensitivity (Figures 7.51 and 7.52) with the biggest improvement in the 1 TeV Z' signal sensitivity. There clearly exists a mid-mass range decay topology that does not fit either of the established topology channels and whose inclusion improves sensitivity to signals ~ 1 TeV, but this channel would probably benefit from training a classification algorithm that can consider multiple variables on semi-boosted signal and background events to define a selection criteria that better distinguishes $t\bar{t}$ events from the W +jets background, and to find the best reconstruction procedure.

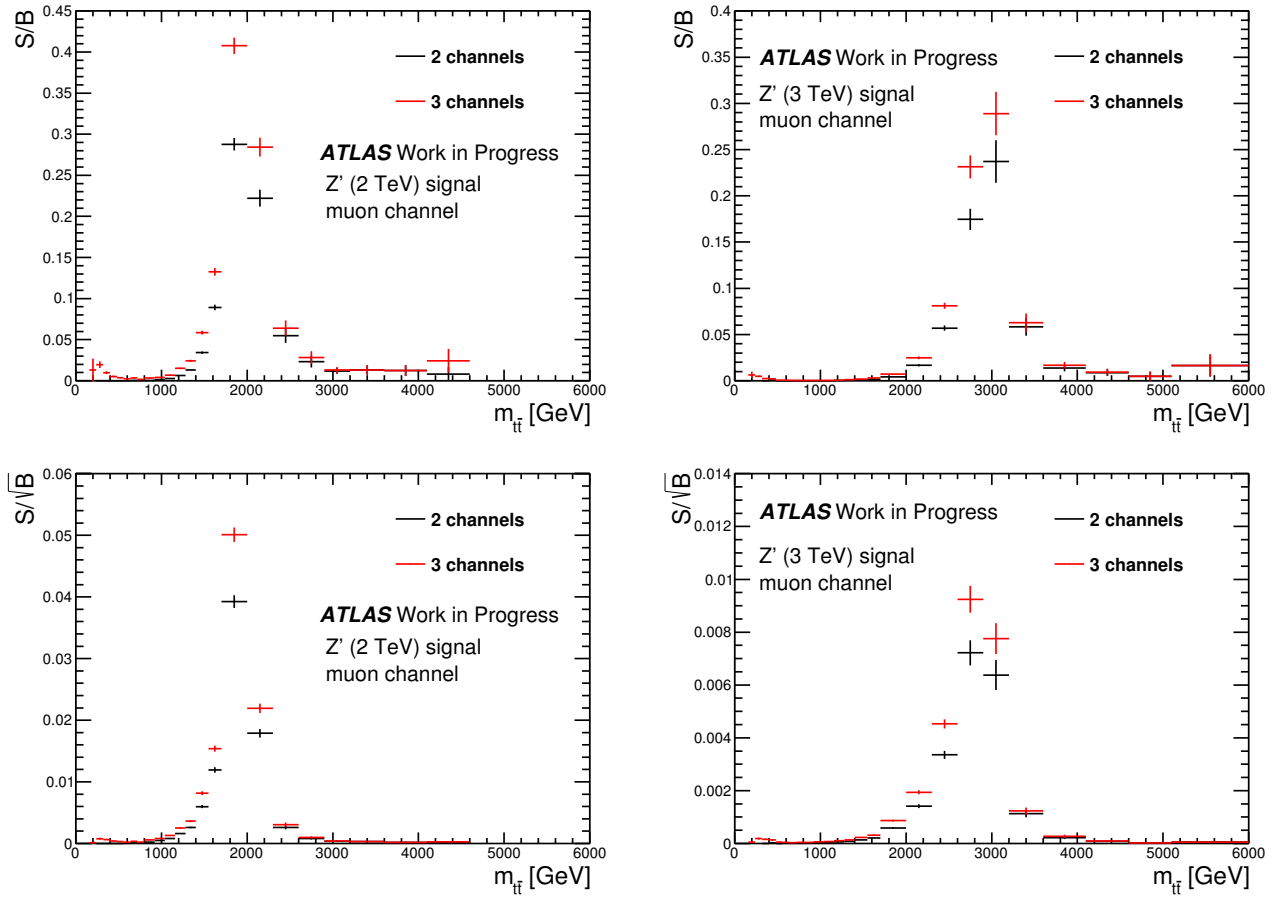


Figure 7.41: Comparing muon channel signal sensitivity (signal/background and signal/ $\sqrt{\text{background}}$) with (3 channels) and without (2 channels) including the very boosted channel.

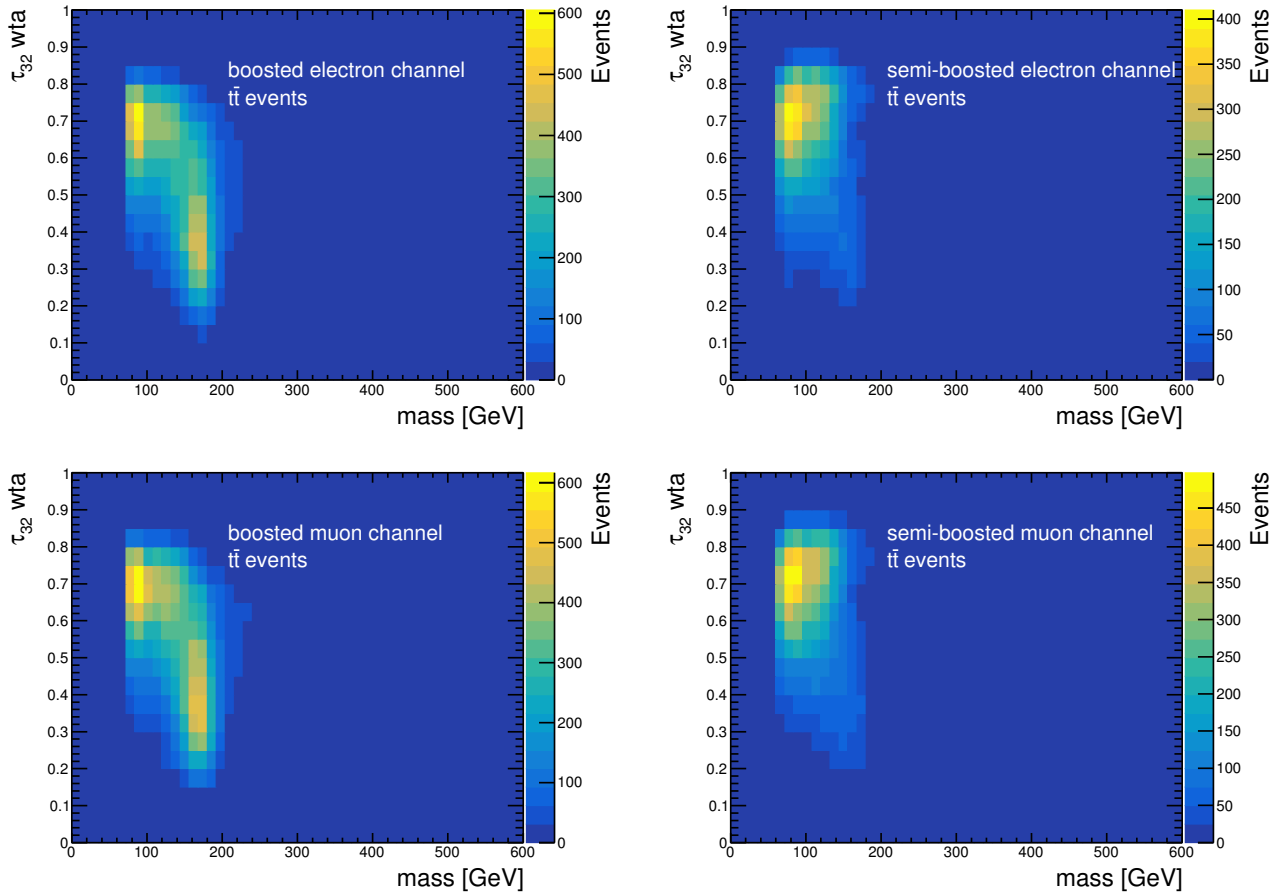


Figure 7.42: Large-R jet mass plotted against τ_{32} (defined in section 4.6) in the boosted and in events that pass the semi-boosted preselection.

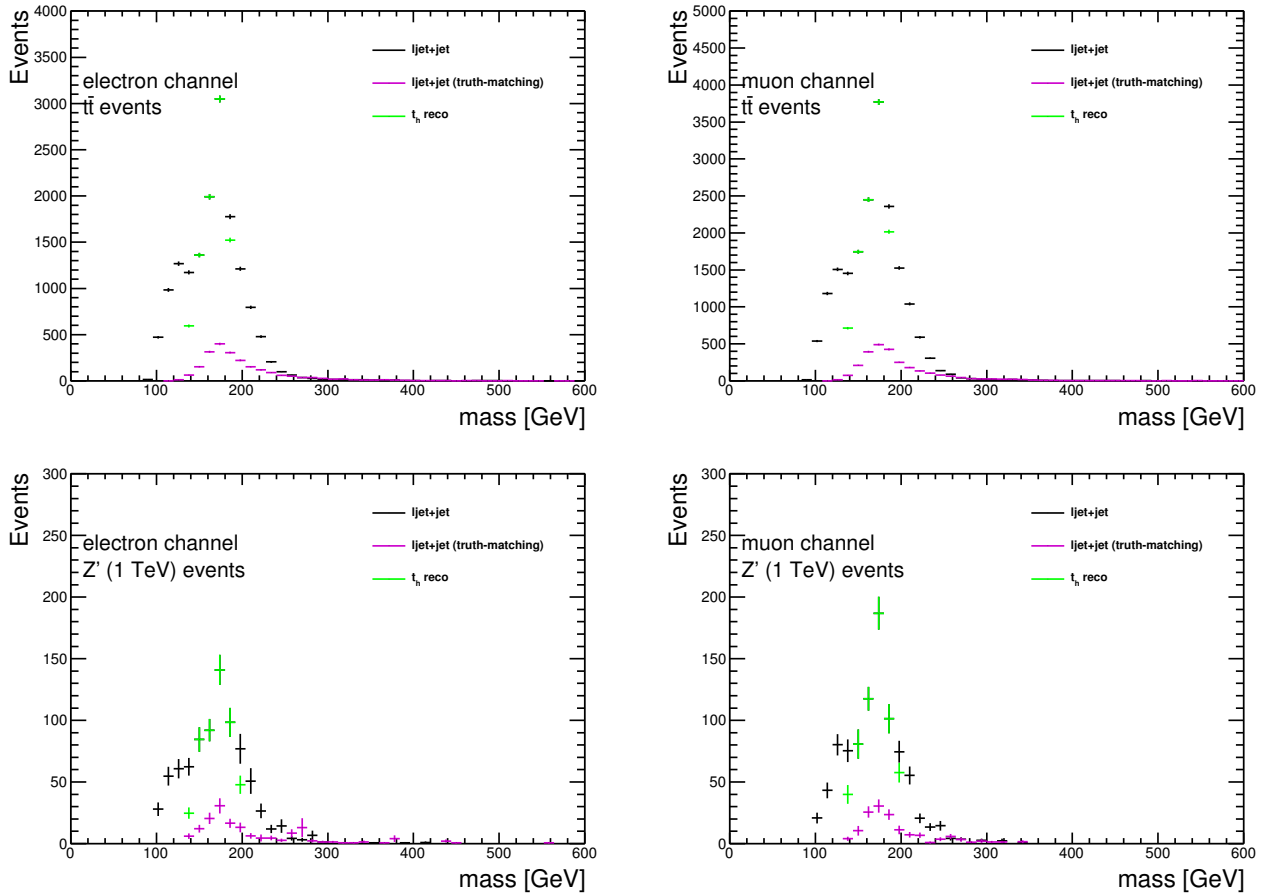


Figure 7.43: Reconstructing t_{had} in the semi-boostered electron channel and semi-boostered muon channel, for SM $t\bar{t}$ events, and for 1 TeV Z' events.

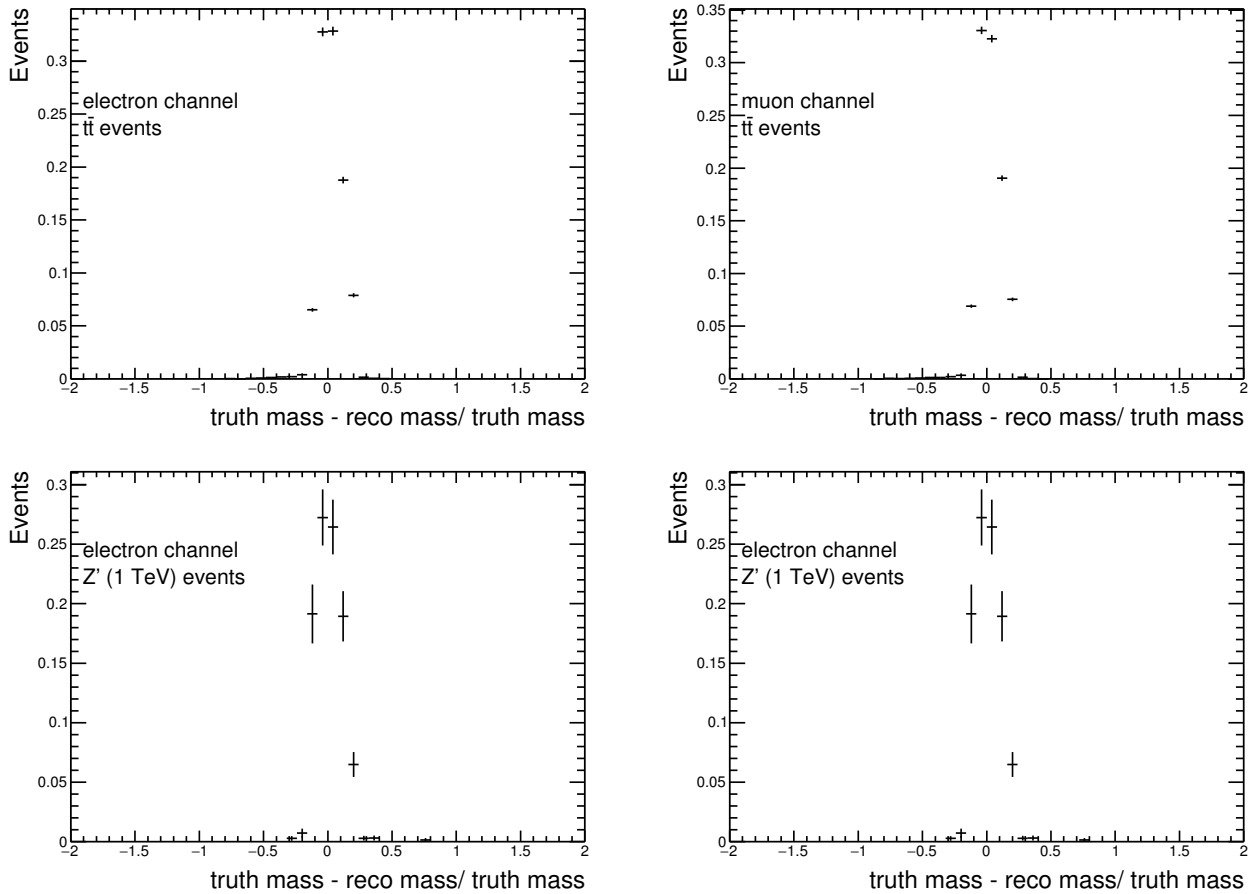


Figure 7.44: t_{had} mass resolution in the semi-boosted electron channel and semi-boosted muon channel, for SM $t\bar{t}$ events, and for 1 TeV Z' events.

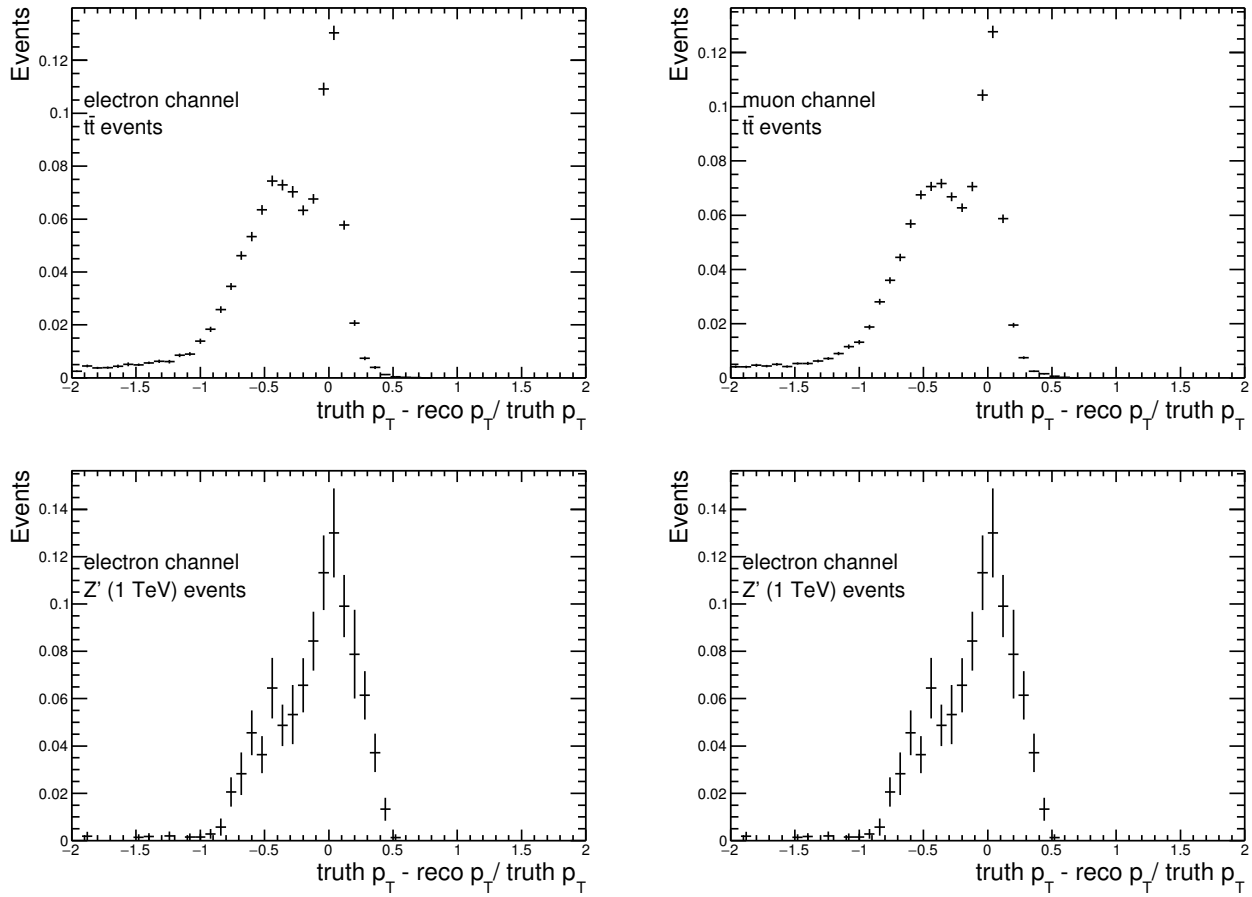


Figure 7.45: $t_{\text{had}} p_T$ resolution in the semi-boosted electron channel and semi-boosted muon channel, for SM $t\bar{t}$ events, and for 1 TeV Z' events.

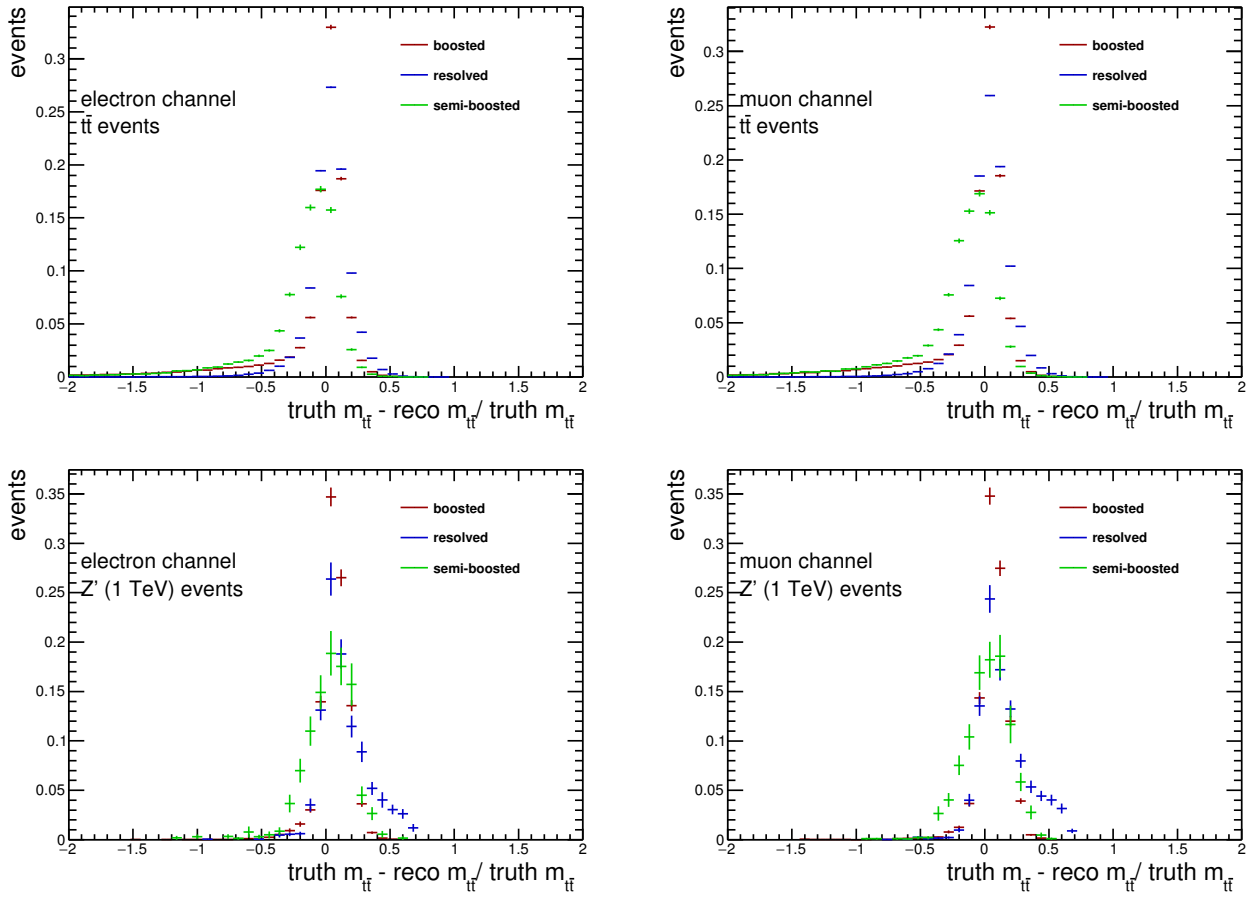


Figure 7.46: $m_{t\bar{t}}$ resolution in the semi-boosted channels (electron and muon) for SM $t\bar{t}$ events and 1 TeV Z' events.

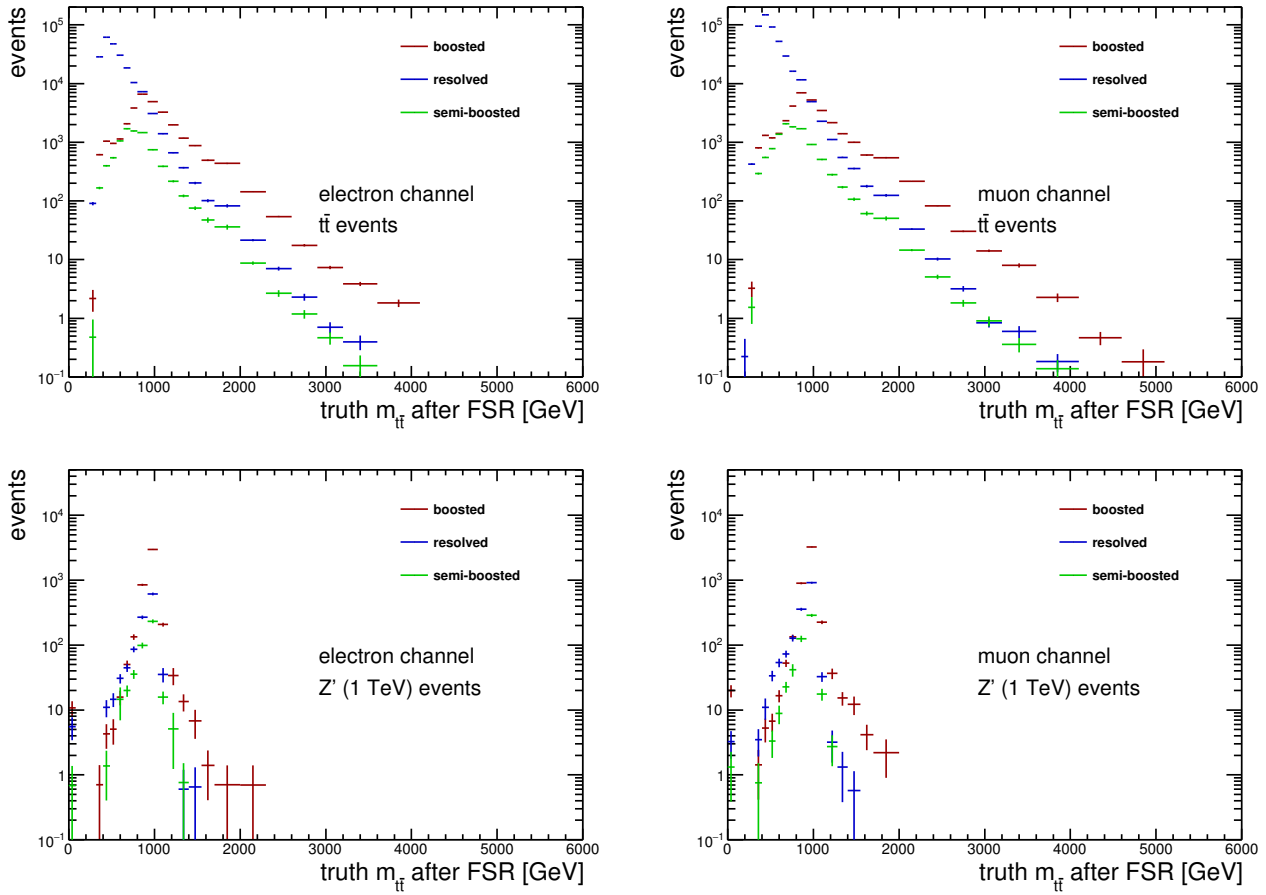


Figure 7.47: Truth $m_{t\bar{t}}$ distribution in the semi-boosted channels (electron and muon) for SM $t\bar{t}$ events and 1 TeV Z' events.

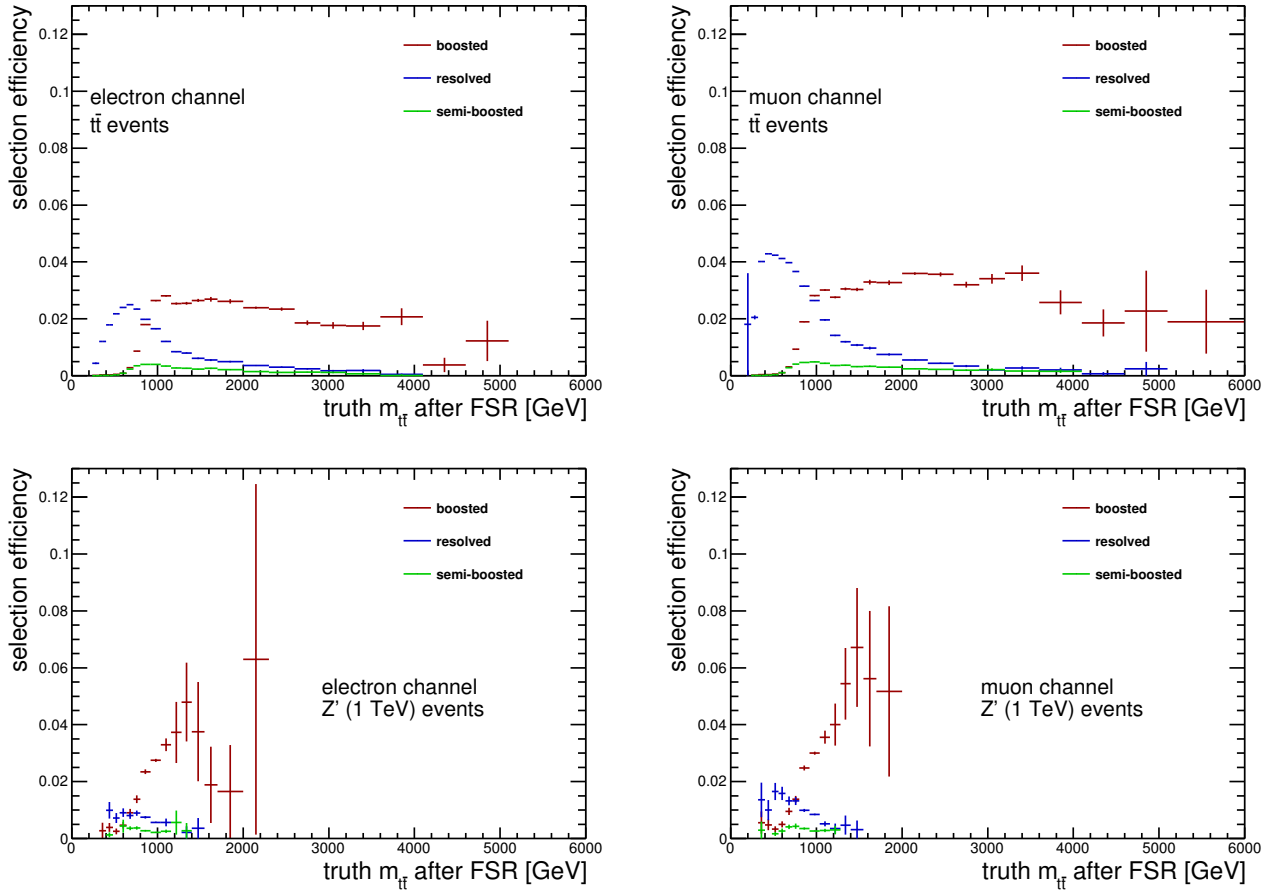


Figure 7.48: Event selection efficiency in the boosted, semi-boosted and resolved channels for SM $t\bar{t}$ events and 1 TeV Z' events. The selection efficiency is shown in bins of truth $m_{t\bar{t}}$ after final state radiation (FSR).

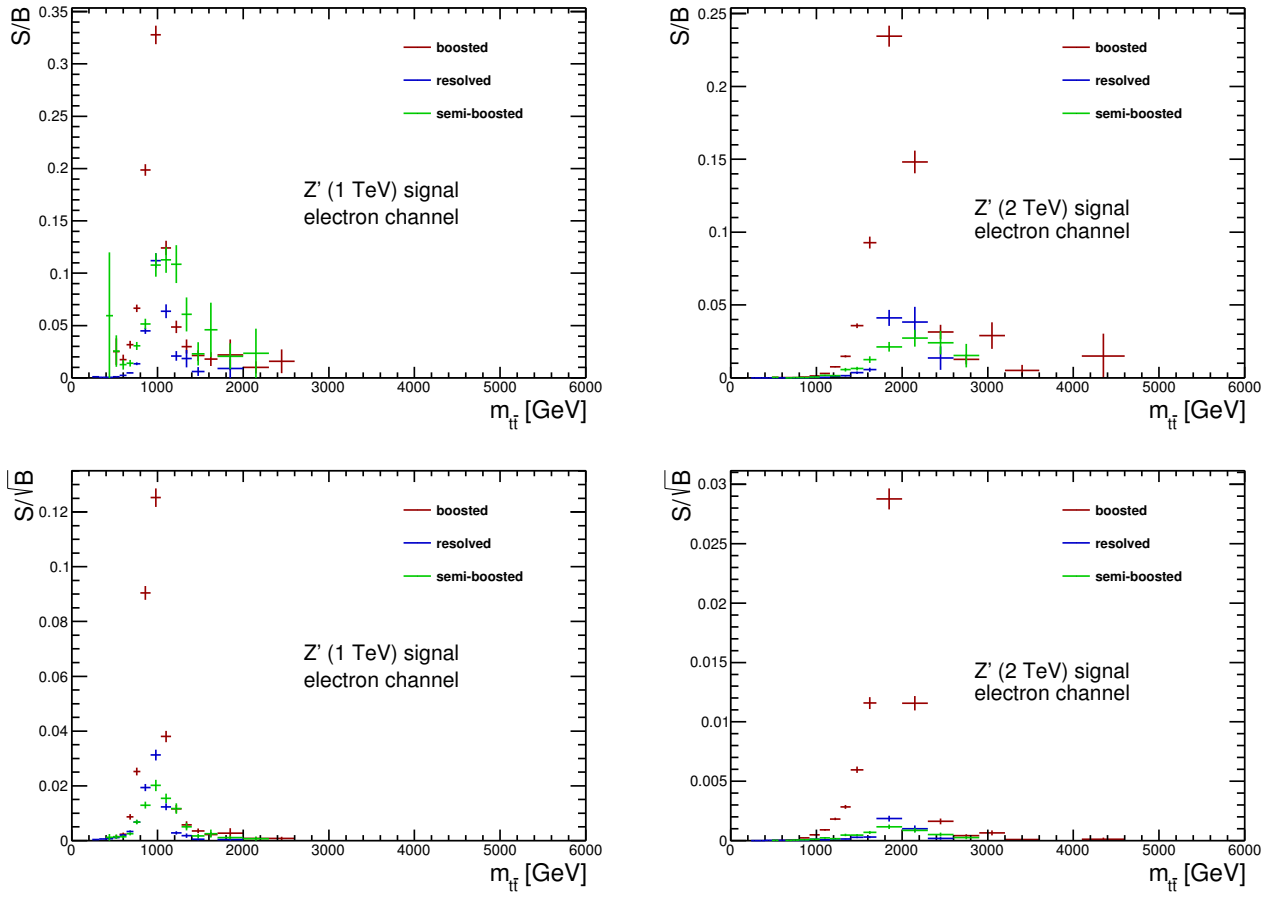


Figure 7.49: Signal sensitivity (signal/background and signal/ $\sqrt{\text{background}}$) in the electron channels.

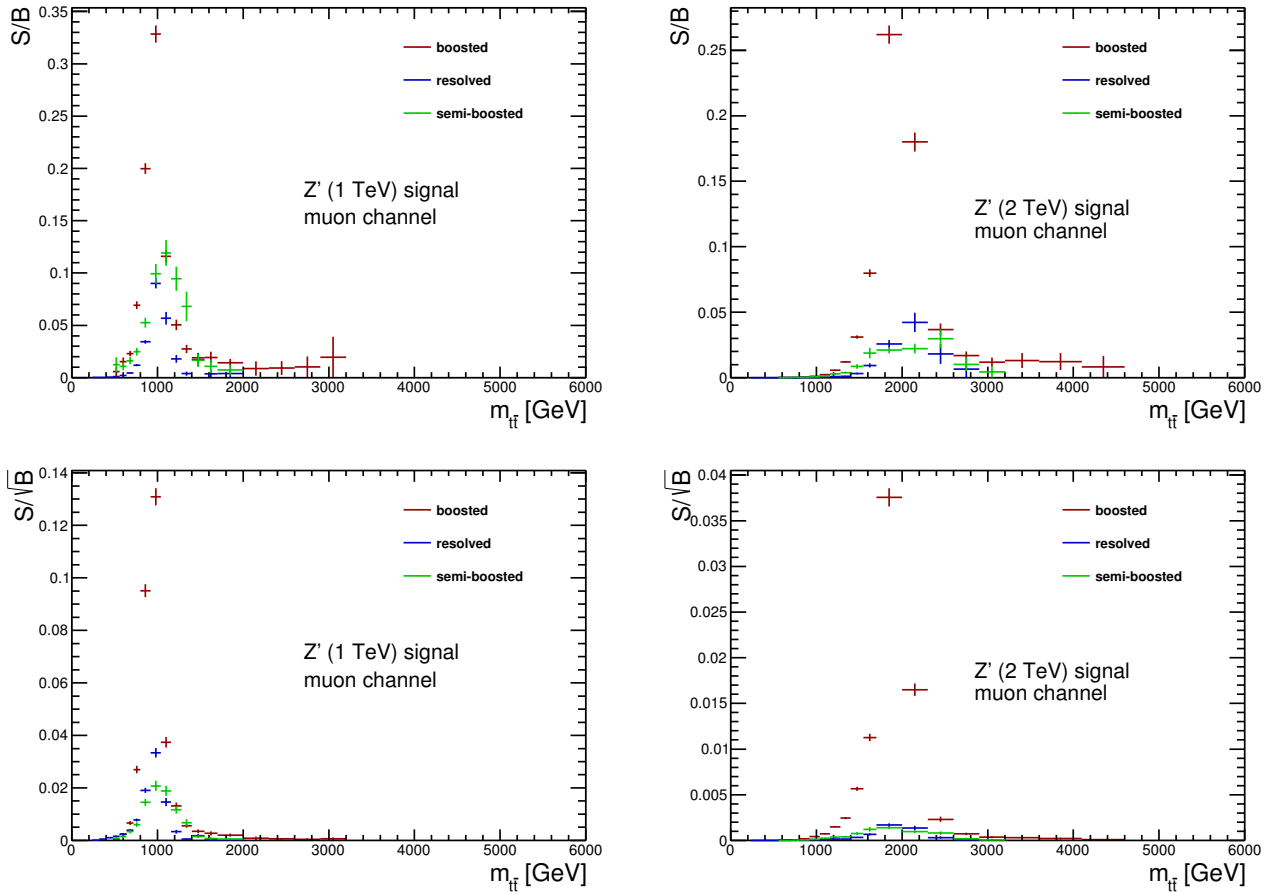


Figure 7.50: Signal sensitivity (signal/background and signal/ $\sqrt{\text{background}}$) in the muon channels.

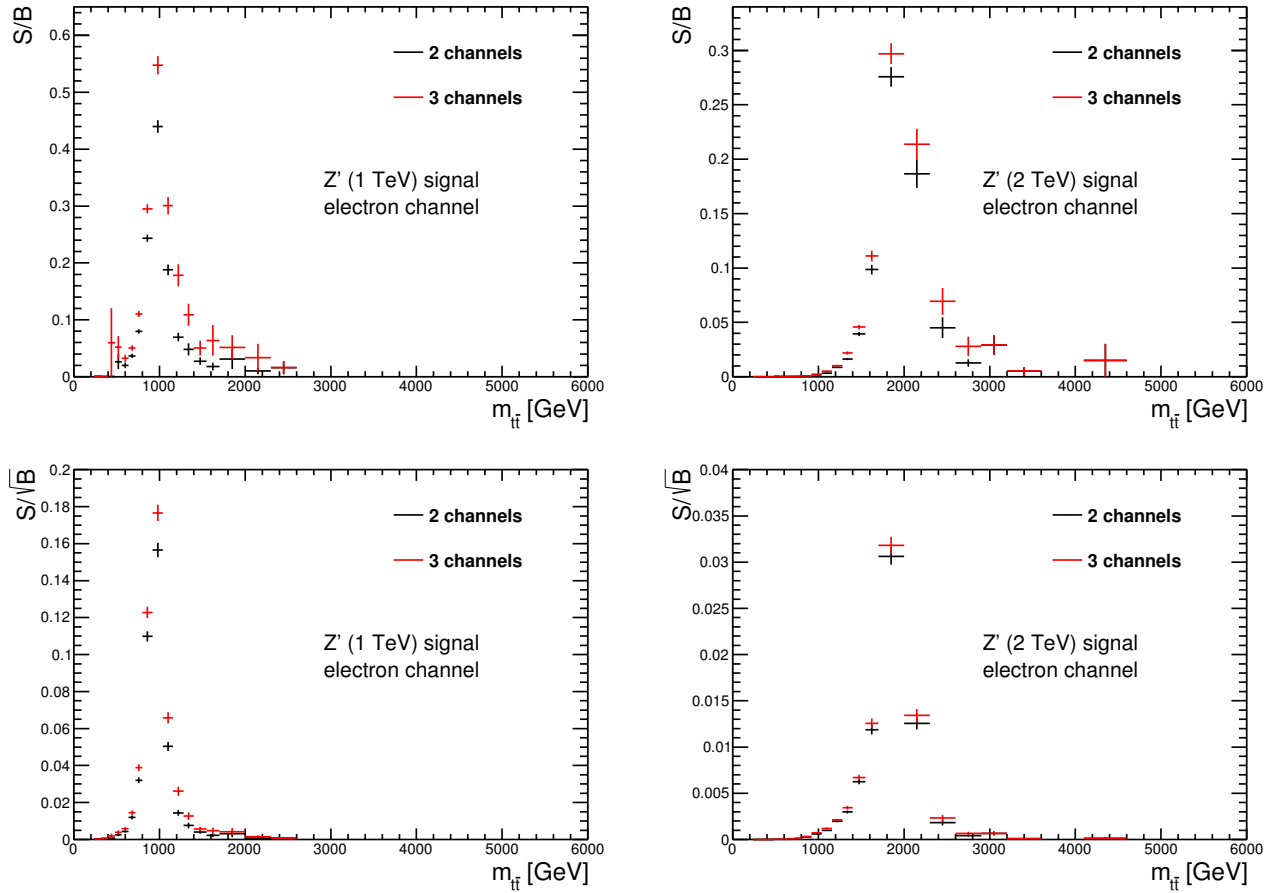


Figure 7.51: Comparing electron channel signal sensitivity (signal/background and signal/ $\sqrt{\text{background}}$) with (3 channels) and without (2 channels) including the semi-boosted channel.

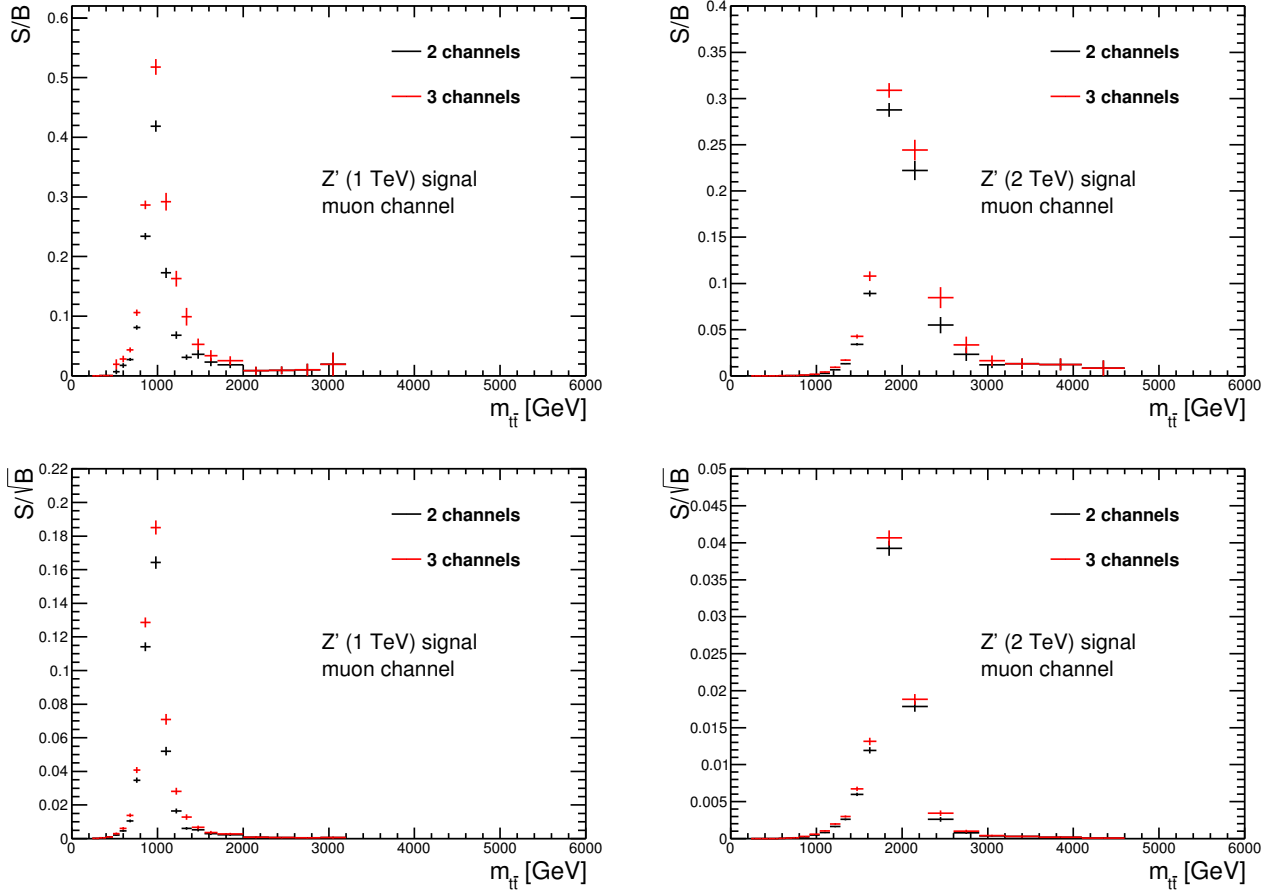


Figure 7.52: Comparing muon channel signal sensitivity (signal/background and signal/ $\sqrt{\text{background}}$) with (3 channels) and without (2 channels) including the semi-boosted channel.

7.4 Summary

This section has described two methods developed to improve the sensitivity of the $t\bar{t}$ resonances search to new heavy particles. The current electron-in-jet overlap removal procedure removes all jets < 0.2 from electrons, assuming them to be fakes, then removes all electrons < 0.4 from remaining jets, assuming them to be non-prompt electrons. However, many high mass signal events would have $\Delta R(\text{prompt electron}, b\text{-jet}) < 0.4$, and the current procedure leads the prompt lepton to be removed from the event, causing it to fail the selection. This procedure disproportionately affects the selection of signal events compared to SM $t\bar{t}$ events. The electron-in-jet subtraction method allows events with $\Delta R(\text{electron}, \text{jet}) < 0.4$ to be saved if it is likely that the jet and electron are independent objects. The increase in the number of signal events salvaged by using this method improves the sensitivity of the boosted electron channel, and strengthens the upper limits that can be set on the cross-sections of new high

mass signals.

Two new topology channels were created to accept $t\bar{t}$ final state events that are not accepted by the boosted and resolved channels. They targeted very high p_T events which have a topology that causes them to fail the boosted selection, and events in a middle p_T range whose topologies cause them to fail both the boosted and resolved selections.

The very boosted channel was designed to select events that fail the current event selection criteria but are likely to be high p_T $t\bar{t}$ final state events because they pass a $t\bar{t}$ preselection and contain a small-R jet with mass > 60 GeV. The inclusion of this channel improves the sensitivity of the analysis to new particles with masses > 2 TeV. This channel may be useful for future searches, especially if the centre of mass energy of collisions is increased, since top quark decays in very high mass signal events are observed to fall into a single high mass small-R jet more frequently than in SM $t\bar{t}$ events.

The semi-boosted channel was designed to select events that fail the current event selection criteria but which contain a large-R jet that could be the result of a hadronic top quark decay. In this channel it is more difficult to distinguish between $t\bar{t}$ final state events and the W +jets background, but including it leads to a small improvement in sensitivity to new particles with masses around 1 TeV. There are many $t\bar{t}$ events that fall into this category however, so if the signal/background discrimination were improved then it could be useful for improving sensitivity to low mass signals which have already been ruled out at certain cross-sections.

Chapter 8

Prospects of a $t\bar{t}$ Resonances Search at the High Luminosity LHC

8.1 HL-LHC and the Phase-II Upgrade

The High Luminosity LHC (HL-LHC) is expected to begin operations in 2026 following Long Shutdown 3, during which new accelerator machinery will be installed and phase-II upgrades to the detectors will be carried out. Its timeline is depicted in Figure 8.1. The project aims to deliver 3000 fb^{-1} of $\sqrt{s} = 14 \text{ TeV}$ proton-proton collisions by 2035 [87]. This is expected to significantly improve the physics capabilities of the LHC experiments. Analyses will be able to probe the multi-TeV scale in searches for new particles, make higher precision Standard Model measurements, and set stronger limits on very rare processes. The impact of the increased collision energy on mass reach is illustrated in the parton luminosity ratio plots in Figure 8.2. In order to achieve the target integrated luminosity, the HL-LHC will reach instantaneous luminosities of up to $L = 7.5 \times 10^{34} \text{ cm}^{-2} \text{ s}^{-1}$ [87], creating a very dense background from which interesting physics processes must be deciphered. An average of 200 inelastic p - p interactions per bunch crossing, $\langle \mu \rangle = 200$, is expected. The resulting occupancy will degrade aspects of event reconstruction, particularly jet reconstruction, and increased data rates will cause a non-linear increase of trigger rates. A superior performance in pile-up rejection, jet reconstruction and flavour tagging will be essential for maintaining or exceeding current physics performance with ATLAS under HL-LHC conditions.

The phase-II ATLAS upgrade will involve replacements of and modifications to the existing ATLAS subdetectors. The current inner detector will be replaced with an all-silicon tracking system: a pixel detector surrounded by a large-area strip tracking detector. It will have higher granularity to reduce occupancy, extended pseudorapidity coverage, $|\eta| < 4.0$, and less material in front of the calorimeters. A new trigger and DAQ architecture will be implemented to cope with increased data rates.

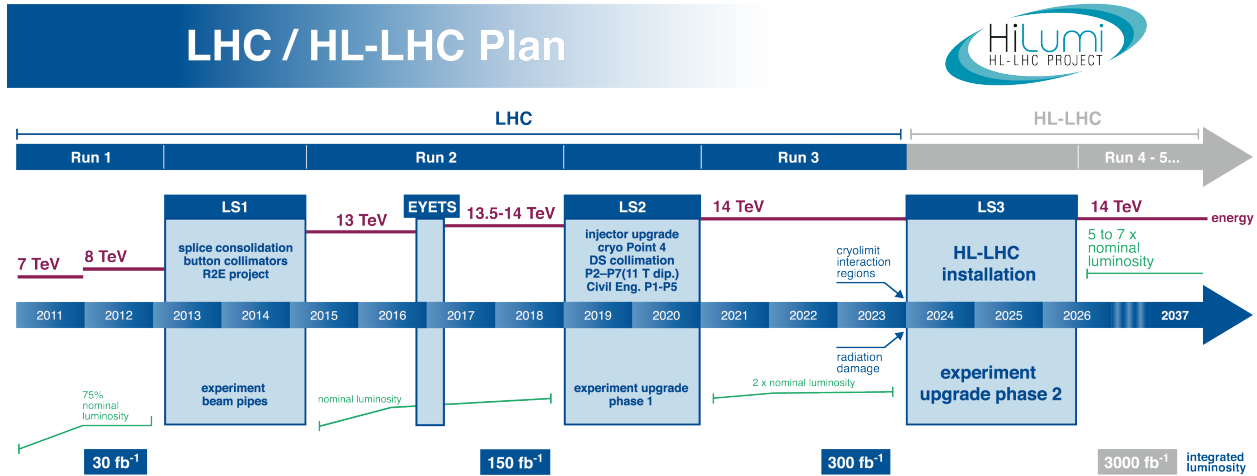


Figure 8.1: Timeline of the LHC program [89]. The HL-LHC machinery and phase-II detector upgrades will be installed during long shutdown 3, prior to run 4. During run 4, the total integrated luminosity delivered by the LHC will be increased from 300 fb^{-1} to 3000 fb^{-1} .

Fast simulation studies have been carried out to evaluate the prospects of benchmark analyses at the HL-LHC. The expected performance of the phase-II upgrade has been estimated for physics objects and trigger/DAQ in studies with a fully simulated detector and assuming nominal HL-LHC conditions including a pile-up of $\langle \mu \rangle = 200$ [88]. Parameterised estimates performances were derived from the full simulation studies for use in the prospects studies, allowing them to be done as “smeared truth” simulations of analyses.

8.2 $t\bar{t}$ Resonances Prospects Study

This section documents a study [2] that was done to investigate the prospects of a $t\bar{t}$ resonances search at the HL-LHC. A $t\bar{t}$ resonances search is a benchmark analysis for evaluating the physics potential of the HL-LHC; the 14 TeV collision energy will improve the mass reach of the search and the large increase in the number of high p_T events will tighten the upper limits that, in the absence of signal, can be set on the cross-sections of hypothesised heavy particles. A simplified version of the run 1 and 2 ATLAS $t\bar{t}$ resonance searches is performed on events selected from Monte Carlo simulations of proton-proton collisions with $\sqrt{s} = 14$ TeV, over a total integrated luminosity of 3000 fb^{-1} . Parameterised estimates of the Phase-II upgrade performance are implemented to emulate the detector effects. A spin-1 Z' boson in a TopColour model [5] is used to quantify the results: the upper limits one can expect to set on the Z' cross-section if the HL-LHC dataset is consistent with Standard Model expectation.

The search is carried out as follows. Truth-level events in signal and background samples are modified to account for detector effects, and pile-up jets are added. Events compatible

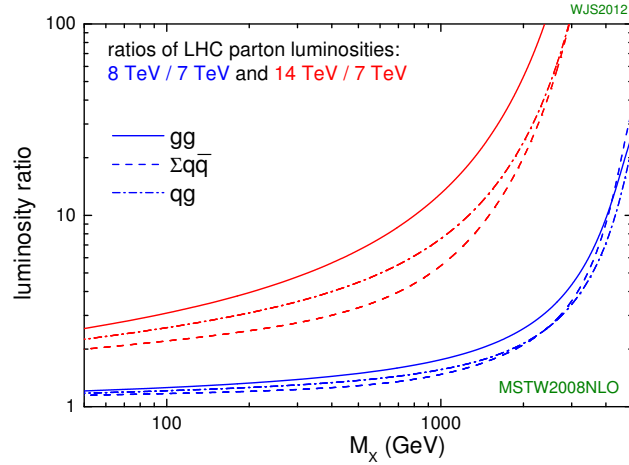


Figure 8.2: Ratios of parton luminosities in LHC collisions [90]. A $\sqrt{s} = 14$ TeV collision energy increases the luminosities by a factor of 10 compared to $\sqrt{s} = 7$ TeV for parton-parton centre of mass energies greater than 1.1 TeV.

with semi-leptonic $t\bar{t}$ decay are then selected from the samples and the $t\bar{t}$ invariant mass spectrum is constructed under the background-only hypothesis and under the signal-plus-background hypothesis for varying signal strength. Expected 95% CL upper limits on cross-section times branching ratio for several Z' masses are calculated using a likelihood model based on the binned mass spectrum. The expected upper limits are compared to the nominal theoretical Z' cross-section at each mass point to estimate the mass reach of the search.

8.3 Signal and Background Samples

The signal simulation $pp \rightarrow Z' \rightarrow t\bar{t}$ was done with Pythia 8 [66] and the A14NNPDF23LO PDF set [91], using leading order cross-sections and assuming a signal width of 1.2%. Seven signal samples were generated, for Z' masses 1-7 TeV and each cross-section is multiplied by a k-factor of 1.3 to account for NLO effects [92]. Interference between Z' signal and $t\bar{t}$ background is considered to be negligible, although this can have a large impact on the shape at low mass.

The largest background is Standard Model $t\bar{t}$ production in the semi-leptonic decay channel, which is irreducible. The $t\bar{t}$ background was generated using Powheg+Pythia [71] with the CT10 PDF set. W +jets and Z +jets background samples were generated using Sherpa [78] with the CT10 PDF set. The single top background was generated using AcerMCPythia [93]. The cross-sections were NNLO, except single top which was NLO.

8.4 Detector Effects and Object Definitions

The results of full-simulation studies on the performance of the upgraded phase-II ATLAS detector at the HL-LHC [94] were used to derive functions that provide performance estimates for physics objects and trigger/DAQ. The performance studies assume a centre of mass energy of $\sqrt{s} = 14$ TeV, instantaneous luminosities of up to $L = 7.5 \times 10^{34} \text{ cm}^{-2}\text{s}^{-1}$ and $\langle\mu\rangle = 200$

The Performance functions return values for energy resolutions, efficiencies and fake rates, which are used to convert truth-level objects into reconstructed objects through modifications to the object's kinematics and particle identification. The values depend on truth p_T , η and particle type, and are calculated independently for each object.

First, efficiencies and fake rates are calculated and used to sort objects into lists of electrons, muons, small-R jets (b -tagged and non b -tagged) and large-R jets. Initially each truth-level object is in the list that matches its truth type. Once the nominal efficiency ($n_{\text{eff}} \in [0, 1]$) for an object is obtained, a random number n_{rand} is generated from a uniform distribution between 0 and 1 and compared to n_{eff} . The object is kept in its list if $n_{\text{rand}} < n_{\text{eff}}$, otherwise it is discarded. Efficiency functions are available for electron identification, muon identification and b -tagging. If there is a possibility that an object of type A will be misidentified as an object of type B, then for each type A object a uniformly distributed random number, $n_{\text{rand}} \in [0, 1]$, is compared to the estimated fake rate for the object, n_{fake} . If $n_{\text{rand}} < n_{\text{fake}}$, the object is moved from the list of type A objects to the list of type B objects. Otherwise, it remains a type A object. There are fake rate functions for jets (sometimes misidentified as electrons), and b -tagging (light, c , and pile-up jets can be mistagged as b -jets).

The four-momenta of truth-level objects are altered to reflect the expected resolution of the detector. A random quantity, called the smeared energy, is extracted from a Gaussian centred on the truth energy with a σ equal to the estimated energy resolution for the object. The truth four-momentum is scaled by the ratio smeared energy/ original energy, leaving the energy of the reconstructed object equal to the smeared energy. Energy resolutions are calculated assuming that the object is the type it is assigned after efficiencies and fake rates are applied. The object selection criteria are applied to smeared quantities. This search relies on a good reconstruction of boosted objects, and is dependent on upgrade tracking performance in a dense environment for b -tagging and lepton isolation.

Leptons

Truth-level electrons and muons are required to pass isolation criteria: the sum of other final state charged particles' p_T within $\Delta R(\ell, \text{object}) = 10 \text{ GeV}/p_{T,\ell}$ must be $< 6\%$ of the lepton p_T in order to suppress the jets background. Lepton identification efficiencies are applied to isolated leptons. The efficiency calculation depends on whether the leptons are required

to pass tight, medium or loose identification criteria. In this analysis tight efficiencies are implemented to mimic tight identification criteria. The energies of the remaining isolated leptons are smeared according to the expected detector resolution. Fake rates for jets faking electrons are applied to all truth-level anti- k_t $R=0.4$ jets, flagging a small fraction of jets which are moved to the electrons list, with their energy smeared to account for them being reconstructed as electrons. Jets faking electrons are not required to pass the lepton isolation criteria. p_T and $|\eta|$ cuts are applied to the remaining lepton candidates after all efficiencies, fake rates and energy resolutions are applied. Electrons must have $p_T > 30$ GeV and $|\eta| \in [0.1, 37] \cup [1.52, 2.47]$, and muons must have $p_T > 25$ GeV and $|\eta| < 2.5$ GeV.

Small-R jets

The anti- k_t algorithm with a radius parameter of $R=0.4$ is used to create small-R jets. As mentioned previously, a fraction of jets misidentified as electrons is removed from the list of truth jets by applying a fake rate function. Pile-up jets are included from a pile-up library built assuming $\langle \mu \rangle = 200$. It is known at truth-level whether a jet. Flavour tagging efficiency functions are applied to truth b -jets, identifying a fraction that are correctly b -tagged by the `mv10` algorithm operating at the 70% working point. Flavour tagging fake rate functions are also applied to light, c , and pile-up jets, identifying jets that do not contain a b hadron but are mis-tagged as b -jets. In real analyses, track confirmation algorithms are used to remove pile-up by rejecting jets whose tracks are not traced back to the primary vertex; here track confirmation efficiencies are applied to hard-scatter and pile-up jets to mimic this process. The energies of the remaining small-R truth jets are smeared, and they are required to have $p_T > 25$ GeV and $|\eta| < 2.5$.

Large-R jets

The anti- k_t algorithm with a radius parameter of $R=1.0$ is used to create large-R jets, which are trimmed with parameters p_T fraction = 0.05 and $R = 0.2$. No top-tagging efficiencies are applied to large-R jets, which are candidates for boosted hadronic top quark decays. The p_T of the large-R jets is smeared by a random amount taken from a Gaussian of width $0.05 \times p_T$. Large-R jets must have $p_T > 300$ GeV and $|\eta| < 2.0$.

Missing transverse momentum

The missing transverse momentum in an event is determined from the vector sum of interacting truth particles within the detector acceptance. The values of missing p_x and missing p_y are smeared in an analogous way to the truth-level objects and are used to calculate missing transverse energy.

Overlap removal

In reality, electron energy deposits in the calorimeter can be clustered by the jet algorithm, resulting in electrons being double counted as jets. In this simulation, the truth jets are made with all final state particles, including electrons. To avoid the double counting of electrons, the nearest jet to an electron is removed from the list of jets if $\Delta R(\text{electron}, \text{jet}) < 0.2$. Then any electron with $\Delta R(\text{electron}, \text{nearest jet}) < 0.4$ is assumed to be a b -jet decay product and is removed from the list of electrons. To counter muon-jet overlap, muons with $\Delta R = 0.04 + (10 \text{ GeV}/p_{T,\mu})$ are removed.

8.5 Event Selection

Events are required to have exactly one lepton (electron or muon). Single lepton trigger efficiencies are applied to these events, causing a fraction of them to be discarded. There must be some missing transverse energy, and some evidence of a leptonically decaying W boson: $E_T^{\text{miss}} > 20 \text{ GeV}$ and $E_T^{\text{miss}} + M_T^W > 60 \text{ GeV}$. Events must contain at least one jet b -tagged by the Mv2c10 algorithm. Events are separated into two channels based on their decay topology: boosted and resolved. The leptonically decaying top quark ($t \rightarrow Wb \rightarrow \ell\nu b$) is referred to as t_{lep} , and the hadronically decaying top quark ($t \rightarrow Wb \rightarrow qq'b$) is referred to as t_{had} . In a boosted event, the t_{had} decay products are detected inside one large-R jet, while in a resolved event they are detected as three well separated small-R jets. Events are further separated into four channels depending on whether the single lepton is an electron or a muon: boosted electron, resolved electron, boosted muon, resolved muon. The $m_{t\bar{t}}$ reconstruction method is channel-dependent (as described in section 6.6), but the four channels are recombined for the limit setting procedure.

8.5.1 Boosted Channel

Events passing the preselection are initially tested against the boosted selection. A boosted event must contain at least one small-R jet such that $\Delta R(\text{jet}, \text{lepton}) < 1.5$. If there is more than one jet that meets this criteria then the one with the highest p_T is chosen as the candidate for the b -jet decaying from t_{lep} . This jet is referred to as the selected jet, j_{sel} . Additionally, boosted events must contain at least one large-R jet such that $\Delta R(\text{large-R jet}, j_{\text{sel}}) > 1.5$ and $\Delta\phi(\text{large-R jet}, \text{lepton}) > 2.3$. If more than one large-R jet satisfies these requirements, the highest p_T jet is chosen as the t_{had} decay.

8.5.2 Resolved Channel

Events are tested against the resolved selection only if they fail the boosted selection, to ensure mutually exclusive channels. Resolved events must contain at least four small-R jets. A χ^2 algorithm, described in section 8.6, is used to iteratively test each four-jet combination in the event and choose the optimal combination, matching them to the decay products of the top quarks. A cut $\chi^2 < 10$ is applied to suppress non $t\bar{t}$ backgrounds with multiple jets.

8.6 Event Reconstruction

Leptonically Decaying W (W_{lep}) The missing p_x and p_y are assumed to be the neutrino p_x and p_y . The neutrino p_z component is determined by imposing a W boson mass constraint (the PDG value) on the mass of the neutrino-lepton system. This yields a quadratic equation, which is solved for the neutrino p_z . If the solution is complex, the real part is used as p_z . If there are two real solutions and the event is boosted, the one with the smallest absolute value is used as p_z . If there are two real solutions and the event is resolved, both p_z solutions are tested in the χ^2 algorithm and the optimal one is chosen.

Boosted Event t_{lep} is reconstructed from W_{lep} and j_{sel} , and t_{had} from the large-R jet.

Resolved Event In a resolved event, a unique small-R jet is identified with each hadronic decay product (the b -jets decaying from t_{lep} and t_{had} and the two jets decaying from W_{had}) using the χ^2 algorithm shown in equation 8.1. Each combination of four small-R jets is tested and the combination yielding the smallest χ^2 value is chosen. If there are two real solutions for p_z , each W_{lep} scenario is also tested in the algorithm. The first three terms in the χ^2 algorithm compare the expected reconstructed top quark and W boson masses to the masses of the reconstructed tops and W built from the candidate decay jets. The σ terms in the denominator account for the expected mass resolution of the reconstructed tops and Ws. (If a large spread in mass values is expected, then the constraint for the reconstructed mass to be close to the expected mass is loosened). The expected mass and resolution values for t_{lep} ($m_{t\ell}, \sigma_{t\ell}$), $t_{\text{had}} - W_{\text{had}}$ (m_{th-W}, σ_{th-W}) and W_{had} (m_W, σ_W) were estimated in the run 1 $t\bar{t}$ resonances search by reconstructing tops and W in events where it is possible to select the correct decay jets using MC truth information and plotting the mass distribution for these events only. This produces a Gaussian distribution, and the expected reconstructed mass and resolution are taken from the mean and σ of the Gaussians used in the run 1 search. The first χ^2 term directly constrains the mass of the two jet system matched to W_{had} to be near the expected W_{had} mass, and the third term does the same for t_{lep} . The second

term indirectly constrains the mass of the reconstructed t_{had} since $m_{t_{\text{had}}}$ and $m_{W_{\text{had}}}$ are highly correlated. The fourth term constrains $\Delta p_T(t_{\text{had}}, t_{\text{lep}})$, favouring events where two top quarks have similar p_T , which is expected in a resonance event. This method aims to maximise the number of resolved events with successful decay product matches in order to achieve the best $m_{t\bar{t}}$ resolution. To remain in the resolved channel events must have $\chi^2 < 10$.

$$\chi^2 = \left[\frac{m_{jj} - m_W}{\sigma_W} \right]^2 + \left[\frac{m_{jjb} - m_{jj} - m_{th-W}}{\sigma_{th-W}} \right]^2 + \left[\frac{m_{j\ell\nu} - m_{tl}}{\sigma_{tl}} \right]^2 + \left[\frac{(p_{T,jjb} - p_{T,j\ell\nu}) - (p_{T,th} - p_{T,tl})}{\sigma_{\Delta p_T}} \right]^2 \quad (8.1)$$

The following values extracted from run 1 Monte Carlo studies are used for the mass and resolution parameters. $m_W = 83.7$ GeV, $m_{th-W} = 91.2$ GeV, $m_{tl} = 167.6$ GeV, $\sigma_W = 8.4$ GeV, $\sigma_{th-W} = 11.1$ GeV, $\sigma_{tl} = 21.8$ GeV, $p_{T,th} - p_{T,tl} = -0.0012$ GeV and $\sigma_{\Delta p_T} = 34.7$ GeV. m_{jj} , m_{jjb} , $m_{j\ell\nu}$, $p_{T,jjb}$ and $p_{T,j\ell\nu}$ are variables reconstructed from the decay candidates from the decay candidates in the interaction.

8.7 Statistical Analysis and Results

HistFactory [95] is used to determine the expected upper limits that can be set on the Z' cross-section in the absence of signal. The $t\bar{t}$ invariant mass spectrum is constructed for the background-only (B) hypothesis and for signal-plus-background (B+ μ S) hypotheses with varying signal strength μ , where $\mu = 0$ corresponds to the background-only model and $\mu = 1$ is the prediction of the nominal signal model. A likelihood function based on the binned $m_{t\bar{t}}$ spectrum is used to exclude values of μ with 95% confidence; the observed data is set to background-only expectation. The expected upper limit set on the signal cross-section is the greatest value of μ that is not excluded with 95% confidence. This procedure is carried out for each signal mass. A luminosity uncertainty of 3% is included, as well as a flat systematic uncertainty on the total signal and background yield in each channel shown in Table 8.1. The

	resolved	boosted
signal	8.8%	18.0%
background	10.8%	13.4%

Table 8.1: Systematic uncertainties on the signal and background yield in each channel.

systematic uncertainties are taken from the run 1 analysis and reflect the average impact of the dominant systematic uncertainties on the event yield. Stacked $t\bar{t}$ mass spectra built with background and two signal samples are shown for each channel in Figure 8.3, and event yield tables are shown in Tables 8.2 - 8.5. The majority of signal events fall into the boosted

channel, where the excess of events is localised around the signal mass; the boosted channel dominates the limit setting result. The expected upper limits set on signal cross-section \times branching ratio as a function of the signal mass are shown in Figure 8.4, with $\int \mathcal{L} = 300 \text{ fb}^{-1}$ and $\int \mathcal{L} = 3000 \text{ fb}^{-1}$. A line showing the theoretical cross-section of the Z' boson at each signal mass intersects with the expected upper limits line at a point that indicates the mass reach of the search: $\simeq 3 \text{ TeV}$ with 300 fb^{-1} and $\simeq 4 \text{ TeV}$ with 3000 fb^{-1} of p - p collisions, using the same detector configuration and pile-up conditions for both luminosity scenarios. A factor of ten increase in the total integrated luminosity is expected to increase the sensitivity of the search to the Z' signal by $\simeq 1 \text{ TeV}$.

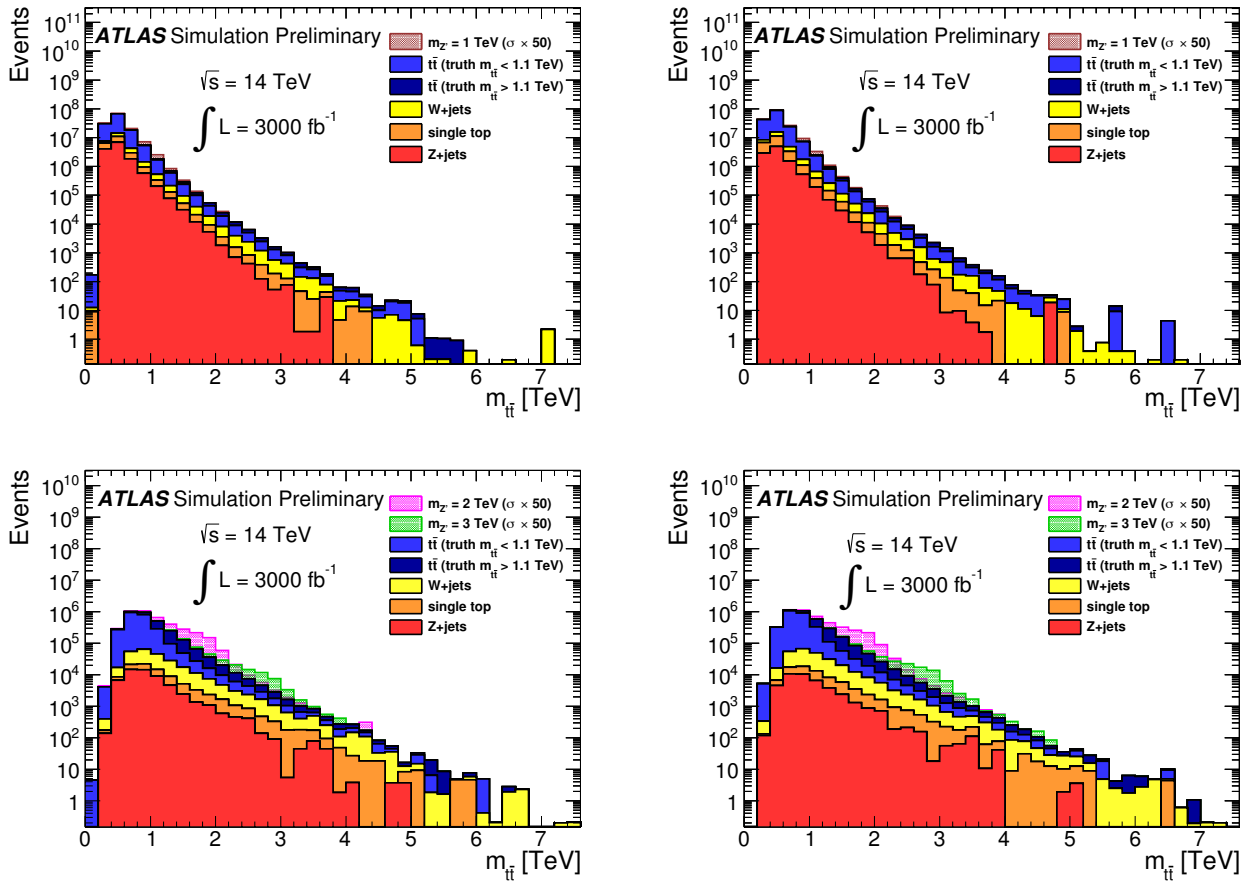


Figure 8.3: The reconstructed mass spectrum of $t\bar{t}$ pairs selected from signal and background events in the resolved electron channel (top left), resolved muon channel (top right), boosted electron channel (bottom left) and boosted muon channel (bottom right), using simulated $\sqrt{s} = 14 \text{ TeV}$ p - p collisions with an integrated luminosity of 3000 fb^{-1} . The background normalisations are obtained from the theoretical cross-sections. The cross-sections of the signal samples, Z' (2 TeV) and Z' (3 TeV), are multiplied by 50 for visibility and shown on the boosted channel plots. These signals are not visible in the resolved channel, so a Z' (1 TeV) sample is shown on the resolved channel plots with its cross-section multiplied by 50.

Z' mass	1TeV	2TeV	3TeV	4TeV	5TeV	6TeV	7TeV
initial events	5.50493e+06	278654	29659	4168.32	696.091	146.204	45.6522
== 1 lepton	1.60691e+06	90563.7	9790.26	1397.9	227.344	46.5364	14.0754
== 1 electron	881340	49024.8	5331.43	777.848	127.399	25.7595	7.71011
$E_T^{\text{miss}} > 20\text{GeV}$	850384	47739.4	5203.88	761.014	124.774	25.1035	7.49518
$E_T^{\text{miss}} + m_T^W > 60\text{GeV}$	822696	46678.7	5092.58	745.953	122.171	24.5074	7.29843
≥ 1 b-tag	672782	38194.3	3856.15	550.521	89.344	18.5213	5.64595
boosted	216597	22134.7	2351.19	324.214	50.8564	9.31107	2.58769
resolved	172094	21104.7	2391.94	325.915	50.488	8.89167	0

Table 8.2: Signal cutflows for 3000 fb^{-1} in the electron channel.

Z' mass	1TeV	2TeV	3TeV	4TeV	5TeV	6TeV	7TeV
initial events	5.50493e+06	278654	29659	4168.32	696.091	146.204	45.6522
== 1 lepton	1.60691e+06	90563.7	9790.26	1397.9	227.344	46.5364	14.0754
== 1 muon	725552	41529.3	4458.01	620.184	99.9539	20.7802	6.36669
$E_T^{\text{miss}} > 20\text{GeV}$	706841	40798.3	4395.08	611.151	98.2537	20.369	6.21816
$E_T^{\text{miss}} + m_T^W > 60\text{GeV}$	690360	40181.7	4343.92	604.486	96.9445	20.0606	6.10672
≥ 1 b-tag	549796	32773.5	3367.23	464.398	75.1207	15.4672	4.74206
boosted	172094	21104.7	2391.94	325.915	50.488	8.89167	2.33202
resolved	188295	3341.92	218.998	32.8042	7.93467	2.62128	1.04673

Table 8.3: Signal cutflows for 3000 fb^{-1} in the muon channel.

sample	$t\bar{t}$	W+jets	Z+jets	single top
initial events	1.36534e+09	3.92115e+08	2.35018e+08	9.3835e+08
== 1 lepton	5.63795e+08	1.4161e+08	8.31015e+07	2.78887e+08
== 1 electron	2.58503e+08	6.35705e+07	3.61718e+07	1.45331e+08
$E_T^{\text{miss}} > 20\text{GeV}$	2.46748e+08	6.03006e+07	3.41876e+07	1.32692e+08
$E_T^{\text{miss}} + m_T^W > 60\text{GeV}$	2.36821e+08	5.75972e+07	3.25767e+07	1.22427e+08
≥ 1 b-tag	1.70615e+08	1.76061e+07	1.876e+07	3.00515e+07
boosted	3.2699e+06	182958	37531.7	55160.7
resolved	1.08288e+08	6.86319e+06	8.9196e+06	1.20525e+07

Table 8.4: Background cutflows for 3000 fb^{-1} in the electron channel.

sample	$t\bar{t}$	W+jets	Z+jets	single top
initial events	1.36534e+09	3.92115e+08	2.35018e+08	9.3835e+08
== 1 lepton	5.63795e+08	1.4161e+08	8.31015e+07	2.78887e+08
== 1 muon	3.06391e+08	7.8035e+07	4.68149e+07	1.33545e+08
$E_T^{\text{miss}} > 20\text{GeV}$	2.92651e+08	7.40668e+07	4.42973e+07	1.22007e+08
$E_T^{\text{miss}} + m_T^W > 60\text{GeV}$	2.80786e+08	7.07346e+07	4.2197e+07	1.121e+08
≥ 1 b-tag	1.99099e+08	2.03131e+07	2.35161e+07	2.5138e+07
boosted	3.56101e+06	203989	39991.6	40739.2
resolved	1.28618e+08	8.02587e+06	1.14136e+07	8.87009e+06

Table 8.5: Background cutflows for 3000 fb^{-1} in the muon channel.

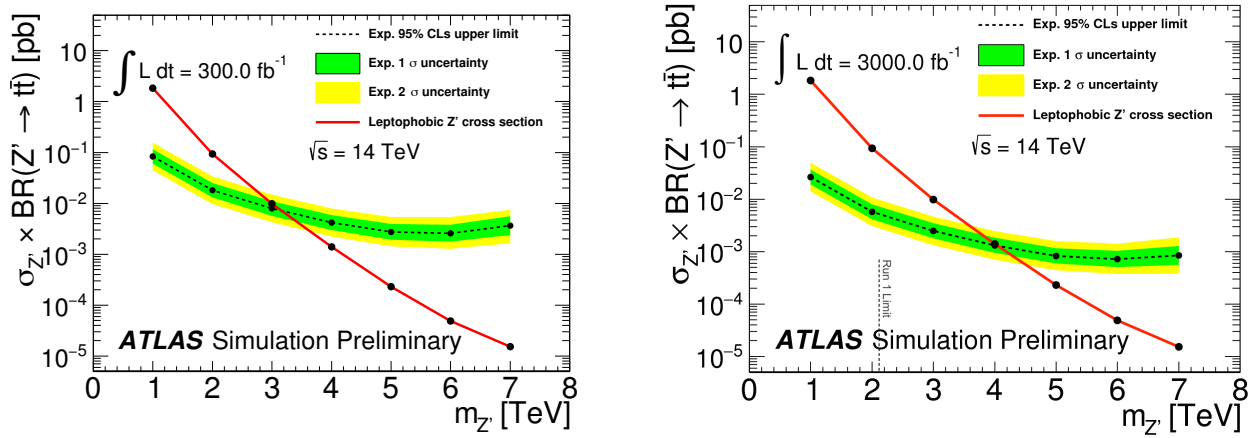


Figure 8.4: The expected upper limits set on the cross-section \times branching ratio of the Topcolour Z' boson for masses 1-7 TeV, with (a) 300 fb^{-1} and (b) 3000 fb^{-1} of simulated $\sqrt{s} = 14$ TeV p - p collisions. The theoretical signal cross-section intersects with the 300 fb^{-1} limits line at $\simeq 3$ TeV and with the 3000 fb^{-1} line at $\simeq 4$ TeV. We can expect to exclude this resonance for $m_{Z'} < 3$ TeV after run 3 and $m_{Z'} < 4$ TeV after HL-LHC.

Chapter 9

Beam-Induced Background in the SCT

9.1 Introduction

Hits recorded by ATLAS are used to study the physics produced in LHC collision events. Additionally, in run 2, hits recorded in the SCT subdetector are used to provide a luminosity measurement [96]. It is therefore important to account for hit occupancy that is not a result of colliding bunches of protons, known as non-collision background (NCB). Sources of NCB include cosmic rays, electronic noise, and the beams themselves. Beam induced background (BIB) events, which are the focus of this study, are fixed target events that occur when a proton originating in the beam interacts with a residual gas molecule inside the beam pipe (known as a beam-gas event), or drifts away from the beam’s circular orbit and hits a collimator (known as a beam-halo event). Beam-halo events occur at fixed positions, e.g. at the position of the collimators near interaction point 1 (IP1). Figure 9.1 shows a beam-halo event initiated at a secondary collimator near IP1. The rate of beam-halo events is influenced by collimator settings and the stability of the beam. Beam-gas events can occur anywhere there are residual gas molecules and have a rate that is proportional to the local pressure of the gas and the intensity of the beam.

Events during the crossing of unpaired, isolated (UI) bunches are appropriate for evaluating the rate of BIB during a run, and its average per-bunch occupancy contribution. A bunch is unpaired if it is filled with protons in one beam, and the corresponding bunch in the other beam is not filled. The corresponding bunch is the one that the original bunch would collide with at IP1. Bunches that collide at IP1 are labelled with the same ordinal number (bcid) in both beams. A bunch is isolated if it is at least 75 ns (i.e. 3 bunches) away from any other filled bunch. Filled bunches nominally contain 10^{11} protons. At injection, “ghost bunches” can be formed. These are nominally empty bunches neighbouring the filled bunch that can contain up to 10^8 protons. The isolation criteria ensures that there are no or very few protons in the nominally empty bunch corresponding to the unpaired bunch, and

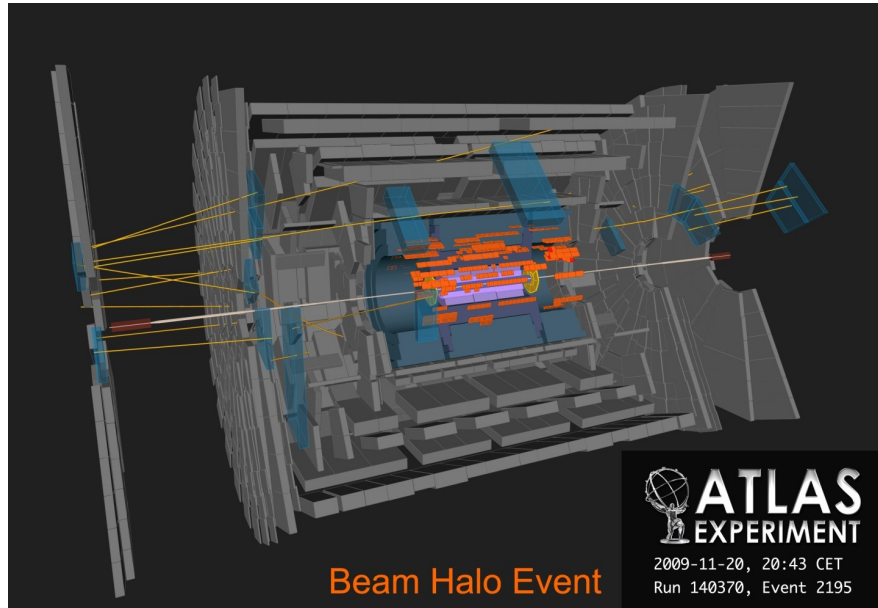


Figure 9.1: A figure from [97] showing a beam halo event in 3D.

therefore that a collision during a UI bunch crossing is unlikely.

All events during UI bunch crossings will contain hits due to electronic noise, and a fraction of the events will contain additional hits from BIB, if there is BIB associated with the bunch. There should be no hits due to collisions, except in cases when the paired bunch in the opposite beam, which is nominally empty, contains a small number of protons. In this case, it is possible that there are hits resulting from a proton-proton collision. Events during UI bunch crossings that are used to study BIB are required to contain no primary vertices, in order to remove events contaminated by collision hits. UI bunches will be used to refer to UI bunch crossings with no primary vertices, and events during such bunch crossings with no primary vertex will be referred to as UI bunch events (UIBE).

The expected characteristics of BIB hits are used to distinguish between UIBE where BIB is present, and events where the hits are due to noise only. The occupancy from BIB is taken to be the average number of excess hits relative to the expected number of noise hits¹ in events identified as containing BIB. The BIB selection is applied to all UIBE in a run; from this, the rate of BIB and its per-bunch occupancy contribution are calculated for different run conditions. The bunches are assumed to be similar enough that it is valid to extrapolate from the BIB rate and occupancy in UI bunches to the rate and occupancy in paired bunches, and calculate the BIB occupancy correction for the paired bunches. Any correlation between bunch intensity and BIB occupancy should be accounted for. A previous

¹The occupancy distributions are made of two separate distributions: occupancy from noise only events and occupancy from events with BIB. There is a distinct low occupancy peak from which the average noise only occupancy is inferred.

study analysed and developed a selection for BIB in run 1 [98].

Five runs are analysed in order to gain information about BIB rates under different run conditions: 276689, 298771, 301918, 283270 and 300279. The time bin pattern of SCT hits was available for run 276689, so BIB characteristics associated with the timing of SCT hits were used to select and analyse BIB events. For the remaining runs, this timing information was not available and an alternative selection was employed. Run 298771 and 301918 were “pressure-bump runs” during which the pressure of residual gas in the beam pipe was varied to investigate the impact on BIB rate. Runs 283270 and 300279 were analysed to compare BIB between a 2015 and 2016 run, since the average intensity of bunches was higher in 2016.

Datasets collected using a background trigger are used for BIB studies. Initially, all events are analysed so that the characteristics of selected BIB events can be compared to noise only events. Then, for runs 283270, 300279, 298771 and 300918, the analysis was carried out on events only if they passed a Beam Conditions Monitor (BCM) trigger, based on the BCM A-to-C and C-to-A background coincidence during UI bunches (A being the half of the ATLAS detector covering the $+z$ side of the beam axis and C being the half covering the $-z$ side. The BCM trigger is fired if hits are 12.5 ns early on one side of the BCM (the side of the incoming beam), and in-time on the opposite side. Beam 1 events had to pass the BCM A-to-C trigger, and beam 2 events had to pass the C-to-A trigger. The purpose of this was to understand the fraction of BCM-triggered BIB events that also have BIB activity in the SCT, and to allow BIB analyses to be compared across the different subdetectors, as the same BCM-triggered events were used.

9.2 Analysis with timing information

9.2.1 Characteristics of Beam-induced Background Events (Run 276689)

The most prominent feature of beam-induced background in the SCT is the time-asymmetry of the hits it produces in the outer end-caps. The geometry of the end-caps is shown in Figure 9.2. The timing information of SCT hits is recorded as follows: every bunch crossing, binary hit information (1 or 0) is read out in three 25 ns time bins ($X_1 X_2 X_3$) for each strip that registers a hit. The centre (in-time) bin corresponds to the expected time of hits from a collision, with an early and a late bin on each side. In general, the SCT is run in X1X mode; only strips recording an X1X time bin pattern are read out (i.e. a hit must be recorded during the in-time bin). $X_n=1$ if the charge collected in the strip exceeds the 1fC threshold during the n^{th} time bin, otherwise $X_n = 0$. A strip is said to have registered an early hit if the hit pattern 1XX is read out (effectively, this means 110 or 111, since 101 hits are discarded). Readout patterns 01X (i.e. 010 or 011) are regarded as in-time hits.

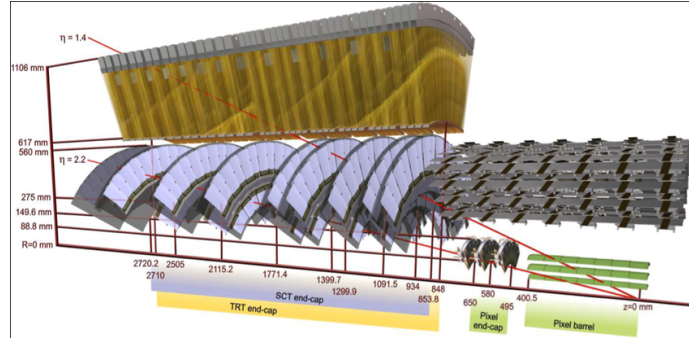


Figure 9.2: A diagram of the inner detector showing the SCT end-cap disks and their distances from IP1, taken from reference [99].

The end-cap disks lie between $|z| = 0.85\text{m}$ and $|z| = 2.72\text{m}$, with disks 7 at $|z| = 2.505\text{m}$ and disks 8 at $|z| = 2.71\text{m}$, where z is the distance along the z -axis from IP1. The outermost disk on end-cap C has one quadrant that is inoperable, so hit information from disk 9 on both end-caps is excluded from this study. Hits from BIB parallel to a bunch will arrive early with respect to hits from a p - p collision in the disks of the upstream end-cap. The upstream end-cap will be referred to as EC1; it is ECA for beam 1 and ECC for beam 2. BIB will produce hits in the downstream end-cap (EC2) approximately in-time with p - p collision hits. BIB hits produced in EC1 will be early by about

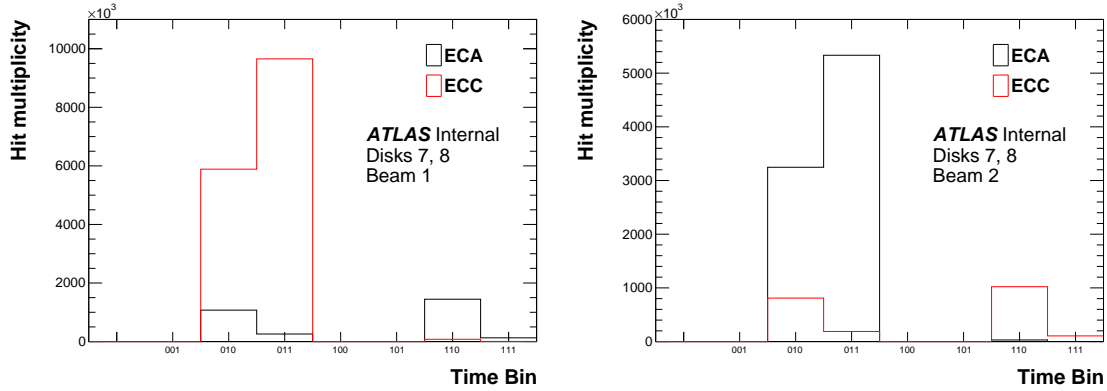
$$\Delta t = \frac{2|z|}{c}. \quad (9.1)$$

This means that BIB hits in disks 7 and 8 will be early by 16 – 18 ns, and are the most likely to register as an early hit. The distribution of the time bin pattern of outer end-cap hits (disks 7 and 8) during UIBE are shown in Figure 9.3. Events from UI bunches in beam 1 have mainly early hits in ECA and mainly in-time hits in ECC, and vice versa for beam 2.

Two quantities that can be used to identify UIBE that contain BIB are the number of early hits in the outer disks of EC1 (N_{early}) and z -asymmetry (z_{asym}), which quantifies the end-cap asymmetry of early hits in the outer end-cap disks:

$$z_{\text{asym}} = \frac{N_{\text{early}}(z > 0) - N_{\text{early}}(z < 0)}{N_{\text{early}}(z > 0) + N_{\text{early}}(z < 0)} \quad (9.2)$$

The z -asymmetry distributions for events during different types of bunches are shown in Figure 9.4. BIB activity in events from unpaired, isolated bunches cause the high z -asymmetry in Figures 9.4(a) and 9.4(b). The noise events in Figure 9.4(c) have an approximately uniform z -asymmetry distribution, with statistical fluctuations. The distribution in Figure 9.4(d) is a result of collision events, which have low z -asymmetry centred on zero due to the symmetry of collision hits. The early and in-time outer end-cap hit multiplicity distributions



(a) Beam 1 unpaired, isolated bunches

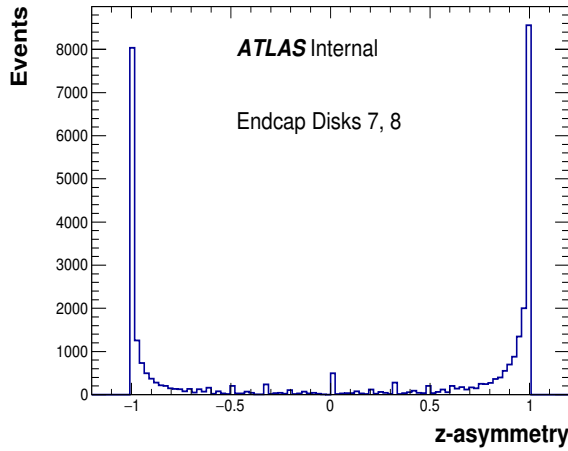
(b) Beam 2 unpaired, isolated bunches

Figure 9.3: Distribution of the time bin pattern of hits in disks 7 and 8 of the SCT end-caps, during unpaired, isolated bunches. During beam 1 unpaired isolated bunches (a), there are fewer hits in the outer disks of end-cap A than end-cap C, and about 50% of end-cap A hits count as early hits, whereas the end-cap C hits are mostly in-time. The result is symmetrical for beam 2 (b).

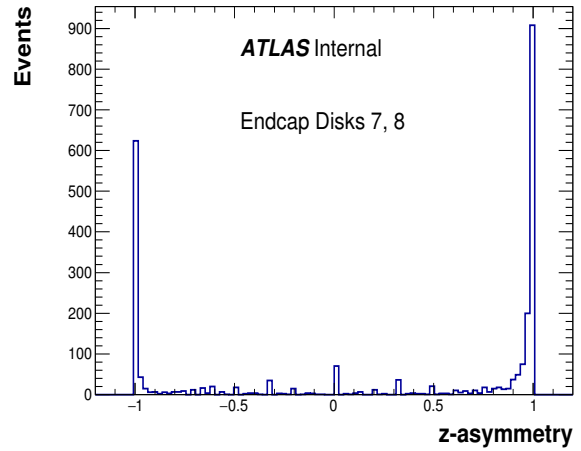
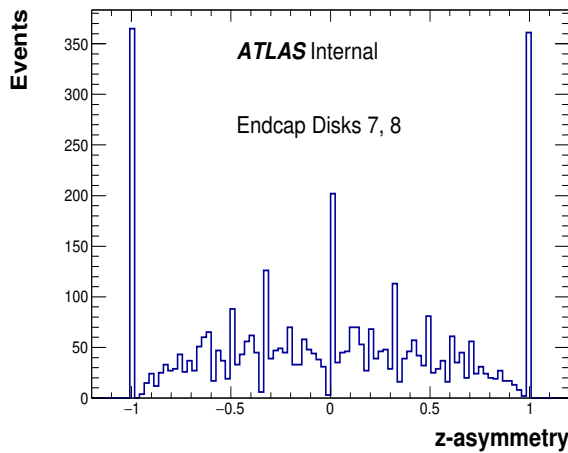
for events during unpaired, isolated bunches is shown in Figure 9.5. When present in an event, BIB is expected to produce excess early hits in EC1, and excess in-time hits in EC2. Figure 9.5 confirms this, and shows that BIB also produces an excess of in-time hits in EC1. Applying a cut to the z -asymmetry of UIBE should ensure that events containing significant (high occupancy) BIB are selected. An additional cut on the number of early hits in the outer disks of EC1 should mitigate noise-only events. The BIB selection applied to UIBE is $N_{\text{early}} > 20$ and $|z_{\text{asym}}| > 0.5$, where N_{early} is the number of early hits in disks 7 and 8 of EC1. This selection is evaluated by comparing the hit multiplicity distributions in selected and non-selected events for each set of disks, shown in Figure 9.6. Beam 1 events are analysed, but the same results hold for beam 2 events if $ECA \rightarrow ECC$ and $ECC \rightarrow ECA$.

Inner disks (1-2): Both selected and non-selected events have a similar early hit multiplicity distribution in EC2; early EC2 hits are expected to be due to noise in both BIB and noise-only events. There is a slight excess of selected events with a large EC1 early hit multiplicity compared to non-selected events. This small difference is due to the small z distance of the disks from IP1, with fewer BIB hits registering as early in EC1. Disk 1 lies at $|z| = 0.85\text{m}$ and disk 2 at $|z| = 0.93\text{m}$; BIB hits are expected to be early by 5-6ns. The in-time EC1 and EC2 distributions for selected events both have a large tail out to 3000-4000 hits. Both tails are an expected result of BIB; BIB hits are registering as in-time in the inner EC1 disks at small z , and as in-time in the downstream EC2.

Middle disks (3-6): Similar to disks 1 and 2, except the difference between the EC1 early



(a) UI bcid, event contains no primary vertices

(b) UI bcid, events contain ≥ 1 primary vertex

(c) non-UI bcid, event contains no primary vertices

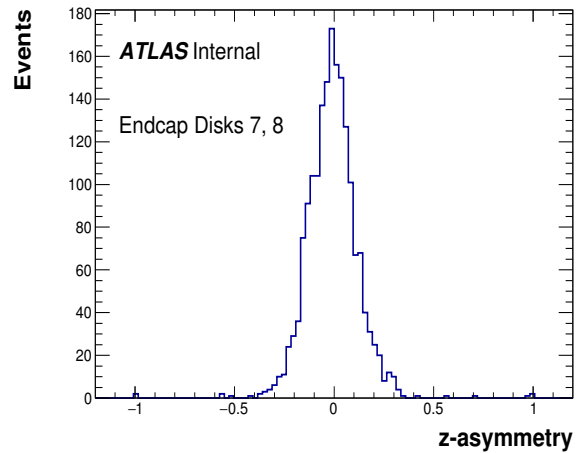
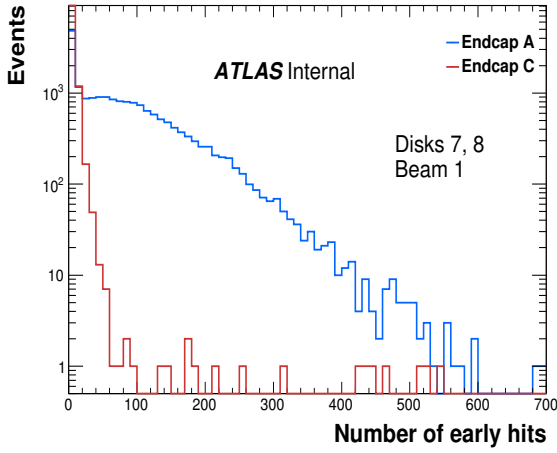
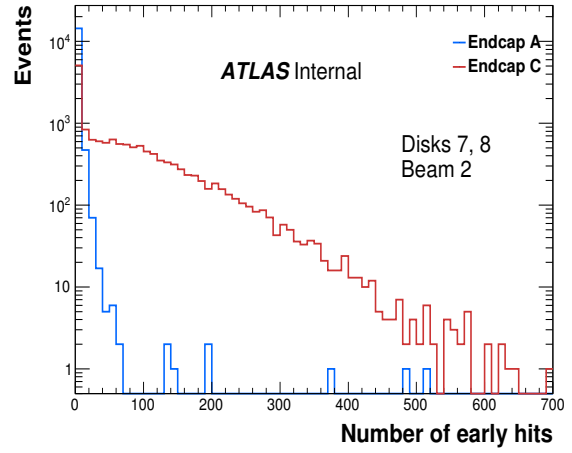
(d) non-UI bcid, event contains ≥ 1 primary vertex

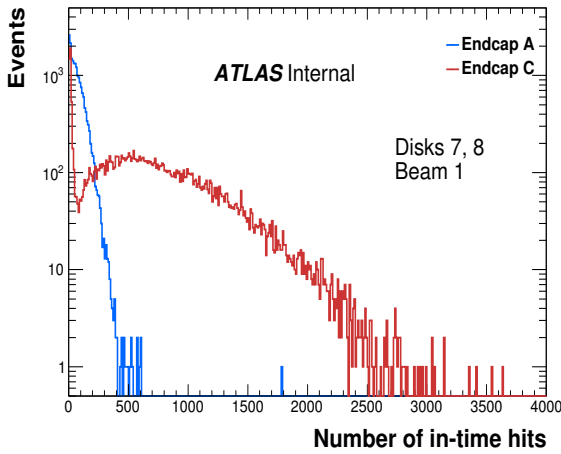
Figure 9.4: The z -asymmetry distribution of (a) events during unpaired isolated bunches containing no primary vertices, (b) events during unpaired, isolated bunches containing a primary vertex, (c) events during non- unpaired, isolated bunches containing no primary vertices, (d) events during non- unpaired isolated bunches containing a primary vertex. Beam-induced background activity during unpaired, isolated bunches causes the high z -asymmetry of events in (a) and (b). In noise-only events (c), the distribution of hits should be random. The z -asymmetry distribution is approximately uniform, with statistical fluctuations. The peaks at $|z_{\text{asym}}| = 1$ in (a), (b) and (c) are a result of events where there are only hits in the outer disks of one end-cap. The peak at 0 is a result of events where there are no or an equal number of hits in the outer end-cap disks. Collision events (d) have a low z -asymmetry, centred on 0; asymmetric BIB effects are negligible compared to the symmetric collision hits.



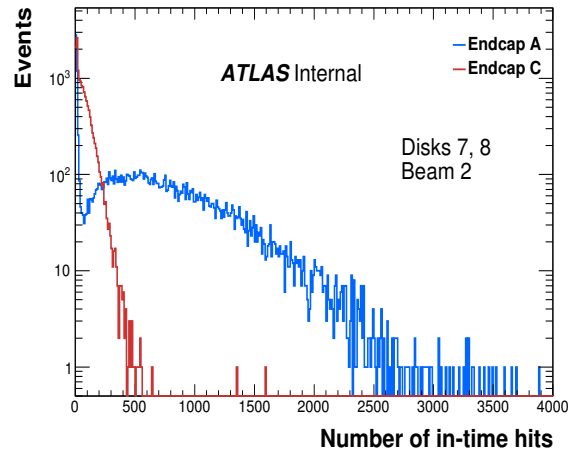
(a) Beam 1 UIBE



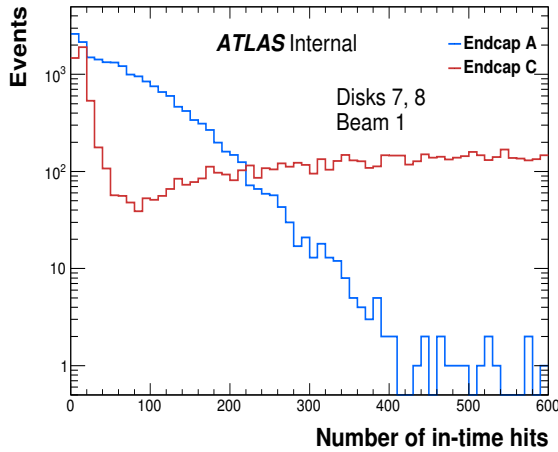
(b) Beam 2 UIBE



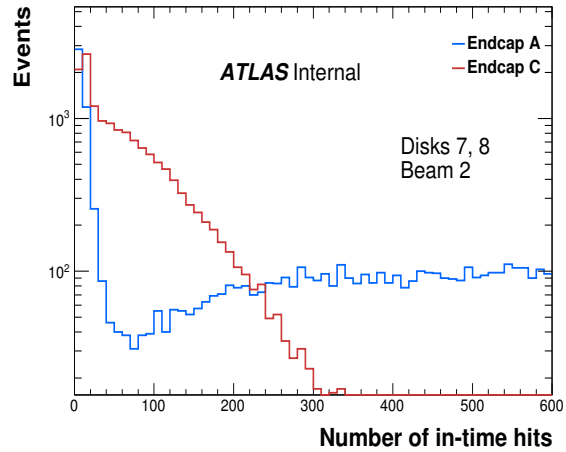
(c) Beam 1 UIBE



(d) Beam 2 UIBE



(e) Beam 1 UIBE



(f) Beam 2 UIBE

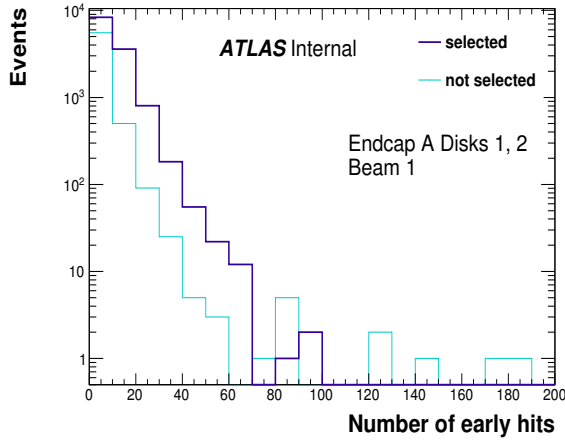
Figure 9.5: The distribution of early hit multiplicity (a), (b), in the outer end-caps, and the distribution of in-time hit multiplicity (c), (d), (e), (f) in the outer end-caps in events during unpaired, isolated bunches. (a) and (b) show that the EC1 early hit multiplicity distribution has a peak at $N_{\text{early hits}} < 25$. This peak is due to events containing little or no BIB activity. The large tail of events with high early hit multiplicity is due to BIB events. The EC2 early hit multiplicity also has a peak at $N_{\text{early hits}} < 25$. This peak is larger than the peak for EC1, since both BIB and noise-only events have low early hit multiplicity in EC2. The EC2 in-time distribution peaks at low multiplicity, the contribution of noise-only events, and has a large tail, due to BIB. The EC1 in-time distribution also peaks at low multiplicity, due to noise-only events, with a smaller tail, a result of EC1 in-time hits during BIB events. Subfigures (e) and (f), zoomed-in versions of (c) and (d), show the in-time hit distributions at low in-time hit multiplicities; it can be seen that the EC1 and EC2 in-time distributions are similar in shape, but the effect is amplified for EC2 hits. The EC1 in-time hits tail extends to ~ 500 hits, the EC1 early hits tail extends to ~ 600 hits, and the EC2 in-time hits tail extends to ~ 4000 hits.

hit multiplicity distribution tail for selected and non-selected events is more pronounced because of the increased z -distance of the disks, and the larger number of BIB hits registering as early in EC1. The high multiplicity tail of the EC1 in-time hit distribution in selected events remains as the z distance increases. The fact that this tail occurs only for the selected events distribution suggests that this is a physical effect related to BIB.

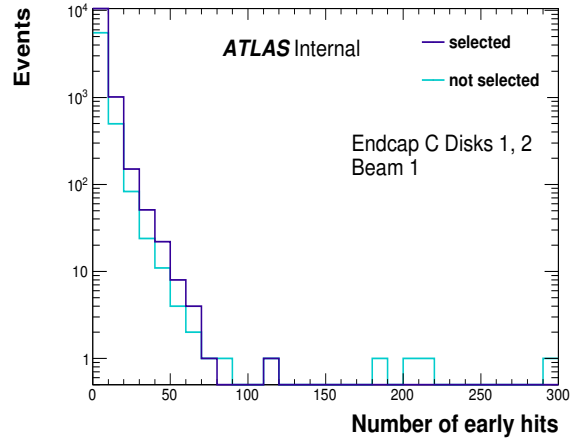
Outer disks (7-8): The outer disks have the largest asymmetry in the EC1 early hits distributions between selected and non-selected events. The in-time hit distribution asymmetry between selected and non-selected events is also present in both EC1 and EC2.

Efficiency and purity: The plots in Figures 9.5(c) and 9.5(d), which show the outer end-cap in-time hit multiplicity distributions for UIBE, suggest that the BIB selection, which is based on early hits, should remove events with fewer than 250 in-time hits in EC2. The initial peak in the EC2 distributions at $n_{\text{hits}} < 100$ (shown more clearly in Figures 9.5(e) and 9.5(f)) is a result of events with no or very little BIB activity in the SCT. EC1 has the same shape of distribution, with a lower average multiplicity. From Figure 9.6 it can be seen that a fraction of selected events have fewer than 250 in-time EC2 hits, and a fraction of non-selected events have more than 250 in-time EC2 hits. The fraction of BIB events failing the BIB selection is estimated to be approximately 10% for both beams, under the assumption that all events with > 250 in-time hits in EC2 are BIB. The fraction of noise events passing the selection is negligible.

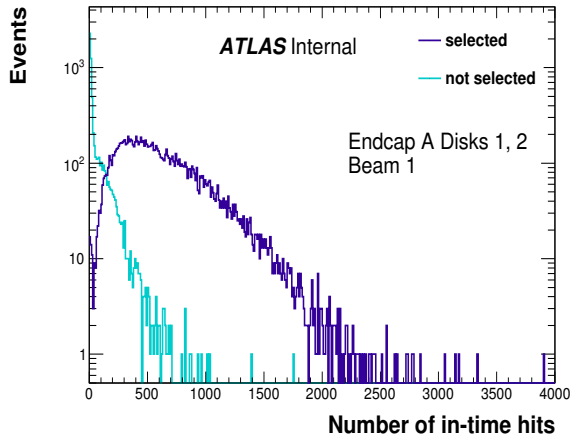
EC1 in-time excess: Figure 9.7 shows the in-time end-cap hit multiplicity plotted against early end-cap multiplicity in all, selected, and non-selected beam 2 events. In-time hit multiplicity is proportional to early hit multiplicity in EC1 during selected events, indicating that a component of BIB is responsible for the extra in-time hits in outer EC1. The same pattern is found in beam 1 events. Excluding the hits from non-selected BIB events, there are few in-time and early EC1 hits during noise-only events; the in-time EC1 excess is only present in BIB events. In EC2, in-time hits are dominant in BIB events and are not correlated with early hits (which should be from noise). To determine whether the EC1 in-time excess BIB effect is always present in the run, the average number of in-time EC1 hits per event, per selected event, and per non-selected event are shown Figure 9.8. The EC1 in-time occupancy contribution appears is fairly uniform in lumi block and bcid, over the lumi blocks available in the dataset.



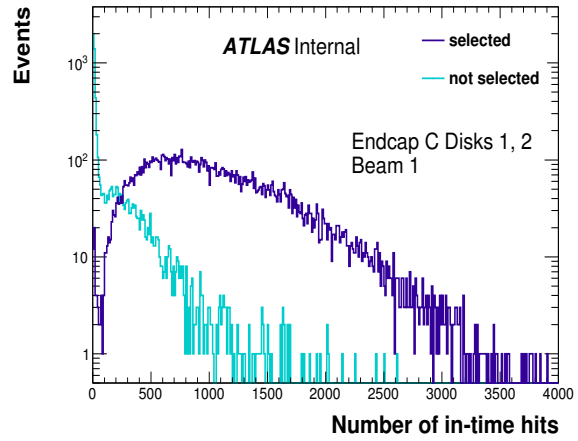
(a) End-cap A disks 1, 2



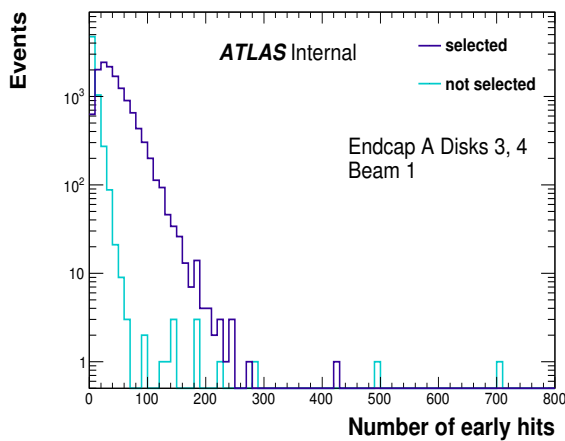
(b) End-cap C disks 1, 2



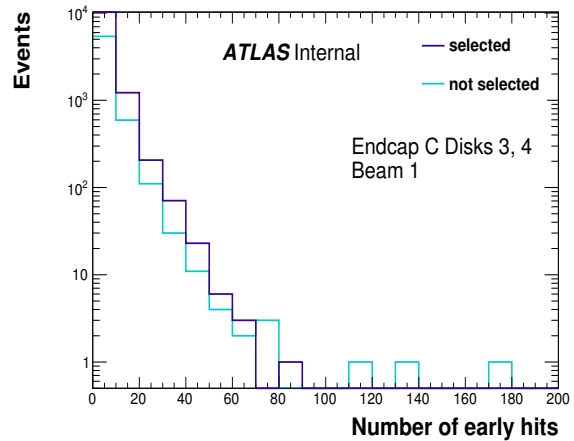
(c) End-cap A disks 1, 2



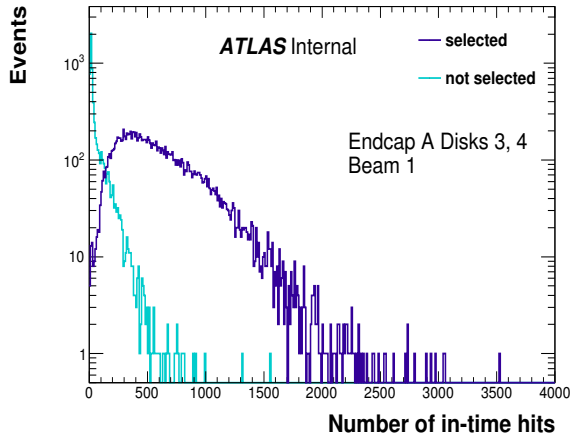
(d) End-cap C disks 1, 2



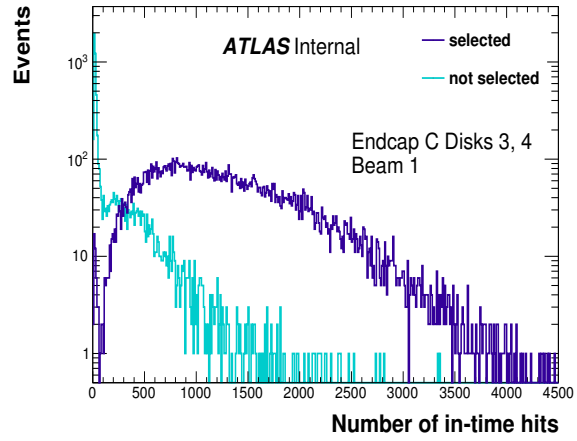
(e) End-cap A disks 3, 4



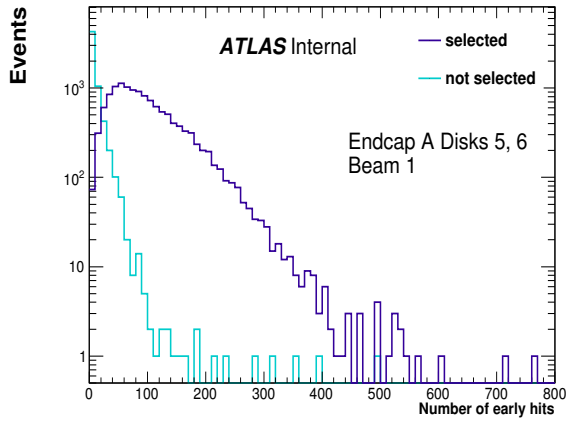
(f) End-cap C disks 3, 4



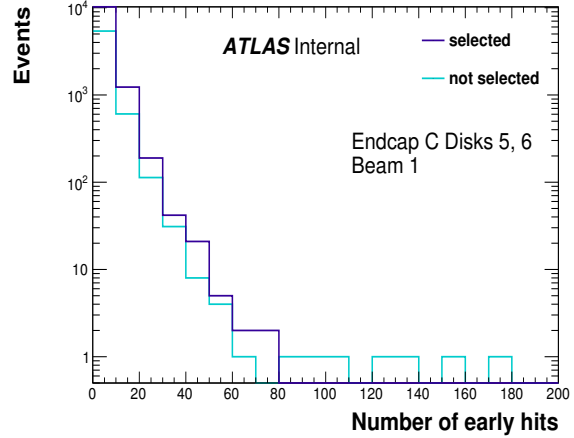
(g) End-cap A disks 3, 4



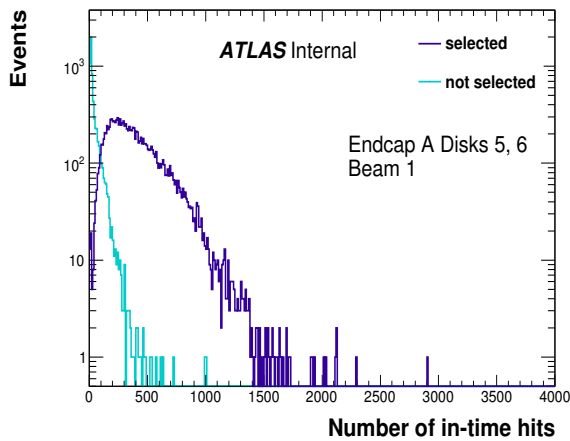
(h) End-cap C disks 3, 4



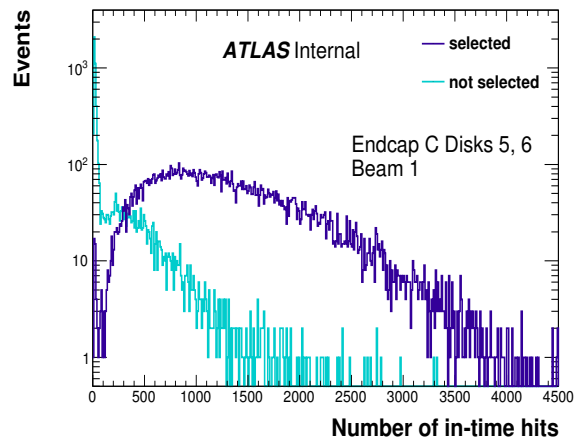
(i) End-cap A disks 5, 6



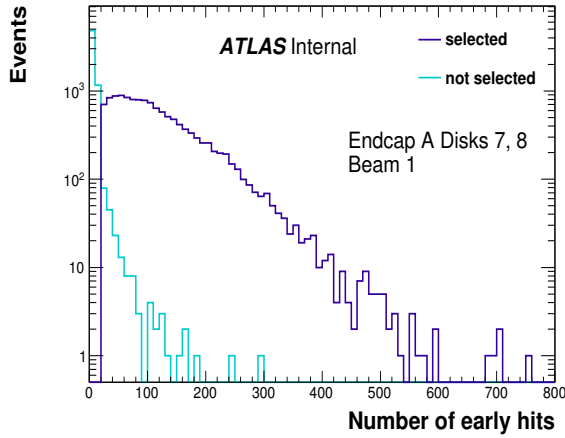
(j) End-cap C disks 5, 6



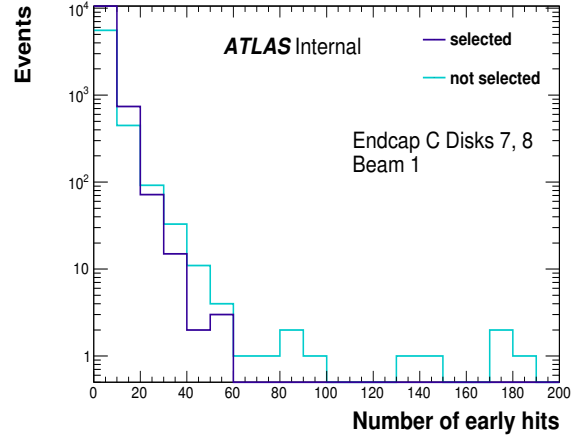
(k) End-cap A disks 5, 6



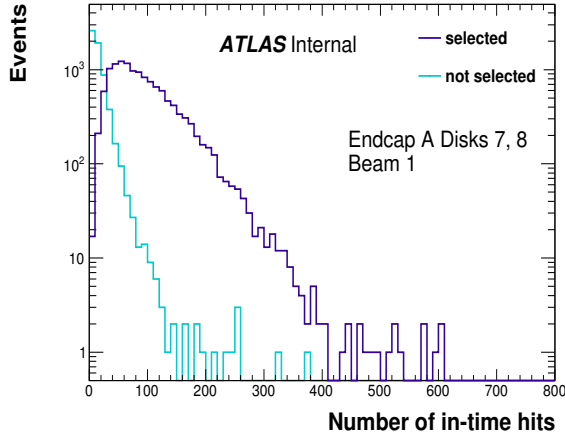
(l) End-cap C disks 5, 6



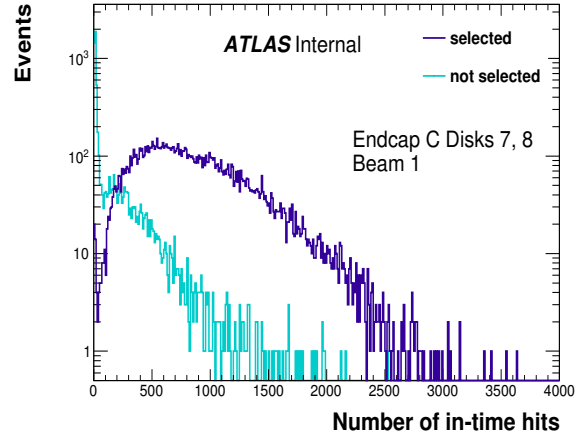
(m) End-cap A disks 7, 8



(n) End-cap C disks 7, 8



(o) End-cap A disks 7, 8



(p) End-cap C disks 7, 8

Figure 9.6: The early and in-time hit multiplicity distributions in each pair of end-cap disks are shown for events selected as BIB, and events not selected as BIB. This illustrates the relationship between the distance of the end-cap from IP1 and the average occupancy contribution from BIB. The distributions (b), (f), (j), (n), show that the EC2 early hit multiplicity distributions are very similar for selected and non-selected events, as these hits are from noise only. The distributions (a), (e), (i), (m), show that the average EC1 early hit multiplicity in selected events increases with the z distance of the disk from IP1. (c), (g), (k), (o), show that the average in-time EC1 hits is significantly greater in selected BIB events than noise events. This is expected for disks closer to IP1, as many BIB hits will arrive at the disk in-time with expected collision hits. The EC2 in-time distribution tail extends out to ~ 3000 hits for the inner disks, and decreases with distance from IP1, extending to ~ 600 hits for the outer disks, indicating that BIB hits still cause in-time EC1 hits in the outer disks. (d), (h), (l) and (p) show that the largest occupancy difference between selected BIB and noise events is the average EC2 in-time hit multiplicity, and this difference is present in all disks.

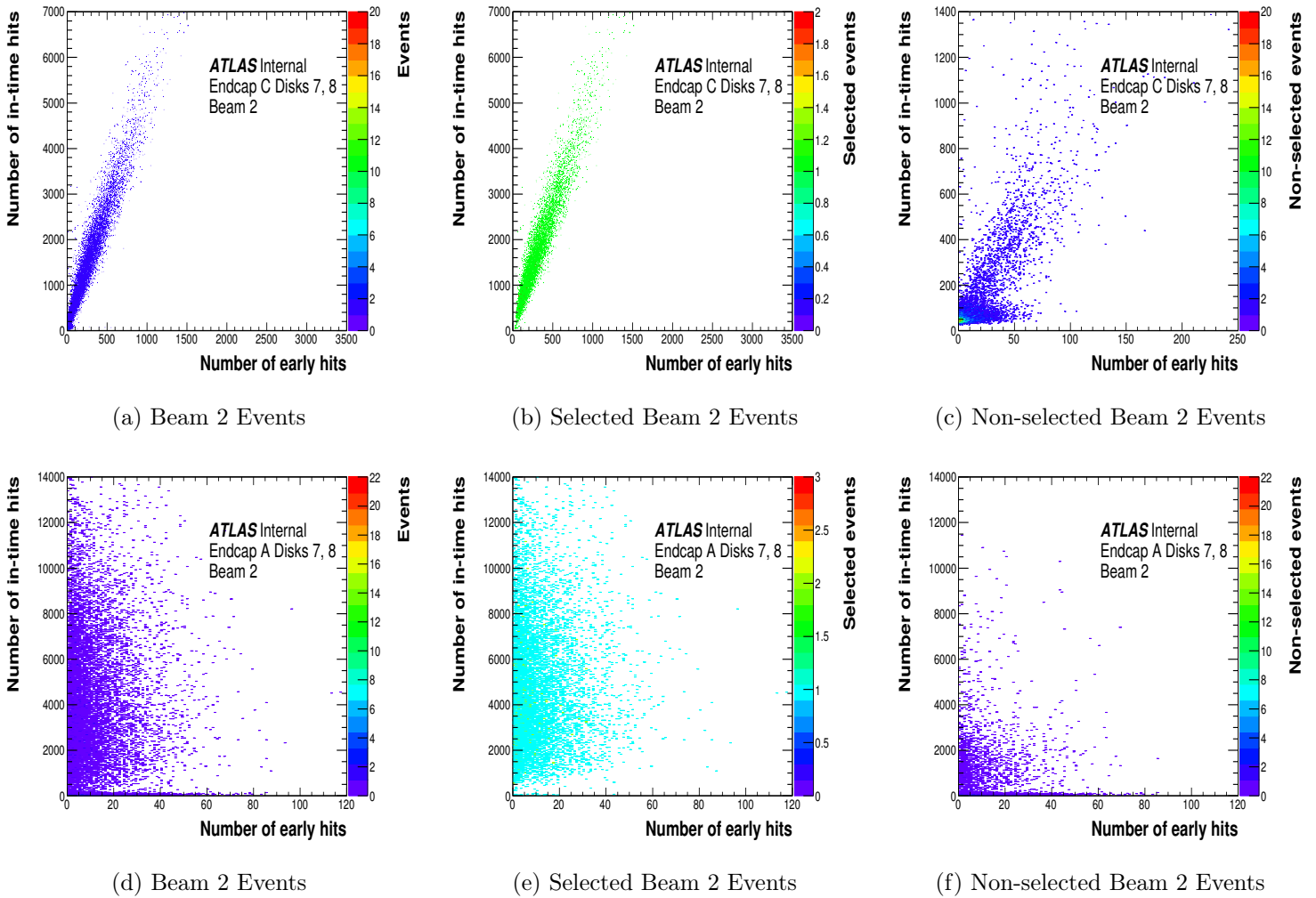


Figure 9.7: In-time outer end-cap hits plotted against early outer end-cap hits for all ((a), (d)), selected ((b), (e)), and non-selected ((f), (g)) unpaired, isolated beam 2 events. In-time outer EC1 hit multiplicity is proportional to early outer EC1 hit multiplicity in selected BIB events. The EC2 hits in selected BIB events are mainly in-time.

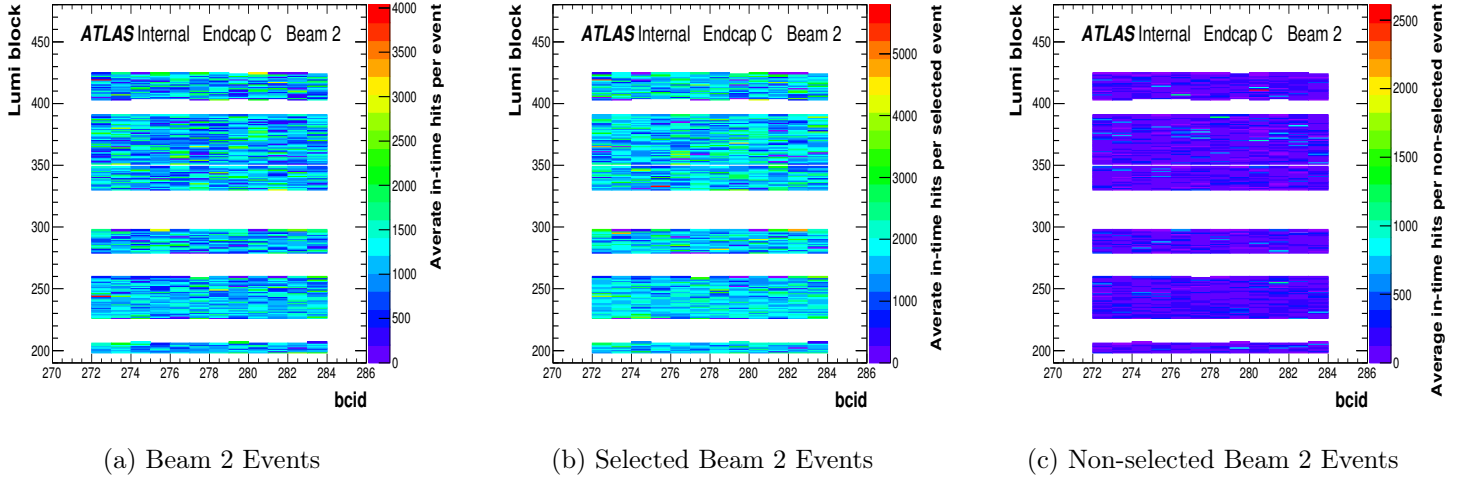


Figure 9.8: The average in-time EC1 hit multiplicity per UIBE (a), selected UIBE (b) and non-selected UIBE (c). The high in-time EC1 occupancy in BIB events appear to be uniformly distributed in lumi block and bcid.

9.3 Analysis Without Timing Information

After run 304178 (22/07/16), the SCT was operated in 01X mode (i.e. only strips which register no hit in the early bin and a hit in the in-time bin are read out) to control data rates which increase with increasing instantaneous luminosity. The BIB selection was modified to exploit BIB event characteristics based on all hits, instead of early and in-time hits. In BIB events, there are more hits in EC2, the downstream end-cap, than EC1. This is because the in-time excess in EC2 from BIB hits is greater than the combined early and in-time excess in EC1. z -asymmetry is redefined as:

$$z_{\text{asym}} = \frac{N_{\text{hits}}(z > 0) - N_{\text{hits}}(z < 0)}{N_{\text{hits}}(z > 0) + N_{\text{hits}}(z < 0)} \quad (9.3)$$

where N_{hits} is the total number of hits in disks 7 and 8 of the end-caps.

9.3.1 Comparing 2015 and 2016

Runs 283270 and 300279 were analysed to compare BIB between a 2015 run and a 2016 run.

End-cap hits during UIBE: Noise and BIB events can be distinguished by looking at the total number of outer EC2 end-cap hits in an event. Figure 9.9 shows the end-cap hit multiplicity distributions for beam 1 and beam 2 UIBE. The EC2 distribution can be separated into a peak at low hit multiplicity, comprised of noise-only events, and a long tail extending to ~ 3000 hits, comprised of events where there is significant BIB activity. The z -asymmetry

	2015 run	2016 run
Beam 1 events	0.758	0.787
Beam 2 events	0.696	0.739

Table 9.1: Fraction of events selected as BIB in run 283270 (2015) and 300279 (2016).

distributions for beam 1 and beam 2 UIBE are shown in Figure 9.10.

The BIB selection applied to the 2015 and 2016 run is:

Beam 1: ≥ 25 early hits in disks 7 and 8 of end-cap C, $z_{\text{asym}} \leq -0.5$

Beam 2: ≥ 25 early hits in disks 7 and 8 of end-cap A, $z_{\text{asym}} \geq 0.5$

The outer end-cap hit multiplicity distributions for selected and non-selected events are shown in Figure 9.11. The EC2 distribution for selected events has a small peak at low multiplicity from selected noise events, and a tail extends to ~ 3000 hits for selected events. The EC1 distributions show that selected events have a higher average EC1 hit multiplicity compared to non-selected events, and this difference is less than the differences in EC2 hits; the EC2 hit multiplicity is a better variable for rejecting noise-only events.

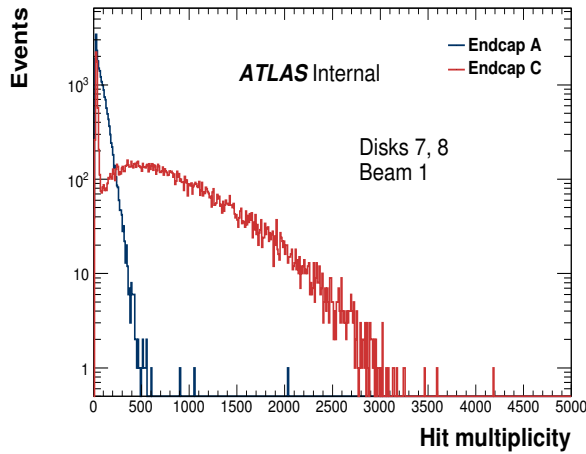
The rate of BIB in a run is obtained by applying the BIB selection to all UI events; it is defined to be:

$$\text{BIB rate} = \frac{\text{number of selected events}}{\text{total UIBE}} \quad (9.4)$$

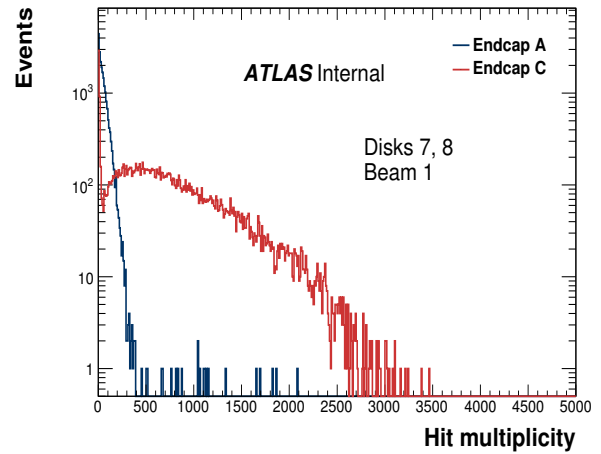
Table 9.1 shows the fraction of UIBE events that contain BIB. It is assumed that this rate is approximately constant for the whole run. There is a slightly larger fraction of BIB events in the 2016 run. This is consistent with the z -asymmetry plots in Figure 9.10; the 2015 run has a higher percentage of noise events with low z -asymmetry than the 2016 run.

9.3.2 Pressure Bump Runs

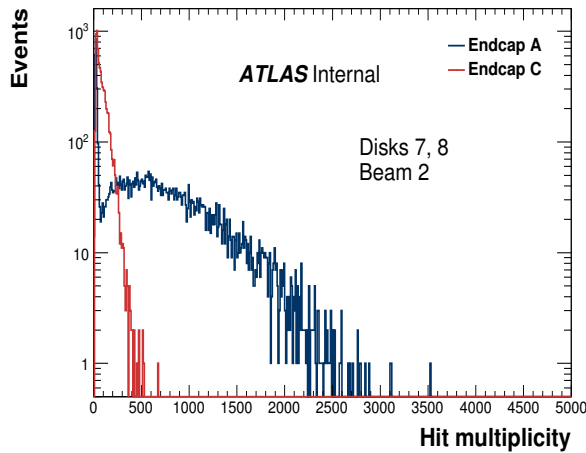
During run 298771, fill 4905, the residual gas pressure inside the beam pipe was increased in a localised area for a period of several lumi blocks at distances along the z -axis of ± 150 m, ± 58 m and ± 19 m from IP1; details of the pressure bumps are shown in Table 9.2. The width of the increased pressure was ~ 1 metre around the non evaporative getter. The purpose of this was to test the impact of a localised increase in beam pipe pressure, and its distance from ATLAS, on the BIB rate. The frequency of beam gas events is expected to be proportional to the residual gas pressure. As before, events during unpaired, isolated bunches were analysed to study BIB; there were 12 unpaired, isolated bunches per beam in the fill.



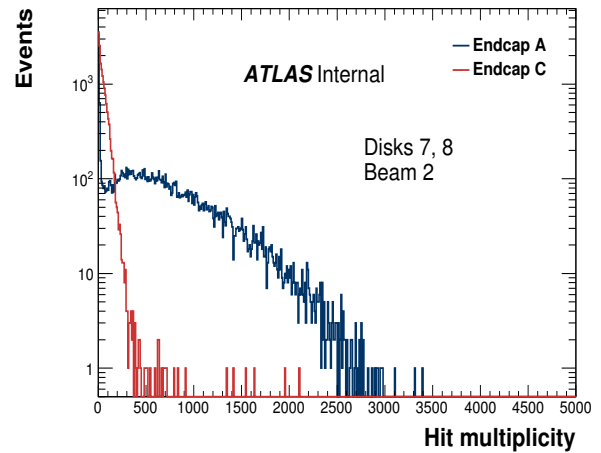
(a) 2015



(b) 2016

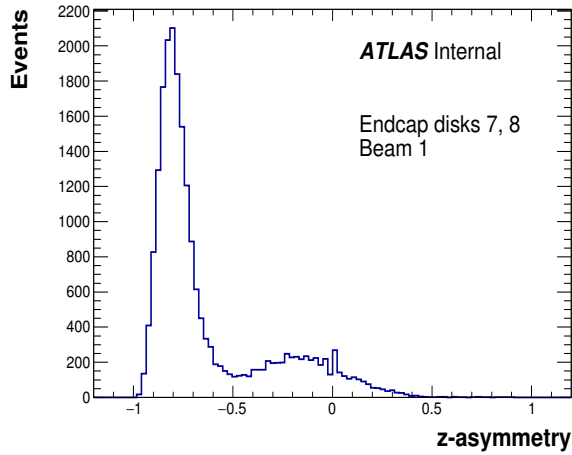


(c) 2015

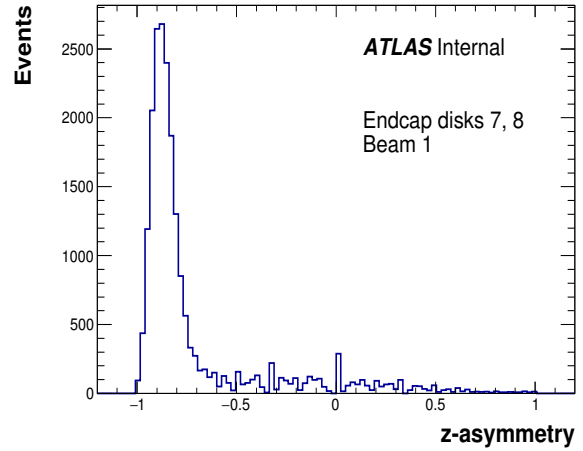


(d) 2016

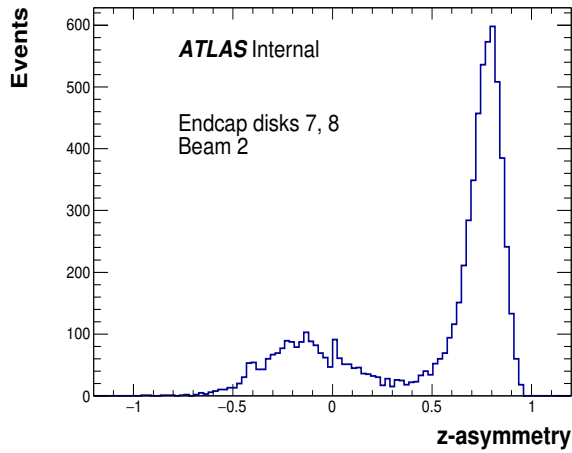
Figure 9.9: EC1 and EC2 hit multiplicity distributions for events during unpaired, isolated bunches. The EC2 distribution has a peak at low multiplicity due to noise-only events, and a tail out to high multiplicity due to events with BIB activity. The EC1 distribution also has a peak at low multiplicity, and a smaller tail due to excess early and in-time EC1 hits in BIB events.



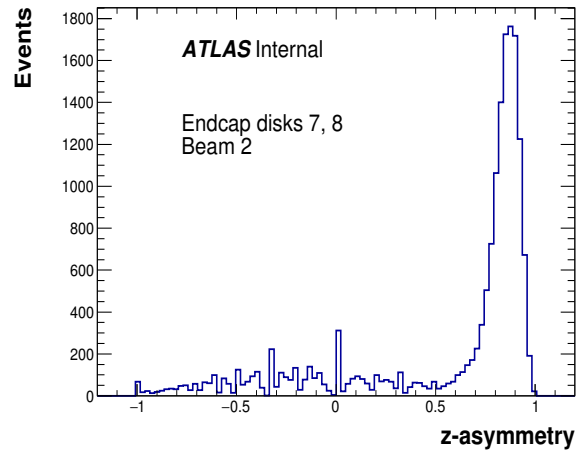
(a) 2015



(b) 2016

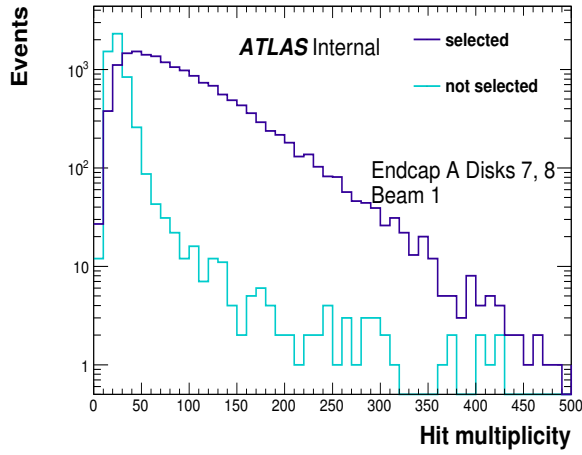


(c) 2015

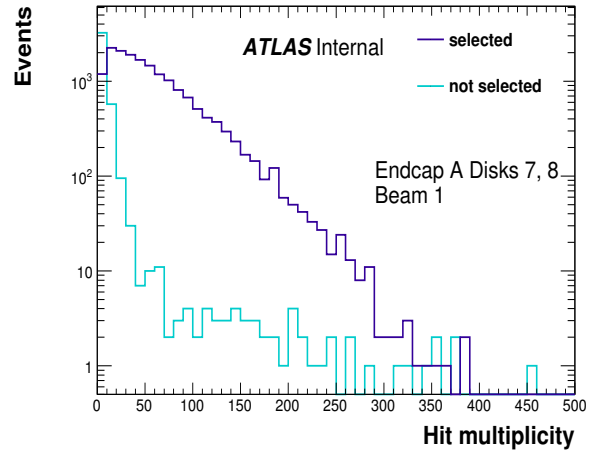


(d) 2016

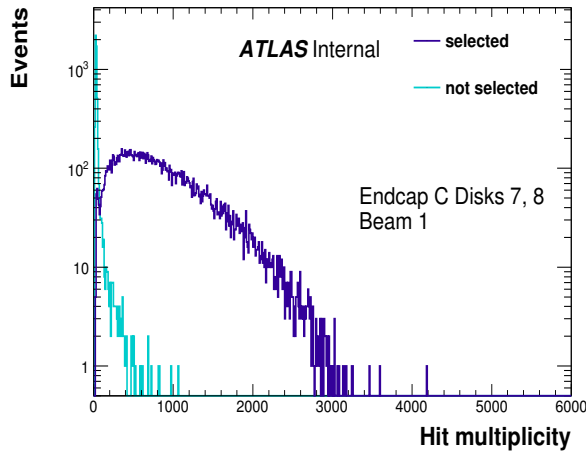
Figure 9.10: The z -asymmetry distributions for events during unpaired, isolated bunches, comprised of high z -asymmetry BIB events, and noise events with uniform z -asymmetry. The average BIB event z -asymmetry for beam 1 (2) has changed $+z \rightarrow -z$ ($-z \rightarrow +z$) because all hits, instead of early hits, are now used.



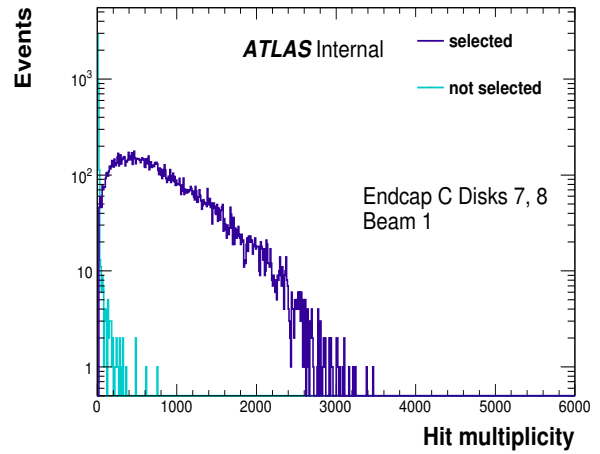
(a) 2015



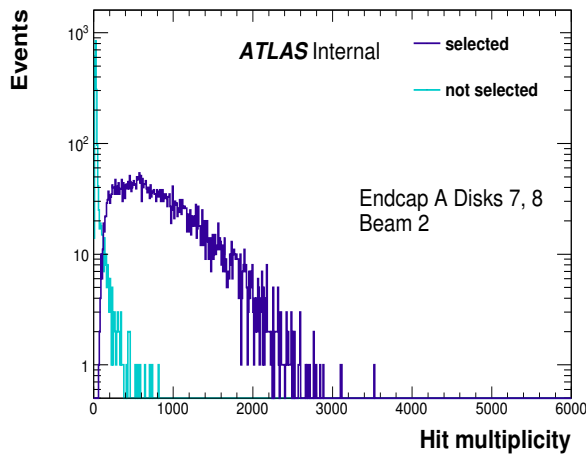
(b) 2016



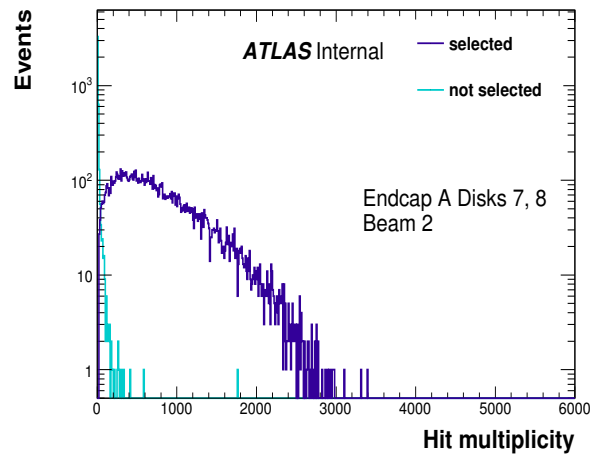
(c) 2015



(d) 2016



(e) 2015



(f) 2016

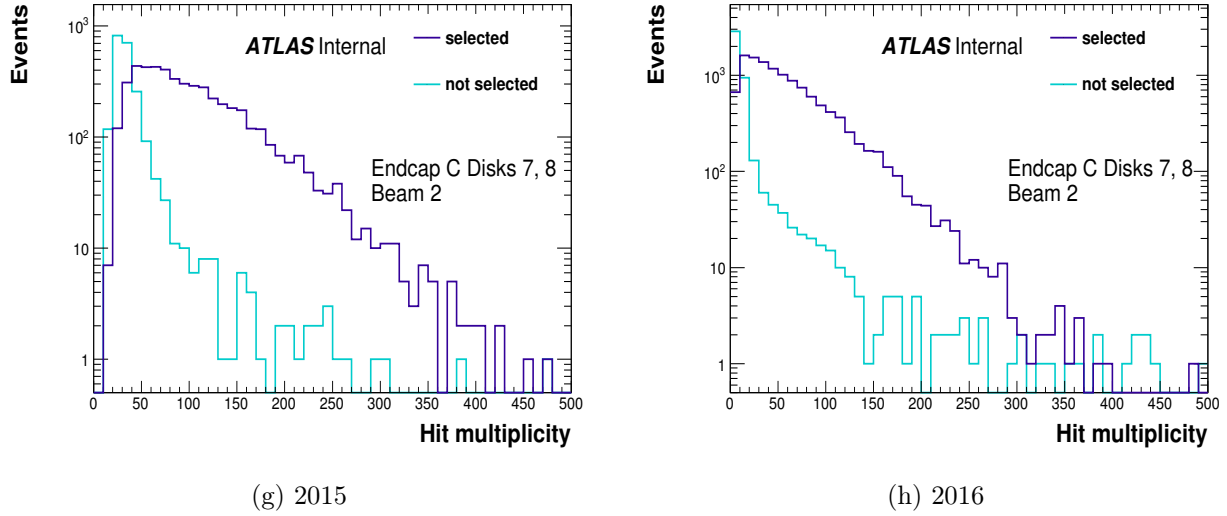


Figure 9.11: EC1 and EC2 hit multiplicity distributions for beam 1 and beam 2 UIBE in the 2015 and 2016 runs. Selected events have on average a larger EC1 and EC2 hit multiplicity than non-selected events. The greatest difference between noise and BIB events is the average EC2 hit multiplicity.

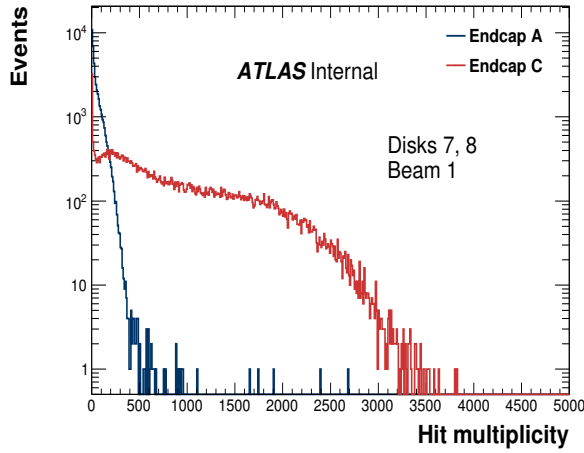
Pressure bump distance	Lumi block range	Pressure (beam 1)	Pressure (beam 2)
150 m	260-270	180 pbar	220 pbar
58 m	310-320	500 pbar	400 pbar
19 m	360-366	20 pbar	60 pbar
none	212-220	8×10^{-2} pbar	8×10^{-2} pbar

Table 9.2: Information about the pressure bumps in run 298771. The average bunch intensity was 0.99×10^{11} protons in beam 1 and 0.98×10^{11} protons in beam 2.

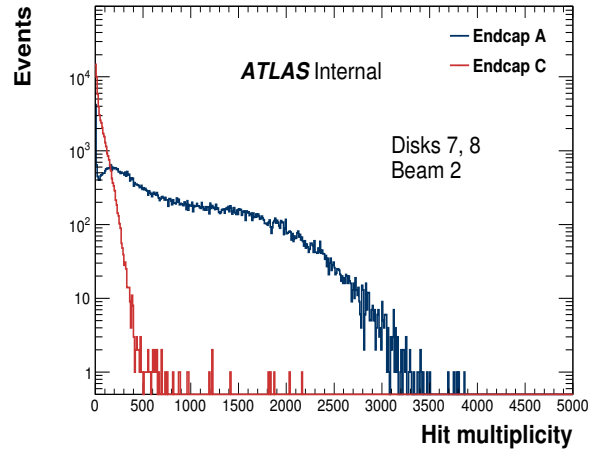
End-cap hits during UIBE: EC1 and EC2 hit multiplicity distributions for UIBE during the lumi blocks corresponding to each pressure bump, and during lumi blocks where there was no pressure bump, are shown in Figure 9.12. Compared to the distribution for normal pressure, the pressure bump distributions show a larger number of events with a higher average EC2 hit multiplicity. The distance of the pressure bump from IP1 also appears to affect the shape of the distribution.

z -asymmetry of UIBE: Figure 9.13 shows the z -asymmetry of UIBE during the 150 m pressure bump and with normal pressure. The ratio of high z -asymmetry events to low z -asymmetry (noise) events is greater during the pressure bump.

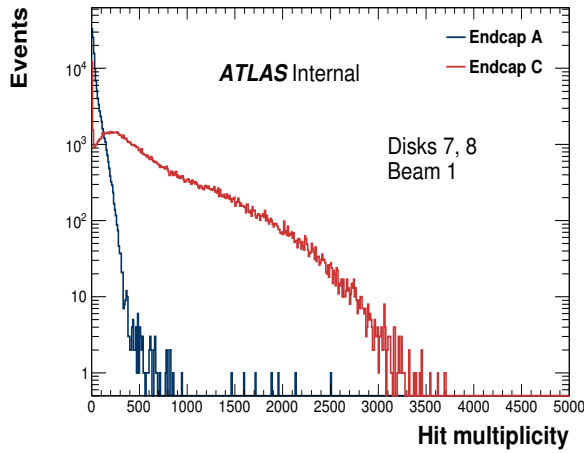
Phi variation: Beam induced background created during a beam gas or beam halo event travels outwards from the beam axis and can be influenced by the LHC's magnet system



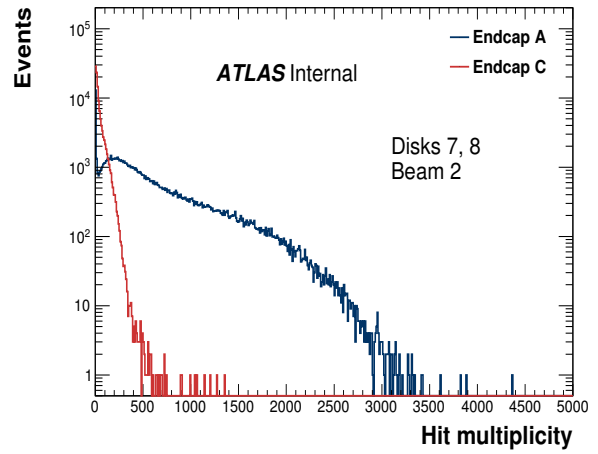
(a) 150 m pressure bump



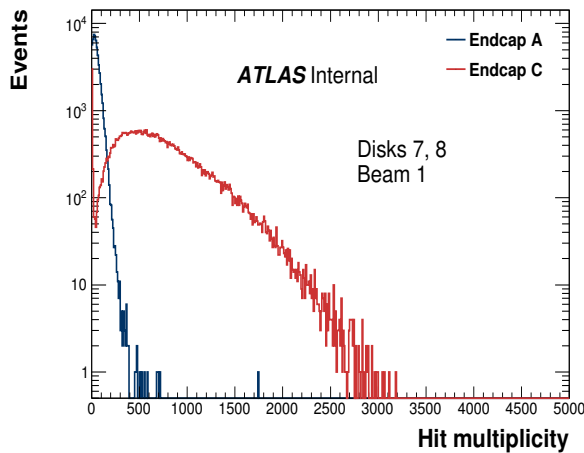
(b) 150 m pressure bump



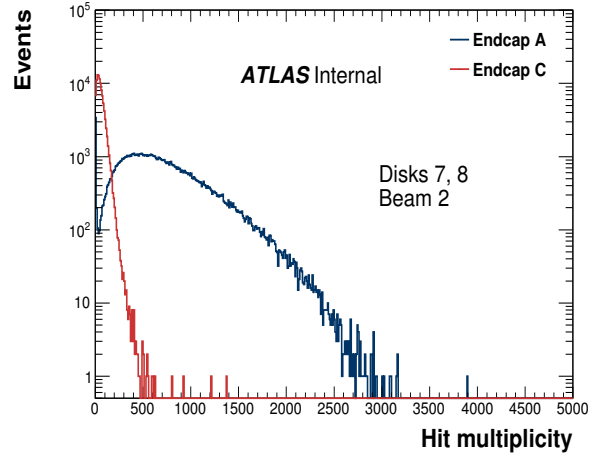
(c) 58 m pressure bump



(d) 58 m pressure bump



(e) 19 m pressure bump



(f) 19 m pressure bump

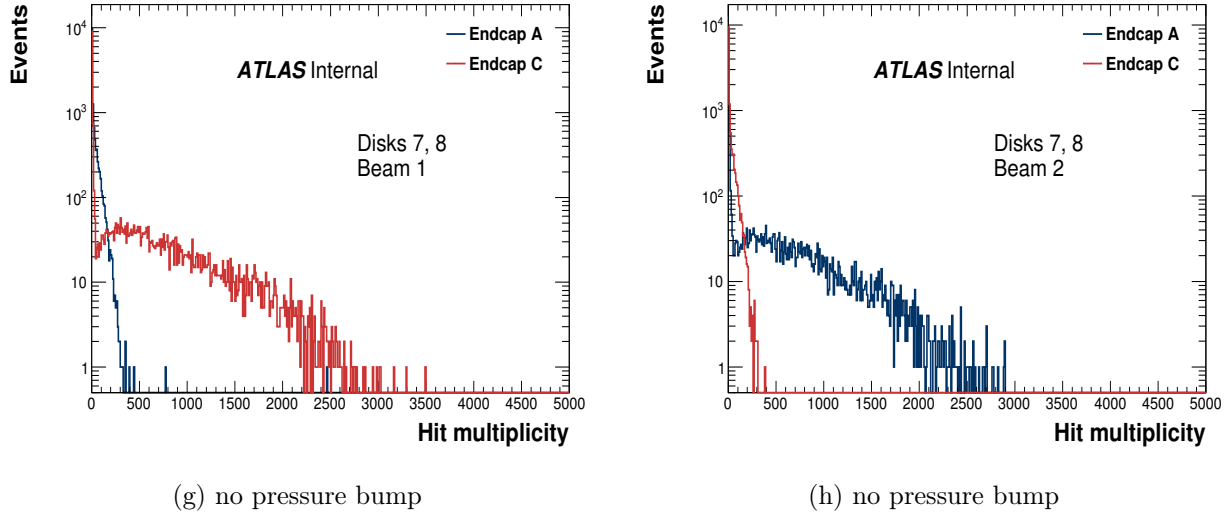


Figure 9.12: EC1 and EC2 hit multiplicity distributions for UIBE during lumi blocks corresponding to the 150 m, 58 m and 19 m pressure bumps, and during lumi blocks where there was no increase in pressure. The high multiplicity tails on the pressure bump distributions indicate that there are more high occupancy BIB events during pressure bumps.

	150 m	58 m	19 m	flat
Beam 1 events	0.904	0.877	0.939	0.361
Beam 2 events	0.905	0.863	0.959	0.296

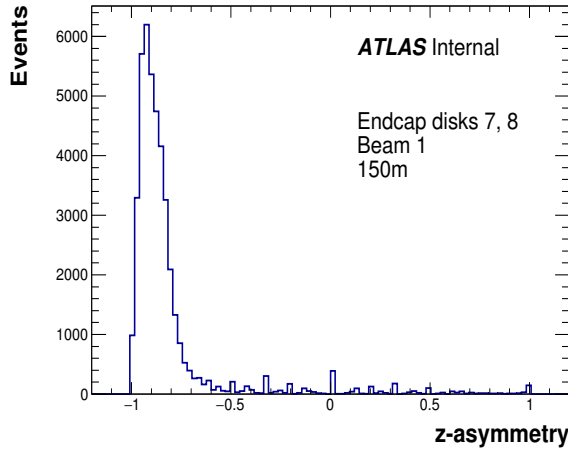
Table 9.3: Fraction of events in run 298771 selected as BIB.

before reaching ATLAS. This has an effect on the phi distribution of BIB hits, which is dependent on the distance of the beam-gas events from ATLAS. This effect most noticeable in downstream end-caps since $n_{\text{in-time hits}} \text{ in EC2} > n_{\text{early hits}} + n_{\text{in-time hits}} \text{ in EC1}$ during BIB events. Distributions of the global phi of end-cap hits are shown in Figure 9.14. A phi asymmetry in EC2 hits can be seen during pressure bump UIBE.

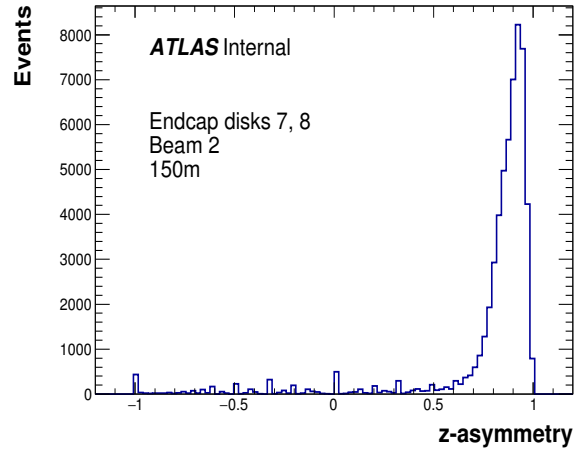
BIB selection: The end-cap hit multiplicity distributions for selected and non-selected events in each pressure bump and no pressure bump are shown in Figure 9.15. The BIB rate is calculated as in equation 9.4 and shown in Table 9.3. An additional pressure bump test was carried out during run 301918, fill 5005. Details of these pressure bumps can be found in Table 9.4. There were 12 unpaired, isolated bunches in each beam. The same selection was applied to UIBE in run 301918 and the BIB rates are shown in Table 9.5.

9.3.3 BCM Trigger

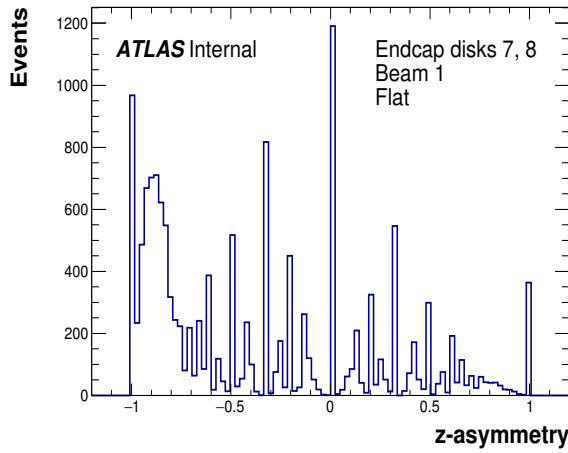
This section summarises the previous analysis applied only to events that passed the BCM trigger described in the introduction. The fraction of selected events for runs 283270, 300279,



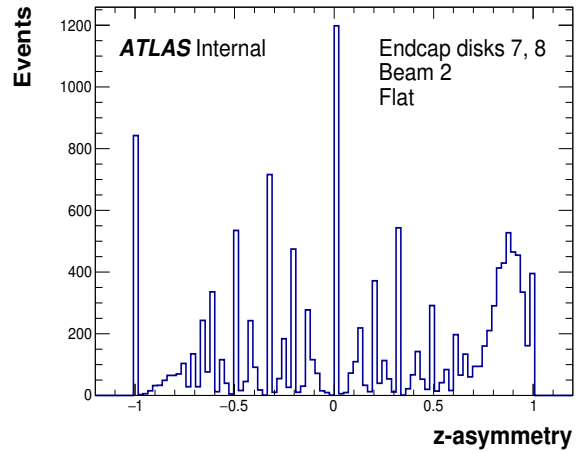
(a) 150 m pressure bump



(b) 150 m pressure bump



(c) no pressure bump



(d) no pressure bump

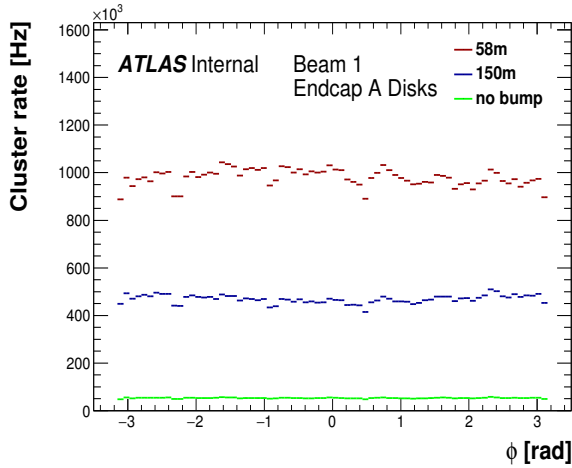
Figure 9.13: z -asymmetry distributions for UIBE during the 150 m pressure bump, and with normal pressure. A larger fraction of high z -asymmetry events can be seen in the pressure bump plots.

Pressure bump distance	Lumi block range	Pressure (beam 1)	Pressure (beam 2)
58 m	175-185	600 pbar	600 pbar
22 m	120-135	50 pbar	n/a
none	4-9	8×10^{-2} pbar	8×10^{-2} pbar

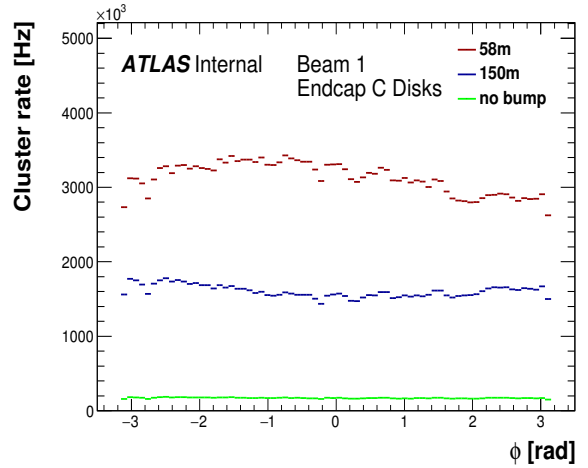
Table 9.4: Information about the pressure bumps in run 301918. The average bunch intensity was 1.02×10^{11} protons in beam 1 and 1.07×10^{11} in beam 2.

	58 m	22 m	flat
Beam 1 events	0.972	0.989	0.838
Beam 2 events	0.965	0.958	0.837

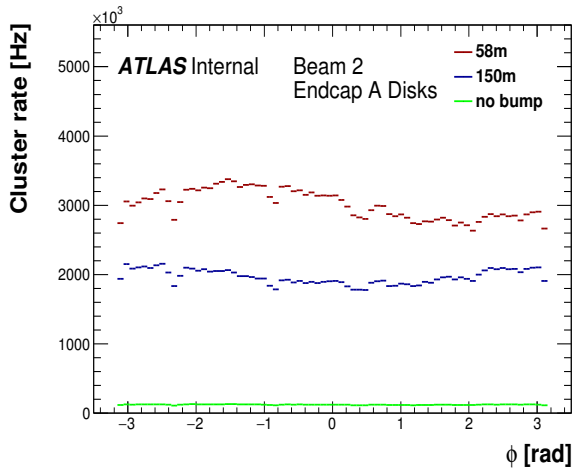
Table 9.5: Fraction of events in run 301918 selected as BIB.



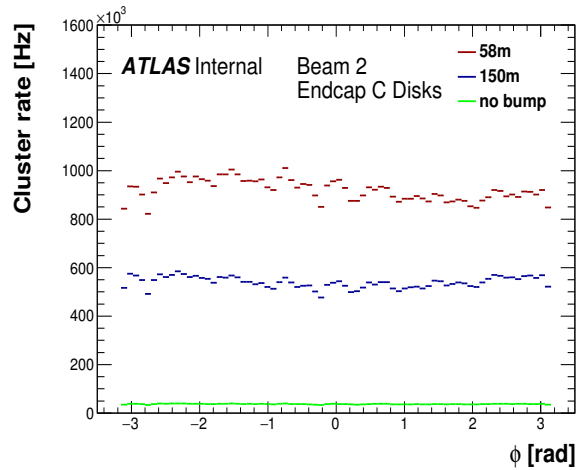
(a) Beam 1 Events



(b) Beam 1 Events

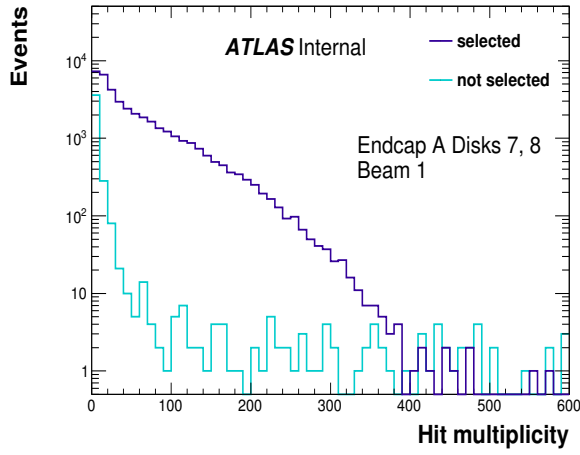


(c) Beam 2 Events

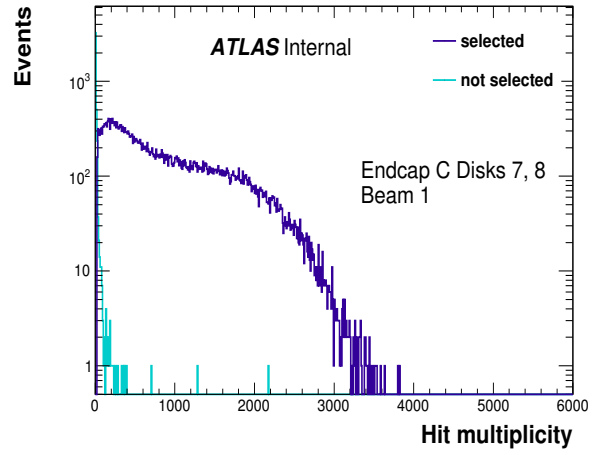


(d) Beam 2 Events

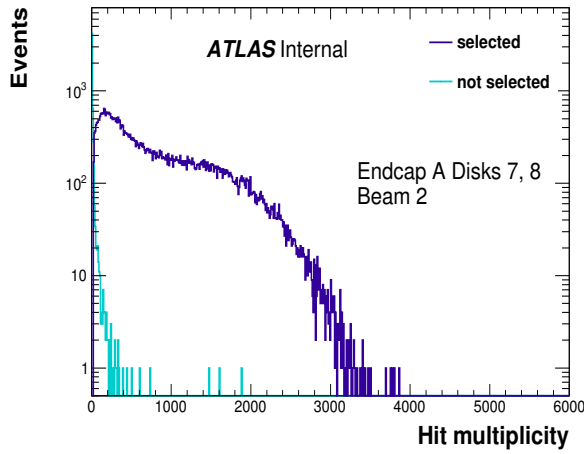
Figure 9.14: Global phi distributions of end-cap hits for UIBE during the 150 m, 19 m and 58 m pressure bumps, and no pressure bump. A phi asymmetry can be seen in the EC2 hit distribution for events during the pressure bump.



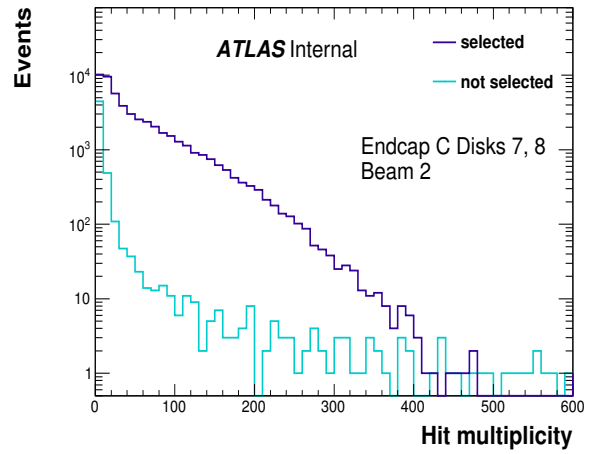
(a) 150 m pressure bump



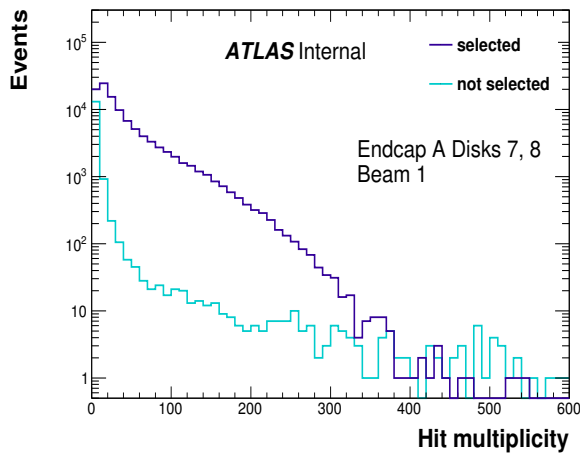
(b) 150 m pressure bump



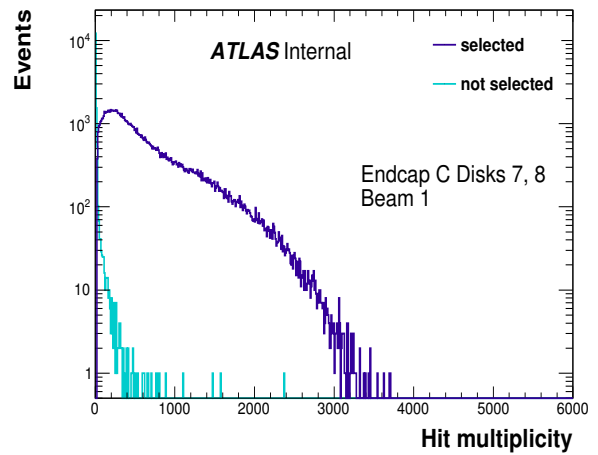
(c) 150 m pressure bump



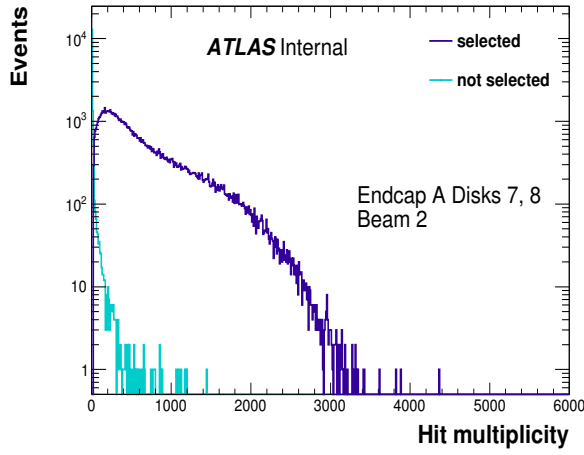
(d) 150 m pressure bump



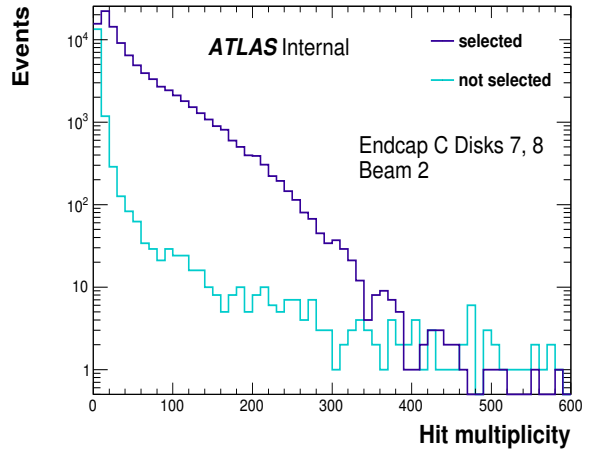
(e) 58 m pressure bump



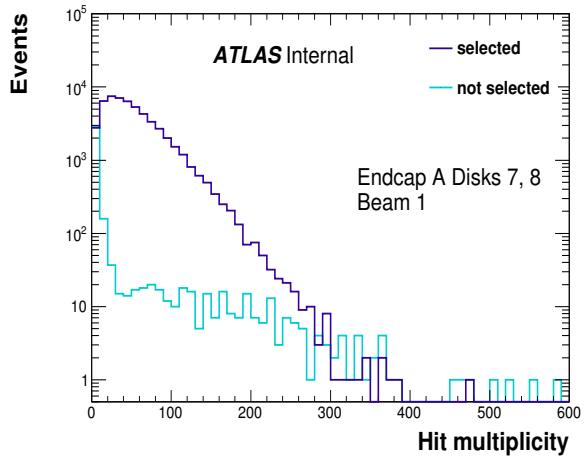
(f) 58 m pressure bump



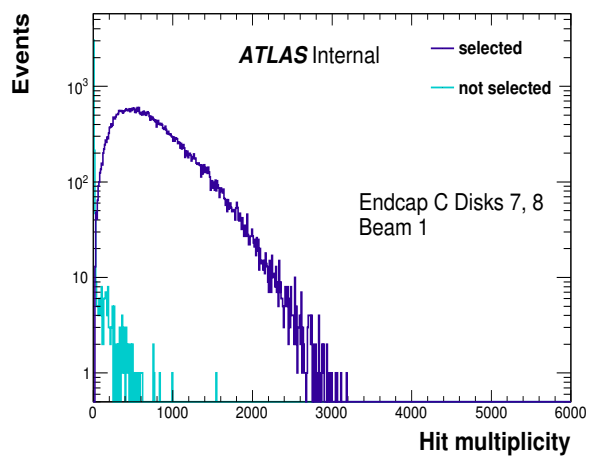
(g) 58 m pressure bump



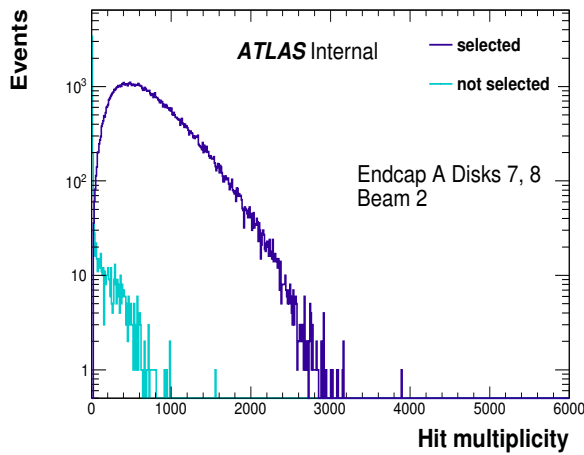
(h) 58 m pressure bump



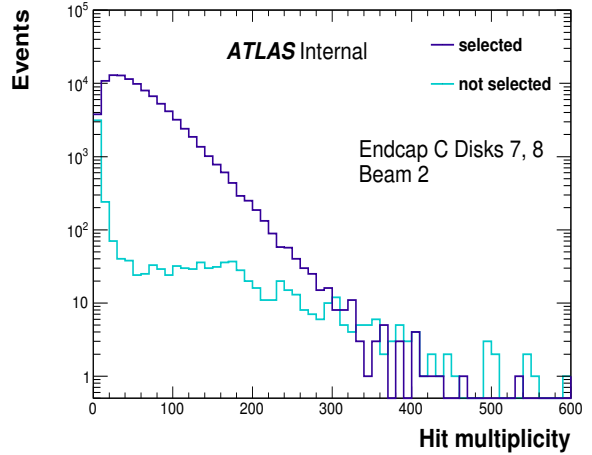
(i) 19 m pressure bump



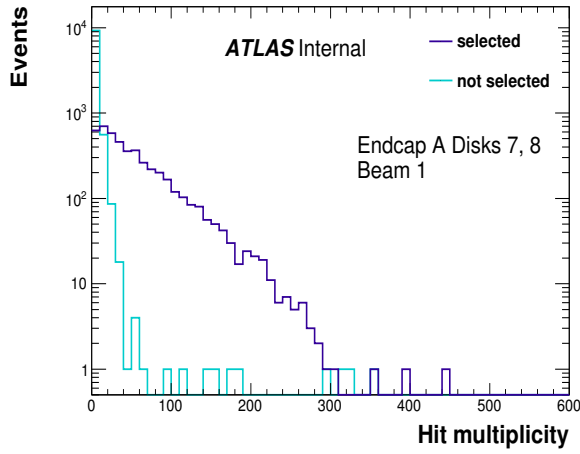
(j) 19 m pressure bump



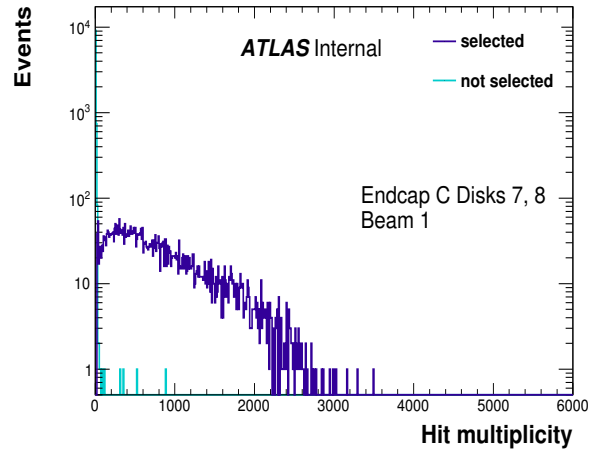
(k) 19 m pressure bump



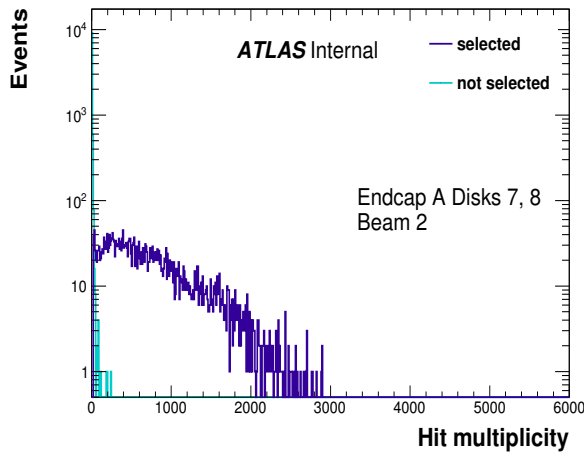
(l) 19 m pressure bump



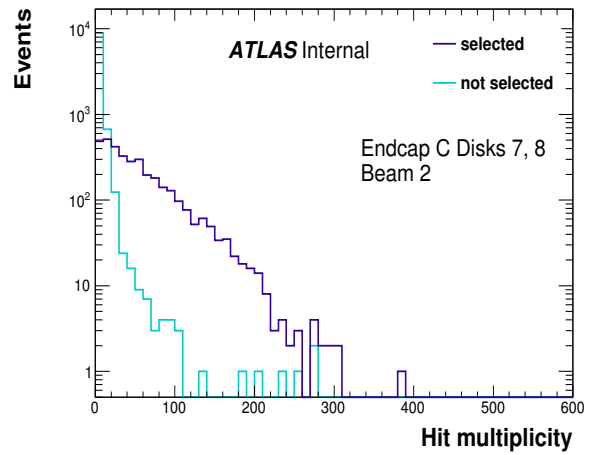
(m) no pressure bump



(n) no pressure bump



(o) no pressure bump



(p) no pressure bump

Figure 9.15: End-cap hit multiplicity distributions for selected and non-selected BIB events during each pressure bump and no pressure bump.

	2015 run	2016 run
Beam 1 events	0.936	0.956
Beam 2 events	0.921	0.934

Table 9.6: Fraction of events passing the BCM trigger selected as BIB

	150 m	58 m	19 m	flat
Beam 1 events	0.889	0.947	0.987	0.943
Beam 2 events	0.901	0.941	0.983	0.948

Table 9.7: Fraction of run 298771 events passing the BCM trigger selected as BIB.

298771, 301918 are shown in Tables 9.6-9.8.

9.4 Summary

9.4.1 Analysis with timing information

A selection, $N_{\text{early hits in disks 7 and 8 of EC1}} > 20$ and $|z_{\text{asym}}| > 0.5$, is applied to events during unpaired, isolated bunches in order to separate events containing BIB activity from noise-only events. This selection appears to be successful, yielding selected events which on average have a high in-time occupancy in the downstream end-cap (with respect to the travelling bunch), and a high early and in-time occupancy in the upstream end-cap. The unselected events have a low average occupancy in both end-caps, consistent with noise. The average occupancy contribution of BIB hits to an event containing significant BIB activity is determined by estimating the average number of in-time and early hits in a selected BIB event. The noise occupancy is negligible in this estimate. The estimated occupancy from BIB for each disk is shown in Table 9.9. The EC2 in-time occupancy is the greatest contribution for each disk. This may be explained by a combination of particle showers resulting from BIB hits, and a geometrical effect. There is a smaller contribution from early EC1 hits, and also from in-time EC1 hits which is present even in the outer disks, where most BIB hits are expected to be early.

	58 m	22 m	flat
Beam 1 events	0.947	0.986	0.966
Beam 2 events	0.935	0.959	0.922

Table 9.8: Fraction of run 301918 events passing the BCM trigger selected as BIB.

	EC1	EC2
Disks 1 & 2	~700 hits	~1000 hits
Disks 3 & 4	~600 hits	~1000 hits
Disks 5 & 6	~500 hits	~1000 hits
Disks 7 & 8	~200 hits	~1000 hits

Table 9.9: Approximate average BIB occupancy contribution for each pair of end-cap disks.

9.4.2 Analysis without timing information

It is possible to estimate the BIB rate and end-cap occupancy in a run where the SCT is read out in 01X mode. The modified selection applied to events during unpaired, isolated bunches is ≥ 25 early hits in disks 7 and 8 of end-cap C, $z_{\text{asym}} \leq -0.5$ (beam 1), or ≥ 25 early hits in disks 7 and 8 of end-cap A, $z_{\text{asym}} \geq 0.5$ (beam 2). The average BIB occupancy contribution in Table 9.9 is still appropriate as the dominant contribution comes from EC2 in-time hits.

The contribution to SCT occupancy from BIB is low compared to the occupancy from collisions and therefore has a small effect on the luminosity measurement. The rate of BIB events, which is obtained by applying the selection to all unpaired, isolated bunches, is extrapolated to all bunches in the run. The rate ought to be calculated for individual runs as run conditions impact the rate of BIB.

9.4.3 Pressure Bump Runs

Increasing the residual gas pressure inside the beam pipe is expected to increase the frequency of beam-gas events, and there is a noticeable increase in the fraction of events selected as containing BIB. The hit multiplicity distributions are affected by the distance of the localised pressure increase from ATLAS. There is a high incidence of low multiplicity BIB events when the beam-gas events occur at a large distance from IP1.

Chapter 10

Summary

The motivation for this analysis comes from the various extensions to the Standard Model that predict a heavy particle that would be produced at unknown rates in LHC proton-proton collisions and decay to a top-antitop quark pair. These theories of physics beyond the Standard Model are diverse, ranging from an extended gauge group to extra dimensions, and lead down diverging paths towards more fundamental theories of nature. It is therefore important to rule out false theories where we can, determine the parameters of theories that cannot be ruled out with the current dataset (i.e. where to keep searching), and maximise discovery potential in case one of the particle exists and is being produced in collisions.

The LHC has made progress towards these aims with $t\bar{t}$ resonances searches performed on data collected by the ATLAS and CMS detectors from proton-proton collision data at $\sqrt{s} = 8$ TeV and $\sqrt{s} = 13$ TeV for different $t\bar{t}$ decay modes. The run 2 ATLAS analysis, presented in chapter 6, searches 36 fb^{-1} of $\sqrt{s} = 13$ TeV proton-proton collision data collected by the ATLAS detector and sets upper limits on the cross-sections of new particles in a set of benchmark models. This search improved upon the existing mass constraint set on a Z' boson in a topcolour-assisted technicolour model, excluding a 1% width Z' at masses below 3.0 TeV, and a Kaluza-Klein gluon in a Randall-Sundrum model, excluding a 30% width g_{KK} at masses below 3.7 TeV, and a 15% width g_{KK} at masses below 3.8 TeV. Previous searches in the $t\bar{t}$ decay mode have set cross-section limits but not mass constraints on a Kaluza Klein graviton in a Randall-Sundrum model; this search excluded a G_{kk} in the mass interval $0.45 < m_{G_{kk}} < 0.65$ TeV.

No evidence of a $t\bar{t}$ resonance has been found so far. By the end of the High Luminosity LHC project, the LHC's dataset will have grown to 3000 fb^{-1} , and the collision energy may have increased to $\sqrt{s} = 14$ TeV. Most of this data will have been collected with an upgraded ATLAS detector. The study in chapter 7 evaluates the prospects of a $t\bar{t}$ resonances search at the HL-LHC. It is estimated that a search using 3000 fb^{-1} of data will be able to exclude a narrow Z' boson at masses below ~ 4 TeV.

Improvements in the mass reach and discovery potential of the search, above those ensured by the increase in data and collision energy, can be achieved by further refining the analysis. Many ATLAS wide techniques involving the treatment of jets, pileup, etc. are being developed and are expected to benefit ATLAS analyses in general. Additionally, methods specific to the $t\bar{t}$ resonances search that further adapt it to a boosted environment could be used to improve the sensitivity of the search to high mass signals. These include methods of treating overlapping objects and incorporating new $t\bar{t}$ decay topologies, which were presented in this thesis, and any other methods that would help differentiate $t\bar{t}$ events from background.

Bibliography

- [1] B. Abbott et al M. Aaboud G. Aad. “Search for heavy particles decaying into top-quark pairs using lepton-plus-jets events in proton–proton collisions at $\sqrt{s} = 13\text{TeV}$ with the ATLAS detector”. In: *Eur. Phys. J. C* 78 (2018). DOI: 10.1140/epjc/s10052-018-5995-6. arXiv: 1804.10823 [hep-ex].
- [2] *Study on the prospects of a $t\bar{t}$ resonance search in events with one lepton at a High Luminosity LHC*. Tech. rep. ATL-PHYS-PUB-2017-002. Geneva: CERN, Feb. 2017. URL: <https://cds.cern.ch/record/2243753>.
- [3] Anna Kathryn Duncan. *Beam Induced Background in the SCT*. Tech. rep. ATL-COM-INDET-2016-084. Geneva: CERN, Oct. 2016. URL: <https://cds.cern.ch/record/2228516>.
- [4] M. Tanabashi et al. “Review of Particle Physics”. In: *Phys. Rev. D* 98 (3 Aug. 2018), p. 030001. DOI: 10.1103/PhysRevD.98.030001. URL: <https://link.aps.org/doi/10.1103/PhysRevD.98.030001>.
- [5] Christopher T. Hill. “Topcolor assisted technicolor”. In: *Phys. Lett.* B345 (1995), pp. 483–489. DOI: 10.1016/0370-2693(94)01660-5. arXiv: hep-ph/9411426 [hep-ph].
- [6] Ben Lillie, Lisa Randall, and Lian-Tao Wang. “The Bulk RS KK-gluon at the LHC”. In: *JHEP* 09 (2007), p. 074. DOI: 10.1088/1126-6708/2007/09/074. arXiv: hep-ph/0701166 [hep-ph].
- [7] Kaustubh Agashe et al. “Warped Gravitons at the LHC and Beyond”. In: *Phys.Rev.* D76 (2007), p. 036006. DOI: 10.1103/PhysRevD.76.036006. arXiv: hep-ph/0701186 [hep-ph].
- [8] Georges Aad et al. “A search for $t\bar{t}$ resonances using lepton-plus-jets events in proton-proton collisions at $\sqrt{s} = 8\text{ TeV}$ with the ATLAS detector”. In: *JHEP* 08 (2015), p. 148. DOI: 10.1007/JHEP08(2015)148. arXiv: 1505.07018 [hep-ex].
- [9] “Search for resonant $t\bar{t}$ production in proton-proton collisions at $\sqrt{s} = 8\text{ TeV}$ ”. In: *Phys. Rev. D* 93 (1 Jan. 2016), p. 012001. DOI: 10.1103/PhysRevD.93.012001. URL: <https://link.aps.org/doi/10.1103/PhysRevD.93.012001>.

- [10] CMS Collaboration. “Search for $t\bar{t}$ resonances in highly boosted lepton+jets and fully hadronic final states in proton-proton collisions at $\sqrt{s} = 13$ TeV”. In: *JHEP* 07 (2017), p. 001. DOI: 10.1007/JHEP07(2017)001. arXiv: 1704.03366 [hep-ex].
- [11] Michael E. Peskin and Dan V. Schroeder. “An Introduction To Quantum Field Theory”. In: Westview Press (1995).
- [12] Vernon Barger, Paul Langacker, and Gabe Shaughnessy. “TeV physics and the Planck scale”. In: *New Journal of Physics* (Sept. 2007). DOI: 10.1088/1367-2630/9/9/333. URL: <https://doi.org/10.1088/1367-2630/9/9/333>.
- [13] M. Fabbrichesi F. Bazzocchi. “The little hierarchy problem for new physics just beyond the LHC”. In: (). DOI: 0.1103/PhysRevD.87.036001.
- [14] Wim de Boer. “The Discovery of the Higgs Boson with the CMS Detector and its Implications for Supersymmetry and Cosmology”. In: *Time and Matter 2013 (TAM2013) Venice, Italy*. 2013. arXiv: 1309.0721 [hep-ph]. URL: <http://inspirehep.net/record/1252561/files/arXiv:1309.0721.pdf>.
- [15] P. de Jong. *Top Physics at the LHC*. URL: https://indico.cern.ch/event/26995/contributions/604968/attachments/484312/669783/hq108_PauldeJong.pdf.
- [16] Kevin Kröniger, Andreas B. Meyer, and Peter Uwer. “Top-Quark Physics at the LHC”. In: *The Large Hadron Collider: Harvest of Run 1*. Ed. by Thomas Schörner-Sadenius. 2015, pp. 259–300. DOI: 10.1007/978-3-319-15001-7_7. arXiv: 1506.02800 [hep-ex]. URL: <http://inspirehep.net/record/1375310/files/arXiv:1506.02800.pdf>.
- [17] URL: <http://pdg.lbl.gov/2018/reviews/rpp2018-rev-ckm-matrix.pdf>.
- [18] T. Aaltonen et al. “Combination of the top-quark mass measurements from the Tevatron collider”. In: *Phys. Rev. D* 86 (2012), p. 092003. DOI: 10.1103/PhysRevD.86.092003. arXiv: 1207.1069 [hep-ex].
- [19] URL: <https://twiki.cern.ch/twiki/bin/view/AtlasPublic/TopPublicResults>.
- [20] Morad Aaboud et al. “Measurement of the $t\bar{t}$ production cross-section using $e\mu$ events with b-tagged jets in pp collisions at $\sqrt{s}=13$ TeV with the ATLAS detector”. In: *Phys. Lett. B* 761 (2016). [Erratum: *Phys. Lett. B* 772,879(2017)], pp. 136–157. DOI: 10.1016/j.physletb.2016.08.019, 10.1016/j.physletb.2017.09.027. arXiv: 1606.02699 [hep-ex].
- [21] In: (). URL: <https://atlas.web.cern.ch/Atlas/GROUPS/PHYSICS/CombinedSummaryPlots/TOP/>.

- [22] G. Altarelli and G. Parisi. “Asymptotic freedom in parton language”. In: *Nuclear Physics B* 126.2 (1977), pp. 298–318. ISSN: 0550-3213. DOI: [https://doi.org/10.1016/0550-3213\(77\)90384-4](https://doi.org/10.1016/0550-3213(77)90384-4). URL: <http://www.sciencedirect.com/science/article/pii/0550321377903844>.
- [23] B. R. Webber. “A QCD Model for Jet Fragmentation Including Soft Gluon Interference”. In: *Nucl. Phys.* B238 (1984), pp. 492–528. DOI: 10.1016/0550-3213(84)90333-X.
- [24] Bo Andersson et al. “Parton Fragmentation and String Dynamics”. In: *Phys. Rept.* 97 (1983), pp. 31–145. DOI: 10.1016/0370-1573(83)90080-7.
- [25] P. Bartalini et al. “Multi-Parton Interactions at the LHC”. In: 2011. arXiv: 1111.0469 [hep-ph]. URL: <http://inspirehep.net/record/944170/files/arXiv:1111.0469.pdf>.
- [26] S. Höch. “Matching fixed-order Matrix Elements and Parton Showers, in MCnet-LPCC School on Event Generators for LHC.” In: (2012).
- [27] S. Agostinelli et al. “GEANT4: A Simulation toolkit”. In: *Nucl. Instrum. Meth.* A506 (2003), pp. 250–303. DOI: 10.1016/S0168-9002(03)01368-8.
- [28] ATLAS Collaboration. “The simulation principle and performance of the ATLAS fast calorimeter simulation FastCaloSim”. In: (2010).
- [29] URL: <https://home.cern/science/accelerators/accelerator-complex>.
- [30] URL: https://www.lhc-closer.es/taking_a_closer_look_at_lhc/0.beam_lifetime.
- [31] Julie Haffner. “The CERN accelerator complex. Complexe des accélérateurs du CERN”. In: (Oct. 2013). General Photo. URL: <https://cds.cern.ch/record/1621894>.
- [32] Werner Herr and B Muratori. “Concept of luminosity”. In: (2006). URL: <https://cds.cern.ch/record/941318>.
- [33] ATLAS Collaboration. “Luminosity Public Results Run 2”. In: (2017). URL: <https://twiki.cern.ch/twiki/bin/view/AtlasPublic/LuminosityPublicResultsRun2>.
- [34] Karolos Potamianos. “The upgraded Pixel detector and the commissioning of the Inner Detector tracking of the ATLAS experiment for Run-2 at the Large Hadron Collider”. In: *PoS EPS-HEP2015* (2015), p. 261. arXiv: 1608.07850 [physics.ins-det].
- [35] N J Buchanan et al. “Design and implementation of the Front End Board for the readout of the ATLAS liquid argon calorimeters”. In: 3 (Mar. 2008), P03004.

- [36] Florent Fayette. “Strategies for precision measurements of the charge asymmetry of the W boson mass at the LHC within the ATLAS experiment”. PhD thesis. Paris U., VI-VII, 2009. arXiv: 0906.4260 [hep-ex]. URL: <http://inspirehep.net/record/823897/files/arXiv:0906.4260.pdf>.
- [37] Chris Meyer. “The ATLAS Tile Calorimeter Calibration and Performance”. In: *EPJ Web Conf.* 60 (2013), p. 20051. DOI: 10.1051/epjconf/20136020051. arXiv: 1310.2945 [physics.ins-det].
- [38] N Ilic. “Performance of the ATLAS Liquid Argon Calorimeter after three years of LHC operation and plans for a future upgrade”. In: *Journal of Instrumentation* 9.03 (2014), p. C03049. URL: <http://stacks.iop.org/1748-0221/9/i=03/a=C03049>.
- [39] G. Aad et al. “Readiness of the ATLAS Tile Calorimeter for LHC collisions. Readiness of the ATLAS Tile Calorimeter for LHC collisions”. In: *Eur. Phys. J. C* 70. arXiv:1007.5423. CERN-PH-EP-2010-024 (July 2010). Comments: Submitted for publication in EPJC, 1193–1236. 64 p. URL: <https://cds.cern.ch/record/1282535>.
- [40] Georges Aad et al. “Muon reconstruction performance of the ATLAS detector in proton–proton collision data at $\sqrt{s} = 13$ TeV”. In: *Eur. Phys. J. C* 76.5 (2016), p. 292. DOI: 10.1140/epjc/s10052-016-4120-y. arXiv: 1603.05598 [hep-ex].
- [41] Antonio Salvucci. “Measurement of muon momentum resolution of the ATLAS detector”. In: *EPJ Web Conf.* 28 (2012), p. 12039. DOI: 10.1051/epjconf/20122812039. arXiv: 1201.4704 [physics.ins-det].
- [42] E. Diehl. “Calibration and Performance of the ATLAS Muon Spectrometer”. In: *Particles and fields. Proceedings, Meeting of the Division of the American Physical Society, DPF 2011, Providence, USA, August 9-13, 2011*. 2011. arXiv: 1109.6933 [physics.ins-det]. URL: <http://inspirehep.net/record/930228/files/arXiv:1109.6933.pdf>.
- [43] M. Aaboud et al. “Performance of the ATLAS Track Reconstruction Algorithms in Dense Environments in LHC Run 2”. In: *Eur. Phys. J. C* 77.10 (2017), p. 673. DOI: 10.1140/epjc/s10052-017-5225-7. arXiv: 1704.07983 [hep-ex].
- [44] *Performance of the ATLAS Inner Detector Track and Vertex Reconstruction in the High Pile-Up LHC Environment*. Tech. rep. ATLAS-CONF-2012-042. Geneva: CERN, Mar. 2012. URL: <https://cds.cern.ch/record/1435196>.
- [45] R. Fruhwirth. “Application of Kalman filtering to track and vertex fitting”. In: *Nucl. Instrum. Meth.* A262 (1987), pp. 444–450. DOI: 10.1016/0168-9002(87)90887-4.
- [46] G Borissov et al. “ATLAS strategy for primary vertex reconstruction during Run-2 of the LHC”. In: *Journal of Physics: Conference Series* 664.7 (2015), p. 072041. URL: <http://stacks.iop.org/1742-6596/664/i=7/a=072041>.

- [47] The ATLAS collaboration. “Electron efficiency measurements with the ATLAS detector using the 2015 LHC proton-proton collision data”. In: (2016).
- [48] Georges Aad et al. “Electron reconstruction and identification efficiency measurements with the ATLAS detector using the 2011 LHC proton-proton collision data”. In: *Eur. Phys. J. C* 74.7 (2014), p. 2941. DOI: 10.1140/epjc/s10052-014-2941-0. arXiv: 1404.2240 [hep-ex].
- [49] *Electron and photon energy calibration with the ATLAS detector using data collected in 2015 at $\sqrt{s} = 13$ TeV*. Tech. rep. ATL-PHYS-PUB-2016-015. Geneva: CERN, Aug. 2016. URL: <https://cds.cern.ch/record/2203514>.
- [50] Georges Aad et al. “Electron and photon energy calibration with the ATLAS detector using LHC Run 1 data”. In: *Eur. Phys. J. C* 74.10 (2014), p. 3071. DOI: 10.1140/epjc/s10052-014-3071-4. arXiv: 1407.5063 [hep-ex].
- [51] Georges Aad et al. “Measurement of the muon reconstruction performance of the ATLAS detector using 2011 and 2012 LHC proton-proton collision data. Measurement of the muon reconstruction performance of the ATLAS detector using 2011 and 2012 LHC proton-proton collision data”. In: *Eur. Phys. J. C* 74. CERN-PH-EP-2014-151. CERN-PH-EP-2014-151 (July 2014). Comments: 21 pages plus author list + cover pages (34 pages total), 21 figures, 2 tables, submitted to EPJC, All figures including auxiliary figures are available at <http://atlas.web.cern.ch/Atlas/GROUPS/PHYSICS/PAPERS/PERF-2014-05/>, 3130. 34 p. URL: <http://cds.cern.ch/record/1743068>.
- [52] URL: <http://cms.web.cern.ch/news/jets-cms-and-determination-their-energy-scale>.
- [53] Matteo Cacciari, Gavin P. Salam, and Gregory Soyez. “The anti- k_t jet clustering algorithm”. In: *Journal of High Energy Physics* 2008.04 (2008), p. 063. URL: <http://stacks.iop.org/1126-6708/2008/i=04/a=063>.
- [54] The ATLAS collaboration. “Monte Carlo Calibration and Combination of In-situ Measurements of Jet Energy Scale, Jet Energy Resolution and Jet Mass in ATLAS”. In: (2015).
- [55] Matteo Cacciari and Gavin P. Salam. “Pileup subtraction using jet areas”. In: *Phys. Lett. B* 659 (2008), pp. 119–126. DOI: 10.1016/j.physletb.2007.09.077. arXiv: 0707.1378 [hep-ph].
- [56] M. Aaboud et al. “Jet energy scale measurements and their systematic uncertainties in proton-proton collisions at $\sqrt{s} = 13$ TeV with the ATLAS detector”. In: *Phys. Rev. D* 96 (7 Oct. 2017), p. 072002. DOI: 10.1103/PhysRevD.96.072002. URL: <https://link.aps.org/doi/10.1103/PhysRevD.96.072002>.

- [57] Georges Aad et al. “Performance of pile-up mitigation techniques for jets in pp collisions at $\sqrt{s} = 8$ TeV using the ATLAS detector. Performance of pile-up mitigation techniques for jets in pp collisions at $\sqrt{s} = 8$ TeV using the ATLAS detector”. In: *Eur. Phys. J. C* 76.CERN-PH-EP-2015-206. CERN-PH-EP-2015-206 (Oct. 2015). 38 pages, plus author list - 54 pages (total), 19 figures. Published in EPJC. All figures including auxiliary figures are available at <http://atlas.web.cern.ch/Atlas/GROUPS/PHYSICS/PAPERS/PERF-2014-03/>, 581. 54 p. URL: <https://cds.cern.ch/record/2058295>.
- [58] David Krohn, Jesse Thaler, and Lian-Tao Wang. “Jet Trimming”. In: *JHEP* 02 (2010), p. 084. DOI: 10.1007/JHEP02(2010)084. arXiv: 0912.1342 [hep-ph].
- [59] *Jet mass reconstruction with the ATLAS Detector in early Run 2 data*. Tech. rep. ATLAS-CONF-2016-035. Geneva: CERN, July 2016. URL: <https://cds.cern.ch/record/2200211>.
- [60] *Optimisation of the ATLAS b-tagging performance for the 2016 LHC Run*. Tech. rep. ATL-PHYS-PUB-2016-012. Geneva: CERN, June 2016. URL: <https://cds.cern.ch/record/2160731>.
- [61] ATLAS Collaboration. “Performance of top-quark and W boson tagging with ATLAS in Run 2”. In: ().
- [62] Julien Caudron et al. *Boosted hadronic top identification at ATLAS for early 13 TeV data*. Tech. rep. ATL-COM-PHYS-2015-755. Geneva: CERN, July 2015. URL: <https://cds.cern.ch/record/2036200>.
- [63] URL: <https://atlas.cern/glossary/standard-deviation-sigma>.
- [64] Georgios Choudalakis. “On hypothesis testing, trials factor, hypertests and the BumpHunter”. In: *Proceedings, PHYSTAT 2011 Workshop on Statistical Issues Related to Discovery Claims in Search Experiments and Unfolding, CERN, Geneva, Switzerland 17-20 January 2011*. 2011. arXiv: 1101.0390 [physics.data-an]. URL: <https://inspirehep.net/record/883244/files/arXiv:1101.0390.pdf>.
- [65] URL: <https://newonlinecourses.science.psu.edu/stat414/node/307/>.
- [66] Torbjorn Sjostrand, Stephen Mrenna, and Peter Z. Skands. “A Brief Introduction to PYTHIA 8.1”. In: *Comput. Phys. Commun.* 178 (2008), pp. 852–867. DOI: 10.1016/j.cpc.2008.01.036. arXiv: 0710.3820 [hep-ph].
- [67] Richard D. Ball et al. “Parton distributions for the LHC Run II”. In: *JHEP* 04 (2015), p. 040. DOI: 10.1007/JHEP04(2015)040. arXiv: 1410.8849 [hep-ph].
- [68] Lisa Randall and Raman Sundrum. “A Large mass hierarchy from a small extra dimension”. In: *Phys. Rev. Lett.* 83 (1999), pp. 3370–3373. DOI: 10.1103/PhysRevLett.83.3370. arXiv: hep-ph/9905221 [hep-ph].

- [69] Gilad Perez Kaustubh Agashe Hooman Davoudiasl and Amarjit Soni. *Warped Gravitons at the LHC and Beyond*. URL: <https://arxiv.org/pdf/hep-ph/0701186.pdf>.
- [70] J. Alwall et al. “The automated computation of tree-level and next-to-leading order differential cross sections, and their matching to parton shower simulations”. In: *JHEP* 07 (2014), p. 079. DOI: 10.1007/JHEP07(2014)079. arXiv: 1405.0301 [hep-ph].
- [71] Paolo Nason. “A New method for combining NLO QCD with shower Monte Carlo algorithms”. In: *JHEP* 11 (2004), p. 040. DOI: 10.1088/1126-6708/2004/11/040. arXiv: hep-ph/0409146 [hep-ph].
- [72] Hung-Liang Lai et al. “New parton distributions for collider physics”. In: *Phys. Rev. D* 82 (2010), p. 074024. DOI: 10.1103/PhysRevD.82.074024. arXiv: 1007.2241 [hep-ph].
- [73] Torbjorn Sjostrand, Stephen Mrenna, and Peter Z. Skands. “PYTHIA 6.4 Physics and Manual”. In: *JHEP* 05 (2006), p. 026. DOI: 10.1088/1126-6708/2006/05/026. arXiv: hep-ph/0603175 [hep-ph].
- [74] J. Pumplin et al. “New generation of parton distributions with uncertainties from global QCD analysis”. In: *JHEP* 07 (2002), p. 012. DOI: 10.1088/1126-6708/2002/07/012. arXiv: hep-ph/0201195 [hep-ph].
- [75] D. J. Lange. “The EvtGen particle decay simulation package”. In: *Nucl. Instrum. Meth.* A462 (2001), pp. 152–155. DOI: 10.1016/S0168-9002(01)00089-4.
- [76] Matteo Cacciari, Michal Czakon, and Mangano. “Top-pair production at hadron colliders with next-to-next-to-leading logarithmic soft-gluon resummation”. In: *Phys. Lett.* B710 (2012). DOI: 10.1016/j.physletb.2012.03.013. arXiv: 1111.5869 [hep-ph].
- [77] M. Beneke et al. “Hadronic top-quark pair production with NNLL threshold”. In: *Nucl. Phys.* B855 (2012), pp. 695–741. DOI: 10.1016/j.nuclphysb.2011.10.021. arXiv: 1109.1536 [hep-ph].
- [78] T. Gleisberg et al. “Event generation with SHERPA 1.1”. In: *JHEP* 02 (2009), p. 007. DOI: 10.1088/1126-6708/2009/02/007. arXiv: 0811.4622 [hep-ph].
- [79] Zinonas Zinonos and. “Measurement of multi-jet cross-sections in proton-proton collisions at 7 TeV center-of-mass energy in ATLAS”. In: *Journal of Physics: Conference Series* (2011). DOI: 10.1088/1742-6596/323/1/012006. URL: <https://doi.org/10.1088/1742-6596/323/1/012006>.
- [80] *A search for top-antitop resonances in the lepton+jets final state using 36.1 fb⁻¹ of proton-proton collisions at $\sqrt{s} = 13$ TeV*. Tech. rep. ATL-COM-PHYS-2016-1036. Geneva: CERN, Apr. 2018.

- [81] P.Uwer J.H.Kühn A.Scharf. “Weak Interactions in Top-Quark Pair Production at Hadron Colliders: An Update”. In: (). DOI: 10.1103/PhysRevD.91.014020.
- [82] Vladislav Balagura. “Notes on Van der Meer scan for absolute luminosity measurement”. In: *Nuclear Instruments and Methods in Physics Research Section A: Accelerators, Spectrometers, Detectors and Associated Equipment* 654.1 (2011), pp. 634–638. ISSN: 0168-9002. DOI: <https://doi.org/10.1016/j.nima.2011.06.007>. URL: <http://www.sciencedirect.com/science/article/pii/S0168900211011181>.
- [83] Morad Aaboud et al. “Luminosity determination in pp collisions at $\sqrt{s} = 8$ TeV using the ATLAS detector at the LHC. Luminosity determination in pp collisions at $\sqrt{s} = 8$ TeV using the ATLAS detector at the LHC”. In: *Eur. Phys. J. C* 76.CERN-EP-2016-117. CERN-EP-2016-117. 12 (Aug. 2016). Comments: 53 pages plus author list + cover pages (71 pages total), 19 figures, 9 tables, submitted to EPJC, All figures including auxiliary figures are available at <http://atlas.web.cern.ch/Atlas/GROUPS/PHYSICS/PAPERS/DAP2013-01>, 653. 71 p. URL: <https://cds.cern.ch/record/2208146>.
- [84] URL: <http://pdg.lbl.gov/2018/reviews/rpp2018-rev-top-quark.pdf>.
- [85] Georges Aad et al. “Electron reconstruction and identification efficiency measurements with the ATLAS detector using the 2011 LHC proton-proton collision data. Electron reconstruction and identification efficiency measurements with the ATLAS detector using the 2011 LHC proton-proton collision data”. In: *Eur. Phys. J. C* CERN-PH-EP-2014-040. CERN-PH-EP-2014-040 (Apr. 2014). Comments: 38 pages plus author list (62 pages total), 20 figures, 4 tables, submitted to JHEP, All figures including auxiliary figures are available at <https://atlas.web.cern.ch/Atlas/GROUPS/PHYSICS/PAPERS/PERF-2013-03/>, 74. 38 p. URL: <https://cds.cern.ch/record/1694142>.
- [86] URL: <https://cds.cern.ch/record/2292175/files/CERN-THESIS-2017-222.pdf>.
- [87] URL: <https://project-hl-lhc-industry.web.cern.ch/content/hiluminutshell>.
- [88] *Expected performance for an upgraded ATLAS detector at High-Luminosity LHC*. Tech. rep. ATL-PHYS-PUB-2016-026. Geneva: CERN, Oct. 2016. URL: <https://cds.cern.ch/record/2223839>.
- [89] HL-LHC project. *LHC Timeline*. URL: <https://project-hl-lhc-industry.web.cern.ch/content/project-schedule%7D>.
- [90] *W.J. Stirling, private communication*.
- [91] *ATLAS Run 1 Pythia8 tunes*. Tech. rep. ATL-PHYS-PUB-2014-021. Geneva: CERN, Nov. 2014. URL: <http://cds.cern.ch/record/1966419>.

- [92] Jun Gao et al. “Next-to-leading order QCD corrections to the heavy resonance production and decay into top quark pair at the LHC”. In: *Phys. Rev. D* 82 (2010), p. 014020. DOI: 10.1103/PhysRevD.82.014020. arXiv: 1004.0876 [hep-ph].
- [93] Borut Paul Kersevan and Elzbieta Richter-Was. “The Monte Carlo event generator AcerMC versions 2.0 to 3.8 with interfaces to PYTHIA 6.4, HERWIG 6.5 and ARIADNE 4.1”. In: *Comput. Phys. Commun.* 184 (2013), pp. 919–985. DOI: 10.1016/j.cpc.2012.10.032. arXiv: hep-ph/0405247 [hep-ph].
- [94] *Expected performance for an upgraded ATLAS detector at High-Luminosity LHC*. Tech. rep. ATL-PHYS-PUB-2016-026. Geneva: CERN, Oct. 2016. URL: <https://cds.cern.ch/record/2223839>.
- [95] Kyle Cranmer et al. “HistFactory: A tool for creating statistical models for use with RooFit and RooStats”. In: (2012).
- [96] Claire Malone. *Feasibility Study on the use of the ATLAS SCT as a Luminometer*. Tech. rep. ATL-COM-INDET-2016-022. Geneva: CERN, Mar. 2016. URL: <https://cds.cern.ch/record/2139620>.
- [97] The ATLAS Collaboration. *ATLAS Event Images*. URL: <http://www.atlas.ch/photos/events-beam-halo.html>.
- [98] J Roberts et al. *Beam Induced Backgrounds Measured in the ATLAS Semiconductor Tracker*. Tech. rep. ATL-COM-INDET-2012-032. Geneva: CERN, May 2012. URL: <https://cds.cern.ch/record/1452627>.
- [99] Manuel Kayl. “Tracking Performance of the ATLAS Inner Detector and Observation of Known Hadrons”. In: *Hadron collider physics. Proceedings, 22nd Conference, HCP 2010, Toronto, Canada, August 23-27, 2010*. 2010. arXiv: 1010.1091 [physics.ins-det].